Dissertation zur Erlangung des Doktorgrades

der Fakultät für Chemie und Pharmazie

der Ludwig-Maximilians-Universität München

Biomimetics for Lanthanide and Calcium Dependent Alcohol Dehydrogenases

Violeta Aleksandrova Vetsova

aus Plovdiv, Bulgarien

2023

Erklärung

Diese Dissertation wurde im Sinne von § 7 der Promotionsordnung vom 28. November 2011 von Frau Prof. Dr. Lena J. Daumann betreut.

Eidesstattliche Versicherung

Diese Dissertation wurde eigenständig und ohne unerlaubte Hilfe erarbeitet.

München, 09.11.2023

……...

Violeta A. Vetsova

Dissertation eingereicht am:	14.11.2023
1. Gutachterin:	Prof. Dr. Lena J. Daumann
2. Gutachter:	Prof. Dr. Konstantin Karaghiosoff
Mündliche Prüfung am:	13.12.2023

Diese Arbeit wurde in der Zeit von Dezember 2018 bis November 2023 am Department für Chemie der Ludwig-Maximilians-Universität München unter Anleitung von Frau Prof. Dr. Lena J. Daumann durchgeführt.

ACKNOWLEDGEMENTS

First and foremost, I would like to thank Prof. Dr. Lena Daumann for giving me the opportunity to carry out my PhD research in her group. I am deeply grateful for her supporting guidance during my research, for giving me the freedom to explore my ideas, coupled with the trust she put in me. Her enthusiasm and generosity were truly inspiring and constant motivation to pursue new ideas within the remarkable working environment she created.

I am very thankful to Prof. Dr. Konstantin Karaghiosoff for agreeing to be the second reviewer of my thesis and for his constant support throughout the last years.

I would also like to thank the members of my defense committee, Prof. Dr. Lena Daumann, Prof. Dr. Konstantin Karaghiosoff, Prof. Dr. Ivana Ivanović-Burmazović, Prof. Dr. Oliver Trapp, Prof. Dr. Franz Bracher and Prof. Dr. Silvija Markic for their interest shown in this manuscript.

I would like to thank PD Dr. Patrick Weis, Prof. Dr. Michael Seitz, Prof. Dr. Manfred Kappes and their coworkers for the collaborations in the past years. In addition, I want to thank Dr. Katherine Fisher for her help with the interpretation of the EPR data.

My gratitude goes to Ioana Ciubotaru, Annika Menke, Rachel Janßen and Sophie Gutenthaler-Tietze for the careful corrections of this manuscript.

I would like to thank all past and present members of the Daumann group whom I have had the pleasure of meeting. In particular, I want to mention my former and current lab mates Ioana Ciubotaru, Annika Menke, Rachel Janßen and Dr. Henning Widmann. Thank you for giving me the best working atmosphere, for being wonderful friends both inside and outside the lab, and for making our daily working routine enjoyable. A special thanks goes to Helena Singer for the fantastic Zumba classes – they were really the best! I also want to acknowledge Rachel Janßen for her exceptional organization of all group events, especially the game nights. Additionally, I would also like to thank Dr. Bérénice Jahn, Sophie Gutenthaler-Tietze, Mahn Tri Phi, Michael Mertens, Doreen Reuter, Philippe de Bary and Dr. Niko Lindlar for the great time we spend together, for the enjoyable coffee breaks, and so much more.

I would also like to thank my former students Rachel Janßen, Jonas Weiser, Almuth Schmid and Sophia Glocker for their contributions during their internships.

I would like to thank Lida Holowatyj-den Toom for her excellent support in administrative questions. My gratitude goes to all members of the central analytics department at LMU Munich and especially to Brigitte Breitenstein for her invaluable help.

A special thanks goes to my friends, and especially Keily and Maria for their friendship and encouragement.

I would like to thank Marius for his invaluable support, patience and love, which contributed more to this work, than one can imagine.

Finally, I want to express my deepest gratitude to my parents Hristina and Aleksandar for their unwavering support and their never-ending love throughout my life. Their encouragement, sacrifices and guidance have been the foundation of my journey, and I am endlessly thankful for all that they have done for me.

LIST OF PUBLICATIONS AND STATEMENT OF CONTRIBUTION

- **Publications Published as Part of this Thesis**

Pyrroloquinoline Quinone Aza-Crown Ether Complexes as Biomimetics for Lanthanide and Calcium Dependent Alcohol Dehydrogenases

Violeta A. Vetsova, Katherine R. Fisher, Henning Lumpe, Alexander Schäfer, Erik K. Schneider, Patrick Weis and Lena J. Daumann

Published in: *Chem. Eur. J.* **2021**, *27*, 10087–10098. DOI: 10.1002/chem.202100346.

Ludwig Maximilian University of Munich (supervisor: Prof. Dr. Lena Daumann): Violeta Vetsova wrote the main part of the manuscript, certain parts of the introduction, optimized the synthesis and purification of the reported aza-crown ether ligand, performed all NMR experiments described in the sections "Metal ion coordination" and "Alcohol oxidation", discussed the received results, wrote the respective part of the experimental section and generated all of the related figures, reaction schemes and tables. Violeta Vetsova also conducted all EPR experiments, described in the section "EPR investigations" and in the supporting information. The processing and discussion of the data from the EPR experiments was realized by Dr. Katherine Fisher. Dr. Henning Lumpe wrote parts of the introduction, performed the initial synthesis of the PQQ compounds, discussed the results and wrote the respective parts of the experimental section. In every aspect, Prof. Dr. Lena Daumann contributed in guidance and advice, wrote the abstract and the conclusion.

Karlsruhe Institute of Technology (supervisor: PD Dr. Patrick Weis): Alexander Schäfer, Erik K. Schneider and PD Dr. Patrick Weis performed the mass spectrometry and ion mobility experiments and DFT calculations described in the section "Impact of the counterions on the complex species", discussed the received results, wrote the respective part of the experimental section and generated all of the related figures and tables.

All authors contributed in revising the manuscript.

Ion Mobility Studies of Pyrroloquinoline Quinone Aza-Crown Ether–Lanthanide Complexes

Alexander Schäfer, Violeta A. Vetsova, Erik K. Schneider, Manfred Kappes, Michael Seitz, Lena J. Daumann and Patrick Weis

Published in: *J. Am. Soc. Mass Spectrom.* **2022**, *33*, 722–730. DOI: 10.1021/jasms.2c00023.

Ludwig Maximilian University of Munich (supervisor: Prof. Dr. Lena Daumann): Violeta Vetsova synthesized the PQQ aza-crown ether ligand. She also conducted the temperature-dependent NMR measurements described in the supporting information and discussed the respective results. Prof. Dr. Lena Daumann contributed in guidance and advice.

Karlsruhe Institute of Technology (supervisors: Prof. Dr. Manfred Kappes and PD Dr. Patrick Weis): Alexander Schäfer, Erik K. Schneider, Prof. Dr. Manfred Kappes and PD Dr. Patrick Weis wrote the main part of the manuscript, performed and discussed all ion mobility and mass spectrometry studies, and conducted all quantum-chemical calculations.

Prof. Dr. Michael Seitz (University of Tübingen) contributed in guidance and advice.

All authors contributed in revising the manuscript.

Modular Synthesis of New Pyrroloquinoline Quinone Derivatives

Rachel Janßen, Violeta A. Vetsova, Dominik Putz, Peter Mayer and Lena J. Daumann

Published in: *Synthesis* **2023**, *55*, 1000-1006. DOI: 10.1055/s-0041-1738426.

Violeta Vetsova (supervisor: Prof. Dr. Lena Daumann) started the project, conducted part of the syntheses, discussed the respective results and generated all reaction schemes in the manuscript. She also supervised Rachel Janßen during her research internship. Rachel Janßen performed part of the syntheses during her research internship, and optimized the experimental procedures during her master thesis and PhD studies. She also wrote the main part of the manuscript. During his research internship, Dominik Putz assisted in the synthesis of certain precursors under the guidance of Rachel Janßen. The X-ray analysis, including data collection and structure elucidation, was conducted by Dr. Peter Mayer. Prof. Dr. Lena Daumann contributed in guidance and advice.

Rachel Janßen, Violeta Vetsova and Prof. Dr. Daumann contributed in revising the manuscript.

- **Publications which are not Part of this Thesis**

Die vier Neuen: Nihonium, Moscovium, Tenness und Oganesson

Violeta A. Vetsova and Lena J. Daumann

Published in: *Nachrichten aus der Chemie* **2018**, *66*, 713–716. DOI: 10.1002/nadc.20184077083.

- **Publications Published Prior to this Thesis**

Chromium-Catalyzed Cross-Coupling Reactions of Alkylmagnesium Reagents with Halo-Quinolines and Activated Aryl Chlorides

Andreas B. Bellan, Olesya M. Kuzmina, Violeta A. Vetsova and Paul Knochel

Published in: *Synthesis* **2017**, *49*, 188–194. DOI: 10.1055/s-0035-1561615.

POSTER PRESENTATIONS

The Surprising Bioinorganic Chemistry of Rare Earth Elements - Spectroscopic Models for the Characterization of REE-dependent Methanol Dehydrogenases

Henning Lumpe, Bérénice Jahn, Violeta A. Vetsova, Patrick Grassl, Sina Witzel, Arjan Pol, Huub J. M. Op den Camp and Lena J. Daumann

13. Koordinationschemie-Treffen, Potsdam (Germany), **2017**.

PQQ and its Derivatives and their Relevance to Lanthanide Dependent Enzymes

Violeta A. Vetsova and Lena J. Daumann

URCUP, Irsee (Germany), **2018**.

PQQ Aza-Crown Ether Complexes as Biomimetics for Lanthanide Dependent Methanol Dehydrogenases

Violeta A. Vetsova, Henning Lumpe, Marianne Friemert, Jens Kalmbach, Michael Seitz and Lena J. Daumann

16. Koordinationschemie-Treffen, Freiburg (Germany), **2020**.

An Active Site Model for Lanthanide and Calcium Dependent Alcohol Dehydrogenases

Violeta A. Vetsova, Katherine R. Fisher, Henning Lumpe, Alexander Schäfer, Erik K. Schneider, Patrick Weis and Lena J. Daumann

EuroBIC-16, Grenoble (France), **2022**.

ORAL PRESENTATIONS

Pyrroloquinoline Quinone Aza-Crown Ether Complexes as Biomimetics for Lanthanide and Calcium Dependent Alcohol Dehydrogenases

Violeta A. Vetsova, Katherine R. Fisher, Henning Lumpe, Alexander Schäfer, Erik K. Schneider, Patrick Weis and Lena J. Daumann

XXX. Tage der Seltenen Erden (Terrae Rarae), Montpellier (France), **2021**.

An Active Site Model for Lanthanide and Calcium Dependent Alcohol Dehydrogenases

Violeta A. Vetsova, Katherine R. Fisher, Henning Lumpe, Alexander Schäfer, Erik K. Schneider, Patrick Weis and Lena J. Daumann

17. Koordinationschemie-Treffen, Jena (Germany), **2022**.

An Active Site Model for Lanthanide and Calcium Dependent Alcohol Dehydrogenases

Violeta A. Vetsova, Katherine R. Fisher, Henning Lumpe, Alexander Schäfer, Erik K. Schneider, Patrick Weis and Lena J. Daumann

JAWSChem Webinar Series, **2022**.

DISCLOSURE OF PARTICIPATION

The people mentioned underneath contributed in the practical laboratory work of this thesis, as part of their research internships and Bachelor Theses. I want to express my gratitude and acknowledge their contributions.

RACHEL JANßEN assisted in the synthesis of some of the precursors for the novel PQQ derivatives **$P_{ME}QQ_{MEM}$** and **$P_{K}QQ_{MEM}$** described in Chapter II.1 as part of her research internship. She further optimized the entire synthesis during her master thesis and PhD studies.

JONAS WEISER investigated the synthesis of ligand **PQQ_{DFO}** described in Chapter II.6.

ALMUTH SCHMID attempted the synthesis of anhydrous lanthanide salts described in Chapter VI.4.1.

SOPHIA GLOCKER assisted in the synthesis of the reduced PQQ dimethyl ester species **$PQQMe_2H_2$** described in Chapter II.5. Furthermore, she performed the initial spectrophotometric analyses with ligand **$PQQMe_2$** together with La^{3+}, Eu^{3+} and Lu^{3+} and conducted the UV-Vis titration experiments by incremental addition of methanol to different **$PQQMe_2$**/Ln^{3+} complex solutions described in Chapter III.3.2.

SUMMARY

Methanol dehydrogenase (MDH) is an enzyme responsible for catalyzing the two-electron oxidation of methanol to formaldehyde. It belongs to the family of the quinoproteins which utilize quinone-containing compounds such as pyrroloquinoline quinone (PQQ) as prosthetic groups in their active sites. For a long time, it was assumed that most methanotrophic and methylotrophic bacteria metabolize methanol solely through the well-known calcium(II)-dependent MDH. However, recent discoveries have unveiled that certain strains are strictly lanthanide-dependent due to a second type MDH, which carries a lanthanide(III) ion in its active site. Lanthanides were traditionally considered biologically irrelevant, but this and further recent findings have demonstrated that lanthanide utilizing bacteria not only exist, but are also widespread in nature.

The goal of this thesis was the synthesis of PQQ-based ligands and the characterization of their metal complexes as functional models for calcium and lanthanide-dependent MDHs. Possible differences between the metals and their interactions with various ligands were evaluated. Furthermore, the ability of the model complexes to facilitate alcohol oxidation was studied. An additional project aimed to develop a new and optimized analytical method for monitoring the progress of alcohol dehydrogenation reactions.

Chapter I provides an encompassing introduction to lanthanides in a broader context, emphasizing crucial aspects of lanthanide biochemistry, with a specific focus on calcium(II)- and lanthanide(III)-dependent MDH enzymes.

Considering that the investigation of biomimetics could shed some light into fundamental aspects of structure and reactivity of their biological counterparts, Chapter II deals with the synthesis of different PQQ-based compounds as ligands for MDH-inspired biomimetics. Based on the total synthesis of PQQ published by Corey and Tramontano,[1] two novel PQQ derivatives bearing methyl and ketone groups instead of carboxylic acid moieties were synthesized. In addition, various ligands were synthesized through amide coupling of PQQ dimethyl ester with different co-ligands.

Chapter III focuses on the coordination chemistry of PQQ derivatives with biologically relevant metal ions such as alkaline earth metal ions and lanthanide ions. Understanding the nature of interaction between the ligands and metal ions is crucial for advancing the field of MDH biomimetics. ^{1}H NMR investigations with ligand PQQMe$_2$-1-aza-15-crown-5 gave evidence for a metal ion coordination at the biologically relevant pocket of PQQ. In addition, UV-Vis titration studies demonstrated different lanthanide(III) selectivity patterns as well as different chelator affinities for different ligands. Moreover, the chapter gives a short overview of the luminescent properties of different europium(III)

complexes and presents the results of a gas phase characterization of PQQ and lanthanide-PQQ-crown ether ligand complexes.

Chapter IV presents the spectroscopic evaluation of PQQ-based biomimetic complex systems capable of facilitating the oxidation reaction of benzylic alcohols to the respective aldehydes. The investigations were conducted employing methods such as NMR, EPR and GC-MS. Thereby, the importance of ligand nature, charge and size of the complex cation, as well as counterions and base were demonstrated. Furthermore, a PQQ-based radical was observed under substrate turnover conditions. Finally, a new method for analyzing the progress of alcohol oxidation reactions was evaluated using GC-MS.

TABLE OF CONTENTS

I. INTRODUCTION

"The seeds of technology",[2] "the vitamins of modern industry"[3] – these are just a few of the designations used to describe the lanthanides (Ln) – the elements usually represented near the bottom of the periodic table, which constitute crucial components integrated into a diverse array of everyday applications. However, the impact of lanthanides on biological systems remained insufficiently explored for years. Since their initial discovery in the late 1800s, it was generally assumed that these elements had no role in biology because of their low solubility in neutral water, which limits their bioavailability. This led to the dismissal of the possibility of an evolutionary adaptation favoring lanthanide-dependent biochemistry.[4–7] As a consequence, the essential biological role of the lanthanides remained undiscovered until 2011. Subsequent investigations have revealed, however, that some lanthanides serve as vital cofactors for bacterial enzymes, overturning prior assumptions that these elements are biologically inert.[3,8–10] These young breakthroughs have emerged to a major and rapidly expanding research area, shedding light on the widespread presence of lanthanide-utilizing organisms in the environment and recognizing the lanthanides as the "new life metals".[5]

1. Lanthanides

The lanthanide series includes the 14 elements from cerium to lutetium and together with lanthanum (by common usage also numbered among the lanthanide series although "lanthanide" means "like lanthanum") and the chemically similar scandium and yttrium makes up the group known as rare earth elements (REEs). Unlike their name suggests, the rare earth elements are not as rare as it may seem.[11] The REEs are relatively abundant in the earth's crust and particularly the lightest REEs (Sc, Y, La, Ce, Pr, Nd) are found in concentrations comparable to other important metals like copper, zinc, and lead.[12–14] Even the occurrence of the two least abundant ones, thulium and lutetium, is higher than the one of bismuth, gold, silver or platinum.[15]

In 1869, when Mendeleev first introduced his periodic table, it only featured lanthanum, cerium and didymium (now recognized as a mixture of praseodymium and neodymium), along with another mixture blend resembling erbium and yttrium.[16–18] It took a little over a century to isolate and characterize the remaining non-radioactive lanthanides, with lutetium being the final one in 1907. The

radioactive promethium, which lacks natural stable isotopes, was first synthesized after World War II in 1947.[19] The pronounced similarity among the lanthanides made their classification and eventual separation a highly challenging endeavor.

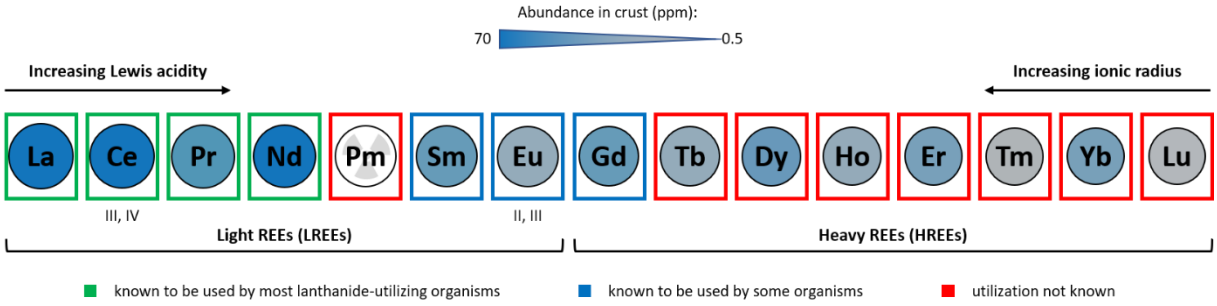

Figure I.1: The elements of the lanthanide series and their properties. The elements are scaled by ionic radius (Ln^{3+}, CN = 9).[20] The crustal abundances are depicted on a scale from blue (most abundant) to gray (least abundant).[14] Pm has no stable isotopes. Lewis acidity increases across the series from left to right in conjunction with decreasing ionic radius. All lanthanides are commonly found in the +III oxidation state, with Ce and Eu being the only ones capable of adopting different oxidation states under biologically accessible conditions (+IV and +II, respectively).[19,21] The lanthanides are conventionally subdivided into two primary groups, light (LREEs, La to Eu) and heavy (HREEs, Gd to Lu). Among lanthanide-utilizing organisms, it has been demonstrated that mainly the lighter lanthanides are utilized by all presently known species, while the heavier lanthanides are either less preferred by certain lanthanide-utilizing organisms or have not been observed to have any known biological utilization.[6] Adapted from Cotruvo,[22] Featherston et al.[23] and Mattocks et al.[24]

The elements following lanthanum are commonly referred to as the 4f elements, owing to their distinctive electronic configuration. Their electrons exhibit a partial occupancy of the inner 4f orbitals, which are well shielded by the electrons in the filled 5s, 5p, 6s and, in the cases of cerium, gadolinium and lutetium, also 5d subshells. Consequently, the 4f shell is not actively involved into the chemical bonding, leading to predominantly ionic character of the lanthanide complexes. As a result, the coordination numbers (CNs) and complex geometries are defined primarily by steric properties and almost not by electronic ones.[19] Due to the absence of strong ligand field effects, the coordination chemistry of the lanthanides has only a limited degree of predictability.[25] Coordination numbers generally range between 3 and 12, with 8 and 9 being the most common.[21] In addition, the lanthanides behave as hard Lewis acids, hence a coordination with hard bases with highly electronegative donors is favored.[26] In this context, the order of preference for donor atoms follows O > N > S. Thus, in a biological environment for example, preferred ligands would be either the carboxyl groups of proteins or the phosphate groups of nucleotides and nucleic acids.[21]

Another crucial characteristic of the lanthanide series, widely addressed in textbooks on this subject, is a phenomenon referred to as lanthanide contraction.[27,28] It describes the decrease in the internuclear distance between a lanthanide ion and a set of ligand atoms as the atomic number of the lanthanide ion increases.[19] This has conventionally been attributed to the electron cloud contracting as the nuclear charge increases.[28] The magnitude of the lanthanide contraction depends on the number of ligand atoms attached to the cation, i.e. the CN, whereby for a higher CN a more pronounced

contraction may be observed.[29,30] Trivalent lanthanide ions can accommodate variable CNs and the disparity between the radii for CNs 6 and 12 is approximately 30 pm, which makes Ln^{3+} ions highly adaptable to diverse coordination environments.[31] While much of the literature centers on Shannon's published Ln^{3+} ionic radii,[20] the lanthanide contraction remains a subject of ongoing investigations in recent analyses.[28,29,32] Moreover, many reviews have discussed the significance of the lanthanide contraction in fields such as lanthanide separation,[12,33] coordination chemistry,[26] and biology.[6,34] Notably, the ionic radii of the elements situated in the middle of the lanthanide series are analogue to that of calcium(II).[21] Consequently, the lanthanide contraction exerts an influence not only on the chemical synthesis of lanthanide complexes, but also on biological systems.[2] Thus, trivalent lanthanum ions may function as analogues to calcium in biological contexts, potentially displacing calcium in various proteins, including enzymes and cell membranes.[35,36] Furthermore, in comparison to calcium, the lanthanides are assumed to serve as superior catalysts, owing to their stronger Lewis acidity.[4] Additionally, the substitution of calcium with lanthanide ions can unlock a variety of spectroscopic techniques that can offer insights into the biochemical behavior of biological systems.[21]

Nevertheless, due to their subtle variations in ionic radius and coordination number, factors that also contribute to their co-occurrence in rare earth-bearing minerals, the separation of the REEs presents a formidable challenge, demanding significant energy inputs.[12,37,38] Additionally, concerns regarding environmental contamination have been documented in close proximity to rare earth processing facilities.[39,40] Conventional hydrometallurgical liquid–liquid extraction techniques employed in REE production yield substantial quantities of hazardous, radioactive and heavy metal contaminated waste, and require numerous purification stages to attain high-purity individual RE oxides.[37,41–43] Given these chemical, ecological, and economic considerations, the development of novel, environmentally sustainable methods for the separation of REEs is a paramount objective.[33] Recently, several promising advancements have been presented, providing exciting prospects for REE separation and recycling.[44–57]

Interestingly, during the first 150 years of their documented existence, the rare earth elements held primarily scientific significance. It wasn't until the middle of the 80s that the first magnets containing REEs became available on the market.[58] This development marked a monumental expansion in their applications. Owing to their extraordinary physical properties, REEs have since gained increasing importance, proving irreplaceable in numerous fields including medicine, high-tech industries, and sustainable energy solutions (Figure I.2).[33,59–61] Nowadays, rare-earth magnets are ubiquitous, powering electric engines, speakers, wind turbines, smartphones, and hard disk drives.[58] Beyond magnets, rare earths play an integral role in diverse applications, comprising essential components in metal alloys, phosphors, glasses, ceramics, and polishing agents. Moreover, these elements are frequently employed as contrast agents[62–67] and for radioisotopic labelling,[68,69] in addition to playing

pivotal roles in cutting-edge technologies such as photoactive processes[70,71] and small molecule catalysis.[72,73]

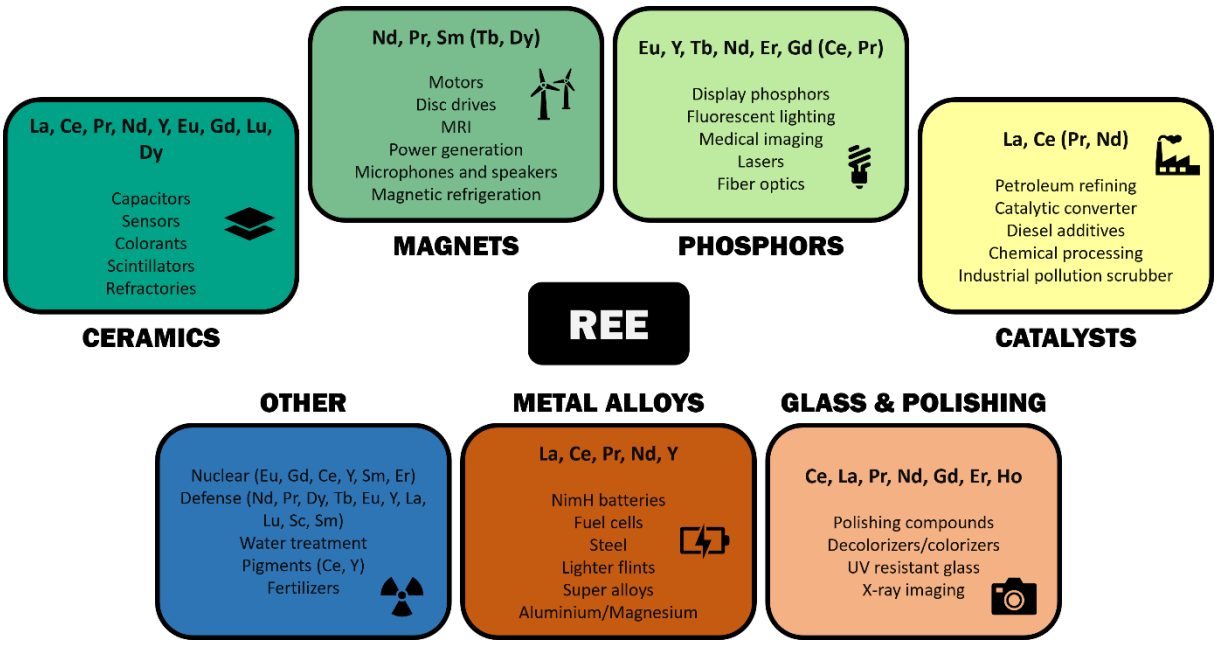

Figure I.2: Application of the rare earth elements in different fields. Adapted from a British Geological Survey report.[59]

The impact of lanthanides on biological systems had long been overlooked. Only a handful of studies hinted at their potential biological significance, highlighting their stimulatory effects on certain plants and bacteria.[74–76] In 2004, there was a hypothesis proposing that lanthanides might surpass calcium in their role within enzymes. However, it was then suggested that their limited bioavailability had hindered the evolution of lanthanide-dependent enzymes.[4] Despite their relatively abundant presence in the earth's crust, the lanthanides exhibit very low solubility in water at near-neutral pH levels.[77] Nevertheless, this solubility is notably higher than that of iron(III), a commonly accessed element by bacteria, plants, and fungi through small-molecule siderophores.[78,79] There are numerous biological advantages to utilize lanthanides such as their high oxidation state and Lewis acidity which turn them into valuable catalysts. Additionally, their wide abundance, relatively large ionic sizes, and high coordination numbers enable selective acquisition from the environment.[23] All these distinctive characteristics render the lanthanides potentially biologically accessible, from a chemical point of view.[80,81] It was not until 2011 that the first biochemical evidence supporting lanthanides as intrinsic metals in bacterial enzymes was reported.[8] This discovery inaugurated a whole new research area, formally acknowledging lanthanides as newcomers in the field of cell biology, standing alongside with previously recognized metals such as calcium, iron and zinc.[5]

2. Calcium and Lanthanide-Dependent Alcohol Dehydrogenases

Methanol dehydrogenase (MDH) is a soluble periplasmic quinoprotein, which plays an integral part in the metabolism of methylotrophs and methanotrophs, which are microorganisms with the ability to utilize C_1-compounds such as methanol and methane as their sole energy source.[3,82] Thereby, MDH catalyzes the two-electron oxidation of methanol to formaldehyde.[83–85] The first MDH was discovered and isolated by Anthony and Zatman in 1964.[83,84] Since then, it has undergone thorough study by many research groups with the perspective of characterizing its structure, function and catalytic mechanism. MDH bears a redox cofactor called pyrroloquinoline quinone (PQQ, Figure I.3) in its active site to sequentially transfer two electrons to its physiological electron acceptors cytochrome c_L (Scheme I.1). [86,87] PQQ, which is the only known example for a cofactor where the prosthetic group is non-covalently bound, is part of many bacterial dehydrogenases.[87]

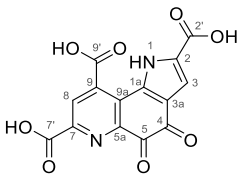

Figure I.3: Structure of pyrroloquinoline quinone (PQQ) and its numbering scheme.[88] PQQ is an aromatic tricyclic o-quinone, which functions as a redox cofactor for many quinoprotein dehydrogenases.[89–95] It is also known under its trivial name "methoxatin". It was first isolated in 1964 from GDH and MDH.[83,84,96] The first X-ray crystal structure of PQQ was reported in 1979 by Salisbury et al.[97] followed by PQQ's extensive chemical characterization by Duine and coworkers in the 80's.[89]

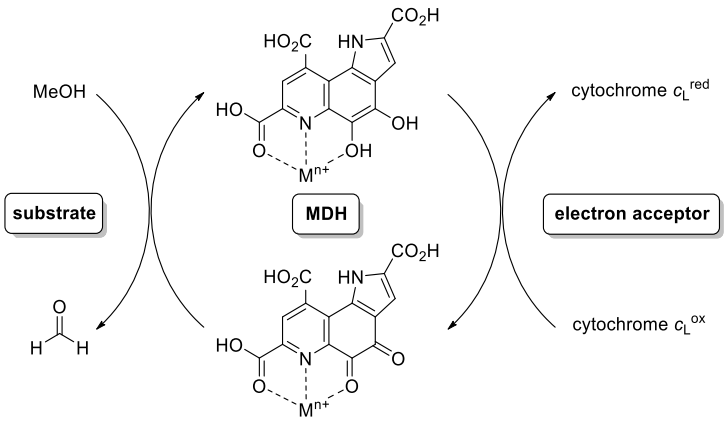

Scheme I.1: Catalytic cycle of methanol oxidation by MDH (M^{n+} = Ca^{2+} for MxaF and Ln^{3+} for XoxF-MDH).

In addition to PQQ, the active site also incorporates a metal ion acting as a Lewis acid. For over 50 years, it was widely believed that methylotrophic bacteria catalyze methanol oxidation by only using the well-known Ca^{2+}-dependent MxaF-type MDH, encoded by the *mxaF* gene.[2,98] However, genome sequencing studies on several methylotrophs, such as *Methylorubrum extorquens* AM1, led to the identification of gene homologs of *mxaF*, subsequently annotated as *xoxF*.[99] The investigation into

xoxF revealed an approximately 50% sequence identity with the *mxaF* gene, prompting the assumption that *xoxF* encodes a second PQQ-linked dehydrogenase.[100,101] Even though metaproteogenomic analyses demonstrated the abundance of XoxFs proteins in the plant phyllosphere,[102] the exact role of the *xoxF* genes remained cryptic for years.[6,23,95]

Eventually, two seminal publications from 2011 by Kawai and coworkers marked the beginning of a wave of groundbreaking discoveries. They observed that the addition of lanthanum(III) and cerium(III) to the cultures of *Methylobacterium radiodurans* and *Bradyrhizobium* sp. MAFF211645 had a significant impact on the activity of a MDH-type protein.[8,9] It was established that the XoxF-type MDH, encoded by the *xoxF* gene, plays a pivotal role in the activity of the bacteria in the presence of lanthanides, providing the initial evidence for the physiological function of these metals in living organisms. A year later, Nakagawa *et al.* demonstrated that *M. extorquens* AM1 could thrive on methanol with La^{3+} instead of Ca^{2+}.[3] This led to the conclusion that XoxF functions as a La^{3+}-dependent methanol dehydrogenase in the bacterial metabolism of *M. extorquens* AM1.

However, in 2014 Op den Camp and coworkers published the most insightful results that unequivocally confirmed the environmental significance of the lanthanides.[10] The research team conducted a comprehensive study of the recently discovered acidophilic methanotrophic bacteria culture *Methylacidiphilum fumariolicum* SolV, initially found in 2007 in the Solfatara,[103] a shallow volcanic crater at Pozzuoli near Naples. The strain thrives on methane, even in environments with pH levels as low as 0.8 – considerably lower than the optimal pH range for any previously documented methanotroph.[103] Op den Camp and coworkers demonstrated that SolV was unable to grow in laboratory cultures without the addition of mud pot water from its original habitat to the growth medium. Trace metal analysis of this water revealed high concentration of lanthanides, reaching up to 2–3 μM higher than those found in other ecosystems, yet still characteristic of highly acidic environments. Given the environmental conditions of the fumaroles, with temperatures up to 70 °C and pH values down to 1.8,[104] the requisite solubility for lanthanides was met.[10] The research team substituted the mud-pot water with lanthanide salts thereafter, prompting exponential growth in the strain. This crucial observation led to the conclusion that lanthanides are indeed the essential growth determinant for this particular strain. Purification and subsequent crystallization of the XoxF-MDH from this strain revealed a lanthanide ion (good convergence with Ce^{3+}) in the active site, directly coordinated to PQQ. Presently, four different XoxF-MDH crystal structures can be found in the literature: in addition to the Ce-MDH and Eu-MDH from *M. fumariolicum* SolV, a La-MDH from *Methylomicrobium buryatense* 5GB1C and Nd-MDH from *Methylacidimicrobium thermophilum* AP8 have been reported.[10,105–107]

With a crystal structure of XoxF in hand, a direct structural comparison between the lanthanide-dependent and the canonical calcium-dependent MDH was possible. MxaF, a heterotetrameric $\alpha_2\beta_2$ protein, comprises two large and two small subunits. Each heavier α-subunit (66 kDa) carries one PQQ and one calcium(II) ion, which together play an essential role for the enzymatic activity. The β-subunit on the other hand is smaller with a molecular mass of 8.5 kDa and its function is elusive.[87,108] Interestingly, the genomic organization of XoxF is simpler, as it does not engage with a small subunit, but rather forms an α_2 homodimer.[10,108]

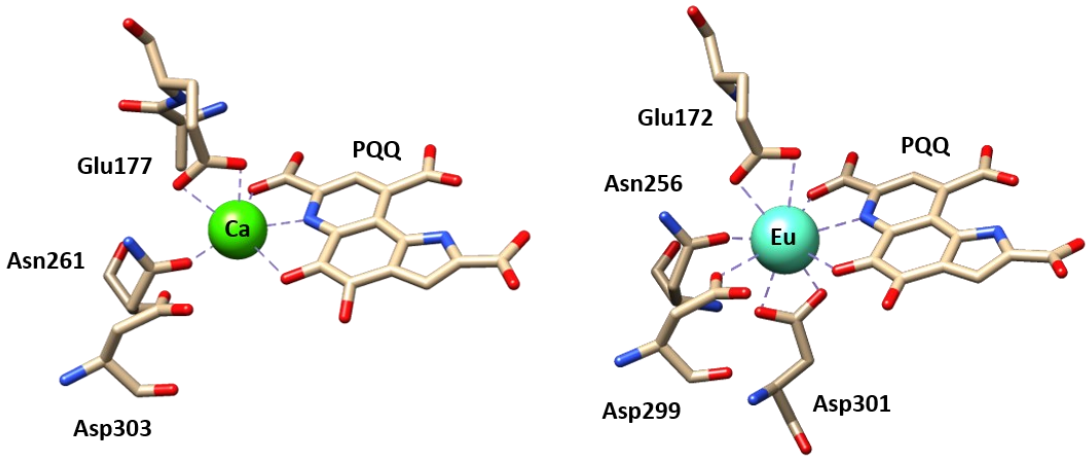

Figure I.4: Active sites of MxaF-MDH from M. extorquens AM1 (left; PDB: 1H4I)[109] *and XoxF-MDH from M. fumariolicum SolV (right; PDB: 6FKW).*[106] *Images generated with the UCSF Chimera package.*[110]

While both, lanthanides and calcium share similarities in their coordination chemistry properties as hard Lewis acids, the lanthanides often exhibit higher coordination numbers. These coordination chemistry preferences are distinctly reflected in the active sites of MDH enzymes. In the case of MxaF (Figure I.4, left), Ca^{2+} is tridentately coordinated to the C-5 quinone oxygen, N-6 pyridine nitrogen and the C-7 carboxyl group of PQQ, bidentately by a glutamate residue and monodentately by an asparagine.[111] In XoxF's active site (Figure I.4, right), a high degree of structural conservation is evident in the amino acid's position in the sequence and spatial orientation in the structure. However, there is only one striking difference – the active site of XoxF features an additional bidentate aspartate residue, replacing an alanine found in MxaF. This alteration aligns with the preference for higher coordination numbers of the trivalent lanthanides compared to the divalent calcium.[10,106,108] This specific amino acid has been demonstrated as crucial for the coordination of the lanthanide ion, thereby playing an essential role in enzyme activity.[112] XoxF appears to exhibit greater catalytic efficiency compared to MxaF, which is thought to be attributed to the enhanced activation of the redox cofactor PQQ by the lanthanide ion.[10,106,113]

There are two major types of lanthanide-utilizing bacteria: those that possess only the *xoxF* gene, rendering them strictly dependent on lanthanides, like *M. fumariolicum* SolV, and those possessing

both *mxaF* and *xoxF* genes, like *M. extorquens* AM1.[114] In microorganisms that have the ability to employ both proteins, the expression of *xoxF* and *mxaF* is inversely regulated, i.e. the concentration of lanthanides in the environment influences the level of transcription. When Ln^{3+} are absent from the growth medium (or only present at sub-nanomolar concentrations), *xoxF* expression is suppressed while *mxaF* expression is heightened. Conversely, if Ln^{3+} are available in nanomolar or higher concentrations, *mxaF* expression is down-regulated and *xoxF* is significantly up-regulated.[112,115] This particular feature to transition between the different metabolic pathways has been called the "lanthanide-switch".[6,115–117]

However, it is important to highlight that different lanthanides do not consistently lead to similar growth rates in lanthanide-utilizing bacteria.[6] Specifically, the more abundant, early lanthanides (La to Sm) have been demonstrated to enhance growth and promote MDH activity.[6,10] Recently, Daumann and coworkers investigated the effects of the lanthanide contraction on the catalytic efficiency of XoxF.[118] Through a combination of DFT calculations and kinetic analyses, they demonstrated that while Lewis acidity and cofactor activation play crucial roles in MDH activity, they are not the sole determining factors. Considerations also extend to preferences in coordination numbers, rates of ligand exchange, substrate orientation and activation, as well as hydrogen bonding.[118]

3. Further Insights into the Lanthanide Biochemistry

Since the initial identification and characterization of the first lanthanide-dependent MDH enzyme, our understanding of the significance of the lanthanides in the microbial realm has steadily progressed.[23] Subsequent investigations have shown that, apart from extremophiles thriving in lanthanide-rich environmental niches, a wide array of microorganisms in various ecosystems carry the gene that encodes for lanthanide-dependent metalloenzymes.[119] Scientists have since discovered that lanthanide-dependent bacteria are widespread in marine habitats, soils, and the phyllospheres of plants.[108,120–124] Furthermore, it has been postulated that lanthanides may play a crucial role in other types of alcohol dehydrogenases. In 2016, Good *et al.* presented a study focused on the first non-XoxF-type alcohol dehydrogenase, which relies on lanthanides as cofactors.[125] This ExaF enzyme showed to be a highly effective PQQ-dependent ethanol dehydrogenase, significantly expanding our understanding of the pivotal role that lanthanides play in bacterial metabolism. This finding not only extends the relevance of lanthanides beyond methanol dehydrogenases, but also illuminates their significance in the broader context of multicarbon metabolism.

Later, the scope of lanthanide-utilizing bacteria was expanded beyond the methylotrophs. In 2017, Wehrmann *et al.* reported that one of the two PQQ-dependent alcohol dehydrogenases (PedH) produced by the soil-dwelling model organism *Pseudomonas putida* KT2440 also relies on Ln^{3+} as a crucial cofactor.[126] This study underscored the pivotal role of lanthanides in bacterial metabolism. Nevertheless, numerous questions persist regarding the specific mechanisms by which the lanthanides are selectively recognized, acquired, and utilized in biological systems.[127] In 2018, Cotruvo *et al.* reported the discovery and thorough characterization of the first highly selective Ln^{3+}-binding protein, other than an alcohol dehydrogenase, known as lanmodulin (LanM), which was isolated from *M. extorquens* AM1. This protein exhibits a remarkable ability to selectively bind lanthanides,[128] akin to the well-known Ca^{2+} calmodulin. Within LanM, three carboxylate-rich metal-binding sites exhibit a picomolar affinity for Ln^{3+}, alongside one site displaying a micromolar affinity. Most notably, there is a striking hundred-million-fold selectivity for Ln^{3+} over Ca^{2+}. This study represents a milestone, providing the initial biochemical and structural insights into how biological systems discern low-abundance lanthanides from the more prevalent calcium.

While it is evident that lanthanides are indeed taken up by the lanthanide-dependent microorganisms, as indicated by the response of numerous methanotrophs and methylotrophs to these elements, the precise mechanism remains elusive.[123] The lanthanide uptake presents a particularly formidable challenge due to their poor solubility and difficult extraction from mineral sources in which they are embedded. Consequently, several researchers have postulated that some lanthanide-utilizing organisms may deploy small chelators (“lanthanophores” or lanthanide carrier) to facilitate the acquisition of the Ln^{3+} ions.[6,108,122,123,128] This process would be resembling to bacterial chelator-mediated uptake mechanisms for metals like iron and copper, which employ siderophores[78,79] and chalkophores,[129] respectively. The issue about the lanthanide uptake serves as an illustrative example of how, despite the substantial advancements in our knowledge about lanthanide-utilizing organisms over the past decade, there still exists a considerable amount of unknown territory and numerous questions yet to be addressed.

II. SYNTHESIS OF PQQ DERIVATIVES AND LIGANDS

1. Synthesis of PQQ Derivatives

The following section is part of the publication:

Modular Synthesis of New Pyrroloquinoline Quinone Derivatives

Rachel Janßen, Violeta A. Vetsova, Dominik Putz, Peter Mayer and Lena J. Daumann

Published in: *Synthesis* **2023**, *55*, 1000-1006.

Abstract. Pyrroloquinoline quinone (PQQ) is an important cofactor of methanol dehydrogenases and glycose dehydrogenases. In addition, isolated PQQ is used as a central component in sensors and biomimetic complexes. The synthesis of PQQ derivatives is of interest for developing new alcohol oxidation catalysts and redox sensors. This work describes a modular synthesis for derivatives of PQQ bearing methyl and ketone groups instead of carboxylic acid moieties. These modifications reduce the possible coordination sites of PQQ for metal ions outside the protein environment.

Pyrroloquinoline quinone (PQQ) is an aromatic tricyclic *o*-quinone, which functions as a redox cofactor for many quinoprotein dehydrogenases.[89,90,92,94,95] In methanol dehydrogenase (MDH), for example, PQQ is reduced to its quinol form, concurrently to the oxidation of methanol. In addition, PQQ can be found in glucose dehydrogenase, an enzyme that is routinely used as a sensor for glucose or other biomolecules.[130,131] As well as PQQ, the active sites of these enzymes contain a Lewis acid, like calcium(II) or a lanthanide(III) ion (Ln), for cofactor and substrate activation.[10,111] PQQ has recently attracted new interest, not only for its role in biological systems together with lanthanides, but also as chelator for Ln separation or as sensor for Hg(II) or L-fucose.[44,132,133] In addition, model complex studies have been aimed toward understanding the activation of PQQ by Lewis acids (Ca or Ln).[134–136] In the biological systems, PQQ coordinates metal ions in the ONO pocket and can be considered one of the few natural pincer ligands.[137] It has been shown that outside a protein environment PQQ acts as a versatile ligand, often forming coordination networks or dimers with one

or more carboxylic acid moieties.[44,138–140] Thus, for catalyst design and for generating monomeric PQQ-metal complexes, the functionalization of certain residues, but especially the moieties not involved in metal ion coordination *in vivo*, is often necessary to modify the cofactor. Hudson and coworkers has previously reported the synthesis of several PQQ isomers, where the pyridine moiety or pyrrole ring were flipped by 180 degrees.[141] Only one of the isomers retained the ONO pocket and the derivative still featuring the carboxylates, which often lead to unwanted dimer or coordination network formation.

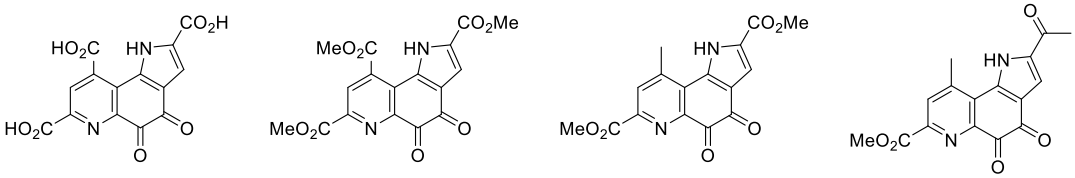

Chart II.1: PQQ and related derivatives discussed in this study.

In this work, we report the synthesis of two PQQ derivatives **P**$_{ME}$**QQ**$_{MEM}$ (**m**ethyl **e**ster-substituted pyrrole, **m**ethyl **e**ster- and **m**ethyl-substituted quinoline quinone) and **P**$_{K}$**QQ**$_{MEM}$ (**k**etone-substituted pyrrole, **m**ethyl **e**ster- and **m**ethyl-substituted quinoline quinone), which could be potentially used as ligands in quinoprotein-inspired model complexes or as starting materials for advanced sensor development. Compared to PQQ itself, the derivatives possess fewer alternative coordination sites for metal cations, albeit still retaining the ONO pocket for metal coordination. The synthetic route was adapted from the total synthesis of PQQ published by Corey and Tramontano,[1] which includes the formation of the trimethyl ester of PQQ (**PQQMe$_3$**) as an intermediate; this was previously often used as a model for MDH.[142–144] In the active site of MDH, the carboxylic functions of PQQ are occupied by interactions with amino acids.[111] For the trimethyl ester, the literature presents a seven-step synthesis with an overall yield of approximately 22%.[1] Other authors published partly similar syntheses, as well as alternative approaches,[145–151] but the cofactor PQQ itself could also be obtained by fermentation.[152] The derivatives aimed for in this work, however, require adjustments within the synthesis, wherefore we established the adapted procedure described herein.

The first step toward the new derivatives was performed according to the PQQ synthesis by Corey and Tramontano[1] by starting from 2-methoxy-5-nitroaniline (**1**). As described, the amino group was protected with a formyl group using *in situ* generated acetic formic anhydride (Scheme II.1). In a difference to the literature report, the paste-like reaction mixture was stirred with an overhead stirrer, resulting in an almost quantitative yield of **2**. Product **2** was then reduced with H_2 and Pd/C to yield the aniline derivative **3** in good yield (87%, Scheme II.1).

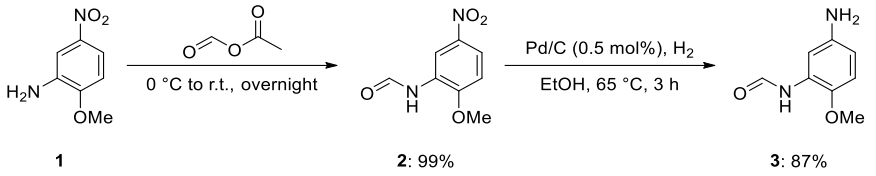

*Scheme II.1: N-formylation of 2-methoxy-5-nitroaniline (**1**) and palladium-catalyzed reduction of nitro compound **2** to aniline derivative **3**.*

Methyl 3-oxobutanoate (**4**), which was needed for the next step, had to be prepared prior to the synthesis. Therefore, reactant **4** was synthesized according to a literature procedure[153] and obtained in 65% yield.

In the literature procedure,[1] the ensuing Japp-Klingemann reaction of **3** and **4** to form the ester-substituted arylhydrazone **5** was reported to give up to 80% yield. Various attempts to repeat the published result were discarded for two reasons: either the high yields described in the paper could not be reproduced or the reaction yielded a mixture of the ester- and ketone-substituted hydrazones **5** and **6** that was difficult to separate.

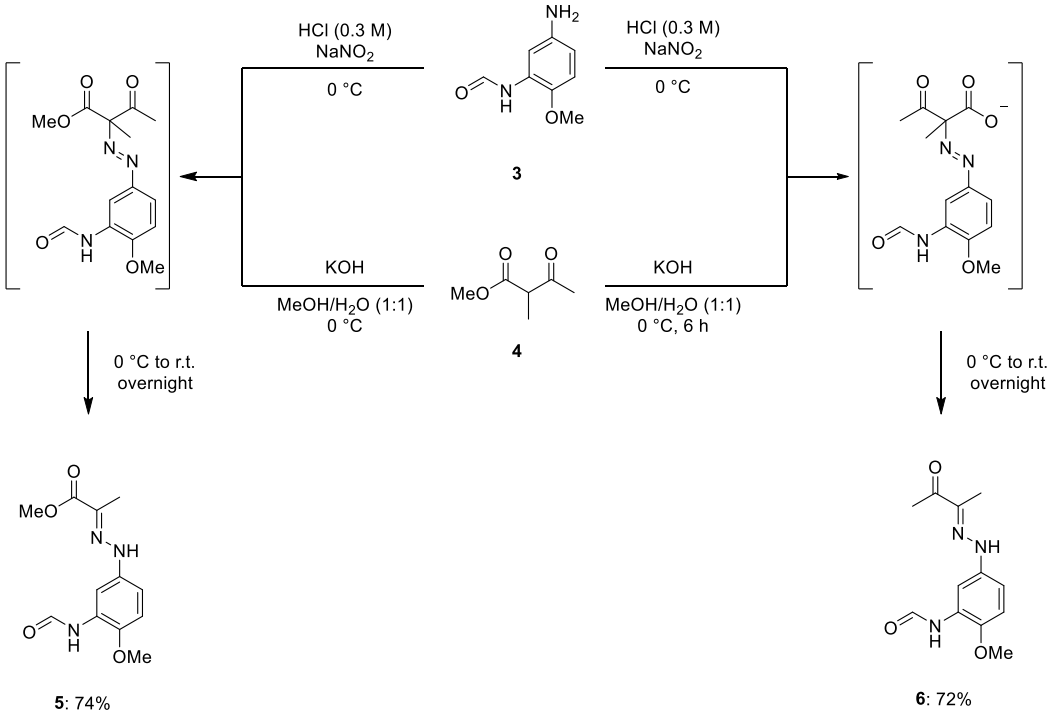

*Scheme II.2: Formation of ester- and ketone-substituted arylhydrazones **5** and **6**.*

While investigating the different outcomes in comparison to the literature, we found that the ester-substituted compound **5** can be synthesized exclusively if the reaction scale is kept under approximately 5 mmol, whereas higher scales led to a mixture of both products. Further optimization of the reaction protocol, such as changes to the addition speed and method, showed that a transfer cannula is most suited to allow constant cooling of the diazonium salt suspension while maintaining a

slow addition speed. With this setup, **5** was afforded in 74% yield (Scheme II.2). Differentiation between the ester- and ketone-substituted products can be achieved by distinct treatment of reactant **4**. To obtain the ketone-substituted product **6** exclusively and in good yield (72%), precursor **4** was saponified with 1.2 equiv. KOH at 0 °C overnight prior to addition (Scheme II.2). Saponification can also be achieved at room temperature within approximately 1 h. However, the yields are lowered significantly if either solution is not cooled and kept at low temperatures throughout addition. In the case of **5**, the elongated time needed for slow addition and insufficient cooling at higher reaction scales might be why mixtures are obtained because some of reactant **4** could be saponified. It should also be mentioned that higher concentrations of hydrochloric acid lead to deprotection of the formylated amino group in both reactions.

In a reaction known from Fischer indole syntheses,[154] the afforded hydrazones were converted by temperature- and acid-mediated indolization (Scheme II.3). Products **7** and **8** were synthesized in 60% and 56% yield, respectively, and subsequent deprotection of the amino group by using hydrochloric acid afforded **9** (84%) and **10** (79%).

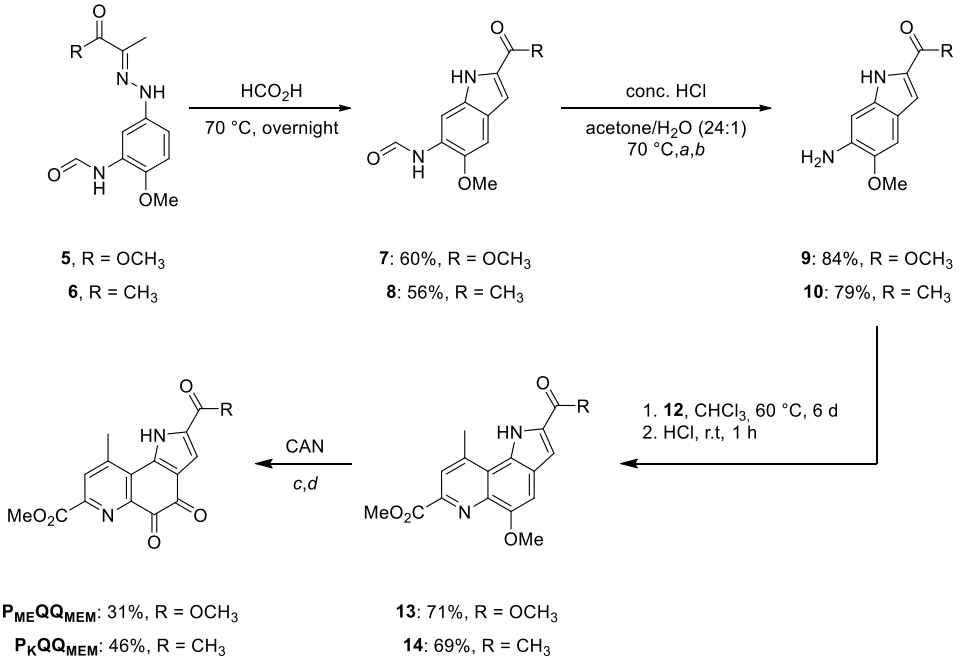

*Scheme II.3: Fischer indolization of **5** and **6** to amino idoles **7** and **8** and subsequent deprotection of the amine group, Doebner-Miller reaction and subsequent dehydrogenation of **9** and **10** to form precursors **13** and **14**, and oxidation reaction of **13** and **14** to form **PMEQQMEM** and **PKQQMEM**. Reaction conditions: (a) 2 h for **9**; (b) 90 min for **10**; (c) acetonitrile/water (4:1), 0 °C, 30 min for **PMEQQMEM**; (d) acetonitrile/water (3:1), 0 °C, 40 min for **PKQQMEM**.*

For the introduction of the third ring, Corey and Tramontano[1] used an α,β-unsaturated carbonyl derived from dimethyl 2-oxoglutarate in a Doebner-Miller type[155] reaction. As the desired PQQ derivatives contain a methyl group instead of an ester function, a suitable reactant was synthesized by a similar procedure to that described in the literature. Thus, methyl levulinate (**11**) was treated with

bromine, and after removal of the resulting hydrogen bromide with a nitrogen gas flow, a double bond was established by an elimination reaction induced by triethylamine, affording product **12** (Scheme II.4). In contrast to the literature procedure, dry chloroform and reaction under a nitrogen atmosphere afforded better yields than the reaction performed in dichloromethane. The purification of this reaction, however, was nontrivial owing to the low melting point of the product. In solution, the product **12** can co-evaporate during removal of solvents in a conventional rotary evaporator at 40 °C. Therefore, the reaction mixture was carefully concentrated in a rotary evaporator at room temperature, but the solvent was not completely removed. The remaining brown liquid was then distilled by using a SCHLENCK tube and a cooling finger, resulting in the disposition of the product as colorless crystals, while the remaining solvent was captured in a connected cooling trap. Once obtained in solid form, the crystals were scraped off and could be dried under high vacuum. Product **12** was obtained in 44% yield.

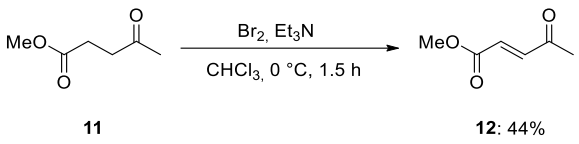

Scheme II.4: Bromination and subsequent elimination of methyl levulinate to form ***12****.*

With this product at hand, the Doebner-Miller reaction with amino indoles **9** or **10** and **12** was performed. It was found that higher temperatures were needed, as previously described; therefore, dichloromethane was substituted with chloroform. In addition, the reaction time was extended to 6-7 days until TLC indicated full consumption of the starting material. To fully convert the intermediate, *in situ* formed hydrogen chloride was bubbled through the reaction mixture. After purification, the desired tricyclic products **13** and **14** were afforded in yields of 71% and 69%, respectively (Scheme II.3).

In the final step, oxidation into the quinones was performed by using ceric ammonium nitrate (CAN). In contrast to the previously reported **PQQMe$_3$**, however, the products exhibit lower solubility in water, precipitate from the reaction mixture, and can be filtered off and washed without further purification. The target molecules **P$_{ME}$QQ$_{MEM}$** and **P$_K$QQ$_{MEM}$** were obtained in 31% and 46% yield, respectively.

In summary, we have successfully adapted the synthetic route towards **PQQMe$_3$** and present herein two new PQQ derivatives, which may be useful in chemical investigations of the cofactor methoxatin in enzymatic contexts or as sensor moieties. The modification on the quinoline ring reduces the possible coordination sites that the PQQ derivatives can exhibit in solution in addition to the biologically relevant binding sites. The exchange of functional groups on the aromatic structure could also have an impact on the redox properties or kinetics of PQQ for alcohol oxidation.

2. Synthesis of PQQ Aza-Crown Ligands

Biomimetic chemistry has its primary focus on the synthesis and detailed characterization of small analogues of enzymes, which resemble either their functional or structural and spectroscopic properties.[156–161] The investigation of such models or synthetic analogues could shed some light into fundamental aspects of structure, spectroscopy, magnetic and electronic features, reactivity and chemical mechanism of their biological counterparts.[156] The model systems usually show significantly lower activity than their corresponding native metal-containing sites, however, systematic and targeted variations in coordination geometry, ligation or local environment in the synthetic models could provide useful information about the factors that influence the enzyme reactivity.[158,159] The design of synthetic analogues is nontrivial and the process is often iterative in order to improve, if required, the accuracy of the model.[158,160] Typical functional groups, which often occur in the natural compounds, are carboxylates, phosphates, amines, imines, amides, ethers, hydroxyls, phenols and heterocyclic groups. Hence an accurate synthetic model should either incorporate or mimic these functionalities. In the last years, many research projects focused on the interaction of f-elements with organic ligands carrying binding sites related to those of biomolecules.[162]

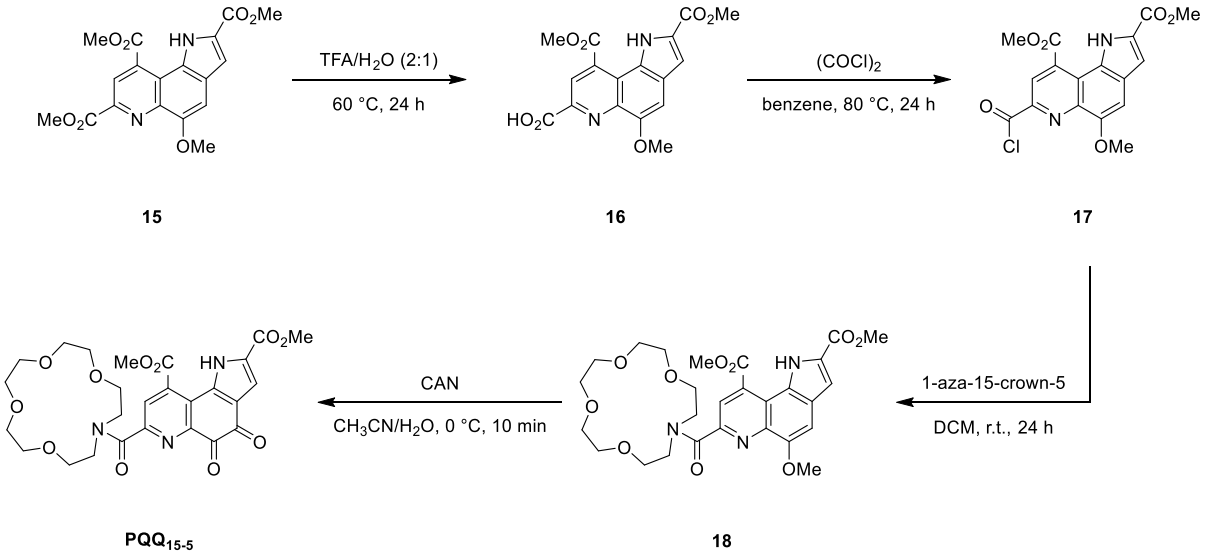

*Scheme II.5: Synthetic route to ligand **PQQ**$_{15\text{-}5}$ reported by Itoh and Fukuzumi.*[163] *Compound **15** is available only as a synthetic intermediate of the total synthesis of PQQ reported by Corey and Tramontano.*[1]

With the perspective to obtain more knowledge about the nature of the interactions in the active site of XoxF- and MxaF-MDH, studies of several structural model complexes were described in the literature.[143,144,164–166] Twenty years ago Itoh and Fukuzumi developed a synthetic functional model of the calcium-dependent alcohol dehydrogenase, which incorporates a PQQ moiety coupled through an amide linkage at the C-7 position to an 1-aza-15-crown-5 ether (Scheme II.5).[163] Thus, the crown ether oxygen atoms in ligand PQQMe$_2$-1-aza-15-crown-5 (**PQQ**$_{15\text{-}5}$) mimic the amino acid donor atoms of

MDH and coordinate calcium(II) in addition to PQQ. The study examined the coordination ability of **PQQ$_{15\text{-}5}$** towards various alkaline earth metal ions.

In order to expand this study and unravel the possible differences of lanthanides over calcium in alcohol oxidation reactions, the following project aimed to synthesize ligand **PQQ$_{15\text{-}5}$** and investigate its interaction with various Ln^{3+} salts. In addition, a second model ligand PQQMe$_2$-1-aza-18-crown-6 (**PQQ$_{18\text{-}6}$**) was synthesized, using the larger 1-aza-18-crown-6 ether.

2.1. PQQMe$_2$-1-aza-15-crown-5 (PQQ$_{15\text{-}5}$)

The following section is part of the publication:

Pyrroloquinoline Quinone Aza-Crown Ether Complexes as Biomimetics for Lanthanide and Calcium Dependent Alcohol Dehydrogenases

Violeta A. Vetsova, Katherine R. Fisher, Henning Lumpe, Alexander Schäfer, Erik K. Schneider, Patrick Weis and Lena J. Daumann

Published in: *Chem. Eur. J.* **2021**, *27*, 10087–10098.

Results and Discussion

Ligand synthesis

Based on the work of Itoh and Fukuzumi[163] an aza-crown ether was attached to the PQQ scaffold. As precursor **16** is only available in low yields through an 8-step synthesis, the usage of methylated and selectively hydrolyzed **PQQMe$_2$** as a precursor starting from PQQ was evaluated.[167] We have previously reported the facile isolation of pure PQQ at low-cost from vitamin capsules.[136] The further advantage of **PQQMe$_2$** is that the quinone moiety is already formed, avoiding the oxidation with ceric ammonium nitrate (CAN), and thus introduction of possible cerium traces to the system. Duine *et al.* described direct methylation of PQQ by Me_2SO_4 and K_2CO_3 but used a very small scale of only 0.5 mg PQQ starting material.[168] The method was tested on a 50 mg scale and gave analytically pure **PQQMe$_3$** as an orange solid in 91% yield. The scale was successively increased in further reactions and can easily be run in a 500 mg scale, with only a slightly decreased yield of 86%. **PQQMe$_3$** was then selectively hydrolyzed, using TFA (Scheme II.6).[169] The product **PQQMe$_2$** precipitated after addition of water with isolated yields over 90%.

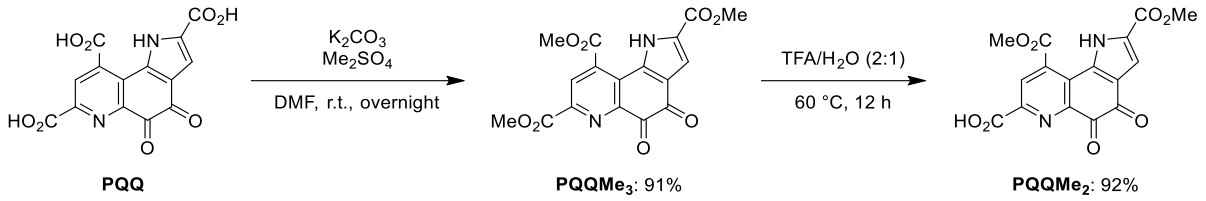

*Scheme II.6: Conversion of **PQQ** to **PQQMe3** followed by acidic hydrolysis in position C-7 to **PQQMe2**.*

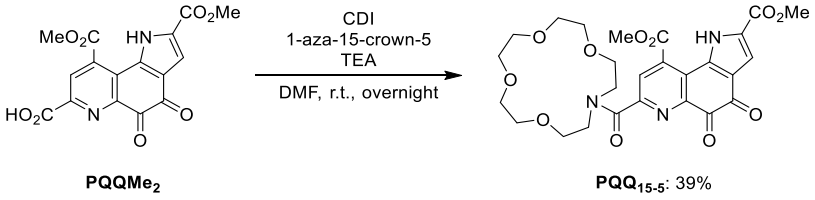

*Scheme II.7: Amide coupling between **PQQMe2** and 1-aza-15-crown-5 using CDI.*

The aza-crown ether precursor was then coupled to **PQQMe2** using 1,1'-carbonyldiimidazole (CDI; Scheme II.7). This coupling reagent has the advantage of producing only CO_2 and imidazole as byproducts which can easily be removed (for further discussion on different amide coupling reagents see chapter II.3.). Nevertheless, the purification of ligand **PQQ15-5** showed to be challenging. The implementation of the purification conditions proposed by Itoh and Fukuzumi,[163] which involve column chromatography with silica and a 80:20 EtOAc/EtOH mixture as an eluent, did not give a pure product. Unfortunately, variation of the eluent, including the use of different solvent systems such as CH_2Cl_2/MeOH and EtOAc/*iso*-hexane, did also not lead to the separation of the product from the impurities in our hands. It should be mentioned that the silica exhibited a greenish color after every purification attempt. A sample of the stationary phase was analyzed by CW EPR and showed radical formation, thus this purification method was abandoned (Figure II.1).

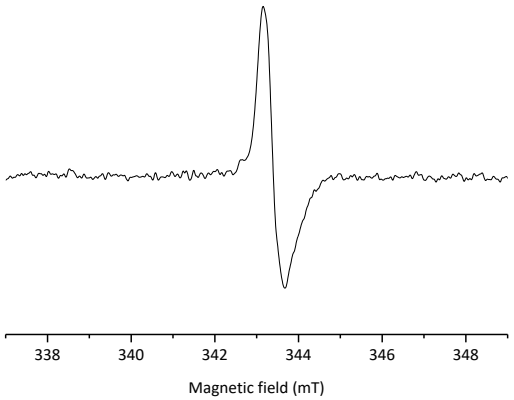

*Figure II.1: CW EPR spectrum at X-band (9.5 GHz) of a sample from the stationary phase, after a flash column chromatography of the crude ligand **PQQ15-5** has been performed.*

However, experiments have shown that **PQQ15-5** could be partially precipitated by addition of water to the crude product. The NMR spectra showed no major impurities except for traces of H_2O, DMF and CH_2Cl_2 and the elemental analysis was in good agreement with the calculated values. Thus, we hope this new and convenient synthesis route with only 3 steps instead of 11 steps to ligand **PQQ15-5** (33% instead of 0.6% overall yield) will provide fast access to future PQQ-based model complexes of MDH.

2.2. PQQMe2-1-aza-18-crown-6 (PQQ18-6)

Considering the preference of the lanthanides for higher coordination numbers, this project aimed the synthesis of a further PQQ-aza based ligand incorporating a bigger aza-crown cavity. Thus, the ligand PQQMe2-1-aza-18-crown-6 (**PQQ18-6**) was synthesized from PQQ dimethyl ester (**PQQMe2**) and 1-aza-18-crown-6 using CDI and TEA (Table II.1, for further discussion on different amide coupling reagents see chapter II.3.). Due to the good solubility of **PQQ18-6** in water, however, the product could not be precipitated from the crude mixture, as described in the experimental procedure for ligand **PQQ15-5**. Nonetheless, the NMR spectra of the crude product showed no major impurities and the elemental analysis was in good agreement with the calculated values with small deviations caused by residual water or DMF.

*Table II.1: Amide coupling between **PQQMe2** and 1-aza-18-crown-6.*

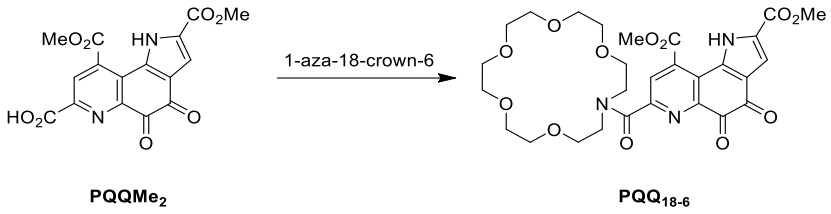

Entry	Reagent	Base	Solvent	Temperature	Time	Yield (%)
1	CDI	TEA	DMF	r.t.	24 h	60
2	EDC·HCl, HOBt·H_2O	TEA	DMF	0 °C to r.t.	6 d	39

In addition, an EDC·HCl/HOBt·H_2O mediated coupling reaction was examined with the aim of increasing the product yield. Both NMR and TLC indicated the formation of the product, however even after 6 days the starting materials were not completely consumed and no further product was formed. Hence, the reaction was quenched, worked up and the crude product was purified by flash column chromatography (DCM/MeOH, gradient from 99:1 to 94:5, R_f = 0.32). The product was isolated in a relatively low yield of 39%. Therefore, for all further studies on ligand **PQQ18-6** the CDI mediated

coupling reaction was applied. Thus, starting from PQQ, the ligand was synthesized in 3 steps with an overall yield of 50%.

3. Synthesis of Ligand L_{PQQ}

In 2018 the group of Schelter reported the first synthetic functional model of lanthanide-dependent alcohol dehydrogenase based on ligand $\mathbf{L}_{QQ}$, which incorporates a directing and sterically bulky chelator **19**, coupled to a PQQ related quinoline quinone **20** (Scheme II.8).[166] The X-ray crystal structure of the complex [La($\mathbf{L}_{QQ}$)(NO_3)$_3$] (**21**) revealed metal ion binding similar to the coordination arrangement found in MDH, where PQQ acts as a tridentate ligand with O-5, N-6 and O-7′ as donors. Additionally, cyclic voltammogram investigations revealed a shift to higher potentials upon La^{3+} coordination for the quinone/semiquinone reversible couple of $\mathbf{L}_{QQ}$, which reflected the stabilization of the semiquinone anion state by the metal ion. Furthermore, the stoichiometric as well as catalytic dehydrogenation of a benzyl alcohol was studied under neutral and mildly basic conditions and it was indicated that both La^{3+} as well as ligand are required for a catalytic turnover. Finally, both, the hemiketal and hydride transfer mechanism pathways for the alcohol oxidation reaction of the functional model were calculated using DFT and it was shown that the hydride transfer was preferred with either a weak base or without a base.

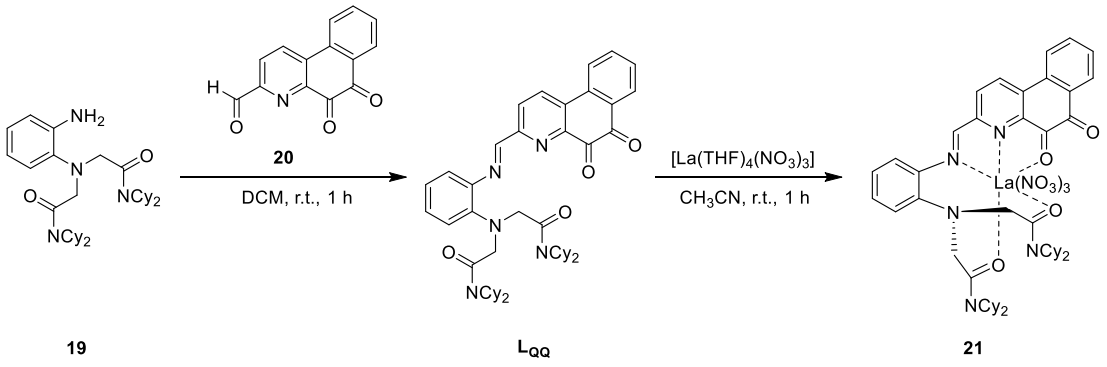

*Scheme II.8: Synthesis of model ligand $\mathbf{L}_{QQ}$ and its La^{3+}-complex [La($\mathbf{L}_{QQ}$)(NO_3)$_3$] (**21**).*[166]

To further expand the studies on lanthanide-dependent alcohol dehydrogenases, this project aimed to afford a $\mathbf{L}_{QQ}$ inspired ligand with integrated PQQ moiety instead of the quinoline quinone **20**. The five-step synthesis of chelator **19** has been discussed in detail in my Master Thesis (Scheme II.9).[170]

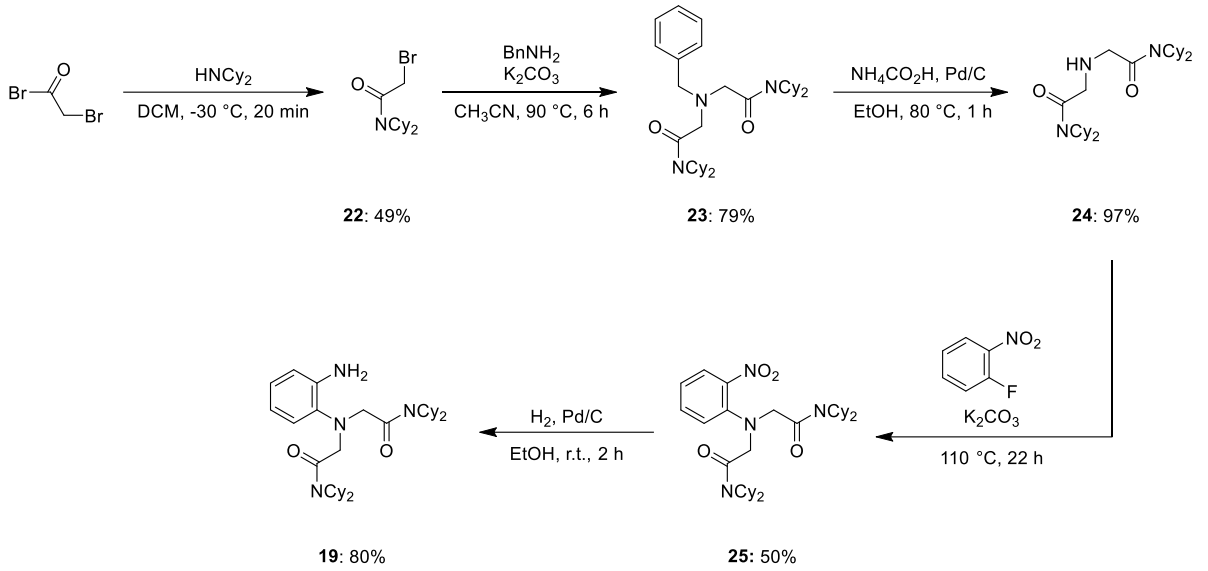

*Scheme II.9: Five-step synthesis of chelator **19**.*

With chelator **19** in hand, different strategies for the coupling with the PQQ scaffold were investigated. The first attempt was inspired by the synthetic route to ligand **PQQ15-5** previously described by Itoh and Fukuzumi (Scheme II.5).[163] Starting from the PQQ precursor **15** from Corey's total synthesis,[1] a selective hydrolyzation of the methyl ester functionality at C-7′ using TFA had to be performed, a procedure also presented and discussed in a previous work by Itoh *et al.* in 1987.[169] According to the literature, the second and the third ester groups also undergo a hydrolysis at higher temperatures, hence it is important to maintain the temperature at or below 60 °C in order to hydrolyze selectively at C-7'.

*Table II.2: Selective ester hydrolysis of **15** to **16**.*

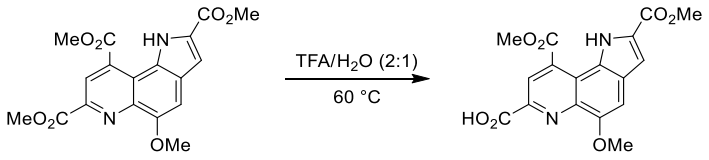

15 **16**

Entry	Reaction scale (mg)	TFA/H2O volume (mL)	Time (h)	Yield (%)
1	100	5	24	-
2	100	5	48	-
3	100	1	3	-
4	100	1	24	52

Unfortunately, the attempt to reproduce the synthesis using the conditions published in the previous works failed to accomplish and led to the reisolation of the starting material (Table II.2, Entry 1 and 3). Variation of the reaction scale to the TFA/H_2O volume ratio showed that the reaction mixture concentration as well as the reaction time play an essential role for the reaction outcome. As shown in Table II.2 (Entry 4), the desired product **16** was obtained in a moderate yield from a reaction performed on a 100 mg scale employing 1 mL of the TFA/H_2O (2:1) mixture and stirred at 60 °C for 24 h.

According to the literature,[1] all of the three ester groups in **15** undergo a saponification reaction at 60 °C under alkaline conditions. However, it was shown on analogue compounds that a selective ester hydrolysis could be performed in the presence of potassium carbonate at low temperatures.[171] Therefore, an attempt was made to convert **15** to **16** using diluted potassium carbonate solution at 0 °C (Scheme II.10). Unfortunately, the desired product could not be observed, hence it was decided to further apply the TFA hydrolyzation method described above.

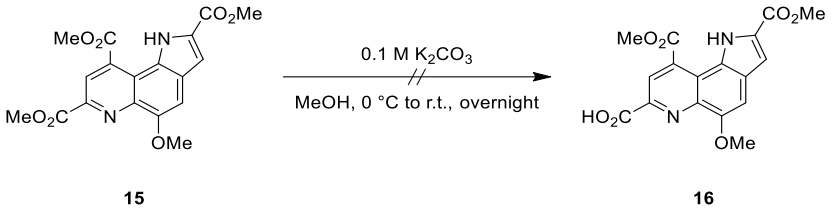

*Scheme II.10: Attempted selective ester hydrolysis of **15** with potassium carbonate.*

With the single-hydrolyzed PQQ intermediate **16** in hand, an attempt to form the ligand precursor **26** was made. As shown in Scheme II.11, **16** had to be activated by treatment with oxalyl chloride and the resulting acid chloride intermediate **17** had to be coupled to chelator **19**.

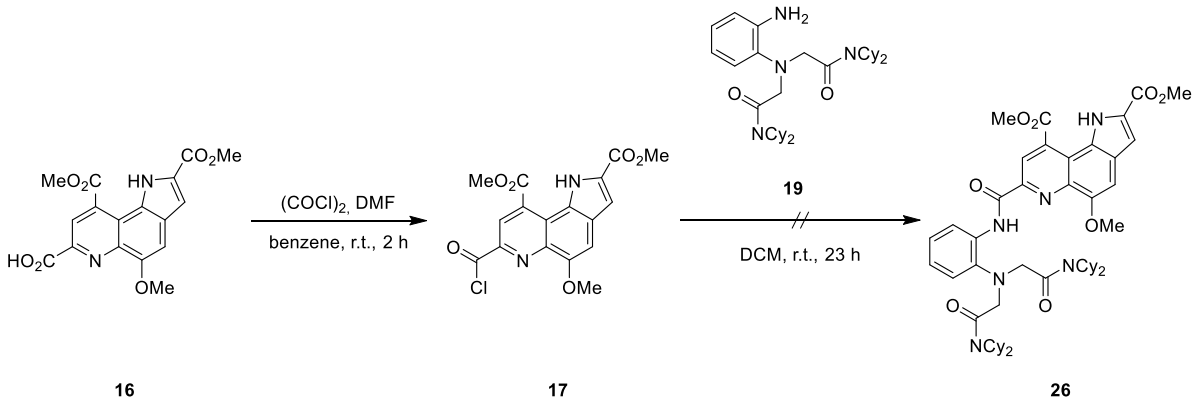

*Scheme II.11: Attempted coupling reaction of PQQ precursor **16** and chelator **19** to ligand precursor **26**.*

Unfortunately, the attachment of both building blocks failed to accomplish as shown by ^{1}H NMR and ESI. Although the reaction is known to proceed on intermediate **17** with other amines such as 1-aza-

15-crown-5,[163] either no conversion or slow decomposition of the starting materials were observed under the examined conditions.

A further attempt to attach the chelator **19** to PQQ was made starting directly from **PQQMe2** (Scheme II.12). Unfortunately, the treatment with oxalyl chloride led once more to undesirable side reactions and the ligand **L**PQQ could not be obtained.

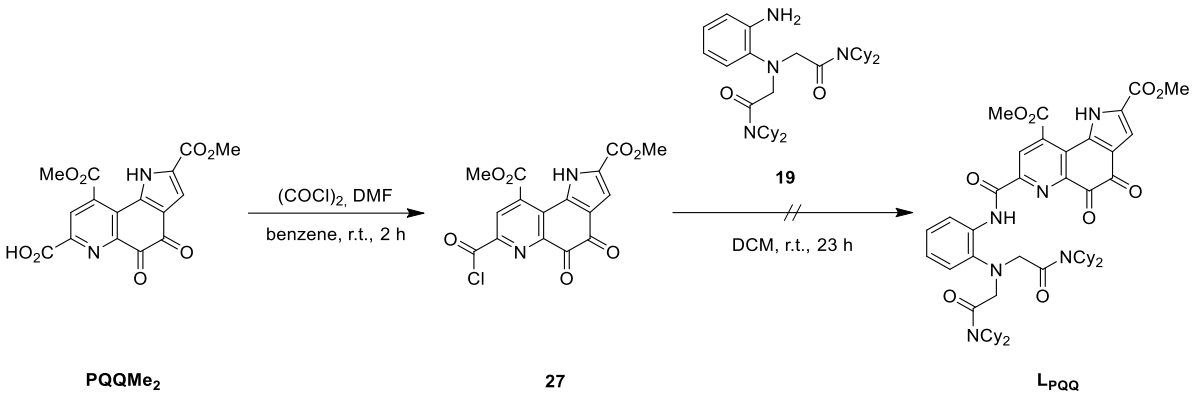

*Scheme II.12: Attempted coupling reaction of **PQQMe2** and chelator **19** to ligand **L**PQQ.*

Since it was shown that coupling with oxalyl chloride was not feasible for the described system, an alternative method towards the ligand preparation was examined using a different activation agent. PyBOP (benzotriazol-1-yl-oxytripyrrolidinophosphonium hexaflorophosphate) is a hydroxy-benzotriazole-based onium salt coupling reagent widely used in peptide synthesis and it is well known for its useful activating properties.[172] In comparison to the reactions with the analogue reagent BOP (benzotriazol-1-yloxytris(dimethylamino)phosphonium hexafluorophosphate), the reactions with PyBOP do not produce HMPT (hexamethylphosphoramide) as a carcinogenic side product (Chart II.2).[172]

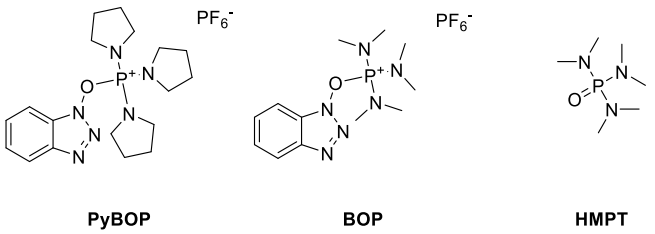

Chart II.2: Molecular structures of PyBOP, BOP and HMPT.

During the PyBOP mediated one-pot amidation reaction (Scheme II.13), a base such as TEA or Hünig's base deprotonates the carboxylic acid, which reacts with PyBOP to form an activated acylphosphonium species and hydroxylbenzotriazole. Subsequently, the hydroxybenzotriazole moiety attacks the activated acid to form a reactive benzotriazole ester, which subsequently reacts with the amine.[173]

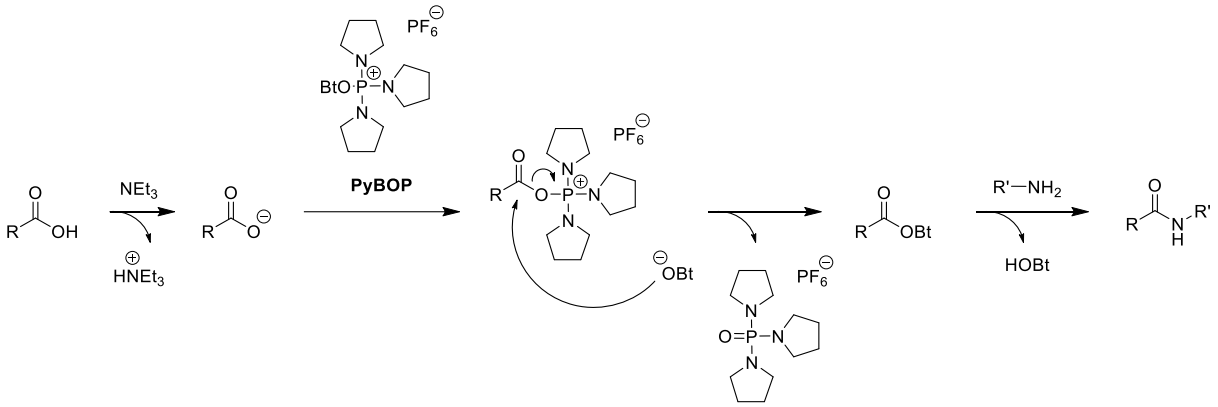

Scheme II.13: Amide bond formation using PyBOP as a coupling reagent. Reaction scheme adapted from literature.[173]

As shown in Scheme II.14, PQQ dimethyl ester (**PQQMe$_2$**) was coupled successfully to chelator **19** in the presence of PyBOP and triethyl amine in dry DMF to yield the desired ligand **L$_{PQQ}$**.

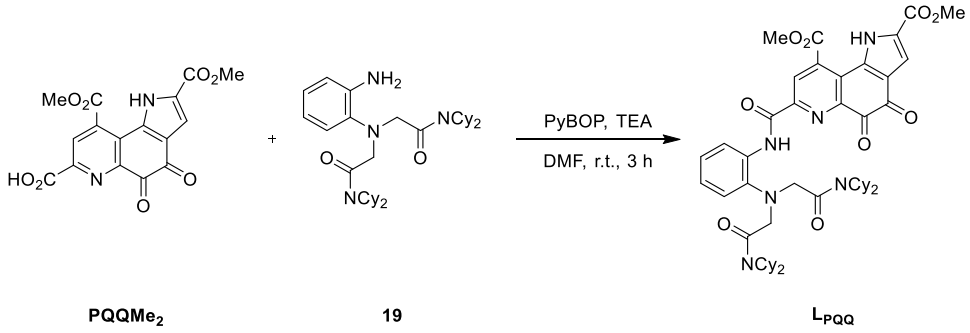

*Scheme II.14: Coupling reaction of **PQQMe$_2$** and chelator **19** to ligand **L$_{PQQ}$** using PyBOP and TEA.*

The reaction progress was monitored by TLC and a complete consumption of the starting materials was indicated within 3 h. The formation of the ligand was verified by ESI-mass spectrometry as well as X-ray analysis of a single crystal (Figure II.2). However, purification of the crude mixture was necessary, since 1,1',1''-phosphoryltripyrrolidine was generated as a by-product during the reaction. Unfortunately, the purification showed to be challenging, since the crude mixture exhibited only low to no solubility in ethyl acetate, acetonitrile, 1,4-dioxane, methyl tert-butyl ether, diethyl ether and toluene. Different purification methods such as recrystallization and trituration from boiling solvents or solvent systems as well as filtration over a pad of Celite or silica were tested, however the ^{1}H NMR analysis of the product still indicated a significant amount of contamination. Furthermore, purification attempts by flash column chromatography with different eluent systems were made, including ethyl acetate/iso-hexane/TEA, DCM/MeOH or a combination thereof. However, a clean ^{1}H NMR spectrum could not be obtained. The only method, which showed to be promising, was crystallization by vapor diffusion using DCM and diethyl ether, nonetheless product crystals could only be obtained in a scale of 5.0 to 8.0 mg.

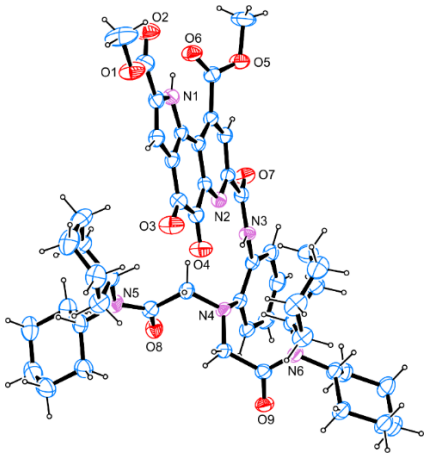

Figure II.2: Crystal structure of ligand **L**$_{PQQ}$.

To avoid the need for elaborate purification methods, an alternative coupling approach was examined. The coupling reagent 1,1'-carbonyldiimidazole (CDI) was considered as a suitable candidate, since it allows one-pot amide formation with only water-soluble by-products.[174]

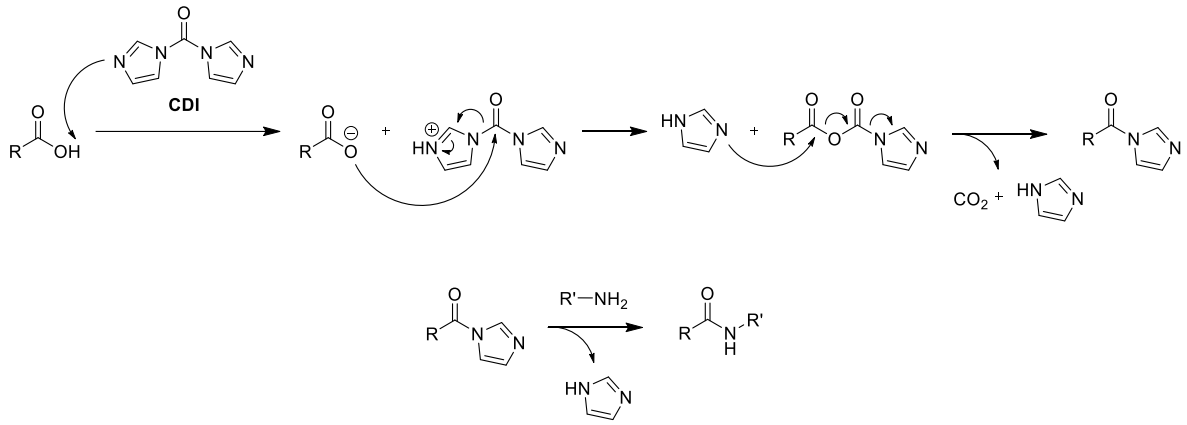

Scheme II.15: Amide bond formation using CDI as a coupling reagent. Reaction scheme adapted from literature.[173]

As shown in Scheme II.15, the reaction mechanism involves the formation of an acyl carboxy imidazole and imidazole, which readily react to give an activated acylimidazole species. A nucleophilic attack at the activated carbon by an amine leads to amide bond formation and elimination of imidazole, which can be easily removed by an aqueous work up.

Various reaction conditions for the coupling of **PQQMe$_2$** and chelator **19** were examined, including the use of different amounts of reagents, different solvents, temperature and time (Table II.3). Unfortunately, the formation of the desired product **L**$_{PQQ}$ was not successful and not even traces of it could be found in the crude mixture. The CDI-mediated amide coupling reaction showed to be convenient for the formation of ligand **PQQ$_{15\text{-}5}$** (see Chapter II.2.), however the coupling of **PQQMe$_2$** and chelator **19** could not be implemented. By comparing both reactions, some differences in the co-ligands could be noted, which were initially considered as the reason for the different reaction

outcomes. 1-Aza-15-crown-5 ether is an aliphatic secondary amine and chelator **19** on the contrary is an aromatic primary amine. However, various literature reports show that CDI-mediated amidation reactions can be successfully conducted on aromatic primary amines and aromatic carboxylic acids.[175–177] Thus, there should be another reason for the unsuccessful conversion under the examined conditions. Due to time reasons, however, further investigations of this method were abandoned.

*Table II.3: Investigated reaction conditions for the coupling of **PQQMe**$_2$ and chelator **19** using CDI and TEA.*

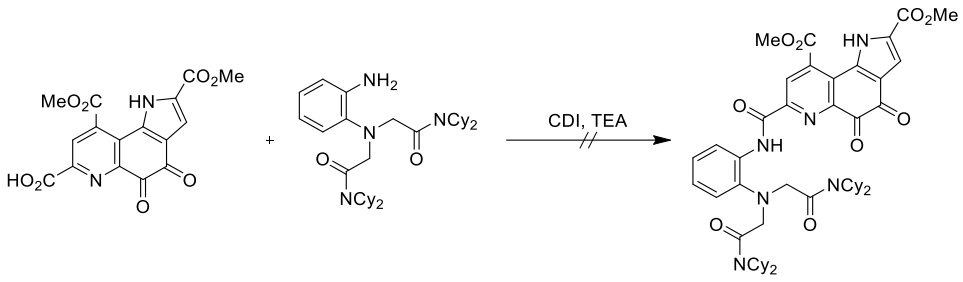

Entry	CDI (equiv.)	TEA (equiv.)	Solvent	Temperature	Time (h)	Yield (%)
1	1.2	2.0	DMF	r.t.	24	-
2	1.2	2.0	DMF	60 °C	24	-
3	1.2	4.0	DMF	r.t.	2	-
4	1.2	4.0	DMF	r.t.	120	-
5	1.9	-	THF	80 °C	24	-
6	2.4	4.0	DMF	60 °C	24	-

In search of an optimal coupling reagent for the synthesis of ligand **L**$_{PQQ}$, 1-ethyl-3-(3′-dimethylamino)carbodiimide hydrochloride salt (EDC·HCl) was considered as a promising candidate.[178] As shown in Scheme II.16, an *O*-acylisourea species can be formed by reacting EDC·HCl with a carboxylic acid. In the presence of an amine, the *O*-acylisourea can directly react to the respective amide and urea by-product, which can be eliminated by aqueous work up. However, the *O*-acylisourea often gets converted to the unreactive *N*-acylurea by racemization and acetyl transfer. Hence, hydroxybenzotriazole (HOBt) is commonly used in combination with EDC·HCl, since it can react fast to a HOBt-activated ester, thus avoiding side reactions.[179] This intermediate exhibits an increased electrophilicity of the carbonyl resulting from the electron-withdrawing character of the OBt-moiety, thus enabling the amide bond formation with a wide range of nucleophiles.

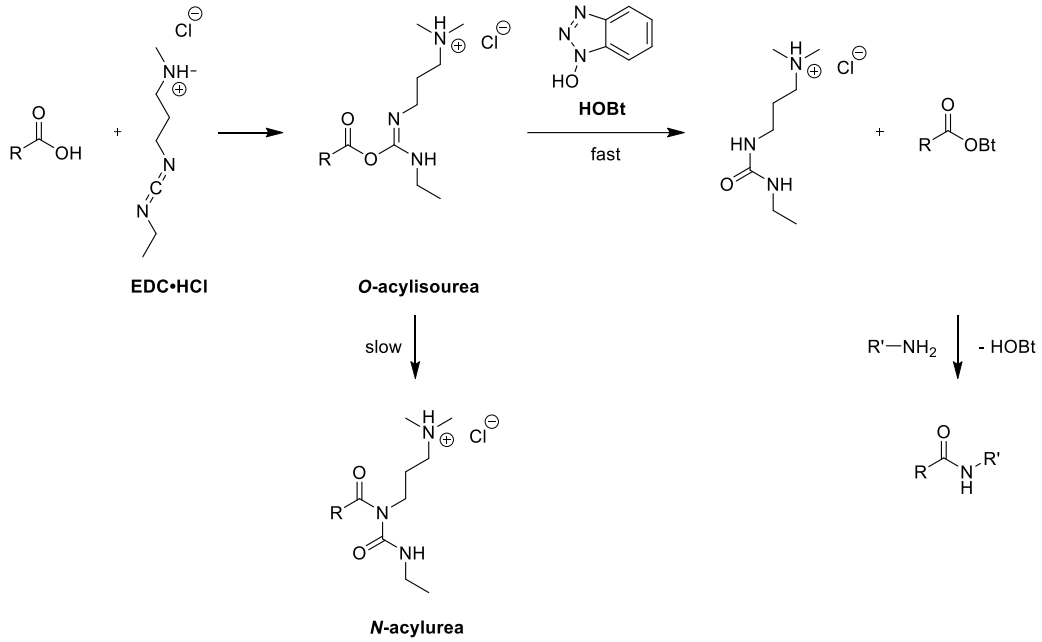

Scheme II.16: Amide bond formation using EDC·HCl and HOBt as coupling reagents. Reaction scheme adapted from literature.[173]

Therefore, two different reaction conditions were investigated using EDC·HCl and HOBt·H_2O and the successful formation of **L**$_{PQQ}$ was determined by TLC and ESI (Table II.4).

*Table II.4: Investigated conditions for the coupling of **PQQMe**$_2$ and chelator **19** using EDC·HCl and HOBt·H_2O.*

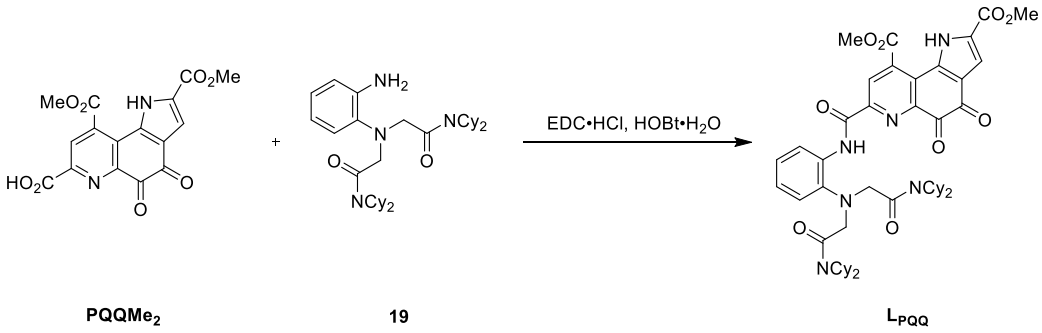

Entry	Solvent	Temperature	Time (h)	Yield (%)
1	DMF	r.t.	48	60[a]
2	DCM	r.t.	2	56[b]

a. Yield related to the crude product.
b. Yield related to the product purified by flash column chromatography.

In the ESI-mass spectra of the crude mixture from the first reaction (Entry 1, Table II.4), the desired product **L**$_{PQQ}$ was observed in the positive (m/z = 891.4673, calc. 891.4651) and negative (m/z = 889.4509, calc. 889.4506) ionization mode. Furthermore, a mass which corresponds to the water adduct could also be observed in the negative (m/z = 907.4623, calc. 907.4611) ionization mode as well as in the

positive ionization mode together with a sodium ion (m/z = 931.4599, calc. 931.4576). Moreover, the mass of the methanol adduct (m/z = 921.4779, calc. 921.4768) was also found, probably due to traces of methanol in the instrument. The observed species show the ability of the ligand, similar to PQQ,[97,142,180,181] to readily form adducts with different nucleophiles.

In order to purify the crude product from the second reaction (Entry 2, Table II.4), a flash column chromatography was performed, using a mixture of diethyl ether and iso-hexane (80:20) as an eluent. It should be mentioned, that the use of pressure during the run of the column could lead to poor separation of the main product from the impurities, hence it is recommended to run the column by gravity and not by using a flash purification system. A TLC of the collected product fractions did not indicate any impurities, however, as already discussed above, the ^{1}H NMR spectrum of the product still showed plenty of additional signals. Considering the ability of the ligand to form adducts with various nucleophiles such as water and methanol, it can be assumed that the formation of these species could be the reason for the ambiguous NMR spectra.

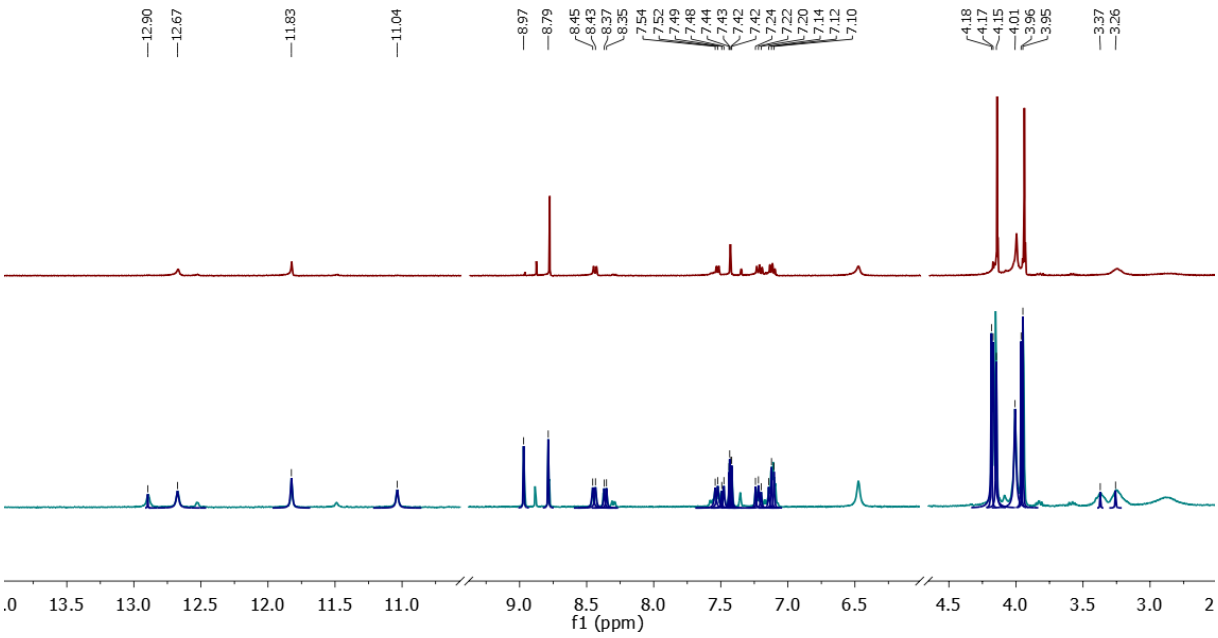

Figure II.3: ^{1}H NMR spectra of ligand **L**$_{PQQ}$ *in CD_2Cl_2 at room temperature. The red spectrum was taken right after the sample preparation and the blue spectrum was obtained by measuring the same sample after 1 day.*

As shown in Figure II.3, a spectrum was recorded immediately after the sample preparation and it showed only signals, which could be assigned to the ligand according to their number and integral values. However, even after short time a second set of signals has appeared, making the interpretation of the spectrum difficult. Often the presence of rotamers in a solution can complicate the NMR analysis,[182] however, in this case a doubling of almost every signal can be observed. This observation further supports the assumption of the existence of some **L**$_{PQQ}$ adducts or an equilibrium between the ligand and a dimer of it.

In addition, the solid was analyzed by CW EPR and as shown in Figure II.4, a low intensity signal was observed indicating the presence of some small amount of radicals in the sample. Together with the observations made by NMR, the results let suspect that the radical species could undergo some self-association processes in solution.

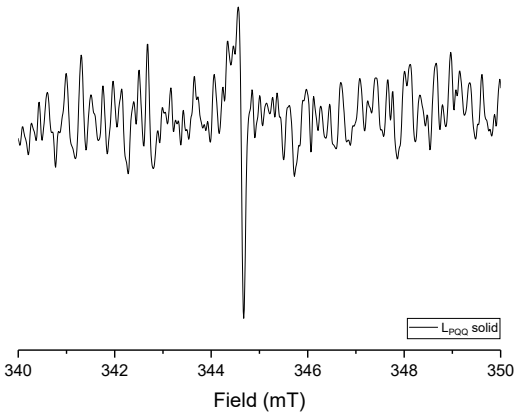

Figure II.4: CW EPR spectrum at X-band (9.5 GHz) of ligand ***L****PQQ at room temperature.*

To summarize, ligand **L**PQQ was synthesized through an EDC·HCl/HOBt·H_2O-mediated amide coupling between **PQQMe2** and chelator **19** in a yield of 56%. Different purification methods were investigated, however the ^{1}H NMR analysis of the compound showed the presence of multiple species in solution. Thus, future experiments should focus on the identification of these species and the removal of the radicals present in the product. This could be achieved by either exploring alternative synthetic routes, handling and analyzing of the product under air- and water-free conditions or changing the purification methods.

4. Synthesis of PQQMe2-Diethyl 3,3'-azanediyldipropionate

With the objective to further expand the library of PQQ-based ligands for MDH-biomimetic investigations, a ligand incorporating PQQ dimethyl ester (**PQQMe2**) and diethyl 3,3'-azanediyldipropionate (**28**) was synthesized (Scheme II.17). A structural advantage of the model compound PQQMe2-**Di**e**t**hyl 3,3'-azanediyl**dip**ropionate (**PQQ**DEDP) is the incorporation of two flexible pendant coordinating arms, that can direct the coordinating cavity to the desired PQQ position. The amidation reaction using CDI and TEA proceeded successfully and yielded 61% of ligand **PQQ**DEDP.

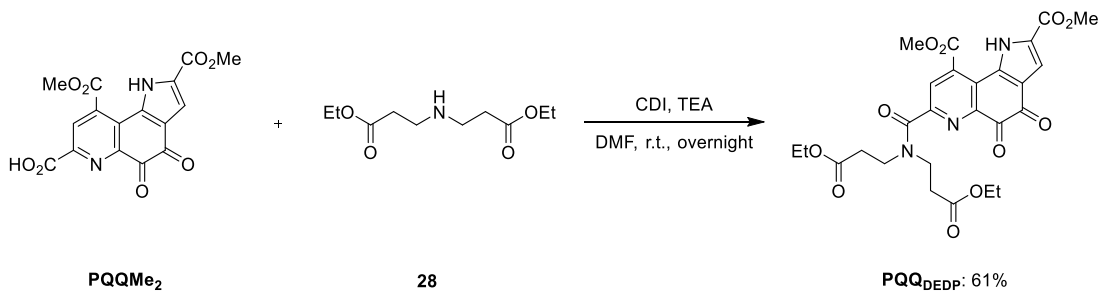

*Scheme II.17: Coupling of **PQQMe**$_2$ and diethyl 3,3′-azanediyldipropionate (**28**) to ligand **PQQ**$_{DEDP}$ using CDI and TEA.*

With **PQQ**$_{DEDP}$ in hand, a further modification was attempted, aiming at the synthesis of a ligand with two flexible pendant carboxylic arms. Previously Itoh *et al.* presented a procedure for the regioselective hydrolysis of the methyl ester functionality at C-7′ of **PQQMe**$_3$ whereby the ester groups at positions C-9′ and C-2′ have been preserved.[169] Therefore, this procedure was also applied on ligand **PQQ**$_{DEDP}$ with the objective to hydrolyze the ethyl ester functionalities of the diethyl 3,3′-azanediyldipropionate moiety by retaining the two methyl ester groups of PQQ. Hence, a mixture of TFA and water (2:1) was added to **PQQ**$_{DEDP}$ and the reaction mixture was stirred at 60 °C overnight. According to the mass spectrometric data, the desired product **29** was successfully synthesized. Unfortunately, addition of water did not result in precipitation of the pure product, as known from the experimental procedure towards the synthesis of **PQQMe**$_2$. Therefore, a work-up procedure including extraction with DCM from neutral and acidic aqueous solutions was performed and the NMR spectra indicated only some minor impurities in the upfield region. In order to purify the product, a semi-preparative HPLC (H_2O·0.1 %TFA/CH_3CN, 90:10 - 60:40) was performed, however, the ^{1}H NMR spectra indicated impurities in the collected product fractions. For time reasons, the purification attempts of **29** were not carried out further, however future trials could include the use of different column sizes, stationary phase materials or solvent gradients.

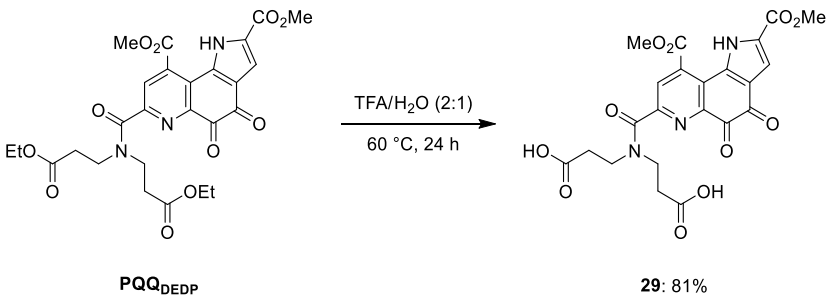

*Scheme II.18: Selective ethyl ester hydrolysis of **PQQ**$_{DEDP}$ to **29**.*

5. Synthesis of $PQQMe_2H_2$

As part of her bachelor thesis, conducted under my supervision, Sophia Glocker examined the synthesis of the reduced **$PQQMe_2$** species **$PQQMe_2H_2$** as a reference for analytical studies. Thereby, a procedure originally reported for the reduction of PQQ by Ikemoto *et al.*, was applied. **$PQQMe_2$** was suspended in water and the mixture was added dropwise to an acidic aqueous solution of L-(+)-ascorbic acid at 10 °C over 1 h (Scheme II.19). The mixture was than stirred overnight at room temperature and after filtration of the precipitated solid, **$PQQMe_2H_2$** was obtained in 65% yield as red-brown solid. The successful formation of the species was confirmed by NMR and IR spectroscopy as well as elemental microanalysis.

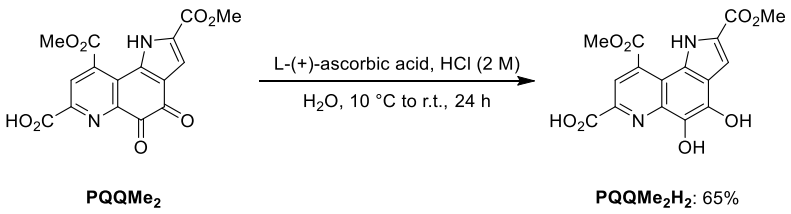

$PQQMe_2$ **$PQQMe_2H_2$**: 65%

*Scheme II.19: Reduction of **$PQQMe_2$** with L-(+)-ascorbic acid to **$PQQMe_2H_2$**.*

6. Synthesis of $PQQMe_2$-DFO

Reasoning that the synthesis of XoxF-MDH-inspired model ligand should regard the distinct preference of the lanthanides for hard oxygen donors,[183,184] siderophore-based ligands could be considered as good candidates. In the last decades different siderophore inspired ligands have been reported to efficiently chelate lanthanides and actinides.[185–190] Siderophores are small compounds produced by bacteria, fungi and graminaceous plants with an extremely high affinity for Fe^{3+}.[191] Thus, their main and essential function is to mobilize iron sources from the environment. However, in addition to iron(III), other di- and trivalent metal ions such as lanthanides(III) can also bind to the siderophores.[192,193] The strong tendency of siderophores to bind these highly charged metal ions reflects the hard oxygen donor atoms present in their respective structures which include catecholates, hydroxamates, carboxylates and amides.[162] Deferoxamine (DFO) is a trihydroxamate siderophore and recent studies have shown that lanthanides are able to form stable complexes with DFO (Chart II.3).[192,194]

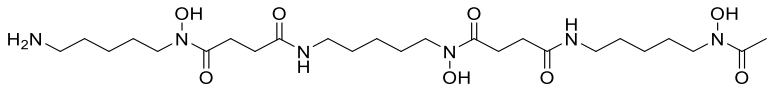

Chart II.3: Structure of deferoxamine B (DFO). DFO is a member of the family of the hydroxamate siderophores. Three hydroxamate groups are responsible for the binding to Fe^{3+} as well as to trivalent lanthanides. A recent study of the stability constants of lanthanide-DFO-complexes showed that the entire lanthanide series, except for Ce^{3+} and Pm^{3+}, exhibits a complexation with a seawater ionic strength.[194]

Hence, this project aimed to afford a PQQ-based ligand with integrated DFO scaffold. In order to estimate the coordination capacity of ligand PQQMe2-DFO (**PQQ**DFO) with lanthanides, a calculation with Spartan was performed by Lena Daumann. As shown in Figure II.5, the lanthanum ion has a nona-coordinate geometry and the ligand, which encircles the metal, allows PQQ to come in close proximity. The bond lengths between the La^{3+} ion and the cofactor are 2.6 Å (La^{3+}-O5), 2.7 Å (La^{3+}-N6) and 2.7 Å (La^{3+}-N-(amide)). These values of the atom distances are fairly close to those in the enzyme: 2.6 Å (Ce-O5), 2.8 Å (Ce-N6) and 2.7 Å (Ce-O7).[10]

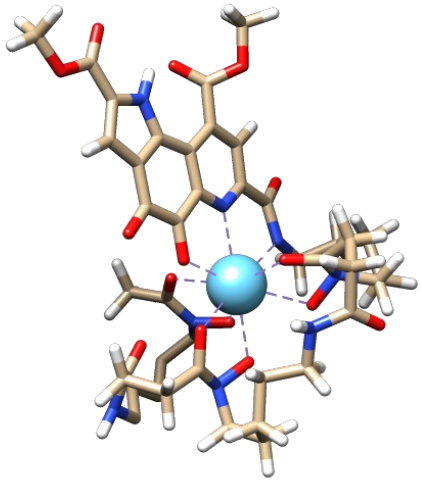

*Figure II.5: Spartan optimized structure of La^{3+} coordinated **PQQ**DFO with deprotonated amide bond between PQQ and DFO. Image generated with the UCSF Chimera package.*[110]

For the coupling reaction of **PQQMe2** and DFO over an amide bond, PyBOP was used as activating reagent and TEA as base (Table II.5, Entry 1). DFO is commercially available as DFO mesylate (DFOM). Mass spectrometric analysis of the crude product verified the successful formation of the desired ligand **PQQ**DFO. Unfortunately, the attempt to purify the product by flash column chromatography, using a very polar eluent mixture of DCM and methanol was not successful. Reasoning that the coupling reaction with PyBOP would complicate the purification of the desired product, because of the side products formed during the reaction (see Chapter II.3.), an alternative approach was chosen.

*Table II.5: : Coupling of **PQQMe2** and DFO mesylate to ligand **PQQ**DFO.*

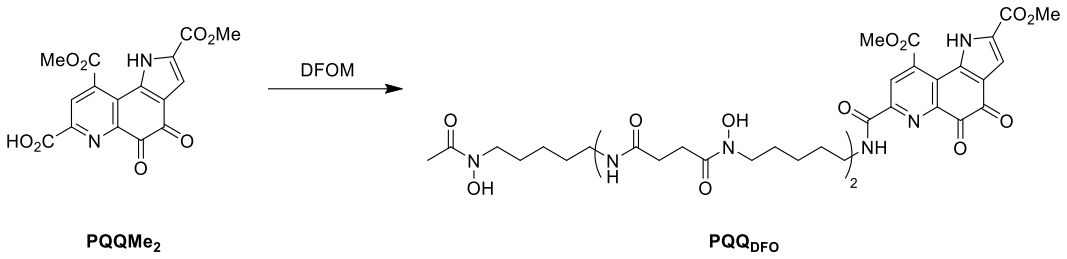

Entry	Reagent	Base	Solvent	Temperature	Time (h)	Yield (%)
1	PyBOP	TEA	DMF	r.t.	18	n.d.
2	EDC·HCl, HOBt·H_2O	TEA	DCM	0 °C to 60 °C	72	0
3	CDI	TEA	DMSO/DMF	60 °C to r.t.	24	n.d.

The EDC·HCl/HOBt·H_2O-mediated amide coupling reaction described in the previous chapter promised to be successful, thus the procedure was examined towards the synthesis of ligand **PQQ**DFO. Various reaction temperatures, solvent volumes and reaction times were investigated (Table II.5, Entry 2), however, the effort to couple **PQQMe2** and DFO was not successful.

In 2018 Laurent and coworkers reported the synthesis of DFO linked aromatic ligands, using CDI and TEA for the amide bond formation.[195] This coupling reagent produces imidazole as a side product, which is soluble in water and can be easily removed from a crude mixture by applying standard work-up procedures. As shown in Table II.5 (Entry 3), **PQQMe2** was stirred with CDI at 60 °C for 1 h. Subsequently, the activated acid was added dropwise to a stirring solution of DFO mesylate and TEA in DMSO, which was also stirred for 1 h at 60 °C. Finally, the reaction mixture was stirred at room temperature overnight. The successful formation of the ligand was verified by ESI-mass spectrometry, where a product signal was observed in both positive (m/z = 901.3963, calc. 901.3938) and negative (m/z = 899.3786, calc. 899.3792) ionization mode. However, the work-up and purification attempts were unsuccessful due to the insolubility of crude mixture in aqueous and organic solvents, except for methanol which on the other hand is known to form adducts with the PQQ moiety. Reversed phase column chromatography, using water and acetonitrile (50:50), as well as normal phase column chromatography, using DCM and methanol (90:10), were performed, however the desired product could not be isolated. Further investigations on this project would be focused on developing a convenient purification method for ligand **PQQ**DFO, including HPLC purification attempts and crystallization experiments.

III. COORDINATION CHEMISTRY OF PQQ DERIVATIVES AND LIGANDS

1. Introduction

For a long time, it was widely believed that only calcium serves as Lewis acid for the activation of PQQ in methanol dehydrogenases.[87] However, recent findings have overturned this conception. It has come to light that numerous methanol-oxidizing bacteria possess the ability to produce not only the extensively studied calcium-dependent MDH, but also a second one, which employs lanthanide ions instead of calcium.[136]

The lanthanide-utilizing bacteria fall into two primary categories: those that possess only the gene for the Ln-MDH and those who carry genes for both Ln- and Ca-MDH enzymes, *xoxF* and *mxaF* respectively.[6] The second type of bacteria exhibit the remarkable capacity to switch between both genes based on the metal ion availability in the environment, with preference for Ln-MDH expression.[115] This intriguing phenomenon has been termed the "lanthanide switch".[116,117,196,197] In addition, studies have shown that these bacteria exhibit different preferences for lanthanides, and the selection of a specific lanthanide has repercussions on their growth rate and also the activity of the alcohol dehydrogenase.[10,106,115,117,118,126,198,199] However, it was shown that all known strains prefer the early lanthanides.[10,22,115] This implies that this tendency is influenced not solely by the bioavailability of the lanthanides, but also by their coordination, chemistry and physical properties.[22] Recent studies utilizing classical molecular dynamics simulations, in conjunction with fragment molecular orbital analysis, as well as DFT calculations support this assumption.[118,200]

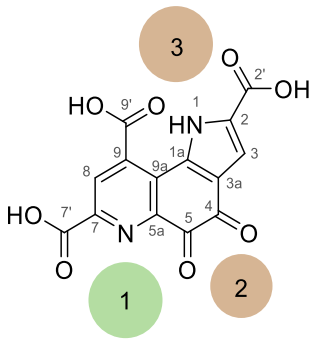

Figure III.1: Possible coordination sites in solution and numbering scheme of PQQ.[88,201]

In the last years, many research projects have underscored the essential role of biomimetics in understanding the dynamics of enzyme active sites. Consequently, functional model studies are regarded as a crucial tool for gaining deeper insights into the nature of interactions occurring within the active sites of XoxF- and MxaF-MDH. While utilizing PQQ to coordinate metal cations appears to be the most direct approach in this case, it should be considered that there is a challenge associated with designing analogues of MDH active sites. PQQ has several donor groups, thus providing several binding sites for metal ions (Figure III.1). The coordination pattern observed in dehydrogenase enzymes that have been crystallographically analyzed from both Ca-dependent and Ln-dependent bacteria features a tridentate PQQ which coordinates the metal ion as a pincer ligand *via* a carboxylic acid moiety (O-7′), a pyridyl nitrogen (N-6) and a quinone oxygen atom (O-5).[10,106,107,111,202] However, studies on PQQ with several transition metals as well as sodium ions have demonstrated that, depending on the specific metal ion and the accompanying ligands, all three possible binding sites of PQQ can be occupied outside of the enzymatic environment.[140,201,203–209] To overcome this potential problem, the design of an active site model required a judicious choice of ligands, hence several studies in this field employed structural model complexes based on either PQQ derivatives or PQQ analogue compounds.[143,144,163,164,166]

As mentioned in the previous chapter, the group around Itoh and Fukuzumi investigated several synthetic functional models of calcium-dependent alcohol dehydrogenases in the past.[142–144,163,164] The study based on the aza-crown ligand **PQQ$_{15\text{-}5}$** examined its coordination ability towards various alkaline earth metal ions and NMR investigations indicated that the binding position of Ca^{2+} to PQQ is the same as in the natural counterpart (site 1).[163] Thereby, a significantly high binding constant for 1:1-complex formation between **PQQ$_{15\text{-}5}$** and Ca^{2+} was determined, showing that Ca^{2+} binds to the quinone most strongly among the examined metals (Table III.1). The experimental data together with the results from a computer simulation pointed the importance of the ionic radius for the complex formation. The authors assumed that larger metal ions such as Sr^{2+} and Ba^{2+} tend to induce a strain around the metal binding site and the smaller Mg^{2+} ion may be too small to bring the PQQ moiety and the crown ether ring together. In addition, UV-Vis titration experiments were carried out with **PQQMe$_3$**, revealing a similar trend in the binding constants for alkaline earth metal ions as observed in the model system based on **PQQ$_{15\text{-}5}$**.[144] Nonetheless, a comparison of the binding constants between both ligand systems highlights a substantial improvement in the metal ion binding capacity of ligand **PQQ$_{15\text{-}5}$** due to the inclusion of the crown ether ring into the PQQ molecule. In addition, as anticipated, the carboxyl group at C-7′ in **PQQMe$_2$** also has an enhancing effect on the binding constant for Ca^{2+}.

Table III.1: Metal ion binding constants reported by Itoh and Fukuzumi.[144,163]

Metal ion	*K* (M^{-1})		
	$PQQ_{15\text{-}5}$	**$PQQMe_3$**	**$PQQMe_2$**
Mg^{2+}	72	< 5	-
Ca^{2+}	210 000	1 900	5 700
Sr^{2+}	110 000	590	-
Ba^{2+}	40 000	380	-

In order to gain a deeper understanding into the chemistry of PQQ and its interaction with lanthanides, Lumpe *et al.* conducted a comprehensive study on PQQ, involving a thorough examination through NMR, IR and UV-Vis spectroscopic techniques.[136] Additionally, they characterized the water adduct of PQQ and investigated the metal ion coordination behavior of PQQ in solution using lanthanides and calcium. The studies indicated that the coordination of lanthanides in non-aqueous solvents occurs within the biologically relevant pocket (site 1). Furthermore, a UV-Vis study revealed that despite the similar chemical properties of lanthanides, the difference in ionic radii along the series affect the electronic structure of the cofactor. In a following study by the same research group, it was found that complexes with early lanthanides are preferentially formed with PQQ.[44] This behavior resembles the preference for early lanthanides by Ln-utilizing bacteria.

Inspired by the natural counterpart, the work outlined in this chapter seeks to enhance our comprehension of the coordination chemistry of PQQ derivatives with biologically relevant metal ions such as alkaline earth metal ions and lanthanide ions. This knowledge is crucial for advancing the field of MDH biomimetics.

2. Interaction of $PQQ^{15\text{-}5}$ with Lanthanide and Alkaline Earth Metal Salts

The following section is part of the publication:

Pyrroloquinoline Quinone Aza-Crown Ether Complexes as Biomimetics for Lanthanide and Calcium Dependent Alcohol Dehydrogenases

Violeta A. Vetsova, Katherine R. Fisher, Henning Lumpe, Alexander Schäfer, Erik K. Schneider, Patrick Weis and Lena J. Daumann

Published in: *Chem. Eur. J.* **2021**, *27*, 10087–10098.

Results and Discussion

Metal ion coordination

Initial efforts were focused on the reproduction of the results from Itoh and Fukuzumi,[163] who had used UV-Vis spectroscopy and calcium perchlorate salts, and comparison with the respective lanthanide perchlorate precursors. However, this turned out to be more challenging than anticipated due to highly fluctuating UV-Vis signatures of the PQQ moieties, the hygroscopic nature of the lanthanide perchlorates and thus a fluctuating water and metal content, which made titrations and data evaluation cumbersome. Lumpe and Daumann have previously reported the problems when assigning species in the UV-Vis spectra of PQQ with lanthanide salts as multiple species such as the PQQ-H_2O adduct can form with trace amounts of water with their own unique UV-Vis signatures.[136] In addition, all attempts to obtain single crystals of the metal complexes of **$PQQ^{15\text{-}5}$** suitable for X-ray analysis were unsuccessful (see chapter VI.1.), a circumstance that showed to be a common problem in this and previous studies focusing on the metal interactions with PQQ and PQQ derivatives.[44,136,163] Hence, the interaction of **$PQQ^{15\text{-}5}$** with metal salts was examined using NMR spectroscopy. The metal ion coordination behavior of $PQQMe_2$-1-aza-15-crown-5 (**$PQQ^{15\text{-}5}$**) in acetonitrile solution was investigated using barium(II) and calcium(II) salts as well the first and last lanthanides from the series, lanthanum (III) and lutetium(III), which are also both diamagnetic (Figure III.2).

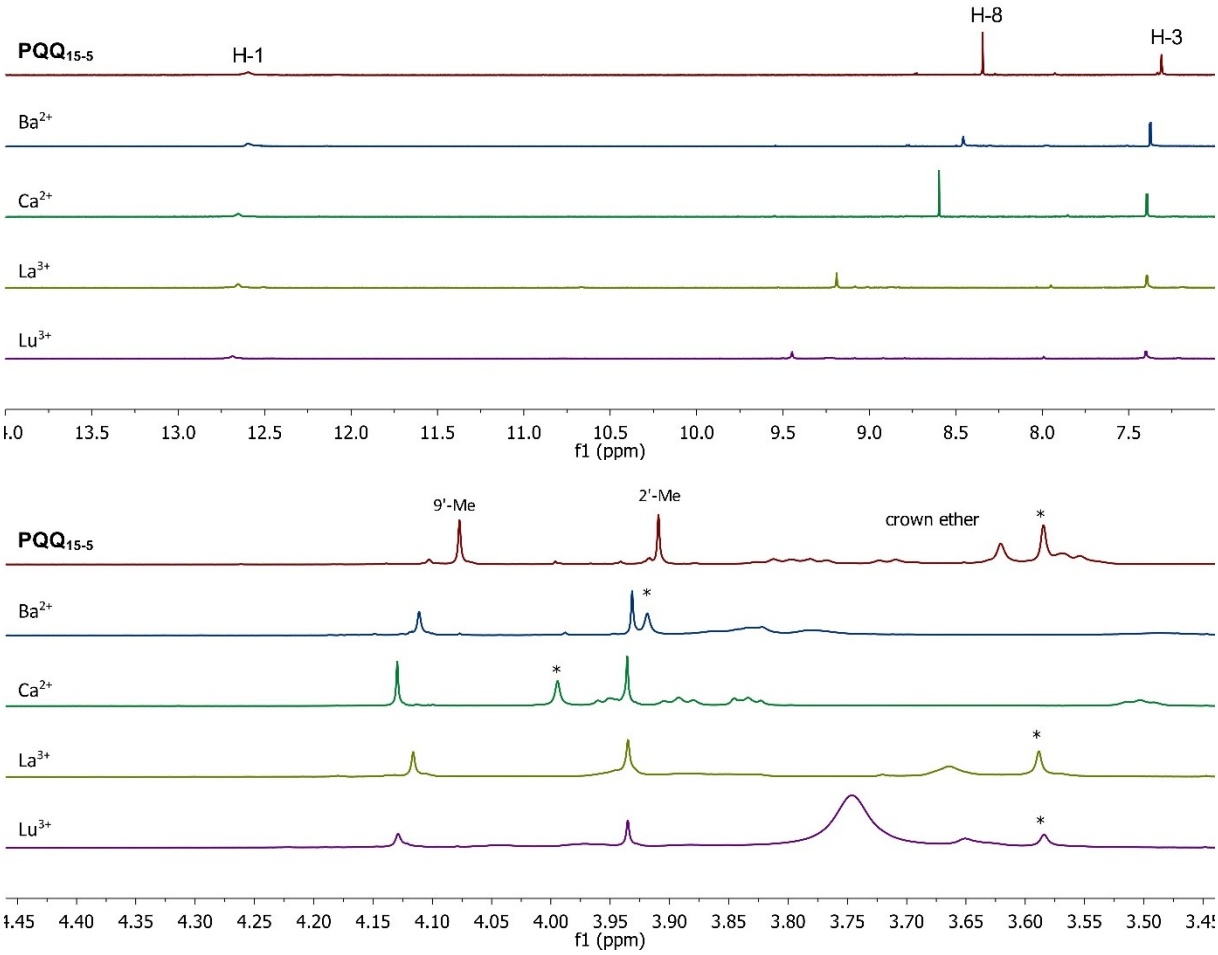

*Figure III.2: ^{1}H NMR spectra of ligand **PQQ**$_{15\text{-}5}$ (6.5 mM) without metal salt (red) and in the presence of 2.0 equiv. barium(II) triflate (blue), calcium(II) triflate (green), lanthanum(III) triflate (yellow) or lutetium(III) triflate (purple) in CD_3CN. The methylene proton resonance with the highest intensity in the crown ether multiplet is marked with (*) for clarity.*

*Table III.2: Selected ^{1}H NMR resonances (ppm) of **PQQ**$_{15\text{-}5}$ in CD_3CN and resonance shifts (ppm) after the addition of different metal triflates.*

Position	δ (PQQ$_{15\text{-}5}$)	Δδ (Ba^{2+})	Δδ (Ca^{2+})	Δδ (La^{3+})	Δδ (Lu^{3+})
1	12.60	0.0	0.05	0.05	0.09
8	8.34	0.12	0.26	0.85	1.11
3	7.31	0.06	0.08	0.09	0.09
9'-Me	4.08	0.03	0.05	0.04	0.05
2'-Me	3.91	0.02	0.03	0.02	0.03
1	12.60	0.0	0.05	0.05	0.09

The addition of solid calcium(II) triflate to the ligand in acetonitrile resulted in an instant color change from orange-yellow to red (UV-Vis spectra demonstrating the absorption change of the ligand upon addition of metals are provided in the Supporting Information, Figure VI.2). In the ^{1}H NMR spectrum,

the H-8 proton of the ligand showed a strong downfield shift ($\Delta\delta$ = 0.26 ppm) upon complexation with Ca^{2+}, which was larger than the shift of the H-3 proton ($\Delta\delta$ = 0.08 ppm). The values are very close to those reported by Itoh *et al.* for **PQQ15-5** and calcium perchlorate ($\Delta\delta$ = 0.22 and 0.06 ppm, respectively).[163] The resonances of the methyl ester protons at the 9′ and 2′ positions were only slightly influenced upon Ca^{2+} binding ($\Delta\delta$ = 0.05 and 0.03 ppm, respectively). The methylene proton resonances of the crown ring on the other hand, showed a clear change in the presence of Ca^{2+}, whereby shifts in both directions, downfield as well as upfield were observed. The tendencies of the chemical shifts in ^{1}H NMR suggest that the interaction between Ca^{2+} and ligand **PQQ15-5** takes place at the crown ether moiety and most probably at the C-5 quinone carbonyl oxygen as well as at the N-6 pyridine nitrogen. Similar shifts were observed upon addition of barium(II) triflate to the ligand solution (Table III.2), albeit with a slightly different shift of the crown ether methylene protons (Figure III.2).

The addition of Ln^{3+} salts to the solution of **PQQ15-5** resulted in a color change from orange-yellow to dark red (Figure VI.2). The obtained ^{1}H NMR spectra showed a very strong metal induced shift of H-8 (La^{3+}: $\Delta\delta$ = 0.85 ppm and Lu^{3+}: $\Delta\delta$ = 1.11 ppm) and a signal broadening. Similar to the experiment with Ca^{2+}, the H-3 resonance was less shifted in the presence of a Ln^{3+} ion ($\Delta\delta$ = 0.09 ppm). However, a major difference in the ligand ^{1}H NMR spectra upon comparison of the divalent alkaline earth metal ions and the trivalent lanthanides emerged by comparing the changes in the crown ether resonances (Figure III.2). The addition of lanthanide(III) triflates resulted only in a small shift of the proton resonance at 3.58 ppm (La^{3+}: $\Delta\delta$ = 0.01 ppm and Lu^{3+}: $\Delta\delta$ = 0.0 ppm, albeit these values are at best estimates as significant signal broadening prevented exact assignment), the alkaline earth metal ion salts on the contrary induced shifts of 0.34 ppm for Ba^{2+} and 0.41 ppm for Ca^{2+}. In the ^{13}C NMR spectra, the addition of metal salts to the ligand caused strong resonance shifts and signal disappearance in the case of the lanthanides (Figure III.3). However, the carbon resonance at C-8 showed a relatively large downfield shift for all four metal ions, while the chemical shift of C-3 was rather small (Table III.3). Thus, this observation further supports the assumption for a metal coordination at the correct binding pocket of PQQ.

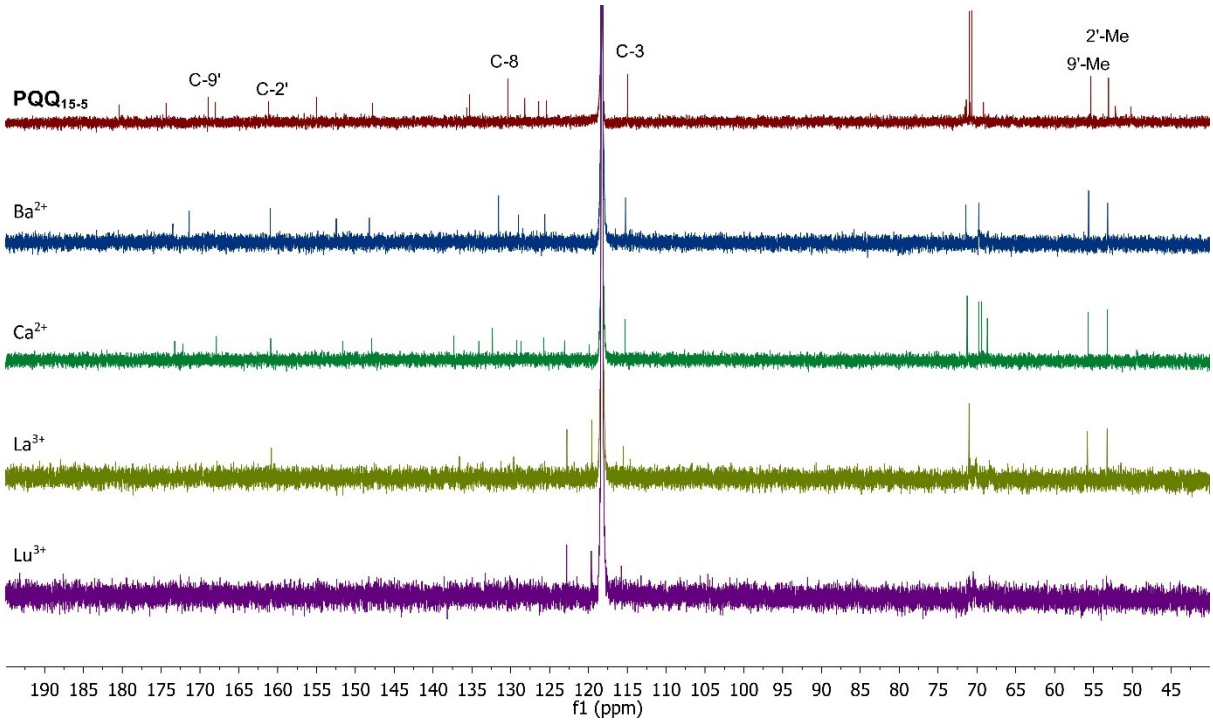

*Figure III.3: ^{13}C NMR spectra of ligand **PQQ**$_{15\text{-}5}$ (6.5 mM) without metal salt (red) and in the presence of 2.0 equiv. barium(II) triflate (blue), calcium(II) triflate (green), lanthanum(III) triflate (yellow) or lutetium(III) triflate (purple) in CD_3CN.*

*Table III.3: ^{13}C NMR resonances (in ppm) of **PQQ**$_{15\text{-}5}$ in CD_3CN and resonance shifts (in ppm) after the addition of different metal triflates.*

Position	δ (PQQ$_{15\text{-}5}$)	$\Delta\delta$ (Ba^{2+})	$\Delta\delta$ (Ca^{2+})	$\Delta\delta$ (La^{3+})	$\Delta\delta$ (Lu^{3+})
9'	168.9	-0.8	-1.0	-1.0	-
2'	161.2	-0.3	-0.3	-0.3	-
8	130.4	1.2	1.9	3.2	4.5
3	115.0	0.2	0.3	0.6	0.8
9'-Me	55.3	0.3	0.4	0.5	0.6
2'-Me	53.1	0.1	0.1	0.2	0.2

* No signals could be observed in the HMBC spectra of the ligand in the presence of Lu^{3+}.

Impact of the counterions on the complex species

To study the possible impact of counterions and to gain more insight into the structures and stabilities of the different species present in solution prior to the reaction with alcohols, we performed mass spectrometry and ion mobility experiments in combination with density functional (DFT) calculations. The concentrations of ligand **PQQ**$_{15\text{-}5}$ and the metal salts were each 0.5 mM in acetonitrile. The metal salts used were $Ba(OTf)_2$ and $Ba(NO_3)_2$, $Ca(OTf)_2{\cdot}H_2O$ and $Ca(NO_3)_2{\cdot}4H_2O$, $Ln(OTf)_3{\cdot}3H_2O$ and $Ln(NO_3)_3{\cdot}6H_2O$ (Ln = La, Lu).

After mixing ligand **PQQ**$_{15\text{-}5}$ and the respective Ln salt (nitrate, triflate) in acetonitrile and performing electrospray ionization in positive mode we observed both the [**PQQ**$_{15\text{-}5}$+Ln+X]$^{2+}$ dication (Ln = La, Lu; X = NO_3, CF_3SO_3) and [**PQQ**$_{15\text{-}5}$+Ln+2X]$^{+}$ monocation. Interestingly, we cannot detect the complex without counterions, i.e. [**PQQ**$_{15\text{-}5}$+Ln]$^{3+}$, in line with the expected strong electrostatic interaction. To gain more information on the structure and bond strength of the complex, we performed collision induced dissociation (CID) experiments. Therefore, we isolated the dication [**PQQ**$_{15\text{-}5}$+Ln+X]$^{2+}$ in the ion trap of the LTQ Orbitrap-instrument, resonantly excited the oscillatory motion of the ions and collided them with helium background gas in the trap. As shown in the Supporting Information (Figure VI.3), we recorded fragment mass spectra as function of the excitation energy (in instrument specific units of normalized collision energy). Independent of counterion (nitrate vs. triflate) and lanthanide (La vs. Lu) we observe CH_3OH-loss as dominant fragmentation channel. This implies that it is easier to break the covalent bond to one of the methoxy-groups in PQQ (plus hydrogen rearrangement) than to break the ionic bond to the counterion. While we observe no nitrate loss at all, we observe for the triflate some CF_2SO_3-loss as minor channel (with ca. 15% relative intensity for La and 5% for Lu) indicating a stronger bond strength of the nitrates, and highlighting the potential different species present during methanol oxidation, depending on the chosen counterion.

The corresponding complexes with divalent metals [**PQQ**$_{15\text{-}5}$+M+X]$^{+}$ (M = Ca, Ba; X = NO_3, CF_3SO_3) show a fragmentation pattern that is even more dominated by CH_3OH-loss (Figure VI.4). In all cases this channel accounts for >93% fragment intensity. Counterion loss is negligible (<3%). This implies that the bond strength of the counterions with Ca^{2+} and Ba^{2+} is comparable to the bond strength with the lanthanide complexes.

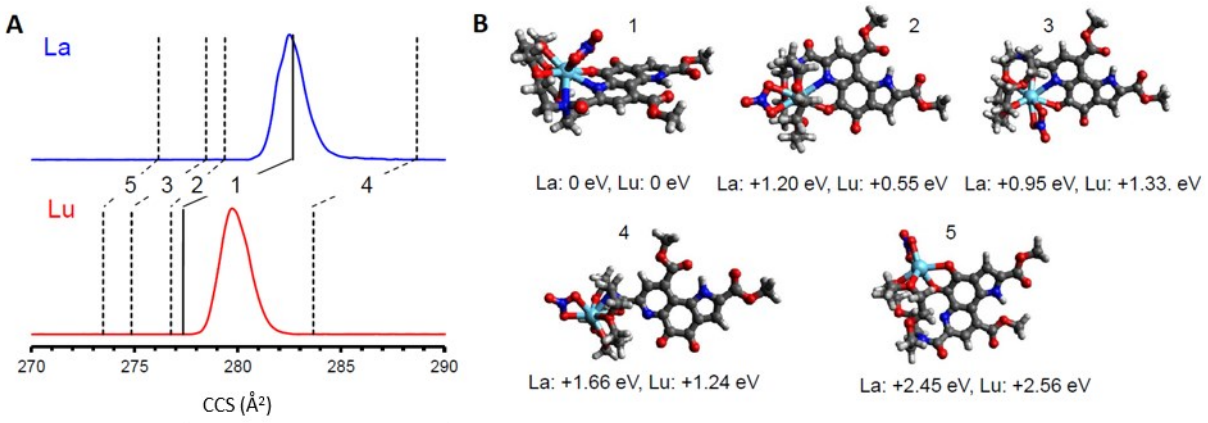

*Figure III.4: (A) Mobilograms of [**PQQ**$_{15\text{-}5}$+La+NO_3]$^{2+}$ (blue) and [**PQQ**$_{15\text{-}5}$+Lu+NO_3]$^{2+}$ (red) along with calculated CCS for five DFT optimized candidate structures. The CCS of the lowest energy isomer (1) is indicated by a full line, the others by dashed lines. (B) DFT-optimized structures along with relative energies. Isomer 1 is clearly favored based on both CCS and relative energies.*

To resolve the structure of the complexes we combined DFT-calculations and gas phase ion mobility measurements (IMS). By comparing experimental (IMS) and calculated (DFT) collision cross sections (CCS) we can assign the dominant isomers of the [**PQQ$_{15\text{-}5}$**+Ln+NO_3] complexes (in gas phase, as dications), see Figure III.4 for Ln = La and Lu. We find that in both cases structure 1 (Ln^{3+} coordinated by counterion, crown ether moiety as well as the C-5 quinone carbonyl oxygen and the N-6 pyridine nitrogen) is by far the most stable isomer, its calculated CCS agrees with the experimental value within the experimental error of ca. 1%. The other isomers can be ruled out based on both CCS and relative energies. Furthermore, the Lu complex has a slightly smaller CCS which is expected due to the lanthanide contraction. For the triflates we find a similar structure.

3. Spectroscopic Studies with PQQ Derivatives and Lanthanide Salts

3.1. Interaction of PQQ$_{18\text{-}6}$ with Lanthanide Salts

As part of this project, a PQQ ligand (**PQQ$_{18\text{-}6}$**) with a bigger aza-crown cavity was synthesized as described in chapter II.2. and analyzed together with different lanthanides. In order to find the best conditions for the intended spectrophotometric metal titrations, several preliminary experiments were conducted.

When examining lanthanide complexation in non-aqueous solutions, one potentially overlooked concern is the incomplete dissociation of the metal salt used to carry out the experiments. Consequently, a crucial aspect of thermodynamic investigations regarding lanthanide complexation in organic media involves the choice of a starting salt which can assure the most precise understanding of the speciation in the solution.[210] Thus, several UV-Vis experiments with ligand **PQQ$_{18\text{-}6}$** in the presence of various lanthanum(III) salts were conducted (see chapter VI.3.). Acetonitrile was the solvent of choice for the measurements, since the ligand shows a good solubility in it and does not form hemiketal adducts with it. Eventually, lanthanide(III) nitrates were chosen as metal salts for the spectroscopic studies described in this chapter since they are soluble in acetonitrile, commercially available and do not form any precipitations with the ligand.

Furthermore, the absorption behavior of the ligand in the presence of La^{3+} was evaluated over a defined period of time. Hence, an acetonitrile solution of **PQQ$_{18\text{-}6}$** with 2.0 equiv. of lanthanum(III) nitrate was measured right after the addition of the metal salt to the ligand as well as over 3 h (Figure VI.9). The position of the significant absorption band around 370 nm did not change over time and thus it could be assumed that no additional species were formed, a circumstance which permits direct and unimpeded metal titration absorption measurements. In addition, further analysis showed that

the UV-Vis spectrum of the complex solution is only slightly influenced by temperature increase (Figure VI.9). A solution of **PQQ$_{18\text{-}6}$** with 2.0 equiv. of lanthanum(III) nitrate was measured at different temperatures whereby each temperature was maintained for 1 h before further increasing it and during this time no absorption change could be observed. The absence of isosbestic points or overlapping transitions rather suggests that no further species were formed within the temperature gradient.

Subsequently, a UV-Vis titration of **PQQ$_{18\text{-}6}$** with La^{3+} was conducted. Upon incremental addition of La^{3+} (0 to 10 equiv.), the absorption band at 354 nm gradually shifted to 370 nm (Figure III.5). A plot of the absorption change at 386 nm versus the added metal equivalents showed a saturation after the addition of 2.0 equiv. La^{3+}.

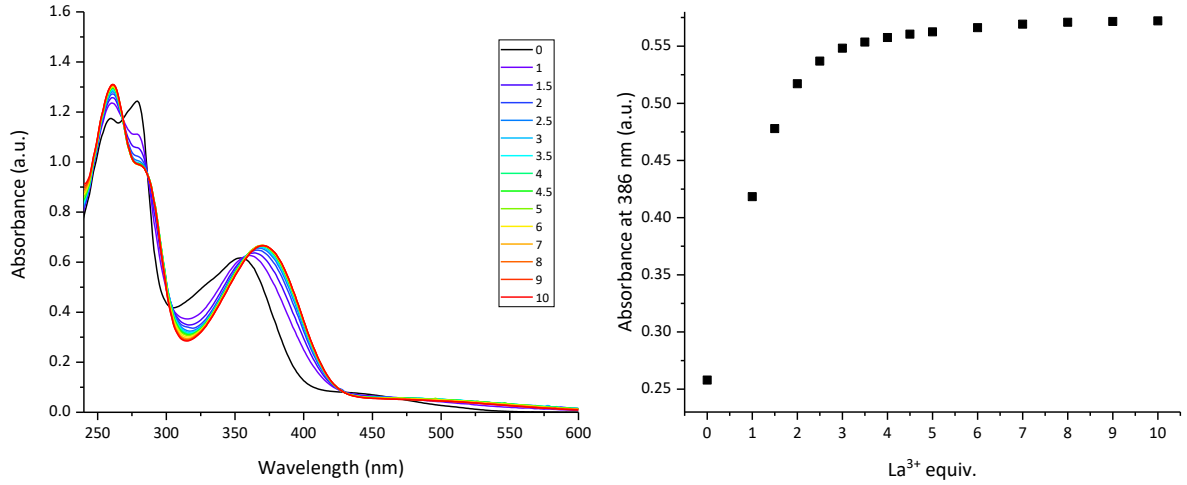

*Figure III.5: Titration of **PQQ$_{18\text{-}6}$** with increasing amounts of $La(NO_3)_3{\cdot}6H_2O$ in acetonitrile at 25 °C (left) and plot of the absorption change at 386 nm vs. the La^{3+} equivalents added to the ligand (right).*

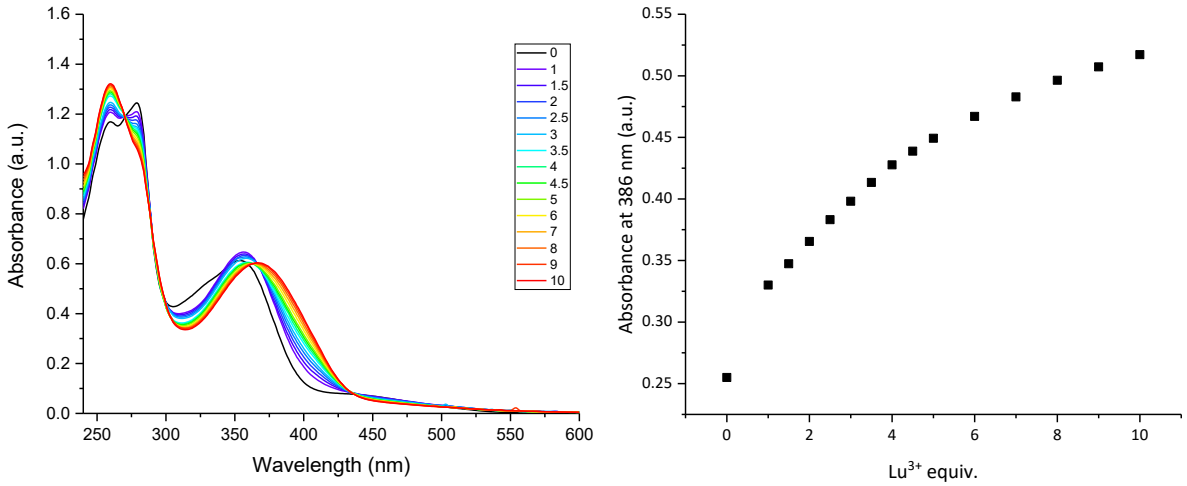

*Figure III.6: Titration of **PQQ$_{18\text{-}6}$** with increasing amounts of $Lu(NO_3)_3{\cdot}6H_2O$ in acetonitrile at 25 °C (left) and plot of the absorption change at 386 nm vs. the Lu^{3+} equivalents added to the ligand (right).*

As the ligand was treated stepwise with increasing amounts of lutetium(III), the absorption band at 354 nm gradually shifted to 367 nm. However, the plot presented in Figure III.6 shows a rather ongoing absorption increase at 386 nm, thus implying that the complex is not fully formed and there is still unbound ligand present in the solution.

In addition, UV-Vis titration experiments were performed with all of the remaining lanthanides (excluding Pm), whereas a trend could be observed (Appendix, Figure VI.12 to Figure VI.15). When titrating **PQQ$_{18\text{-}6}$** with up to 10 equiv. of the early lanthanides (Ce to Nd), a system saturation was achieved, however, the saturation point gradually shifted to higher metal concentrations with increasing atomic number of the metal. Thus, the absorption change plots for metals from Eu to Yb show a similar curve trend as with Lu.

With the results from the spectrophotometric titrations in hand, an attempt to determine the binding constants for the lanthanide complexes of **PQQ$_{18\text{-}6}$** was made. One possibility to calculate the binding constant *K* of a complex is to process the data from spectrophotometric titrations using the Benesi-Hildebrand equation, a method which is often applied in the literature to determine the binding constants of various complexes or to study the host-guest inclusion interactions in supramolecular structures.[211–220] When assuming a 1:1 stoichiometry for the ligand-metal complexation, the association constant *K* of the complex can be determined using the Benesi-Hildebrand equation 1,[211] where A and A_0 represent the absorbance of the ligand at a certain wavelength in the presence and absence of a metal cation (M^{n+}).[216,221] A_{max} is the saturated absorbance of the ligand in the presence of excess amount of metal.

$$\frac{1}{A - A_0} = \frac{1}{K(A_{max} - A_0)[M^{n+}]} + \frac{1}{A_{max} - A_0} \quad (1)$$

Plotting of $1/(A\text{-}A_0)$ versus $1/[M^{n+}]$ should give a linear relationship, where the intercept is equal to $1/(A_{max}\text{-}A_0)$ and the binding constant *K* is equal to the intercept divided by the slope.[216,221]

However, there are several problems and limitations associated with using this approach, which should be taken under consideration. The first one is the requirement for the 1:1 stoichiometry of the complex. In addition, it is assumed that the total concentration of the metal ions equals with the free unbound concentration of the metal (ergo the total concentration of the metal should be much higher than the total concentration of the ligand).[222] Moreover, the method involves the assumption that the complex is fully formed at the end of the titration. These assumptions are often not valid. Nonetheless, the method could still provide some information about possible trends among the evaluated systems and, when used properly, some insights about the nature of the metal-to-ligand binding behavior.

To ascertain whether the requirement for a 1:1 ligand to metal ratio for the **PQQ**$_{18\text{-}6}$/Ln^{3+} complex present in solution is fulfilled, several spectroscopic techniques were employed. According to the literature, a widely adopted approach for determining the stoichiometry of an observable complexation of two species is the method of continuous variation, commonly referred to as the Job plot.[223,224] Instead of varying the concentration of one component at a time, the method of continuous variation maintains the total concentration of added ligand and metal salt constant while altering their relative proportions. The absorbance of each solution is measured and plotted against the mole fraction of either the metal or the ligand. Thus, with the use of UV-Vis spectroscopy and the continuous variation technique, the stoichiometry of the complex produced in solution by the interaction of La^{3+} with **PQQ**$_{18\text{-}6}$ was evaluated (Figure III.7). After subtraction of the absorption of the free ligand (at 377 nm) from the absorption of the complex, the Job plot afforded a maximum at χ = 0.5, suggesting complex formation at a La^{3+} to ligand ratio of 1:1. However, it should be noted that the method does not distinguish 1:1 and 2:2 stoichiometries.

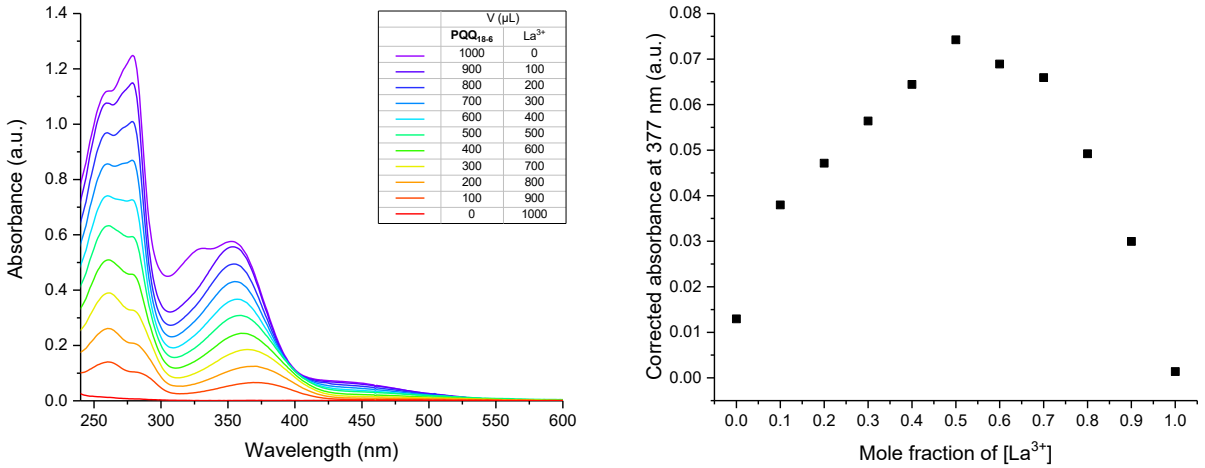

Figure III.7: Spectrophotometric analysis for determination of the **PQQ**$_{18\text{-}6}$*-to-*La^{3+} *molar ratio by the method of continuous variation (left). Job plot of the corrected absorbance at 377 nm vs. the mole fraction of* $[La^{3+}]$ *(right).*

Furthermore, the composition of the complex was confirmed by the mole ratio method.[225] Thereby, mixtures of solutions were prepared with a constant concentration of lanthanum(III) and variable ligand concentration. After spectrophotometric analysis of the solutions, the resulting plot of absorbance versus the mole ratio of the reactants are characterized by two straight lines of different slopes that intersect at the point of the mole ratio which characterizes the complex species. As shown in Figure III.8, the UV-Vis analysis of **PQQ**$_{18\text{-}6}$ and La^{3+} gave a mole ratio of 1:1. However, it should be noted that both the Job plot and mole ratio method come with their own set of challenges. One significant issue arises from the red shift absorption of the complex, which overlaps with the existing peaks of the non-complexed ligand, which complicates the analysis of the complex stoichiometry.

Given the absence of isosbestic points and the overlapping transitions, a correction of the absorbance values was carried out in order to plot the data as accurate as possible. However, depending on the wavelength chosen for the plots, the shapes of the curves varied significantly, making most of them unsuitable for the determination of the complex stoichiometry (Figure VI.10, Figure VI.11). Hence, the presented results have to be interpreted with caution.

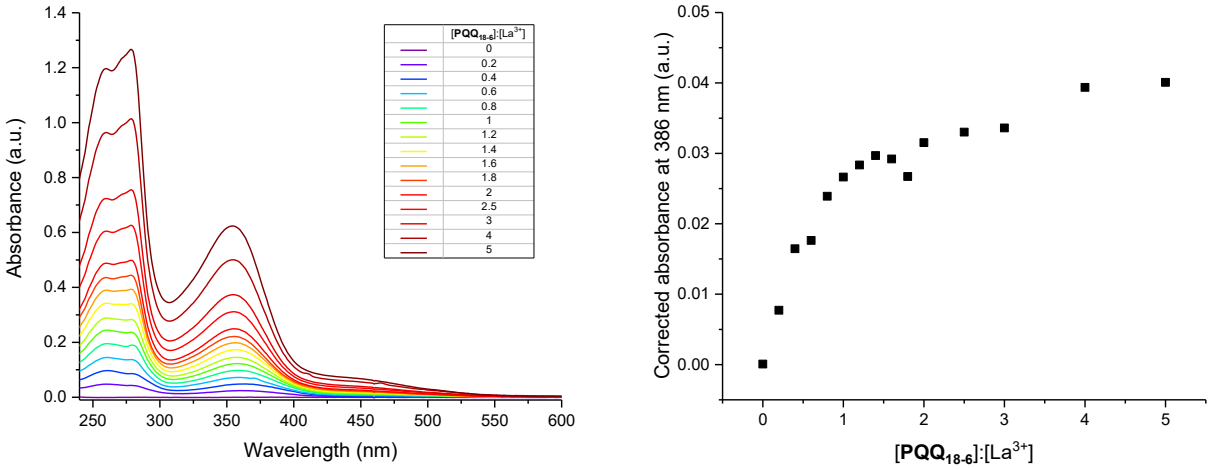

*Figure III.8: Spectrophotometric analysis for determination of the **PQQ**18-6 -La^{3+} complex stoichiometry by the mole ratio method (left). Plot of the corrected absorbance at 386 nm vs. the [**PQQ**18-6]:[La^{3+}] mole ratio (right).*

Recently, Alexander Schäfer, Erik Schneider and Patrick Weis from the Karlsruhe Institute of Technology (KIT) performed mass spectrometry on acetonitrile solutions of **PQQ**18-6 in the presence of different lanthanide(III) nitrates. Thus, they were able to obtain mass spectra from Ln-**PQQ**18-6-complex species with either one or two nitrates as counterions (Figure III.5).

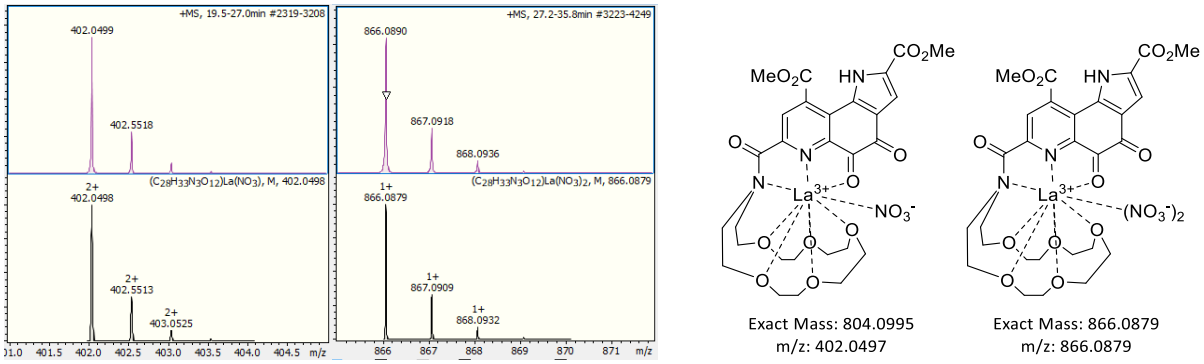

*Figure III.9: ESI spectra of [La(NO3)(**PQQ**18-6)]$^{2+}$ and [La(NO3)2(**PQQ**18-6)]$^{+}$ measured by Alexander Schäfer, Erik Schneider and Patrick Weis (KIT).*

With several experiments suggesting that the 1:1 ligand-to-metal stoichiometry requirement is fulfilled for this ligand, the Benesi-Hildebrand method was applied. As shown in Figure III.10, the Benesi-

Hildebrand plot for the La^{3+}-**PQQ**$_{18\text{-}6}$ system gave a good linear correlation between the plotted values with a R^2 of 0.995. The binding constant K was determined as 52644 M^{-1} or log K = 4.721 (Table III.4).

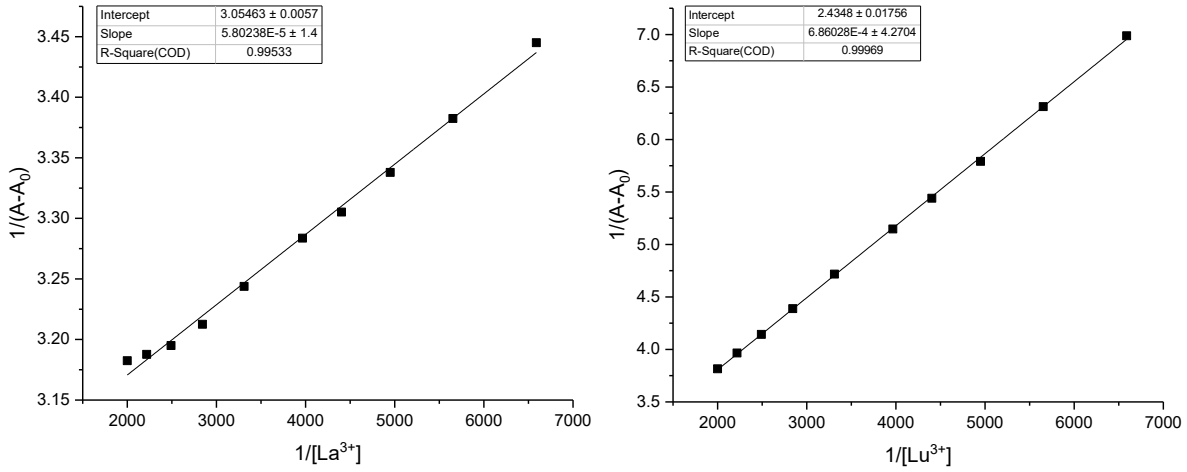

Figure III.10: Benesi-Hildebrand plots of $1/(A-A_0)$ versus $1/[Ln^{3+}]$ for determination of binding constants K for **PQQ**$_{18\text{-}6}$ *complexes (Ln: La, Lu). The Ln^{3+} concentrations used for the plot were from 0.00015 to 0.0005 M (3.0 to 10 equiv.).*

The method was then further applied to calculate the binding constants for all remaining lanthanides in the series, using the results from the UV-Vis titrations, presented above (Figure VI.16 and Figure VI.17).

Table III.4: Calculated binding constants K from titration experiments of **PQQ**$_{18\text{-}6}$ *with different lanthanide nitrates in acetonitrile at 25 °C.*

Ln^{3+}	K (M^{-1})	log K	R^2
La	52644	4.721	0.995
Ce	18120	4.258	0.977
Pr	8159	3.912	0.985
Nd	5232	3.719	0.995
Sm	5117	3.709	0.991
Eu	4342	3.638	0.993
Gd	3334	3.523	0.991
Tb	2915	3.465	0.995
Dy	2673	3.427	0.998
Ho	2754	3.44	0.999
Er	2773	3.443	0.999
Tm	3125	3.495	0.999
Yb	3230	3.509	0.999
Lu	3549	3.55	0.999

Although all plots gave good linear relationships between the plotted parameters, the obtained values for the Ln^{3+} ions from Sm to Lu should be interpreted with caution, since it could not be ensured, if the complexes were fully formed at the end of the titrations due to the absence of clear saturation points. In order to verify the results, titrations with higher amounts of Ln^{3+} should be performed and evaluated. Nonetheless, the obtained preliminary results show an interesting trend among the series, which was also observed in the literature for other macrocyclic systems.[226–228]

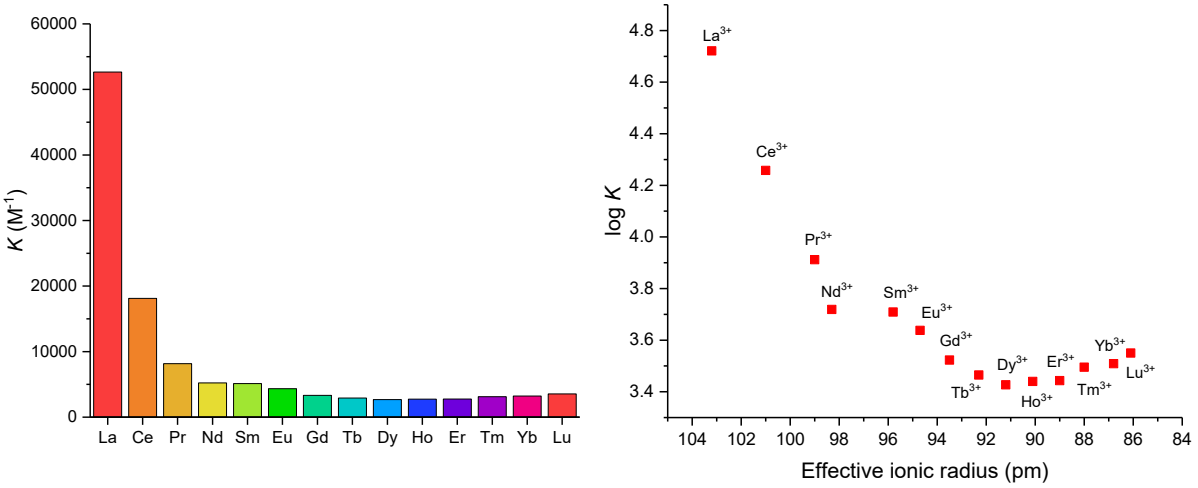

Figure III.11: Comparison of the calculated binding constants K from titration experiments of ***PQQ*****$_{18\text{-}6}$** *with different lanthanide nitrates in acetonitrile at 25 °C (left) and a plot of the estimated log K values versus the effective ionic radii*[20] *of 6-coordinated Ln ions (right).*

Due to the increased charge density of the smaller Ln^{3+} ions, which enhances metal-ligand electrostatic interactions, most ligands usually possess a higher affinity for those ions.[229] However, some ligands, mainly aza-crown ligands, show a rarely observed reverse-size selectivity pattern and a thermodynamic preference for the large over small Ln^{3+} ions.[227,229] The determined binding constant values for **PQQ$_{18\text{-}6}$** rather show a ligand affinity of the second type (Table III.4, Figure III.11). Throughout the Ln^{3+} series the stability decreases (from La^{3+} to Gd^{3+}), reaches a bottom (Tb^{3+} to Er^{3+}), and then slightly increases again (Tm^{3+} to Lu^{3+}). The results suggest a possible ligand-cavity-ion-size relationship, however, previous reports show that there are further factors that contribute significantly to the binding of cations by the crown ether ligands, e.g. the solvation enthalpies and entropies of the cation and the ligand, the number of donor atoms participating in the binding and the conformation of the bound and unbound macrocycles.[230] The reported stability constants for a benzyl aza-18-crown-6 ether with trivalent lanthanide ions (La^{3+} to Gd^{3+}) for instance show that the complex stability increases with the decrease in the radius of the lanthanide ions.[231] On the other hand, Hu *et al.* recently reported the synthesis of a diaza-18-crown-6 ligand with two picolinate donor arms with an unusual selectivity pattern, which decreases from Ce to Dy, and increases again from Ho to Lu.[229] Hence, it could be assumed that additional pendant arms containing additional donor atoms could strongly affect the

cation binding ability and selectivity of a crown ether ligand. Therefore, it could be assumed that the selectivity pattern of ligand **PQQ$_{18\text{-}6}$** is not solely formed by the aza-crown moiety but rather by its assembly with the PQQ dimethyl ester.

3.2. Interaction of PQQMe$_2$ with Lanthanide Salts

In order to extend our knowledge about the coordination aspects between PQQ and the trivalent lanthanide ions, further PQQ-based ligands were examined and compared in addition to **PQQ$_{18\text{-}6}$**.

PQQMe$_2$ is a well-known PQQ derivative comprising two ester functionalities and a carboxy acid at the pyridine ring. The spectrophotometric titration experiment conducted with 0 to 5.0 equiv. lanthanum(III) nitrate resulted in a gradual shift of the absorption band at 358 nm to 376 nm and a slight absorption decrease. By plotting the absorbance at 386 nm versus the added amount of La^{3+}, a nonlinear regression indicated the occurrence of a system saturation after the addition of 2.0 equiv. metal salt (Figure III.12).

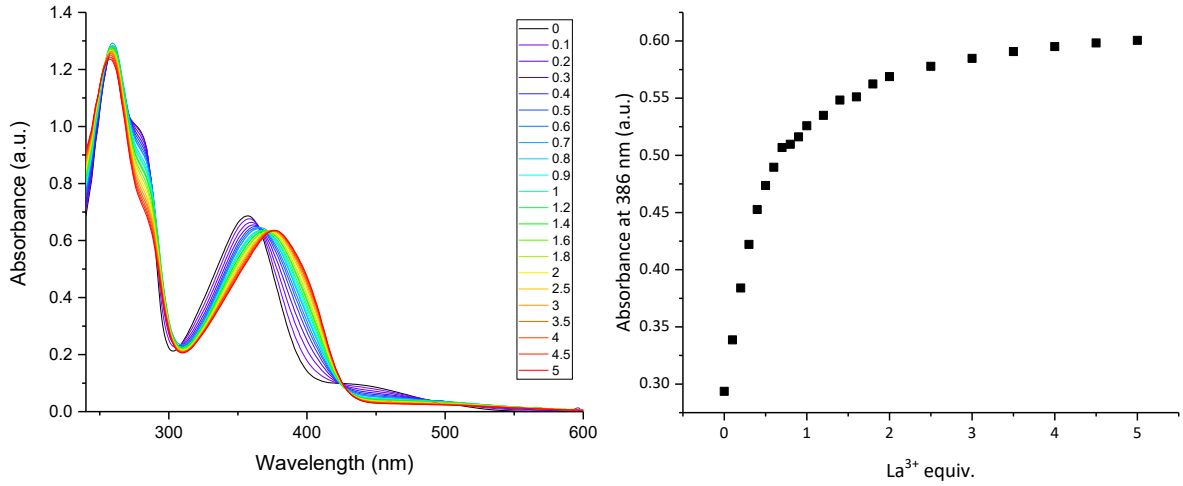

*Figure III.12: Titration of **PQQMe$_2$** with increasing amounts of $La(NO_3)_3 \cdot 6H_2O$ in acetonitrile at 25 °C (left) and plot of the absorption change at 386 nm vs. the La^{3+} equivalents added to the ligand (right).*

In addition, UV-Vis experiments with **PQQMe$_2$** were conducted in the presence of Ce, Pr, Sm, Eu, Gd, Tb, Dy, Tm and Lu and the respective spectra are presented in the Appendix (Figure VI.18 to Figure VI.20). The results show that in the case of Ce and Pr, an absorption saturation is reached upon adding approximately 2.0 equiv. of metal salt, similar to La. Interestingly, it was shown that with all other lanthanides only 1.0 equiv. was required to saturate the system, a circumstance that points to a higher affinity of **PQQMe$_2$** towards later lanthanides.

Assuming a 1:1 complex formation for the Ln-**PQQMe$_2$** system, binding constants were calculated using the Benesi-Hildebrand method (Table III.5, Figure VI.21 and Figure VI.22). As shown in Figure

III.13, the stability increases across the series (La^{3+} to Sm^{3+}), reaches a plateau (Eu^{3+}, Gd^{3+}), and then declines (Tb^{3+}, Dy^{3+}). The calculated log *K* values for Tm^{3+} and Lu^{3+} were found to be higher than the binding constants estimated for the early lanthanides. Moreover, these values deviate from the trend observed among the lanthanides from La^{3+} to Dy^{3+}. This discrepancy could imply a distinct binding configuration with the ligand, possibly attributed to the increased Lewis acidity and the smaller ionic size of these two cations.

*Table III.5: Calculated binding constants K from titration experiments of **PQQMe**$_2$ with different lanthanide nitrates in acetonitrile at 25 °C.*

Ln^{3+}	*K* (M^{-1})	log *K*	R^2
La	46316	4.666	0.999
Ce	59735	4.776	0.993
Pr	78640	4.896	0.981
Sm	114535	5.059	0.998
Eu	129126	5.111	0.984
Gd	133988	5.127	0.995
Tb	115857	5.064	0.997
Dy	92481	4.966	0.999
Tm	118067	5.072	0.993
Lu	122520	5.088	0.843

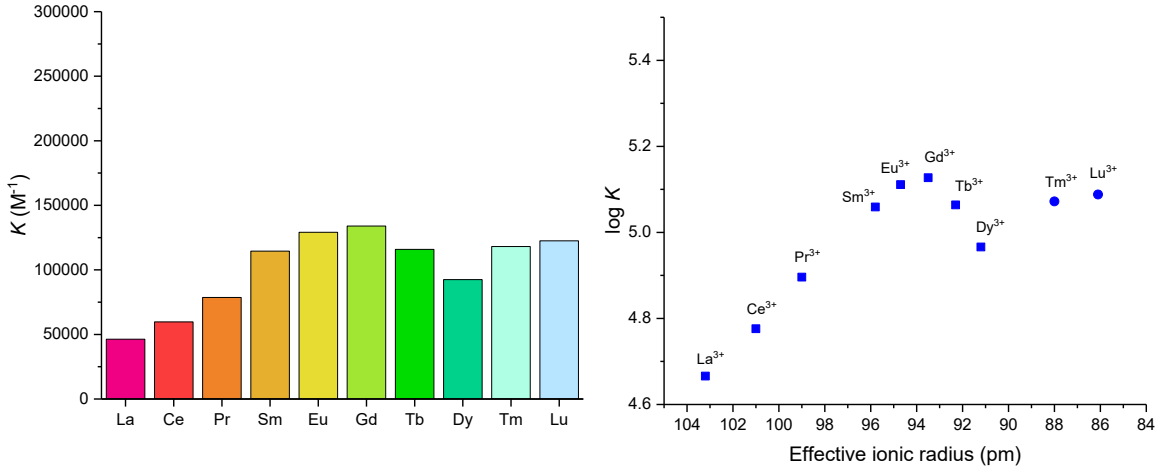

*Figure III.13: Comparison of the calculated binding constants K from titration experiments of **PQQMe**$_2$ with different lanthanide nitrates in acetonitrile at 25 °C (left) and a plot of the estimated log K values versus the effective ionic radii[20] of 6-coordinated Ln ions (right).*

Overall the estimated values for the Ln^{3+} ions from La^{3+} to Dy^{3+} show a trend in the **PQQMe$_2$**-chelator affinity, which strongly differs from that of **PQQ$_{18\text{-}6}$**. Thus, this observation further underlines the importance of the ligand design when studying biomimetics.

Previously, Itoh and Fukuzumi have determined the equilibrium constants K_{add} for the hemiacetal formation in PQQ derivatives in the presence of alkaline earth metal ions *via* UV-Vis investigation.[142–144,163] There is a particular interest in exploring this reaction in the presence of lanthanide cations, as it might play a pivotal role in the initial stages of MDH's catalytic mechanism. During her bachelor thesis, conducted under my supervision, Sophia Glocker carried out UV-Vis titration experiments by incremental addition of substrate to **PQQMe$_2$** in the presence of Ln^{3+}. The measurements were conducted using methanol, which serves as the natural substrate in MDH. Since the previous UV-Vis examinations demonstrated that the **PQQMe$_2$**-Ln^{3+} system became saturated after the addition of approximately 2.0 equiv. of metal nitrate, the substrate titration experiments were performed by dissolving **PQQMe$_2$** (1.0 equiv.) and $Ln(NO_3)_3{\cdot}6H_2O$ (2.0 equiv.; Ln: La, Eu, Lu) in acetonitrile. Subsequently, an excess of methanol was added stepwise to the solution, with a UV-Vis spectrum recorded after each addition. With increasing amounts of methanol, the maximum at 260 nm exhibited a slight shift, which coincided with an absorption decrease in the presence of La^{3+} and an increase in the presence of Eu^{3+} and Lu^{3+} (Figure VI.23). Across all titrations, the shoulder at 280 nm disappeared and the maximum at 372 nm shifted towards higher wavelengths. Interestingly, these changes were observed alongside isosbestic points. Upon examining the saturation curves (plot of absorbance at 372 nm vs. added methanol concentration) for La^{3+}, Eu^{3+} and Lu^{3+}, it became evident that the systems reached saturation after the addition of 4000 equiv. of methanol. Subsequently, using the recorded UV-Vis data, equilibrium constants K_{add} were calculated employing the Benesi-Hildebrand equation (Figure VI.24). The highest K_{add} was measured in the presence of La^{3+} (42.6 M^{-1}), followed by Eu^{3+} (22.8 M^{-1}) and Lu^{3+} (4.6 M^{-1}).

*Table III.6: Hemiacetal formation constants determined by the titration of methanol to **PQQMe$_2$** in the presence of 2.0 equiv. $Ln(NO_3)_3{\cdot}6H_2O$ in acetonitrile at 25 °C.*

Ln^{3+}	K_{add} (M^{-1})	R^2
La	42.6	0.996
Eu	22.8	0.998
Lu	4.6	0.998

La^{3+} demonstrated the highest efficiency in promoting the C-5 hemiacetal formation, followed by Eu^{3+} and Lu^{3+}. Itoh and Fukuzumi reported that, in comparison to Mg^{2+}, Sr^{2+} and Ba^{2+}, Ca^{2+} exhibited the most significant enhancement of the C-5 hemiacetal formation in related PQQ derivatives.[144] This

could potentially be attributed to the good stabilization effect of Ca^{2+} on the hemiacetal. The authors proposed that due to steric repulsion, Sr^{2+} and Ba^{2+} exhibit comparatively smaller effects in stabilizing the hemiacetal. This finding contradicts the current results, as a decrease in equilibrium constant was observed within the lanthanide series. Evidently, various factors seem to influence the hemiacetal formation, including the Lewis acidity, which increases within the lanthanide series. Given that the methanol addition marks the initial step in one of the proposed MDH mechanisms (addition elimination mechanism), these results imply that the different metal cations may exert distinct effects on this crucial step.

3.3. Interaction of other PQQ Derivatives with Lanthanide Salts

UV-Vis measurements

To further study the coordination behavior of lanthanum(III) in the biomimetic systems, UV-Vis titrations with other PQQ-based ligands were performed. As shown in Figure III.14, a spectrophotometric titration was conducted with **PQQ$_{15\text{-}5}$** and the quinone absorption band at 353 nm shifted to 369 nm upon the incremental La^{3+} addition. A plot of the absorbance at 386 nm showed the occurrence of a saturation after the addition of approximately 20 equiv. La^{3+}.

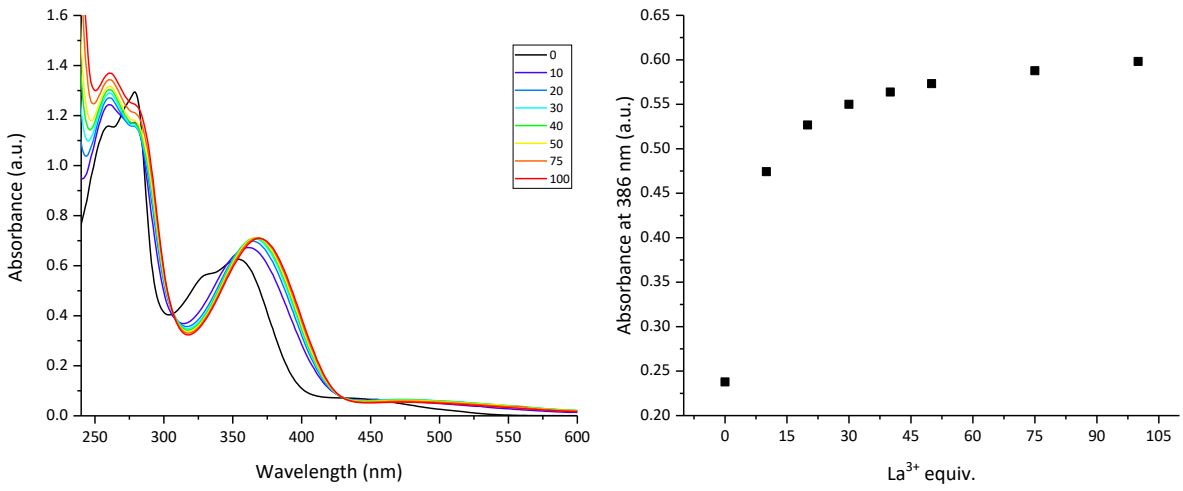

*Figure III.14: Titration of **PQQ$_{15\text{-}5}$** with increasing amounts of $La(NO_3)_3 \cdot 6H_2O$ in acetonitrile at 25 °C (left) and plot of the absorption change at 386 nm vs. the La^{3+} equivalents added to the ligand (right).*

As the trimethyl ester of PQQ was treated with lanthanum(III) nitrate (Figure III.15), the absorption band at 357 nm shifted to 382 nm. By plotting the absorbance at 386 nm versus the added amount of La^{3+}, a nonlinear regression indicated the occurrence of a system saturation after the addition of approx. 150 equiv. metal salt.

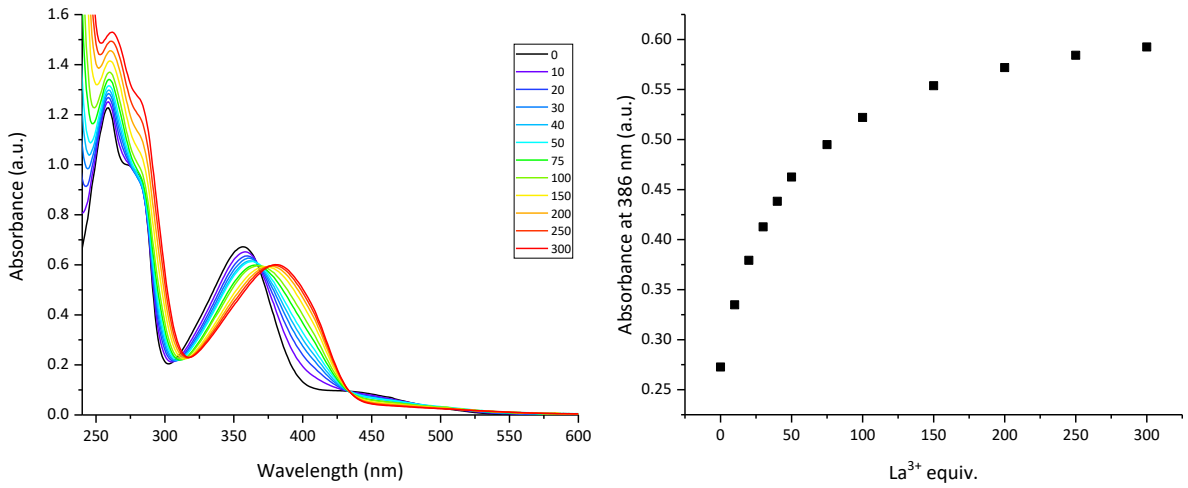

*Figure III.15: Titration of **PQQMe**3 with increasing amounts of $La(NO_3)_3 \cdot 6H_2O$ in acetonitrile at 25 °C (left) and plot of the absorption change at 386 nm vs. the La^{3+} equivalents added to the ligand (right).*

With the perspective to further broaden the scope of PQQ-ligands, a ligand incorporating 3,3'-azanediyldipropionate was synthesized as described in the previous chapter. Thus, **PQQ**DEDP incorporates two flexible pendant arms, which could possibly direct the metal ion coordination to the desired PQQ position which resembles the natural binding position in MDH. As shown in Figure III.16, upon incremental addition of La^{3+} (0 to 300 equiv.), the absorption band at 354 nm gradually shifted to 368 nm. A plot of the absorption change at 386 nm versus the added metal equivalents showed a saturation after the addition of approx. 150 equiv. La^{3+}.

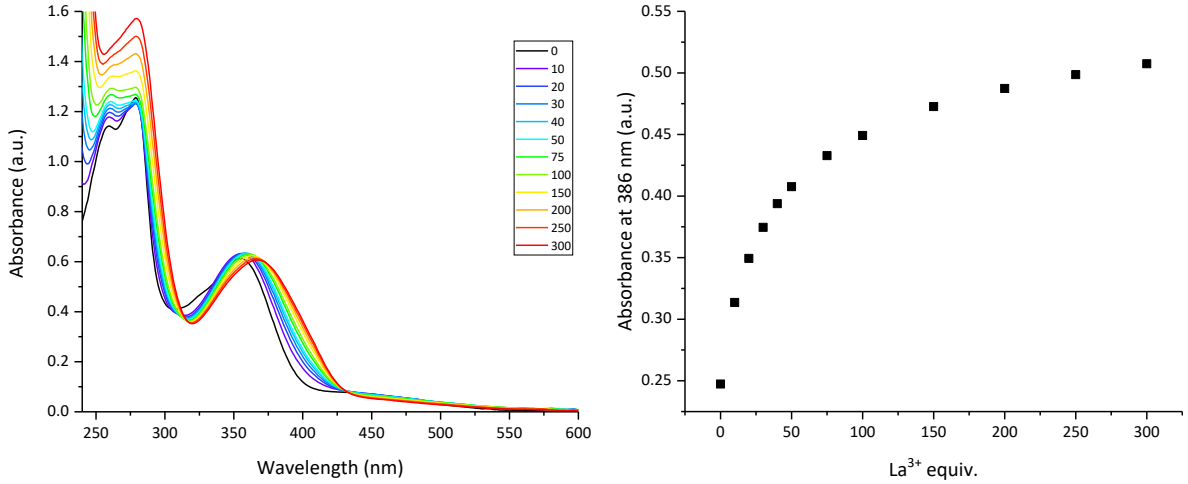

*Figure III.16: Titration of **PQQ**DEDP with increasing amounts of $La(NO_3)_3 \cdot 6H_2O$ in acetonitrile at 25 °C (left) and plot of the absorption change at 386 nm vs. the La^{3+} equivalents added to the ligand (right).*

Recently, we described a route towards the synthesis of a novel PQQ derivative (**P**ME**QQ**MEM) which incorporates two methyl ester functionalities at C-2 and C-7 respectively and a methyl group at C-9.[232] As shown in Figure III.17, the UV-Vis spectrum of the unbound **P**ME**QQ**MEM exhibits a different absorption character compared to all other ligands described in this report so far. For example, the

most distinctive absorption band observed in the spectra of the PQQ-ligands around 354-358 nm, is either missing or strongly blue shifted. In **PMEQQMEM** the absorption band at 316-327 nm exhibits two maxima, and the high-intensity absorption band around 276 nm only one. In addition, a low-intensity absorption maximum around 435 nm can also be observed. The changes in the UV-Vis spectrum of **PMEQQMEM** compared to the other PQQ-ligands most probably result from the substitution of the ester functionality through a methyl group at the quinoline moiety, which assumedly affects the π-system of the compound. In order to better understand the exact nature of the electronic transitions in the system, however, DFT calculations should be performed in addition to the UV-Vis measurements. As **PMEQQMEM** was treated stepwise with increasing amounts of lanthanum(III) nitrate (Figure III.17), the absorption maximum at 315 nm disappeared, the maximum at 327 nm decreased and a shoulder around 350 nm has appeared. The absorbance of the shoulder was subsequently plotted towards the amount of La^{3+} added to the ligand and a complex saturation after the addition of approx. 30 equiv. La^{3+} could be observed.

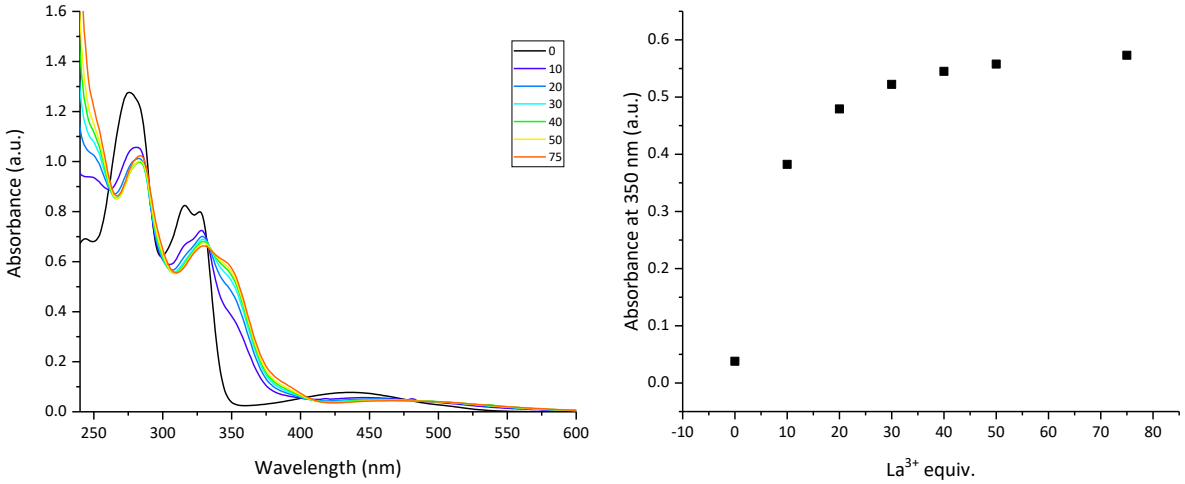

*Figure III.17: Titration of **PMEQQMEM** with increasing amounts of $La(NO_3)_3 \cdot 6H_2O$ in acetonitrile at 25 °C (left) and plot of the absorption change at 350 nm vs. the La^{3+} equivalents added to the ligand (right).*

Assuming a 1:1 complex formation for the La^{3+} complexes of **PQQ15-5**, **PMEQQMEM**, **PQQDEDP** and **PQQMe3**, binding constants were calculated using the Benesi-Hildebrand method (Figure VI.25 and Figure VI.26) and were compared to those of **PQQ18-6** and **PQQMe2** (Table III.7 and Figure III.18). As shown in Figure III.18, the highest *K* value among the different ligand systems in the presence of La^{3+} was determined for **PQQ18-6**, followed by **PQQMe2**. Afterwards a strong decrease in the *K* values with a magnitude of approx. 40000 M^{-1} can be observed. The hard Lewis base character of the carboxylic functionality in **PQQMe2** makes it a suitable ligand for the complexation of trivalent lanthanide ions, hence the difference between the affinities of **PQQMe2**, **PQQDEDP** and **PQQMe3** for La^{3+} is allegeable. However, the significant difference between the *K* values of **PQQ18-6** and **PQQ15-5** is rather interesting. Presumably, the additional donor atom in **PQQ18-6** has an impact on the enhanced complex stability,

despite the fact that the ligand-cavity-ion-size relationship should be more favorable in the case of **PQQ$_{15\text{-}5}$**. Nonetheless, as discussed in the previous chapter, there are further criteria which affect the complex stability.

Table III.7: Calculated binding constants K from titration experiments of different ligands with lanthanum nitrate in acetonitrile at 25 °C.

Ligand	K (M^{-1})	log K	R^2
PQQ$_{18\text{-}6}$	52644	4.721	0.995
PQQMe$_2$	46316	4.666	0.999
PQQ$_{15\text{-}5}$	3264	3.514	0.999
P$_{ME}$QQ$_{MEM}$	2619	3.418	0.998
PQQ$_{DEDP}$	614	2.788	0.996
PQQMe$_3$	379	2.579	0.999

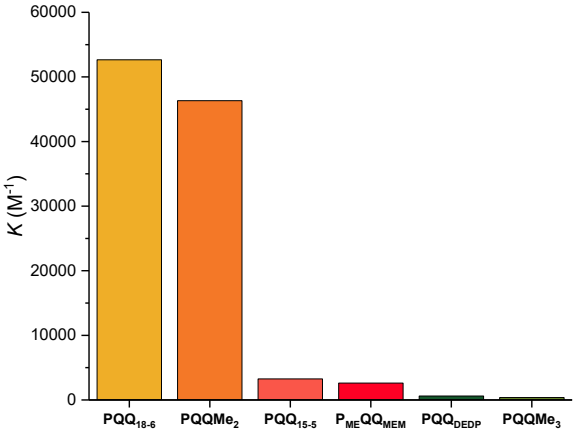

Figure III.18: Comparison of the calculated binding constants K from titration experiments of different ligands with lanthanum(III) nitrate in acetonitrile at 25 °C.

In addition, **L$_{PQQ}$** was subjected to UV-Vis measurements in the presence of lanthanum(III) nitrate. Given the low solubility of the ligand in acetonitrile, a stock solution with 7% DMF in acetonitrile was prepared. As shown in Figure III.19, the spectrum of the unbound ligand has an absorption maximum at 371 nm. Upon incremental addition of La^{3+} (0 to 10 equiv.), the maximum was gradually blue shifted to 361 nm and a shoulder at 282 nm has appeared. A complex saturation was reached with 4.0 equiv. La^{3+}.

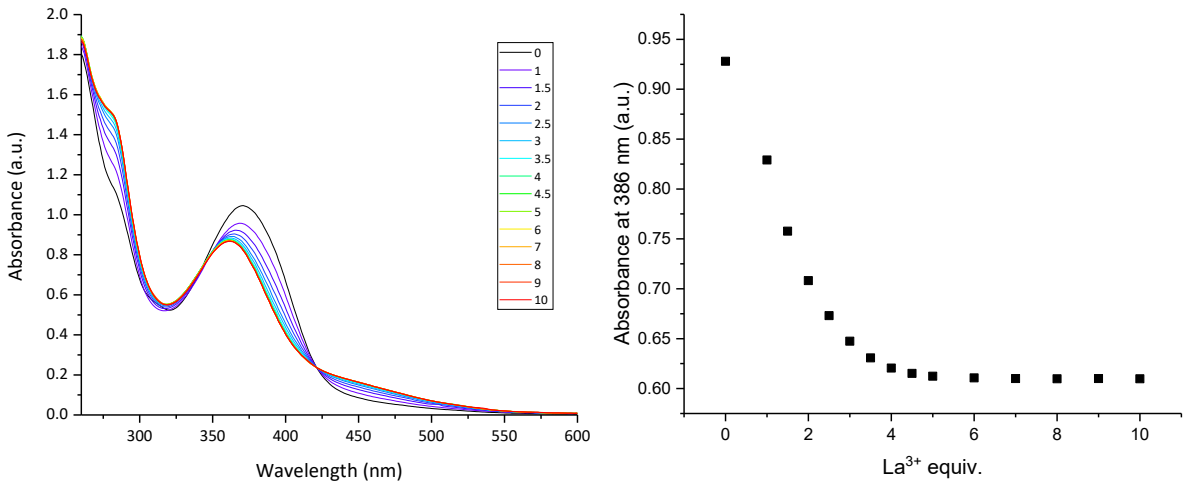

Figure III.19: Titration of **L**$_{PQQ}$ *with increasing amounts of* $La(NO_3)_3 \cdot 6H_2O$ *in acetonitrile/DMF at 25 °C (left) and plot of the absorption change at 386 nm vs. the* La^{3+} *equivalents added to the ligand (right).*

An attempt for binding constant determination was made using the Benesi-Hildebrand method, however, as shown in Figure III.20 the plot resulted in a non-linear regression. Thus, the binding constant could not be estimated. One possible reason for this observation could be a different complex stoichiometry.

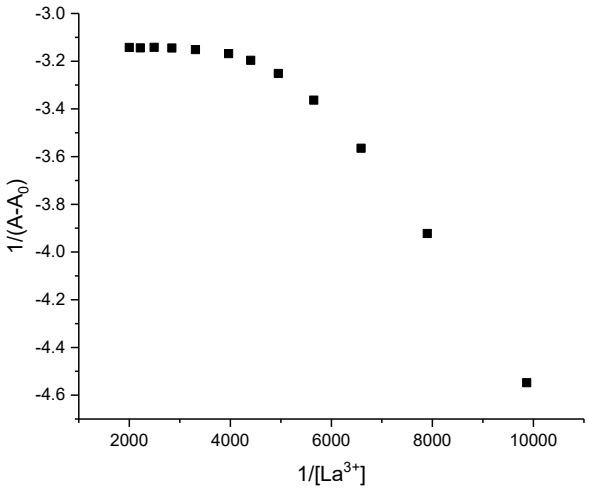

Figure III.20: Benesi-Hildebrand plot of $1/(A-A_0)$ *versus* $1/[La^{3+}]$ *for the attempted determination of binding constant K for* **L**$_{PQQ}$*. The* La^{3+} *concentrations used for the plots were from 0.0001 to 0.0005 M (2.0 to 10 equiv.).*

Utilizing the Nash method (equation 2),[233] where A and A_0 represent the absorbance of the ligand at a certain wavelength in the presence and absence of a metal cation (M^{n+}), and ε_L and ε_C are the molar absorptivities of the ligand and the complex, respectively, a 1:1 stoichiometry has been ruled out, since a plot of the reciprocal of the metal concentration against the reciprocal of one minus the absorbance ratio did not result in a linear plot (Figure III.21, left). According to Nash, the formation of a single more complicated species LM_n could be expressed by raising the reciprocal of the metal concentration to the n'th power. As shown in Figure III.21 on the right, a straight line was observed by plotting the

square of the reciprocal of the metal concentration against the reciprocal of one minus the absorbance ratio, thus suggesting the formation of a $\mathbf{L}_{PQQ}$-La_2 species.

$$\frac{1}{[M^{n+}]} = \frac{1}{1-\frac{A}{A_0}}\left(K - K\frac{\varepsilon_C}{\varepsilon_L}\right) - K \qquad (2)$$

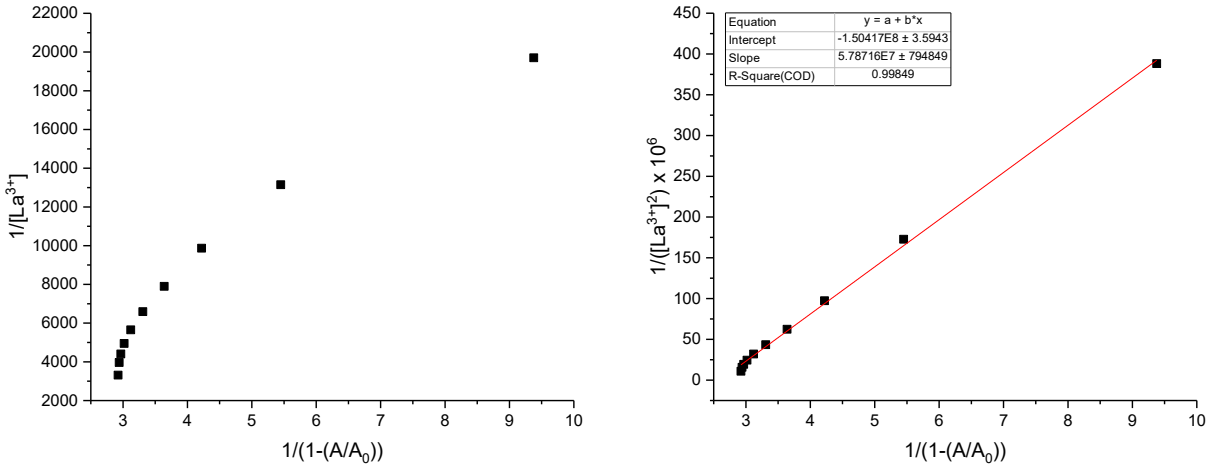

Figure III.21: Nash Plot plot of 1/(1-(A/A₀)) versus 1/[La³⁺] (left) and 1/[La³⁺]² (right) with the spectrophotometric data from the $\mathbf{L}_{PQQ}$-La^{3+} titration experiment.

Luminescence Measurements

To further study the spectroscopic behavior of the PQQ derivatives and their interaction with lanthanides, luminescence measurements were performed.

Ligand-sensitized luminescent lanthanide(III) complexes possess distinctive photophysical characteristics, rendering them promising contenders for a diverse array of applications.[186] These include deployment as luminescent sensors,[234,235] as shift reagents for NMR spectroscopy,[236] in medical diagnostics and for optical cell imaging.[65,67,237–239] With the 4f electrons of the lanthanides not being in the outermost orbitals, they are well shielded by electrons in the filled 5s, 5p, 6s and in the cases of gadolinium and lutetium also 5d subshells. This electronic arrangement preserves the magnetic and spectroscopic properties of the lanthanides even upon ionization or binding. Consequently, the emission wavelengths of the lanthanides remain largely unaffected by the surrounding matrix and ligand field, resulting in sharp, line-like emission bands with the same fingerprint wavelengths. However, the f-f electron transitions are formally forbidden by the spin and Laporte rules, which means that lanthanide ions are not typically directly excited. Indirect excitation can be accomplished *via* the antenna effect. A fluorophore (sensitizer molecule or antenna) is typically

an organic compound, which absorbs light and transfers energy to the lanthanide ion (Figure III.22). The antenna yield energy through high molar absorption to the short-lived singlet excited state (S_1), which can subsequently undergo intersystem crossing to the longer-lived triplet state (T_1). From the triplet state, the fluorophore transfers energy to the excited ^5D_J state of the lanthanide (sensitization). Electronic radiative transitions from the excited ^5D_J state to the ground ^7F_J state of the lanthanide result in luminescence emission, characterized by a series of bands in the UV (Gd^{3+}), visible (Eu^{3+} and Tb^{3+}) and near-IR (Dy^{3+} and Sm^{3+}) wavelengths. Nevertheless, the formation of the lanthanide excited state is a reversible process and the extent of the luminescence is contingent on factors such as the population of T_1, the energy difference between the excited state of the antenna and that of the lanthanide, the distance between the antenna and the lanthanide, and the number of coordinated water molecules.[240] The coordination of water reduces the excited state lifetimes of the Ln^{3+} ions through nonradiative vibrational energy transfer to the high-frequency O-H oscillator. Consequently, the number of water molecules coordinated to the Ln^{3+} center significantly influences lanthanide emission.[62]

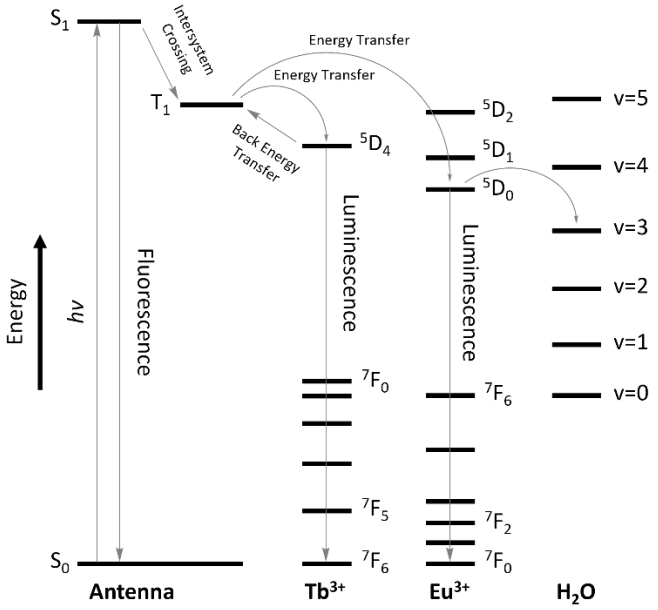

Figure III.22: Electronic energy level diagrams for Tb^{3+} and Eu^{3+}. Adapted from Orcutt et al. [240]

Luminescence measurements were employed with the aim to further characterize the synthesized PQQ ligands and their interaction with lanthanide ions in solution. Thus, solutions of the ligands were prepared in acetonitrile and europium(III) nitrate was added in stoichiometric ratio. The spectra were collected right after the addition of the metal salt to the ligand. In order to observe Eu^{3+} emission, a time-resolved fluorescence (TRF) measurement was conducted, whereby the detection of emitted light was taking place after excitation (λ_{ex} = 350 nm) had occurred.

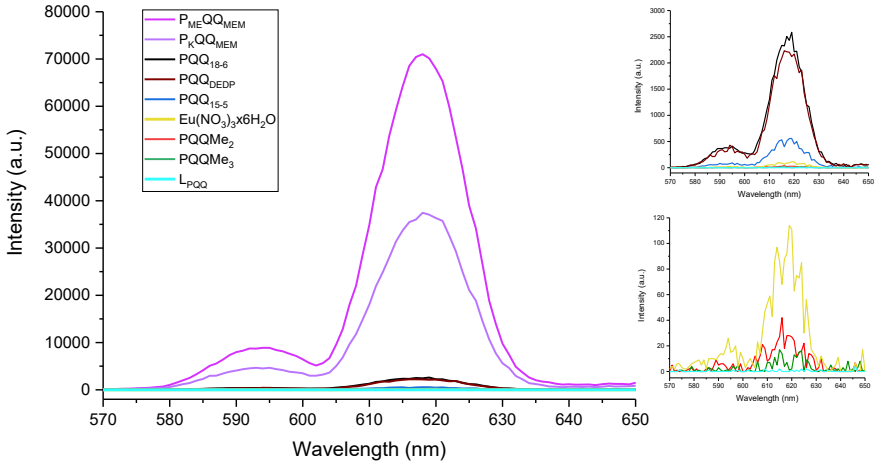

Figure III.23: TRF emission spectra (ex. 350 nm) of freshly prepared solutions of different PQQ-based ligands in the presence of 1.0 equiv. $Eu(NO_3)_3 \cdot 6H_2O$ in acetonitrile.

As shown in Figure III.23, the characteristic Eu^{3+} emission could be observed around 616 nm. The lowest and quasi negligible emission intensity was detected in the solutions containing **PQQMe$_2$** and **PQQMe$_3$** and the highest emission intensity could be assigned to the samples including the novel PQQ derivatives **P_KQQ_{MEM}** and **$P_{ME}QQ_{MEM}$**. These observations underline once more the importance of ligand design and fine-tuning for the properties of the complex species. The changes of PQQ's electronic properties observed in the ligands **P_KQQ_{MEM}** and **$P_{ME}QQ_{MEM}$** through the substitution of the ester functionalities cause a shift of the ligand's triplet states to higher energies, making them notably good antennas for Eu^{3+}. In addition, the presence of co-ligand functionalities, like in the ligands **PQQ_{DEDP}**, **PQQ_{18-6}** and **PQQ_{15-5}**, also influences the triplet states causing a slight energetic increase. Surprisingly, the solution containing ligand **L_{PQQ}** and europium(III) nitrate did not show any luminescent properties, despite the variation of the excitation wavelength as well as the delay time. Nonetheless, as discussed in the previous chapter, the composition of the ligand could not be clearly determined due to the presence of radicals which can possibly undergo some self-association processes. In addition, the UV-Vis studies conducted with **L_{PQQ}** also suggest a different ligand-to-metal interaction in comparison to the other ligands discussed in this study. Hence, the result from the TRF experiment with **L_{PQQ}** further confirms the assumption for a different complex composition than anticipated. Thus, future experiments should primarily focus on the identification of this species before conducting any further luminescence measurements.

Based on these results, a future collaboration project with the Seitz group (University of Tübingen) within CRC 1573 will focus on the photoluminescence characterization of the luminescent PQQ-Eu^{3+} complexes, including exact determination of the triplet states and calculation of luminescence lifetimes. Furthermore, in future collaborations the complexes could also undergo biocompatibility

testing and subsequently be considered for assessment as sensors for monitoring the uptake of lanthanides by bacteria.

4. Gas Phase Characterization of Lanthanide Complexes

The following section is part of the publication:

Ion Mobility Studies of Pyrroloquinoline Quinone Aza-Crown Ether–Lanthanide Complexes

Alexander Schäfer, Violeta A. Vetsova, Erik K. Schneider, Manfred Kappes, Michael Seitz, Lena J. Daumann and Patrick Weis

Published in: *J. Am. Soc. Mass Spectrom.* **2022**, *33*, 722−730.

Abstract

Lanthanide-dependent enzymes and their biomimetic complexes have arisen as an interesting target of research in the past decade. These enzymes, specifically, pyrroloquinoline quinone (PQQ)-bearing methanol dehydrogenases, efficiently convert alcohols to the respective aldehydes. To rationally design bioinspired alcohol dehydrogenation catalysts, it is imperative to understand the species involved in catalysis. However, given the extremely flexible coordination sphere of lanthanides, it is often difficult to assess the number and nature of the active species. Here, we show how such questions can be addressed by using a combination of ion mobility spectrometry, mass spectrometry, and quantum-chemical calculations to study the test systems PQQ and lanthanide-PQQ-crown ether ligand complexes. Specifically, we determine the gas-phase structures of $[PQQH_2]^-$, $[PQQH_2+H_2O]^-$, $[PQQH_2+MeOH]^-$, $[\mathbf{PQQ}_{15\text{-}5}+H]^+$, and $[\mathbf{PQQ}_{15\text{-}5}+Ln+NO_3]^{2+}$ (Ln = La to Lu, except Pm). In the latter case, a trend to smaller collision cross sections across the lanthanide series is clearly observable, in line with the well-known lanthanide contraction. We hope that in the future such investigations will help to guide the design and understanding of lanthanide-based biomimetic complexes optimized for catalytic function.

4.1. Introduction

It was long assumed that lanthanide(III) ions, in spite of their similarity to calcium(II) in size, acidity, and coordination behavior, do not contribute to life on earth in the form of enzymes.[4] However, in 2007, in the volcanic mud pot of Solfatara, a bacterium (*Methylacidiphilum fumariolicum*, SolV) was discovered that could only be cultivated in the laboratory by addition of water from its original habitat.[103] Eventually, it turned out that the high lanthanide concentrations (μM) in the mud pot water were responsible for the bacterial growth.[10] In the past decade, it has been shown that lanthanides play an important role in the active sites of methanol dehydrogenases (MDH), enzymes that catalyze the oxidation of methanol to formaldehyde in the context of the C_1 metabolism in bacteria.[3,6–9,22,121] Despite their chemically very similar properties, the choice of lanthanide shows a sometimes considerable influence on the metabolism and thus on the growth of bacteria with the corresponding lanthanide-containing enzymes. Thus, it is mainly the early lanthanides that stimulate growth.[6] The metal cation on the active site of MDH contains a cofactor called pyrroloquinoline quinone (PQQ).[6] In addition to catalyzing the conversion of methanol to formaldehyde, there is another interesting aspect to the PQQ chemistry. Lumpe *et al.* were recently able to show significant selectivity when precipitating lanthanide ions from aqueous solution by the addition of PQQ.[44] For this purpose, the resulting precipitate from a solution with lanthanum and another lanthanide (Ce–Lu) was analyzed, and depending on the element, La/Ln ratios between 4:6 (Ce) and 7:3 (Lu) were observed. Since it is already known that some aza-crown ethers also prefer the complexation of early lanthanides and that their complexes undergo a structural change in the series of lanthanides,[227] the combination of PQQ and an aza-crown ether in a single molecule is the logical next step. The ligand $PQQMe_2$–1-aza-15-crown-5 (**$PQQ_{15\text{-}5}$**, see Figure III.24) was first synthesized in 2000 by Itoh and Fukuzumi by coupling of a PQQ precursor with an aza-crown ether.[163] Recently, Vetsova *et al.* reported an improved synthesis route toward this ligand and investigated its lanthanide complexing properties as well as their ability to oxidize alcohols to aldehydes.[134] These studies comprised the combination of both condensed and gas-phase methods, such as UV-Vis, NMR, and EPR spectroscopy, as well as ion mobility mass spectrometry (IMMS) and collision-induced dissociation (CID) studies. It turned out that the reaction yield depends not only on the metal center but also on the choice of counterion and base. Since in the condensed phase the chemical environment is not as well-defined as one might hope (various interconverting conformers, protomers, solvent adducts are often simultaneously present), gas-phase studies offer the opportunity to probe the intrinsic molecular properties in a better controlled environment.

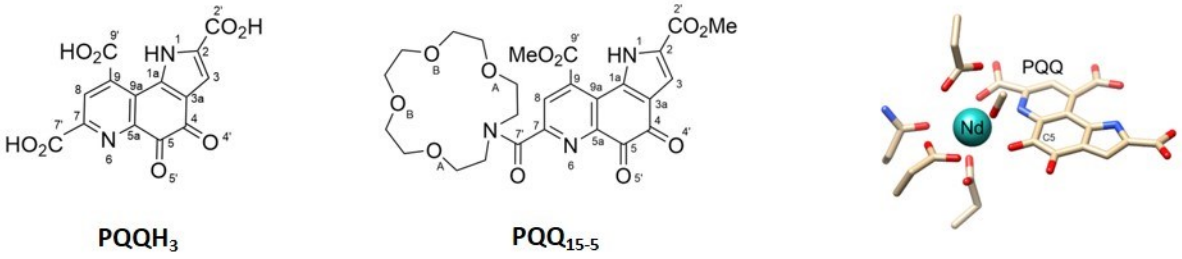

*Figure III.24: Structures of neutral PQQ ($PQQH_3$) and **$PQQ_{15\text{-}5}$**. Active site of Nd-MDH isolated from Methylacidimicrobium thermophilum AP8 (PDB: 7O6Z). Shown are truncated coordinating amino acid residues; the cofactor PQQ and MeOH are shown in a stick representation and neodymium as a green sphere.*[107]

The focus of this gas phase study is therefore on the structure of isolated PQQ and lanthanide-**$PQQ_{15\text{-}5}$** complexes (for all lanthanides except Pm, while the preceding study[134] focused on La and Lu) with a well-defined number of solvent molecules and counterions. For this purpose, we use a combination of ion mobility spectrometry, mass spectrometry, and quantum-chemical calculations. This methodology has been applied by us and others to reveal the structures of molecular ions and complexes as well as reaction intermediates.[241–243] Note that IMS-based structure determination in the gas phase (in contrast to NMR in condensed phase) is still a rapidly developing field which requires validation for new substance classes which have not yet been extensively addressed (such as lanthanide complexes). The fairly rigid structure of deprotonated $[PQQH_2]^-$ thus represents an ideal test system for the ion mobility method. Here, we apply it to more flexible ions such as solvent and counterion adducts with and without lanthanides.

4.2. Experimental Section

Instrumentation

The ion-mobility measurements were performed with a Bruker timsToF instrument. The operating principles of trapped ion mobility spectrometry (TIMS) are described elsewhere.[244] Briefly, an ion packet is pulse injected into an electrodynamical trap (the so-called TIMS tunnel) filled with a flowing buffer gas (N_2). The resulting drift motion is compensated by a variable electrostatic field. The different types of ions contained in the packet are separated in space according to their mobility and eluted by ramping the field. In all experiments, we operated the instrument at the highest feasible mobility resolution (ca. 150–200) by using the slowest feasible ramp speeds (*via* narrow ion mobility windows and long ramp times of 500 ms). The TIMS tunnel is coupled with a quadrupole mass filter and a TOF-MS (resolution >25000) that is operated with a high repetition rate (several kHz). The resulting 2D ion mobility-*m*/*z* data are deconvoluted into mobilograms with the instrument software (Data Analysis 5.0). For ion mobility and mass calibration we use Agilent TuneMix, a mixture for

fluorinated phosphazenes, with the high precision mobility data of Stow *et al.* as reference.[245] Ion mobilities are translated into experimental collision cross sections ($^{TIMS}CCS_{N2}$) with the Mason-Schamp equation.[246] The $^{TIMS}CCS_{N2}$, in turn, can be directly compared with theoretically modeled collision cross sections and thus enable structure determination in gas phase. The simultaneous occurrence of several isomers can be inferred, independent of any modeling, if bi- or multimodal mobilograms are observed or if peaks are significantly broader than the experimental resolution. Experiments were performed both in positive and negative mode (see below).

Theoretical Modeling

In order to identify the relevant isomers/conformers we performed density functional theory (DFT) calculations with the Turbomole package[246–248] using the TPSS functional[249–253] and def2-SVP[254–258] basis set.[255] For each species considered, we created a series of 10−20 meaningful starting geometries (differing in deprotonation site, conformation of the central PQQ-unit, relative orientation of counterion, and solvent adduct). These geometries were constructed and preoptimized at force-field level with the Avogadro package[259] and used as *xyz*-coordinate input files for the DFT-based geometry optimization. All geometries are fully optimized without any symmetry restrictions. Often, different starting geometries converge to the same final geometry. The Turbomole output comprises optimized *xyz*-geometries and relative energies. Since DFT calculations are known to give accurate geometries, but less reliable energies, we consider in the following at least all structures as reasonable candidates that are within 1 eV to the one found to be lowest in energy. Based on these candidate structures, we simulate theoretical collision cross sections. For this purpose, we perform trajectory method calculations to model the drift motion of the respective molecular ion in the buffer gas (N_2). For this, the ion-buffer gas interaction is modeled by a Lennard-Jones (LJ) potential plus ion-induced dipole and ion-quadrupole interaction with element-specific LJ parameters. The ion-induced dipole and ion-quadrupole interaction depend on the partial charge distribution of the drifting ion, we obtain these values by a Mulliken population analysis based on the DFT calculation. With these input parameters, a large number (ca. 106) of ion-buffer gas trajectories is calculated, the thus obtained scattering angles are numerically integrated, and finally, a theoretical cross section $^{theo}CCS_{N2}$ is obtained. The closer the theoretical and experimental cross sections and the lower the relative energy of the respective structure, the more likely it is the dominant species in the experimental mobilogram. All calculations were performed with the IMoS package (IMoS 1.09) with the standard LJ parameters implemented.[260–262]

Sample Preparation

$PQQH_3$ was obtained *via* extraction from Dr's Best vitamin capsules as a disodium salt and obtained in its fully protonated form as described previously.[136] The **PQQ$_{15\text{-}5}$** ligand was synthesized and purified as described elsewhere.[134] The lanthanide nitrates were obtained from Sigma-Aldrich (Germany). The metal-ligand complex was formed by adding the respective Ln^{3+} salt to a solution of **PQQ$_{15\text{-}5}$** (acetonitrile, 0.5 mmol/L, 1:1 ratio).

4.3. Results and Discussion

Upon electrospray ionization of a solution of $PQQH_3$ in DMSO (with 1% v/v H_2O and MeOH) we obtain in negative mode $[PQQH_2]^-$, $[PQQH_2+H_2O]^-$, and $[PQQH_2+MeOH]^-$. The corresponding mobilograms are shown in Figure III.25.

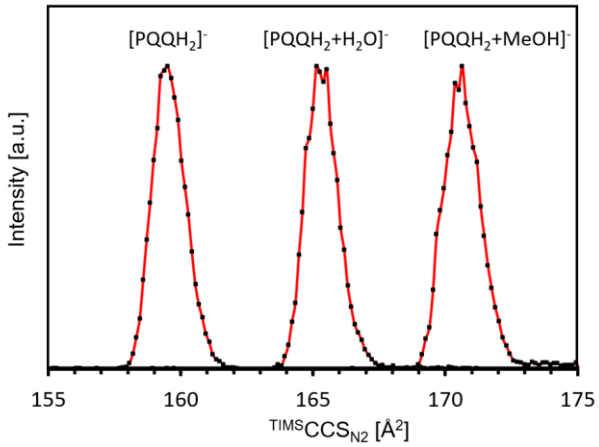

Figure III.25: Typical mobilograms of $[PQQH_2]^-$, $[PQQH_2+H_2O]^-$, and $[PQQH_2+MeOH]^-$.

In all cases, we observe one narrow peak with a peak width corresponding to the instrumental resolution of ca. 200. This can be interpreted in three ways: (1) Only one isomer ion is created upon ESI or (2) several isomers are present, but their CCS differ by less than 0.5% (ca. 1 Å^2). (3) Several isomers with larger CCS differences are present, but they interconvert much faster than the time scale of the experiment (500 ms). To shed more light on this issue, we calculated theoretical CCS ($^{theo}CCS_{N2}$) based on DFT-optimized structures (see Figure III.26) and Mulliken charges. The results are summarized in Table III.8.

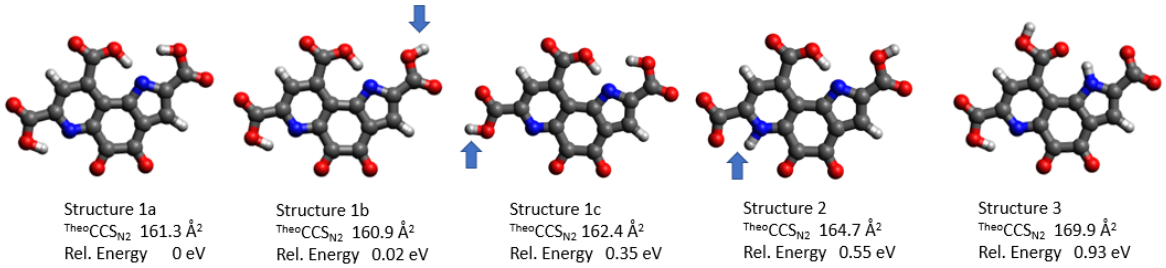

Figure III.26: Calculated structures, relative energies and calculated collision cross sections for $[PQQH_2]^-$. The blue arrows highlight the differences between structures 1a, 1b, 1c, and 2.

Table III.8: Comparison of calculated and experimental CCS for $[PQQH_2]^-$.

	$^{TIMS}CCS_{N2}$ (Å²)	Structure	$^{theo}CCS_{N2}$ (Å²)	Relative Energy (eV)
		1a	161.3	0
		1b	160.9	0.02
$[PQQH_2]^-$	159.5 ± 0.5	1c	162.4	0.35
		2	164.7	0.55
		3	169.9	0.93

$[PQQH_2]^-$

The experimental $^{TIMS}CCS_{N2}$ is 159.5 ± 0.5 Å². In the lowest energy candidate structure that we obtain (structure 1a) N1 is deprotonated, all three carboxylic acid groups remain protonated, and there are two hydrogen bonds to N1 and N6 (for the numbering of the respective atoms see Figure III.24). This structure has a $^{theo}CCS_{N2}$ of 161.3 Å² which is ca. 1% above the experimental value. Structure 1b is a conformer thereof with the hydrogen of the carboxylic group at C2 rotated (see Figure III.26, arrow). Both energy (+0.02 eV) and CCS (160.9 Å²) are basically unchanged. Structure 1c is another conformer of 1a, the carboxylic group at C7 is rotated, and therefore, there is no hydrogen bond to N6 (see Figure III.26, arrow). This increases the energy by 0.35 eV, and the $^{theo}CCS_{N2}$ is increases slightly to 162.4 Å². Based on CCS alone, we cannot distinguish between these structures. Regarding structures 1a–1c, it might be counterintuitive that N1 is deprotonated instead of the carboxylic acid function at C9 (note that the latter is more acidic in condensed phase). This reflects the fact that in aqueous solution a COO^- function can be stabilized more efficiently by solvent molecules. This stabilization is missing in the gas phase. In order to shed more light on this issue we performed some geometry-restricted DFT-calculations. We increased the O–H distance from its optimized value of 1.07 Å (with a corresponding N–H distance of 1.46 Å) up to 1.5 Å and optimized the remaining degrees of freedom. The corresponding N–H distance decreases to ca. 1.1 Å (consistent with a covalent bond), but the energy increases by ca. 0.14 eV (see Figure VI.30). A similar discrepancy between the preferred protonation

sites (O vs N) in both the liquid phase and gas phase is already known in the literature.[263] In structure 2, the C7 carboxylic group is deprotonated and N6 protonated. This structure is 0.55 eV higher in energy and has a cross section of 164.7 Å^2, i.e., ca. 3% above the experimental value. Again, there is an isoenergetic conformer with the C2-carboxylic group rotated, analogous to structure 1a vs 1b (not shown). For a C7-carboxylic group the H−N6 distance variation is determined by geometry-restricted DFT calculations (see Figure VI.31). Other structures are even higher in energy, such as structure 3, +0.93 eV (carboxylic acid group at C2 deprotonated), and have significantly larger CCS: 169.9 Å^2, ca. 7% above experiment. Therefore, such protomers can be ruled out on the basis of relative energy and CCS. (Compare a similar combined IMS, cryo-IR, DFT study on biliverdin, where only conformers within 0.2 eV to the lowest are observed in experiment).[241] To summarize, with the combination of DFT-based geometry optimization and trajectory calculations we can reproduce the experimental CCS for $[PQQH_2]^-$ within 1% if we take only the lowest energy structures calculated (1a and 1b) into account. This validates the method and the choice of input parameters (LJ parameters, Mulliken charges, see above).

$[PQQH_2+H_2O]^-$ and $[PQQH_2+MeOH]^-$

In a second step, we investigated the formation of solvent/reactant adducts with $PQQH_3$ by adding small amounts of water and methanol (1% v/v) to the solution of $PQQH_3$ in DMSO, respectively. In both cases, the adducts are formed in intensities sufficient to measure their CCS. On first sight, this is surprising since the ions have to pass the desolvation region and transfer capillary heated to 300 °C (the high temperature is necessary to remove the DMSO). The resulting $[PQQH_2+H_2O]^-$ anion has a $^{TIMS}CCS_{N2}$ of 164.7 Å^2. Compared with the 159.5 Å^2 for the bare $[PQQH_2]^-$ anion, this is an increase of only 3%, although the overall number of atoms in the ion increases by 10%, from 29 to 32. This implies a rather compact structure of the water adduct. From condensed-phase NMR measurements it is known that the carbonyl group at C5 readily adds water to form a geminal diol.[136,264] The C4 group can also be attacked by nucleophiles as was shown by Itoh *et al.*[163] We performed DFT optimizations for various protomers of both C5-dioles but also for noncovalently bound water adducts. The results are summarized in Table III.9 and Figure III.27. The lowest energy structure is a C5-diol (structure 1) with a cross section of 163.8 eV, slightly below the experimental value of 164.7 Å^2. A conformer thereof (structure 2, protonated carboxylic group at C7 rotated) has one hydrogen bond less, is therefore 0.36 eV higher in energy, and has a $^{TIMS}CCS_{N2}$ of 165.6 Å^2, slightly above the experimental value. It is likely that the two conformers can interconvert by rotation around the C7−C7′ single bond on the time scale of the CCS measurement, and we therefore measure a time average. A C4-diol, as proposed by Itoh *et al.*[163] (structure 3), has a very similar CCS (164.4 Å^2), but it is 0.27 eV above structure 1.

Noncovalently bound water adducts (structures 4 and 5) come very close in energy to structure 1 (+0.06 eV and +0.14 eV). Taking their uncertainty into account, we cannot distinguish between covalently and noncovalently bound adducts on the basis of DFT-based energies alone. However, the $^{TIMS}CCS_{N2}$ of the noncovalently bound water adducts are significantly larger, 169.0 and 169.1 Å², and therefore, structures 4 and 5 can be ruled out.

Table III.9: Comparison of calculated and experimental CCS for $[PQQH_2+H_2O]^-$.

	$^{TIMS}CCS_{N2}$ (Å²)	Structure	$^{theo}CCS_{N2}$ (Å²)	Relative Energy (eV)
		1	163.8	0
		2	165.6	0.36
$[PQQH_2+H_2O]^-$	164.7 ± 0.5	3	164.4	0.27
		4	169.0	0.06
		5	169.1	0.14

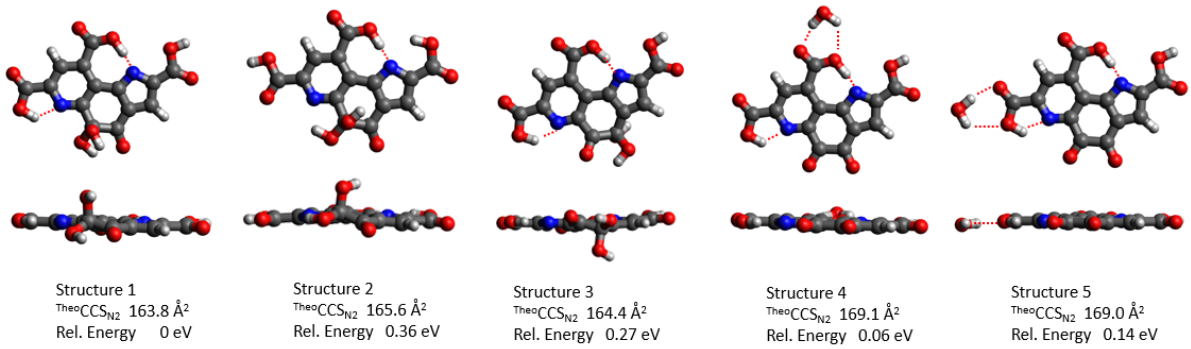

Figure III.27: Calculated structures, relative energies and calculated collision cross sections for $[PQQH_2+H_2O]^-$.

For $[PQQH_2+MeOH]^-$ as well, we obtain a single, narrow peak corresponding to an experimental CCS of 170.1 Å²; see Figure III.25. As for the PQQ–water adducts, we take both covalently (at C5 and C4) and noncovalently bound structures into account in our DFT geometry optimizations. The results are summarized in Table III.10 and Figure III.28. Interestingly, in this case the noncovalently bound adduct with the methanol molecule associated with the C9′ carbonyl group by a hydrogen bond (structure 4) turns out to be lowest in energy. Within 0.1 eV we find two other isomers: structure 5 (+0.05 eV), another noncovalently bound adduct (MeOH hydrogen bonded to O4′), and structure 1 (+0.09 eV) with the methanol covalently bound to the carbonyl group at C5 as a hemiketal. A C4 hemiketal (structure 3) is significantly higher in energy by 0.25 eV. Structure 2 (+0.43 eV) is a conformer of structure 1 with one hydrogen bond less. Based on the ion mobility data, we rule out the noncovalently bound isomers ($^{theo}CCS_{N2}$ = 175.7 Å² and 176.0 Å², respectively versus $^{TIMS}CCS_{N2}$ = 170.1 Å²). On the other hand, we confirm the covalently bound structures, since their CCS agree within

the experimental uncertainty with the measurement. Among these, structure 1 is clearly favored based on energy and CCS.

Table III.10: Comparison of calculated and experimental CCS for [PQQH$_2$+MeOH]$^-$.

	$^{TIMS}CCS_{N2}$ (Å^2)	Structure	$^{theo}CCS_{N2}$ (Å^2)	Relative Energy (eV)
[PQQH$_2$+MeOH]$^-$	170.1 ± 0.5	1	169.9	0.09
		2	171.1	0.43
		3	171.8	0.25
		4	175.7	0
		5	176.0	0.05

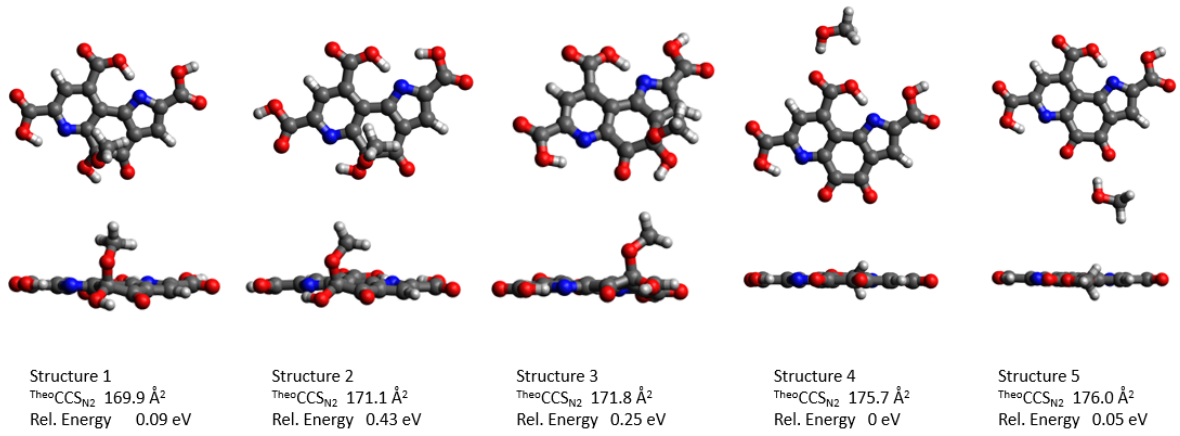

Figure III.28: Calculated structures (top and side views), relative energies, and calculated collision cross sections for [PQQH$_2$+MeOH]$^-$.

[PQQ$_{15\text{-}5}$+H]$^+$

The mobilogram of [**PQQ$_{15\text{-}5}$**+H]$^+$ consists of three distinct peaks, the largest centered at 225.2 Å^2 and two smaller peaks at 222.4 and 228.2 Å^2, respectively, see Figure III.29 and Table III.11. This implies that there are at least three protomers/conformers that do not interconvert on the time scale of our ion mobility measurement, i.e., within ca. 0.5 s. Note that the relative intensities, but not the peak positions, depend somewhat on the choice of TIMS parameters (see Figure VI.32). We performed a series of geometry optimizations and found a total of 15 different structures within 1 eV. In the lowest energy structure (Figure III.30, structure 1) the extra proton is bound to the pyridine-nitrogen N6 and *via* a hydrogen bridge to O$_A$ on the crown ether group (cf. Figure III.24). The arrangement is such that the PQQ and crown ether units are slightly tilted. The $^{theo}CCS_{N2}$ of this structure is 229.0 Å^2, which is ca. 2% below the main peak in the mobilogram. Structure 2 is a variant thereof with a hydrogen bridge

to O_B instead. Both relative energy (+0.1 eV) and CCS (228.8 Å²) are similar to structure 1. We find several conformers (= local minima) in our geometry optimizations that differ by the relative orientations of the methyl ester groups. Their CCS are close to 229 Å². Somewhat higher in energy (+0.43 eV) we find a structure (3) with the extra proton between O_B and O5. As a consequence, this structure is rather flat and therefore has a somewhat larger CCS of 233.3 Å². This structure could be responsible for the third peak (at 228.2 Å²) in the mobilogram, if we accept a deviation of ca. 2%. A more compact geometry (structure 4, 226.4 Å²) is obtained by protonation at N6 and hydrogen bond to O_A. As a consequence, the crown ether is folded back to the PQQ unit with an angle of ca. 60°; see Figure III.30. This structure can explain the first peak in the mobilogram if we accept a 2% deviation between experiment and calculation, as before. However, this structure is ca. 0.55 eV higher in energy. To summarize, due to the rather flexible crown ether function a series of non-interconverting structures with similar energy but different CCS is feasible and obviously realized in the experiment as can be seen by the trimodal mobilogram. The calculations can reproduce the main features. A temperature-dependent NMR experiment of **$PQQ_{15\text{-}5}$** in acetonitrile supports the high flexibility of the aza-crown moiety (Figure VI.33).

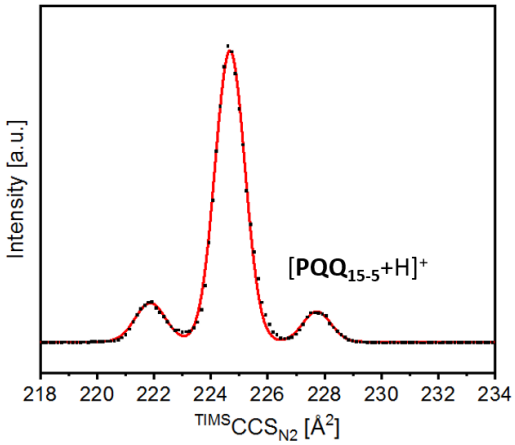

*Figure III.29: Typical mobilogram of **[$PQQ_{15\text{-}5}$+H]⁺**.*

*Table III.11: Comparison of calculated and experimental CCS for **[$PQQ_{15\text{-}5}$+H]⁺**.*

	$^{TIMS}CCS_{N2}$ (Å²)	Structure	$^{theo}CCS_{N2}$ (Å²)	Relative Energy (eV)
[$PQQ_{15\text{-}5}$+H]⁺	222.4 ± 0.5	1	229.0	0
	225.2 ± 0.5	2	228.8	0.1
	228.2 ± 0.5	3	233.3	0.43
		4	226.4	0.55

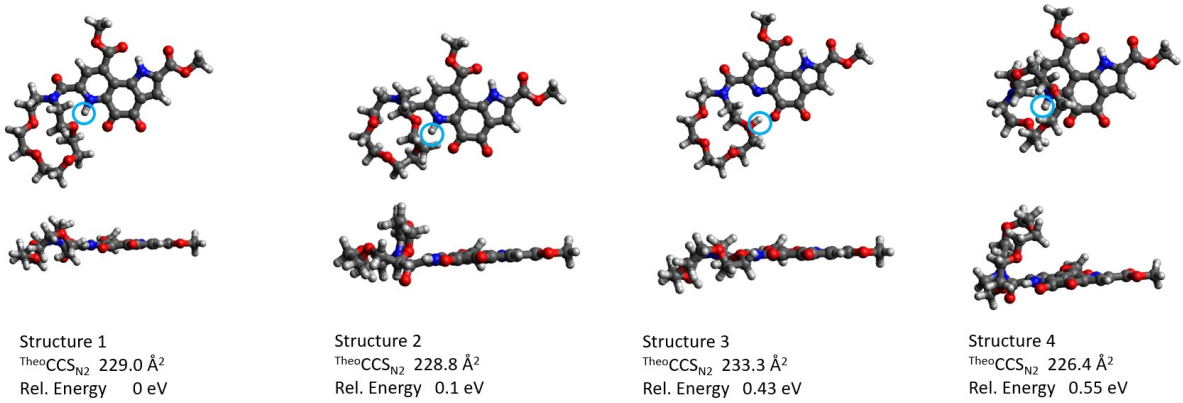

Figure III.30: Calculated structures (top and side views), relative energies and calculated collision cross sections for ***[PQQ***$_{15\text{-}5}$*+H]*$^{+}$*. The blue circle indicates the protonation site.*

[PQQ$_{15\text{-}5}$+Ln+NO$_3$]$^{2+}$

PQQ$_{15\text{-}5}$ easily forms metal complexes upon addition of M^{2+} or M^{3+} salts. With lanthanide(III) nitrates we observe upon electrospray ionization the formation of complexes of the form [**PQQ$_{15\text{-}5}$**+Ln+NO$_3$]$^{2+}$. The nitrate counterion is strongly bound: upon collision-induced dissociation no $NO_3^{0,-}$ or $NO_2^{0,-}$ loss is observed.[134] We see instead predominantly loss of MeOH, most likely from one of the ester functions in **PQQ$_{15\text{-}5}$**. Furthermore, we do not observe the complex ion without counterion, i.e., [**PQQ$_{15\text{-}5}$**+Ln]$^{3+}$. The mobilograms of all [**PQQ$_{15\text{-}5}$**+Ln+NO$_3$]$^{2+}$ complexes are rather simple with one narrow peak (Figure III.31).

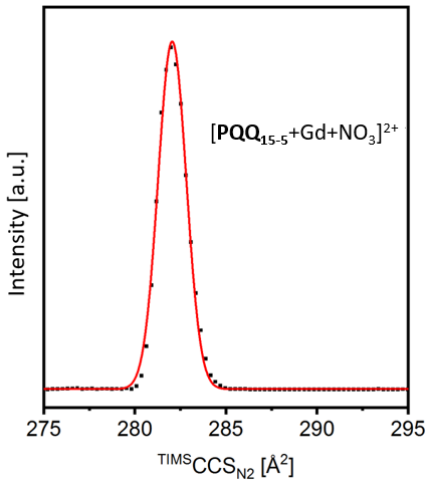

*Figure III.31: Typical mobilogram of [****PQQ***$_{15\text{-}5}$*+Ln+NO*$_3$*]*$^{2+}$*, shown for Ln = Gd. Only one narrow peak is observable close to the instrumental resolution. Basically, the same mobilograms (one narrow peak) are obtained for all Ln = La to Lu.*

For La we obtain a ^{TIMS}CCS$_{N2}$ of 281.8 ± 1.5 Å². There is a clear trend to smaller CCS when going from La to Lu, in line with the well-known lanthanide contraction. For Lu we obtain 278.7 ± 1.5 Å²; see Figure III.32. Note that the 1.5 Å² uncertainty contains both calibration and statistical errors. Since we

determine the CCS of all [**PQQ**$_{15\text{-}5}$+Ln+NO_3]$^{2+}$ ions (Ln = La to Lu, except for Pm) under identical conditions, the relative uncertainties are well below 1 Å^2. We expect the lanthanide ion to interact with the electronegative oxygen and nitrogen atoms of the PQQ- or crown ether moiety, and nitrate counterions.

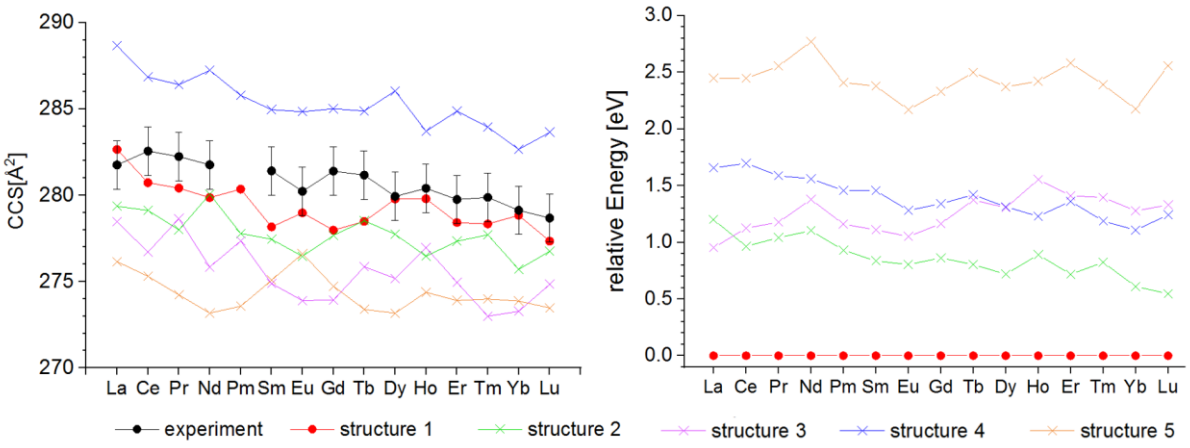

*Figure III.32: (Left) Experimental and calculated CCS of [**PQQ**$_{15\text{-}5}$+Ln+NO_3]$^{2+}$ for Ln = La to Lu. Black circles: measurement. The error bars (±0.5%) comprise statistical and calibration errors. Since all measurements were performed at identical conditions (temperature, voltages across the TIMS-tunnel, ramp speed), we expect the relative errors to be even smaller, ca. 0.3%. The red circles correspond to the structure that has been found to be lowest in energy. The other symbols correspond to structures with higher energies. (Right) Relative energies of DFT-optimized structures.*

To determine the dominating geometry, we performed DFT-based geometry optimizations with the formalism described above. The results are summarized in Figure III.33 with lanthanum as an example. The other lanthanides show very similar, isostructural geometries. In the lowest energy structure (structure 1, Figure III.32, Figure III.33 and Table III.12), Ln is 9-coordinate with **PQQ**$_{15\text{-}5}$ acting as a heptadentate ligand (five donors of the aza-crown ether, pyridine nitrogen N6, quinone-oxygen at C5) and a chelating nitrate binding in bidentate fashion. In order to obtain a more quantitative idea about the coordination geometry and the trends along the lanthanide series, the DFT-optimized structures of all lanthanide complexes were investigated with a continuous shape measure (CShM) approach[265–267] using the computer program SHAPE 2.1.[268] All 13 idealized reference geometries implemented in SHAPE 2.1 for coordination number 9 were taken into account, and the corresponding numerical value *S* for the CShM was calculated.[269,270] *S* can theoretically range between 0 (perfect fit to the ideal reference geometry) and 100 (no geometric similarity). Smaller *S* indicates smaller average deviation from the reference geometry. Table VI.8 shows the CShM values *S* for the seven reference geometries with the *S* smallest values. According to the analysis, the coordination geometries are relatively irregular and cannot be well described as being close to a particular ideal polyhedron. The smallest *S* (values for all lanthanides are found for the capped square-antiprismatic (CSAPR-9: 4.79 > *S* > 2.81) and the muffin-shaped (MFF-9: 4.48 > *S* > 2.68) geometries.[269,270] In addition, the distances Ln-X (X = O, N) in the inner coordination spheres of the

lanthanides decrease as expected by 6.5% and 9.1% for individual bond lengths. This manifestation of the lanthanide contraction is perfectly within the normal range of trends found in the crystal structures of isostructural lanthanide complex series,[20,25,271] which is a very good indicator of the quality of the DFT calculations.

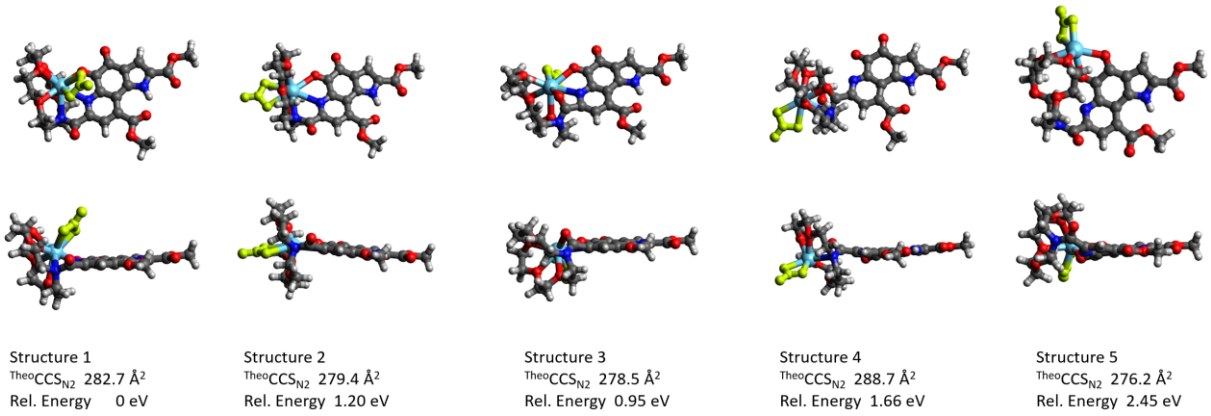

*Figure III.33: Calculated structures (top and side views), relative energies, and calculated collision cross sections for [**PQQ**$_{15\text{-}5}$+La+NO$_3$]$^{2+}$. The nitrate group is marked in yellow, lanthanum light blue.*

Structure 1 of [**PQQ**$_{15\text{-}5}$+La+NO$_3$]$^{2+}$ has a $^{theo}CCS_{N2}$ of 282.7 Å^2 which is within 1 Å^2 (0.3%) of the experimental value of 281.8 Å^2. We performed similar geometry optimizations for all lanthanides. In each case this structural motif is far more stable than other isomers (by more than 0.5 eV). Calculated and experimental CCS deviate by less than 1% (except for Sm, 1.2% and Gd, 1.2%), see Figure III.32 and Table III.12.

Besides this structure, we found four other energy minima: structures 2 and 3 are similar to structure 1, inasmuch as the metal atom is coordinated to the four crown ether oxygens as well as to N6 and the neighboring quinone-oxygen, and the nitrate counterion, but in a different relative orientation, see Figure III.33. In structure 2, the nitrate and PQQ group are almost coplanar and on opposite sides of the metal atom, separated by the crown ether group. This structure is between 1.20 eV (La) and 0.55 eV (Lu) higher in energy than structure 1. Its calculated CCS deviates more (between 0.9 and 1.5%) from experiment than what we observe for structure 1. In structure 3, both nitrate and the PQQ unit cover one side of the metal center and the crown ether the other side. Depending on the lanthanide, this structure is between 1.1 eV (Yb) and 1.7 eV (Ce) higher in energy than structure 1. Its cross section is on average ca. 2% below the experimental value. In structure 4, the metal center is not bound to N6 and the quinone-oxygen; i.e., it is here only complexed by the crown ether and the nitrate. This structure can be clearly ruled out: it is always more than 1.1 eV above structure 1, and its cross section on average ca. 2% above the experimental values (see Table III.12). We found a fifth structure with the metal center coordinated to both quinone-oxygens and only two of the oxygens of the crown ether. For all lanthanides it is more than 2 eV higher in energy, its cross section is more than

2% below the experiment can therefore be ruled out as well. To summarize, both on the basis of relative energy and cross section structure 1 is clearly favored.

*Table III.12: Comparison of calculated and experimental CCS for [**PQQ**$_{15\text{-}5}$+Ln+NO_3]$^{2+}$.*

	Exp	Structure 1		Structure 2		Structure 3		Structure 4		Structure 5	
	CCS (Å²)	CCS (Å²)	ΔE (eV)	CCS (Å²)	ΔE (eV)	CCS (Å²)	ΔE (eV)	CCS (Å²)	ΔE (eV)	CCS (Å²)	ΔE (eV)
La	281.8	282.7	0	279.4	1.20	278.5	0.95	288.7	1.66	276.2	2.45
Ce	282.6	280.7	0	279.1	0.96	276.7	1.13	286.9	1.70	275.3	2.45
Pr	282.2	280.4	0	278.0	1.04	278.6	1.18	286.4	1.59	274.2	2.55
Nd	281.8	279.9	0	280.1	1.10	275.8	1.38	287.2	1.56	273.2	2.77
Pm		280.4	0	277.8	0.93	277.4	1.16	285.8	1.46	273.6	2.41
Sm	281.4	278.2	0	277.5	0.84	274.9	1.11	285.0	1.46	275.1	2.38
Eu	280.2	279.0	0	276.5	0.80	273.9	1.05	284.8	1.28	276.6	2.17
Gd	281.4	278.0	0	277.7	0.86	273.9	1.16	285.0	1.34	274.7	2.33
Tb	281.2	278.5	0	278.5	0.80	275.9	1.37	284.9	1.42	273.4	2.50
Dy	279.9	279.8	0	277.7	0.72	275.2	1.30	286.0	1.31	273.2	2.37
Ho	280.4	279.8	0	276.5	0.89	277.0	1.55	283.7	1.23	274.4	2.42
Er	279.8	278.4	0	277.3	0.72	275.0	1.41	284.9	1.36	273.9	2.58
Tm	279.9	278.3	0	277.7	0.82	273.0	1.40	284.0	1.19	274.0	2.39
Yb	279.1	278.8	0	275.7	0.61	273.3	1.28	282.7	1.11	273.9	2.18
Lu	278.7	277.3	0	276.8	0.55	274.8	1.33	283.7	1.24	273.5	2.56

4.4. Conclusions

By a combination of ion-mobility measurements and quantum-chemical calculations we were able to identify the relevant gas-phase structures of different PQQ derivatives and their complexes with solvent molecules, lanthanide(III) ions, and nitrate counterions. To the best of our knowledge, this is the first ion-mobility measurement across the complete series of complexes with lanthanide metal centers (except promethium). Even though there is only one lanthanide atom in the complexes comprising a total of 74 atoms, the trend to smaller CCS across the series is clearly observable (both experimentally and in the DFT-based geometry optimizations), in line with the well-known lanthanide contraction. PQQ is a notoriously difficult ligand to study, as it reacts readily with a number of nucleophiles and shows complex speciation (including its different redox and protonation states) in solution. Here, we confirm the high reactivity of C5 toward nucleophiles (H_2O and MeOH) in the gas phase and assign structures that are in line with the reported solution models. In a second step, we investigated lanthanide complexes of a PQQ-inspired ligand that has previously been used as a biomimetic model for the alcohol oxidation in methanol dehydrogenases.[134] To evolve highly specific and well-defined lanthanide and quinone-based catalysts it is pivotal to understand different species,

isomers, and structures that may arise during catalysis. Here, we develop a benchmark for the study of such model systems and catalysts in the gas phase which can give hints into the function and optimal design of future biomimetic catalyst systems.

5. Conclusion

In summary, **PQQ$_{15\text{-}5}$** was evaluated as a synthetic model for the active site of quinoprotein alcohol dehydrogenases, whereby the binding of Ba^{2+}, Ca^{2+}, La^{3+} and Lu^{3+} have been examined by NMR spectroscopy. The results gave evidence for a metal ion coordination at the biologically relevant pocket of PQQ (site 1). To gain more information on the structures and impact of counterions of the complexes, collision induced dissociation (CID) experiments were performed and it was observed that the nitrates are more tightly bound than the triflates. In addition, a combination of DFT-calculations and ion mobility measurements (IMS) was applied to resolve the structure of the complexes in the gas phase.

Furthermore, UV-Vis titrations of **PQQ$_{18\text{-}6}$** and **PQQMe$_2$** with different Ln^{3+} ions were performed and binding constants were evaluated using the Benesi-Hildebrand method. Different Ln^{3+} selectivity patterns were observed for **PQQ$_{18\text{-}6}$** and **PQQMe$_2$**. Moreover, the methanol addition to **PQQMe$_2$** was investigated and equilibrium constants K_{add} for the hemiacetal formation were determined. The results indicate an enhancement of the investigated reaction in the presence of La^{3+}, followed by Eu^{3+} and Lu^{3+}. Future research could focus on elucidating the steric effects of various alcohols on the hemiacetal formation.

UV-Vis titrations of further ligand platforms with La^{3+} were conducted and the calculated bindings constants were compared. The highest chelator affinities for La^{3+} were observed in the case of **PQQ$_{18\text{-}6}$** and **PQQMe$_2$**, followed by **PQQ$_{15\text{-}5}$** and **P$_{ME}$QQ$_{MEM}$**. The lowest binding constants were calculated for **PQQ$_{DEDP}$** and **PQQMe$_3$**. In addition, UV-Vis experiments were conducted with ligand **L$_{PQQ}$**, however, the analysis of the collected data suggested a different complex speciation than originally anticipated. Using the Nash method, a 2:1 stoichiometry was proposed for the respective La^{3+} complex.

Nevertheless, it should be noted that the Benesi-Hildebrand method is considered outdated and prone to errors.[222] With modern computer-based non-linear regression methods, these problems can be avoided,[222,272] thus the purchase and application of such software programs could be considered as an outlook for this project.

For further characterization of the PQQ-based ligands, time-resolved fluorescence measurements were conducted with the respective Eu^{3+} complexes in acetonitrile. While for **PQQMe$_2$** and **PQQMe$_3$** a very low emission intensity was observed, the novel PQQ derivatives **P$_K$QQ$_{MEM}$** and **P$_{ME}$QQ$_{MEM}$** showed to be very good antennas for Eu^{3+} since high intensity bands at 616 nm were observed. These observations will be the start of future collaborations within our collaborative research center.

Recently, a collaboration project with Patrick Weis, Manfred Kappes, Michael Seitz and coworkers resulted in publication discussing lanthanide complexes of **PQQ$_{15\text{-}5}$**.[135] The analytical methods applied for the investigations included a combination of ion mobility spectrometry, mass spectrometry and quantum-chemical calculations. Thereby, the gas-phase structures of [**PQQH$_2$**]$^-$, [**PQQH$_2$**+H_2O]$^-$, [**PQQH$_2$**+MeOH]$^-$ and [**PQQ$_{15\text{-}5}$**+H]$^+$ were determined and the high reactivity of C-5 toward nucleophiles was confirmed. In addition, a temperature-dependent NMR experiment was conducted with **PQQ$_{15\text{-}5}$** in CD_3CN. The results pointed on a flexible crown ether moiety exhibiting different possible conformations. In solution the molecule rapidly interchanged among the conformations, however the fluxionality could be reduced at low temperatures, which resulted in sharp hydrogen atom resonances. Furthermore, structures of [**PQQ$_{15\text{-}5}$**+Ln+NO_3]$^{2+}$ complexes were discussed more in detail and it should be noted that no complex ion was observed without counterion. A DFT-based geometry optimization was performed in order to determine the dominating geometry. It was shown that all lanthanide complexes show very similar, isostructural geometries. In the lowest energy structure however, the lanthanide(III) cation has a coordination number of 9. Thereby, **PQQ$_{15\text{-}5}$** acts as a heptadentate ligand, whereby five donor atoms come from the aza-crown ether, one from the pyridine nitrogen N-6 and one from the quinone-oxygen at C-5. Additionally, a nitrate counterion acts as a bidentate ligand. Such kind of studies are anticipated to enhance our understanding of various species, isomers and structures associated with the lanthanide-based biomimetic complexes. This, in turn, will offer valuable insights for design and optimization of catalyst systems in future.

IV. ALCOHOL OXIDATION

Parts of this chapter have appeared in the publication:

Pyrroloquinoline Quinone Aza-Crown Ether Complexes as Biomimetics for Lanthanide and Calcium Dependent Alcohol Dehydrogenases

Violeta A. Vetsova, Katherine R. Fisher, Henning Lumpe, Alexander Schäfer, Erik K. Schneider, Patrick Weis and Lena J. Daumann

Published in: *Chem. Eur. J.* **2021**, *27*, 10087–10098.

1. Introduction

In the metabolism of methylotrophs and methanotrophs, methanol dehydrogenases (MDH) catalyze the two-electron oxidation of methanol to formaldehyde.[84] Although many MDH species have been extensively examined over the years, the exact mechanism of alcohol oxidation still remains controversial.[106] Based on computational,[264,273–276] biomimetic[143,144,163,166] and crystallographic studies,[277] however, two mechanisms have been frequently mentioned (Figure IV.1). The first one involves a base-catalyzed nucleophilic addition of methanol to the quinone C-5 of PQQ to form a hemiketal intermediate. The second mechanism consists of a base-catalyzed proton abstraction from methanol in concert with a hydride transfer from the substrate to the C-5 of PQQ.

The difficulty to trace the catalytic mechanism by kinetic and spectroscopic investigations results from the lack of intermediates that can readily be detected.[87] Isolated enzymes contain the cofactor PQQ either in the fully reduced form or as a semiquinone.[111] Nonetheless, the presence of the semiquinone form is indicative of a two-step reoxidation of PQQ through two single-electron transfers to the electron acceptor cyctochrome *c* (cyt c_L).[108,278] In addition to PQQ, two further components in the active site have been suggested to be essential for the catalysis. The first one is an aspartate (Asp^{303} in MxaF and Asp^{299} in XoxF), which functions as a base, and the second key component is the active site metal (Ca^{2+}, respectively Ln^{3+}), which acts as a Lewis acid for activation of PQQ's carbonyl C-5.[108] Throughout the lanthanide series (from La to Lu) the Lewis acidity increases, due to the decreasing ionic radius, caused by the lanthanide contraction. If the kinetic reaction was solely dependent on the

Lewis acidity of the metal ion, the specific activity of MDH should increase with the late lanthanide ions in the active site. However, the experimentally observed low specific activity or even the absence of any for the late lanthanide ions showed that Lewis acidity and activation of the C-5 carbonyl bond is not the only factor that needs to be considered.[118]

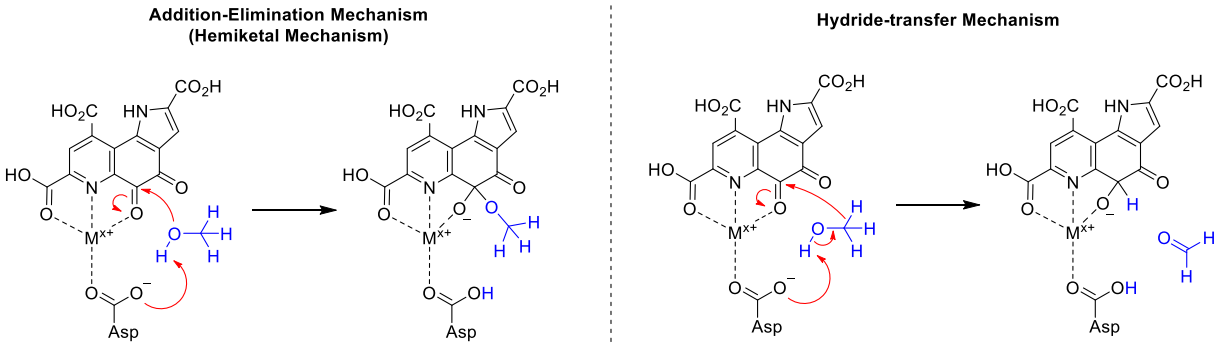

Figure IV.1: Initial key steps of the two proposed mechanisms for the dehydrogenation reaction in MDH with x = 3 for lanthanide ions and x = 2 for calcium.

Several functional model investigations have been reported in the past years, which discussed the mechanism of alcohol oxidation in order to broaden the knowledge of the MDH enzymes. In 2000 Itoh and Fukuzumi reported the results of a comprehensive UV-Vis study based on ligand **PQQ**$_{15\text{-}5}$ and alkaline earth metal ions whereby supporting evidences for the addition-elimination mechanism through the C-5 hemiacetal intermediate were provided. The paper demonstrated enhanced ethanol addition to **PQQ**$_{15\text{-}5}$ through Ca^{2+} coordination in acetonitrile, as the calculated equilibrium constant was six times higher (1.2 M^{-1}) than without the metal ion (0.2 M^{-1}). In addition, the conversion of the quinone [Ca(**PQQ**$_{15\text{-}5}$OEt)]$^{2+}$ to the corresponding quinol [Ca(**PQQ**$_{15\text{-}5}$H$_2$)]$^{2+}$ was presented and it was shown that the addition of the base diazabicycloundecene (DBU) accelerates the ethanol oxidation to acetaldehyde (Scheme IV.1).

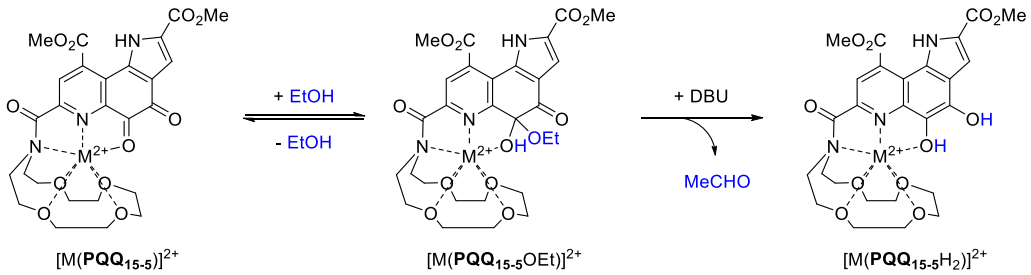

Scheme IV.1: Proposed addition-base catalyzed elimination mechanism for the oxidation of ethanol by Itoh and Fukuzumi.[163]

A comparison of the rate constants, determined for the different alkaline earth metal ions examined in this study, demonstrated a stronger catalytic effect of the larger metal ions (k = 1.7 M^{-1} s^{-1} (Ca^{2+}), k = 58 M^{-1} s^{-1} (Sr^{2+}), k = 2800 M^{-1} s^{-1} (Ba^{2+})). Based on these results, the authors assumed that the binding of larger metal ions such as Ba^{2+} and Sr^{2+} to the hemiacetal of PQQ forces the added alcohol moiety closer

to the C-4 quinone carbonyl oxygen than in the case of Ca^{2+}, making the α-proton abstraction by the carbonyl easier (Figure IV.2).

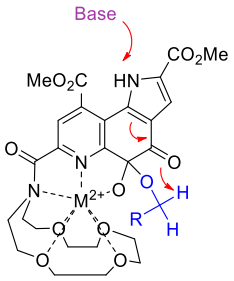

Figure IV.2: Base catalyzed α-proton abstraction from alcohol substrate proposed by Itoh and Fukuzumi.[163]

In 2018 McSkimming *et al.* reported the first synthetic functional model of lanthanide-dependent alcohol dehydrogenase based on ligand **L**$_{PQQ}$.[166] The oxidation of 4-methylbenzyl alcohol to 4-methyl benzaldehyde through lanthanum(III) coordination to **L**$_{PQQ}$ was demonstrated and it was shown that this process can be accelerated by addition of either 2,6-lutidine or DBU. Furthermore, complementary computational studies on the alcohol oxidation mechanism presented evidences that the hydride transfer pathway is clearly favored with either a weak base (2,6-lutidine) or without a base (Scheme IV.2). In the presence of DBU, however, a reduction in the energy barrier was observed for the aldehyde elimination making this pathway energetically possible.

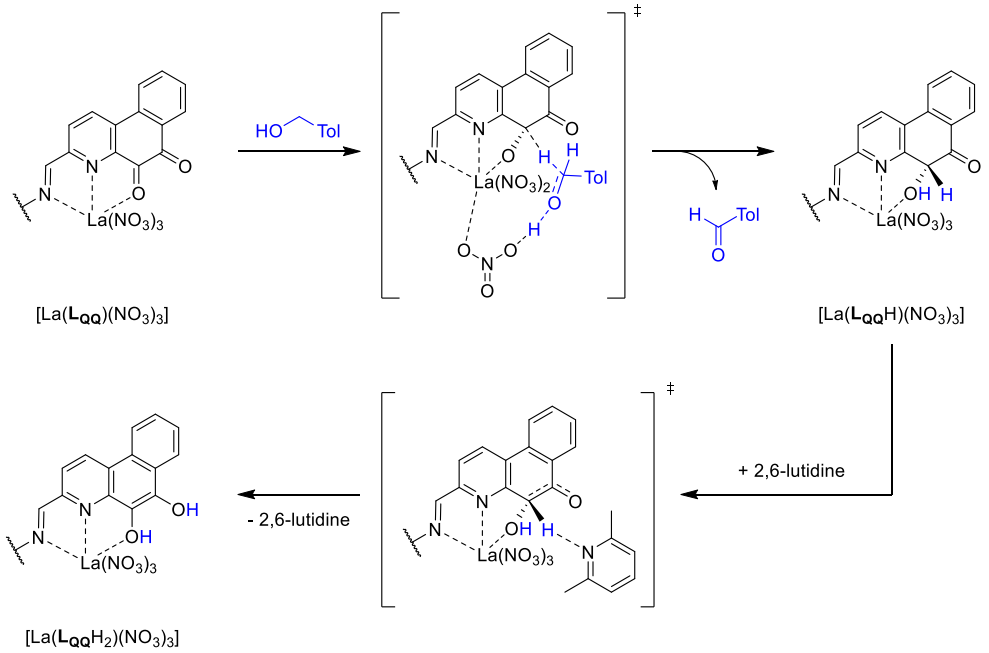

Scheme IV.2: Proposed hydride-transfer mechanism for the oxidation of 4-methylbenzyl alcohol by Schelter et al.[166] *The tetracyclohexyl-3-(2-aminophenyl)pentanediamide moiety is omitted for clarity.*

Recently, Luo *et al.* showed that the semiquinone-lanthanum complex [La(***o*-Q**$^{\cdot-}$)$_2$] can also serve as an efficient catalyst for the oxidation of alcohols under aerobic conditions.[279] The catalysis was initialized

by reduction through single electron transfer of the *ortho*-quinone ligand ***o*-Q** after coordinating with LaI_3. A screening of different conditions showed that the addition of a base did not have an obvious effect on the reaction outcome and a kinetic isotope effect was observed on both O–H and C–H of benzylic alcohol. Based on this and further experimental observations, the authors proposed a coupled proton-hydride transfer mechanism instead of stepwise deprotonation and hydride transfer for the oxidation of alcohols (Figure IV.3).

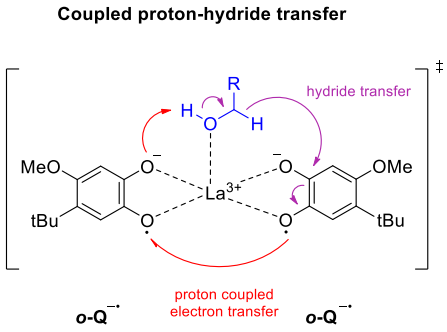

Figure IV.3: Proposed coupled proton-hydride transfer mechanism by Luo et al.[279]

In addition, a Lewis acid screening showed that all lanthanide triflates were able to catalyze the reaction. However, no trend in terms of achieved yields could be observed across the lanthanide series, since the highest yields were calculated for La (89 %), Yb (80%) and Lu (72 %), whereas some members of the early lanthanides like Ce and Nd showed lower yields of 44%. Moreover, the experiment performed with calcium triflate showed no substrate conversion at all. Given the fact that the pyridine (and pyrrole) moiety is lacking in ligand ***o*-Q** and the coordination of Ln is taking place at both quinone oxygens, the system cannot be considered a true MDH biomimetic. Nevertheless, the study presents an interesting use of both quinones and lanthanides in alcohol oxidation reaction and together with previous studies on different PQQ surrogates it further underlines the importance of the cofactor structure for the processes taking place in the active site of the enzyme.[280]

So far only MDH biomimetics containing either alkaline earth ions or lanthanum have been reported.[142–144,163,164,166] In order to unravel the possible differences of lanthanides over calcium in alcohol oxidation reactions, this project aims to evaluate the ligand **PQQ**$_{15\text{-}5}$ and the respective Ca^{2+}, Ba^{2+}, La^{3+} and Lu^{3+} biomimetic complexes. A further goal of this chapter is to answer the question whether a similar trend in alcohol oxidation activity, where only the early lanthanides are active in MDH enzymes and relevant for bacteria, could also be found for the biomimetic system. In addition, the change in the oxidation rate of benzyl alcohol will be studied by replacing the substrate with benzyl alcohol-α,α-d_2. And finally, different PQQ based ligands with different geometries and functionalities will be investigated and compared.

2. Product Analysis with 2,4-DNPH

In related publications by Itoh and coworkers,[143,144,163] the successful alcohol oxidation by PQQ derived model compounds was verified through isolation of oxidation products as their 2,4-dinitrophenylhydrazone derivatives on a preparative scale. Based on these reports, a first attempt to analyze the products of the reaction of **PQQ$_{15\text{-}5}$** and methanol in the presence of europium(III) triflate and DBU was made, using 2,4-dinitrophenylhydrazine (2,4-DNPH). 2,4-DNPH is a reagent widely used for the determination of carbonyl compounds through formation of the corresponding 2,4-dinitrophenylhydrazones.[281,282]

By using standard SCHLENK techniques, **PQQ$_{15\text{-}5}$** (1.3×10^{-4} M) was dissolved in dry acetonitrile (40 mL). $Eu(OTf)_3$ (1.3×10^{-4} M) was added, causing a color change from yellow to brown. The subsequent addition of anhydrous methanol (1.5 M) resulted in a second color change from brown to light yellow. To start the reaction, DBU (2.4×10^{-3} M) was added and the resulted bright yellow solution was stirred for 30 min at room temperature. In separate flasks, attempts to dissolve 2,4-dinitrophenylhydrazine (33 wt.% H_2O) in either dry acetonitrile, water or HCl (10%) failed. 2,4-DNPH dissolved only partially in CH_3CN, thus a solution of the hydrazine with unknown concentration was given to the reaction mixture containing **PQQ$_{15\text{-}5}$**, Eu^{3+}, methanol and DBU. The solution changed its color from bright yellow to dark green. The reaction mixture was stirred for 2 h at room temperature. An aliquot of the solution was analyzed by LC-MS (Figure VI.35).

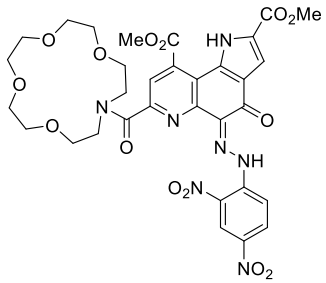

30

*Figure IV.4: Structure of the **PQQ$_{15\text{-}5}$**-2,4-dinitrophenylhydrazine adduct **30**. Calculated exact mass for $[C_{32}H_{34}N_7O_{14}]^+$: m/z = 740.2158.*

Unfortunately, neither the mass of the desired formaldehyde-2,4-DNPH (calc. m/z = 211.0462) nor the mass of a europium(III) complex of **PQQ$_{15\text{-}5}$** could be found in the mass spectrum. According to the literature,[144] low yields of formaldehyde-2,4-DNPH are attributed to the instability of formaldehyde under the used experimental conditions. Therefore, it cannot be concluded that the oxidation reaction of methanol was unsuccessful only by evaluating the results from the LC-MS analysis. As shown in Figure VI.35, the mass of the free ligand as well as its water adduct were also found in the mass spectrum. Additionally, the mass of a further compound was detected, which could be assigned to the

Schiff base adduct of **PQQ$_{15\text{-}5}$** with 2,4-DNPH. Considering the electron-withdrawing nature of the pyridine moiety and the coordination to Eu^{3+}, the C-5 position of **PQQ$_{15\text{-}5}$** is very reactive towards nucleophilic reagents. Thus, the carbonyl oxygen at C-5 position can be substituted by 2,4-dinitrophenylhydrazine *via* a hydrazone bond, leading to the formation of compound **30** (Figure IV.4). A related structure, consisting of PQQ dimethyl ethyl triester and 2,4-DNPH, was already described in the literature,[283] proving the tendency of PQQ-derived compounds to undergo this kind of reactions.

Reasoning that the formation of compound **30** can interfere the detection of oxidation products, an alternative method should be applied. Inspired by a study on a different functional model for alcohol dehydrogenases by Schelter and coworkers,[166] a different approach for product analysis was employed. Hence, a benzyl alcohol was used as a substrate in the catalytic reaction of **PQQ$_{15\text{-}5}$**. The method involves reaction progress monitoring by ^{1}H NMR, which allows a decisive detection of oxidation products.

3. PQQ$_{15\text{-}5}$ Complexes as Biomimetic Systems

Alcohol oxidation

In the course of this study, the ability of the **PQQ$_{15\text{-}5}$**-based model complexes to oxidize alcohols was investigated using ^{1}H NMR, a method that had been previously successfully used by Schelter and coworkers.[166] Previous studies on related systems suggest, that alongside the model complex, the addition of a base accelerates the dehydrogenation of alcohols.[143,144,163,166] Hence, the NMR experiments reported in this study were performed with DBU as a base, unless otherwise stated. Furthermore, hexamethyldisiloxane (TMS_2O) was used as an internal standard. All reaction mixtures were degassed prior to the addition of the base, to remove air oxygen of the system, which could possibly act as a terminal oxidant.

First, a control reaction with ligand **PQQ$_{15\text{-}5}$**, 4-methyl benzyl alcohol and DBU was performed. The reaction progress was monitored over 16 h, however, no traces of substrate turnover could be detected. This underlines the essential role of a Lewis acid for the activation of PQQ and possibly for substrate orientation and activation during alcohol oxidation. The second control reaction further demonstrates the importance of the PQQ function in the ligand **PQQ$_{15\text{-}5}$** for the oxidation of the alcohol: when lanthanum(III) triflate, 4Me-PhCH_2OH and DBU were mixed and monitored over 24 h, no oxidation product 4-methyl benzaldehyde was formed, confirming the assumption that both PQQ-ligand and Lewis acid are required for alcohol oxidation.

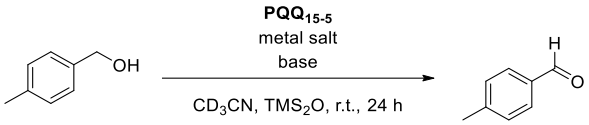

Scheme IV.3: Dehydrogenation reaction of 4-methylbenzyl alcohol to 4-methyl benzyl aldehyde.

With both control reactions in hand, the ability of the model system to promote the oxidation of alcohols to aldehydes was examined, using different metal salts. First, the dehydrogenation reaction of 4-methylbenzyl alcohol shown in Scheme IV.3 was performed using lanthanum(III) triflate and DBU. Here, 4-methyl benzaldehyde was obtained in 37% ± 5% yield after 24 h. Subsequently, the progress of the dehydrogenation reaction was examined in the presence of Lu^{3+}. As confirmed by the spectra, the later lanthanide Lu^{3+} was also able to facilitate the oxidation of the alcohol, however the product yield after 24 h was only 14% ± 2%. Later it was shown, that the recorded ^{1}H NMR spectra of the reaction mixture containing Ca^{2+} showed a higher conversion of the substrate to the corresponding product compared to the Ln^{3+}. After 24 h, a yield of 69% ± 11% was calculated for 4Me-PhCHO. The ability of the alkaline earth metals to promote the dehydrogenation reaction of the alcohol more effectively than the lanthanides was further confirmed through the measurement of the model system containing Ba^{2+}. Here, a product yield of 87% ± 10% was detected after 24 h.

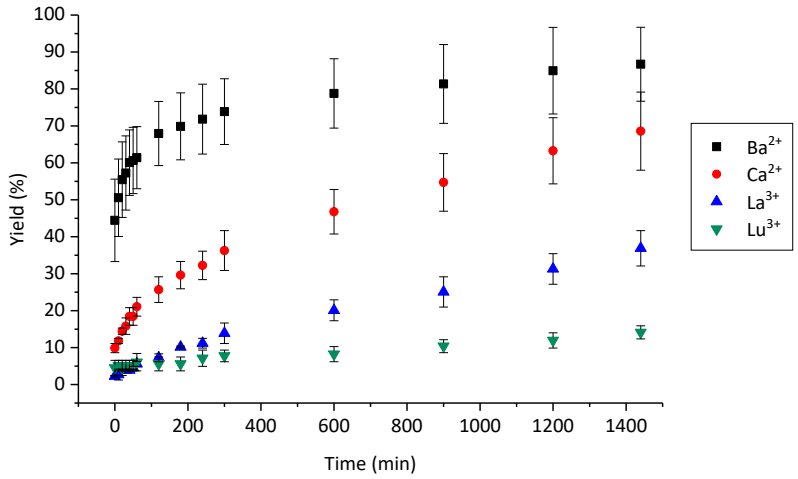

*Figure IV.5: Calculated yields of 4Me-PhCHO from the dehydrogenation reactions of 4Me-PhCH₂OH (26 mM) by ligand **PQQ**15-5 (6.5 mM) and DBU (13 mM) in the presence of barium(II) triflate (13 mM), calcium(II) triflate (13 mM), lanthanum(III) triflate (13 mM) and lutetium(III) triflate (13 mM).*

By comparing the calculated yields of the experiments with all four different metal salts, a clear trend can be observed (Figure IV.5). The model complexes with calcium(II) and barium(II) were able to accelerate the formation of the product more efficiently in comparison to the two chosen lanthanide ions. Furthermore, it was shown, that the representative of the early lanthanides was also able to promote the conversion of the alcohol faster than the later one, a result that is consistent with the

natural MDH enzyme systems.[118] Different factors as for example the stronger Lewis acidity and the smaller ionic radius of lutetium(III) could be considered as a possible explanation for this observation although this might be counterintuitive at first glance. The role of the metal ions here is to act as Lewis acid and activate the C-5 carbon of PQQ as well as possibly facilitating the orientation and activation of the substrate by deprotonation of the alcohol moiety. It is however possible, and this was demonstrated by several computational studies, that Lu^{3+} is too small to effectively bind to PQQ.[118,200,284] Moreover, the NMR investigations of the metal interactions with ligand **PQQ$_{15\text{-}5}$** described in the previous section suggests a slightly different coordination environment for Ca^{2+} and Ba^{2+} in comparison to the Ln^{3+} ions.

Itoh and Fukuzumi have previously suggested that, assuming that the reaction mechanism goes through the formation of a hemiketal species, the binding of larger ions such as Ba^{2+} and Sr^{2+} to PQQ as well as the pushing effect of the crown ether group from the back can force the added alcohol moiety closer to the C-4 quinone carbonyl oxygen, facilitating the α-proton abstraction by the carbonyl oxygen (Figure IV.2).[163] Here, the results obtained in the experiment with Lu^{3+}, would support this assumption, however, the large difference between the yields of the reactions with Ca^{2+} and La^{3+} suggests that additional factors could be involved as well. The most obvious difference is the charge, and it seems plausible that electrostatic effects and possibly attraction to other co-ligands (counterions, solvent molecules) could impact binding and conversion of alcohols. After all, the 1-aza-15-crown ligand platform does not account for the negative charges of the amino acids. However, especially for Ln-MDH (XoxF-MDH) it has been shown that the additional, negatively charged, aspartate residue in the active site is essential for Ln-binding and substrate turnover.[112]

In addition, the impact of the base on the dehydrogenation reaction of 4-methylbenzyl alcohol accelerated by ligand **PQQ$_{15\text{-}5}$** and lanthanum(III) triflate was examined, whereby DBU (pK_a = 24.3 in CH_3CN[285]) was substituted for a different base. The impact of the base was examined using 2,6-lutidine (pK_a = 14.4 in CH_3CN,[285]) and pyridine (pK_a = 12.5 in CH_3CN,[285]). The obtained yields after 24 h are comparable with the yield calculated for DBU (38% ± 2% and 41% ± 2%, respectively). In the absence of a base, it was shown, that the alcohol oxidation to the respective aldehyde was still successful, however, a yield of only 17% ± 5% was achieved after 24 h. This observation is close to that made by Schelter and co-workers in a related functional system,[166] and shows that the base accelerates the dehydrogenation reaction but it is not absolutely necessary for a successful product formation.

To test the ability of the model system with a different counterion to accelerate the conversion of alcohols to aldehydes, the dehydrogenation reaction of 4-methylbenzyl alcohol by **PQQ$_{15\text{-}5}$** and DBU was examined in the presence of lanthanum(III) nitrate. The spectra monitoring the reaction progress

over 24 h showed that the oxidation of the alcohol was successful, and the corresponding aldehyde was produced in a yield of 20% ± 1 %. However, it should be noted that the addition of DBU to the reaction mixture led to formation of a precipitation, which may be also the reason for the lower yield of the experiment when comparing it to that performed in the presence of a triflate salt (Figure IV.6).

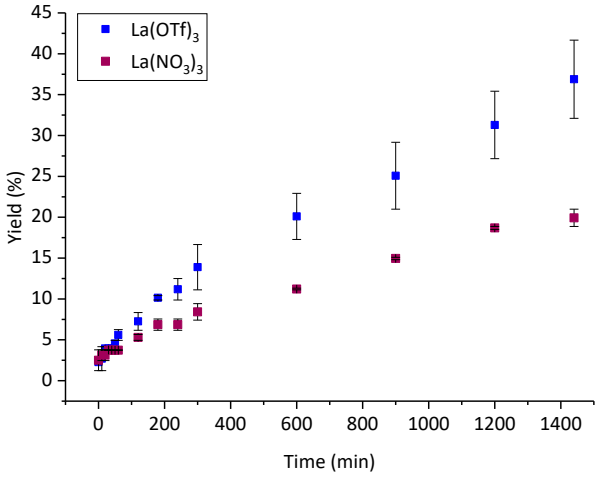

Figure IV.6: Calculated yields of 4Me-PhCHO from the dehydrogenation reactions of 4Me-PhCH₂OH (26 mM) by ligand ***PQQ***$_{15\text{-}5}$ *(6.5 mM) and DBU (13 mM) in the presence of lanthanum(III) triflate (13 mM) and lanthanum(III) nitrate (13 mM).*

EPR investigation

Recently, Luo *et al.* have reported in their preprint that a semiquinone anionic radical species forms upon coordination of LaI_3 with the *ortho*-quinone ***o*-Q** in acetonitrile (Figure IV.3).[279] An EPR spectrum of the system showed the presence of an organic radical species with g = 2.003, which could not be observed in absence of the metal salt. Furthermore, the emergence of traces of radicals when PQQ and lanthanide salts are combined has been observed previously by Daumann and co-workers (see note in the Supporting Information).[44] Hence, we analyzed the reaction mixtures of the dehydrogenation reactions described in the previous section as well as all reaction components for possible radicals.

Control experiments were undertaken to see if the formation of radical species could be observed without the presence of metal ions and other components considered necessary for substrate turnover. X-band CW EPR spectra were recorded under the given conditions for ligand **PQQ**$_{15\text{-}5}$ only, ligand with the addition of DBU and, finally, ligand with the addition of DBU and 4-methylbenzyl alcohol (Figure IV.7). X-band CW EPR spectra were also recorded for the empty tube and solvent to ensure that any signal detected was genuine.

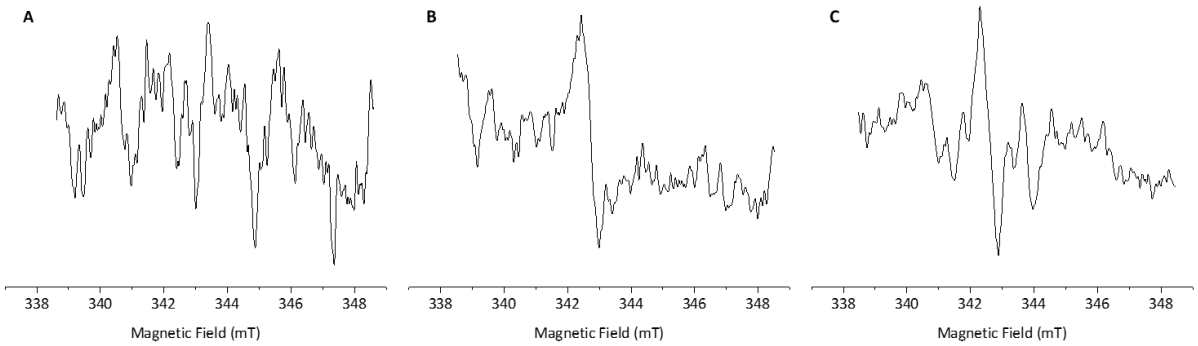

*Figure IV.7: CW EPR spectrum at X-band (9.5 GHz) of (A) ligand **PQQ**$_{15\text{-}5}$ (25 mM), (B) ligand **PQQ**$_{15\text{-}5}$ (25 mM) with addition of DBU (50 mM) and (C) ligand **PQQ**$_{15\text{-}5}$ (25 mM) with addition of DBU (50 mM) and 4-methylbenzyl alcohol (100 mM) at room temperature. The spectra were normalized in each case.*

There was no detectible organic radical for ligand **PQQ**$_{15\text{-}5}$ only. However, for the ligand with base and for the ligand with base and alcohol a very small amount of organic radical could be detected, both with an observable *g* value of 2.005 (ca. ± 0.0005). It was not possible to calculate the peak-to-peak linewidth either due to the lack of resolution from the low concentrations of radical present. Any radical that could be detected upon addition of base, as well as base and alcohol, demonstrates the general tendency of PQQ species to readily form a radical. A more detailed explanation for the formation of small quantities of this radical under these conditions is not explored in this paper, but the reader might want to refer here to the electrochemistry and EPR investigation of PQQ trimethyl ester derivatives in the presence and absence of calcium(II) by Itoh and Fukuzumi.[286]

CW EPR spectra of ligand **PQQ**$_{15\text{-}5}$ bound to Ba^{2+}, Ca^{2+}, La^{3+} and Lu^{3+} with addition of DBU and 4-methylbenzyl alcohol were recorded. The effective *g* values and peak-to-peak linewidths were extracted and are given in Table IV.1. The *g* values are consistent with the isotropic *g* values obtained for the semiquinone radical species observed in alcohol dehydrogenases in the literature.[287,288] For PQQ trimethyl ester derivatives this value was reported to be around 2.004 in CH_3CN or CH_2Cl_2.[286] The approximated error in the *g* value is ± 0.0005 and in the peak-to-peak linewidth is ± 0.05 MHz

*Table IV.1: Extracted g values, peak-to-peak linewidths, T_1 and T_2 relaxation times, and amount of spins per metal ion for different metal ligand **PQQ**$_{15\text{-}5}$ species with DBU and 4-methylbenzyl alcohol added.*

Metal ion	*g* value	Linewidth peak-to-peak [MHz]	Calculated T_1 [ns]	Calculated T_2 [ns]	Amount of spins per metal ion
Ba^{2+}	2.003	0.6	365	44	1.81×10^{-3}
Ca^{2+}	2.005	0.5	170	312	1.82×10^{-4}
La^{3+}	2.003	1.4	57	151	2.34×10^{-4}
Lu^{3+}	2.003	1.6	38	2	4.44×10^{-5}

Peak-to-peak linewidths are fitted based on a Gaussian distribution. The recorded and subsequently simulated spectra are shown below and were normalized in each case (Figure IV.8). There was significantly less radical signal for the Lu^{3+} species, as it can be seen from the poor signal-to-noise ratio and the amount of spins per metal ion are given in Table IV.1 (the absolute spin and spin concentration values are also given in Table IV.2). The trend in the amount of spins per metal ion can be seen in Table IV.1 and in the bar chart shown in Figure IV.9. The large amount of radical formed for Ba^{2+} correlates surprisingly with the reactivity trend which could suggest that radicals are formed as part of the mechanism. However, this is difficult to be certain of as La^{3+} and Ca^{2+} have values on the same order of magnitude as one another despite a difference in their reactivity. It should be noted here that samples for CW EPR measurements were not flash frozen at certain time points, but rather prepared and measured and thus could reflect somewhat different time points in the reaction. The Eu^{3+} analogue with ligand **PQQ**$_{15\text{-}5}$, DBU and 4-methylbenzyl alcohol was also measured but did not produce any detectable EPR signal.

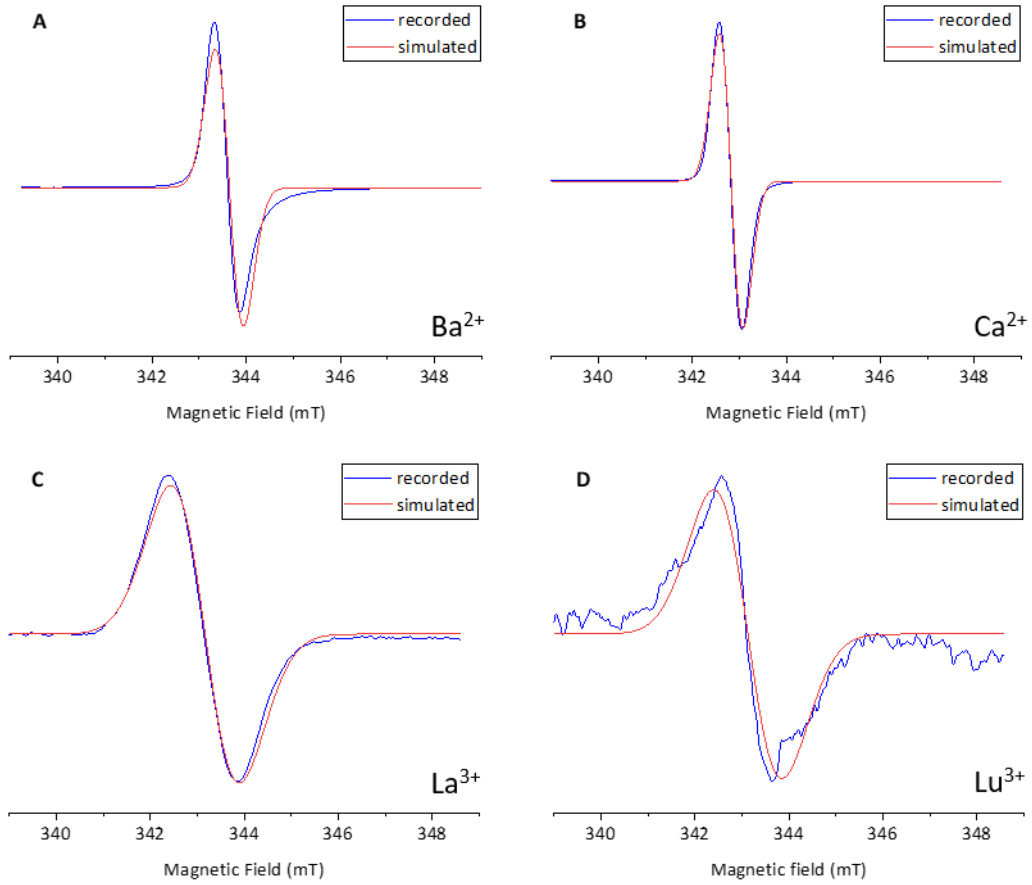

Figure IV.8: CW EPR spectrum at X-band (9.5 GHz) of ligand ***PQQ***$_{15\text{-}5}$ *(25 mM), 4-methylbenzyl alcohol (100 mM) and DBU (50 mM) in the presence of (A) barium(II) triflate (50 mM), (B) calcium(II) triflate (50 mM), (C) lanthanum(III) triflate (50 mM) or (D) lutetium(III) triflate (50 mM) at room temperature. The spectra were normalized in each case.*

*Table IV.2: : Extracted absolute spin and spin concentration values for different metal ligand **PQQ**$_{15\text{-}5}$ species with DBU and 4-methylbenzyl alcohol added.*

Metal ion	Absolute number of spins	Spin concentration (mm^{-3})
Ba^{2+}	4.86×10^{15}	3.64×10^{14}
Ca^{2+}	3.64×10^{14}	2.80×10^{13}
La^{3+}	8.68×10^{14}	5.53×10^{13}
Lu^{3+}	6.82×10^{13}	6.82×10^{12}

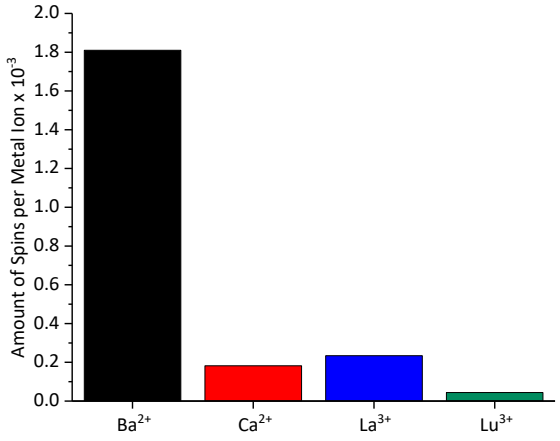

*Figure IV.9: Amount of spin per thousand metal ions for the CW EPR spectra at X-band (9.5 GHz) of ligand **PQQ**$_{15\text{-}5}$, 4-methylbenzyl alcohol and DBU in the presence of different metals ions.*

In order to test how varying the metal ion affected relaxation time, 2D CW EPR experiments were performed. Here the microwave power was incrementally increased by varying the microwave attenuation from 2.0 dB (in the case of Ba^{2+} 6.0 dB) to 25.0 dB and the peak-to-peak amplitude and peak-to-peak linewidth were recorded for Ba^{2+}, Ca^{2+}, La^{3+} and Lu^{3+} with ligand **PQQ**$_{15\text{-}5}$, DBU and 4-methylbenzyl alcohol in each case (Figure IV.10). A rest time of 3000 ms was used between each subsequent measurement, so as to avoid unwanted heating of the sample. By observing both the in peak-to-peak linewidth and peak-to-peak amplitude with microwave power, we could subsequently calculate T_1 and T_2 relaxation times for each of the radical systems (Table IV.1).[289,290] For calculating T_1 and T_2, we assumed in each case that the line-broadening was inhomogeneous. We could reasonably make this assumption as there was unresolvable hyperfine coupling of the radical to nitrogen and hydrogen atoms in the PQQ moiety of the molecule for all the spectra at this temperature.

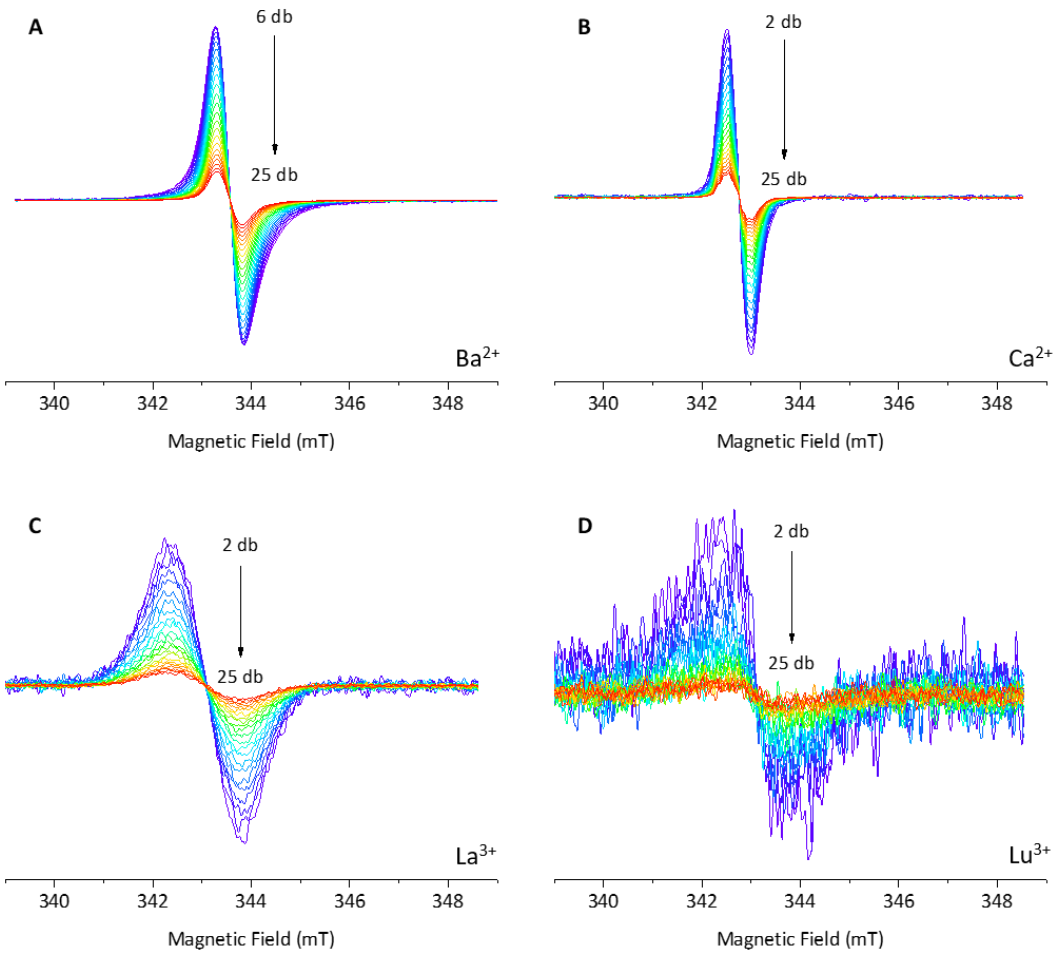

Figure IV.10: CW EPR spectrum at X-band (9.5 GHz) of ligand ***PQQ***$_{15\text{-}5}$ *(25 mM), 4-methylbenzyl alcohol (100 mM) and DBU (50 mM) in the presence of (A) barium(II) triflate (50 mM), (B) calcium(II) triflate (50 mM), (C) lanthanum(III) triflate (50 mM) or (D) lutetium(III) triflate (50 mM) at room temperature and at different microwave powers.*

As presented in Table IV.1. both T_1 and T_2 decrease significantly upon the insertion of a Ln^{3+} ion compared to Ca^{2+}, and the relative relaxation rates therefore increase. The effect is greater for Lu^{3+} compared to La^{3+}. This is also observed in the NMR as the proton resonances in the spectra from the Lu^{3+} analogue are broader and more greatly shifted than for La^{3+}. Ba^{2+} has a longer T_1 time but a shorter T_2 time when compared to Ca^{2+}. The data shows that inserting different metal ions significantly affects the peak-to-peak linewidth. There is also a small shift in the g value depending on whether Ca^{2+} or another metal is bound. Whilst Ba^{2+} has a similar g value to the Ln^{3+} ions, its T_1 and linewidth are more similar to that of Ca^{2+}. This potentially suggests that the Ca^{2+} and Ba^{2+} may be coordinated differently compared to the Ln^{3+} ions as suggested by the results of NMR experiments. However, more advanced experimental techniques would be needed to confirm this. For the Eu^{3+} ligand **PQQ**$_{15\text{-}5}$, base and alcohol complex no CW EPR spectrum is observed as Eu^{3+} may be causing the radical to relax too quickly to be measured effectively due to paramagnetic relaxation enhancement.[291–293] Another reason could be that there is additional redox chemistry occurring involving both Eu^{2+} and Eu^{3+} species.

EPR measurements under different reaction conditions

CW EPR spectra were measured at room temperature of La^{3+}, ligand **PQQ$_{15\text{-}5}$** and DBU without 4-methylbenzyl alcohol under oxygen, with 4-methylbenzyl alcohol with oxygen, nitrogen and under ambient conditions and with 4-methylbenzyl alcohol under ambient conditions with pyridine used as base rather than DBU. The amount of spin per million metal ions was calculated (Table IV.3 and Figure IV.11).

*Table IV.3: Extracted g values, linewidths, spin concentration, absolute number of spins and relative amount of spins per metal ion for La^{3+} ligand **PQQ$_{15\text{-}5}$** species.*

Species	*g* value	Linewidth peak-to-peak [MHz]	Spin concentration (mm^{-3})	Absolute number of spins	Relative amount of spins per metal ion
La^{3+} with DBU, nitrogen and alcohol	2.003	1.4	1.09×10^{15}	1.73×10^{14}	1.83×10^{-3}
La^{3+} with DBU and oxygen	2.003	1.5	7.3×10^{13}	8.5×10^{14}	4.79×10^{-3}
La^{3+} with DBU, oxygen and alcohol	2.003	1.6	1.34×10^{14}	1.68×10^{15}	8.88×10^{-3}
La^{3+} with DBU, alcohol under ambient conditions	2.003	1.4	5.53×10^{13}	8.68×10^{14}	3.67×10^{-3}
La^{3+} with pyridine, alcohol and ambient conditions	2.003	1.3	2.79×10^{13}	2.63×10^{14}	1.85×10^{-3}

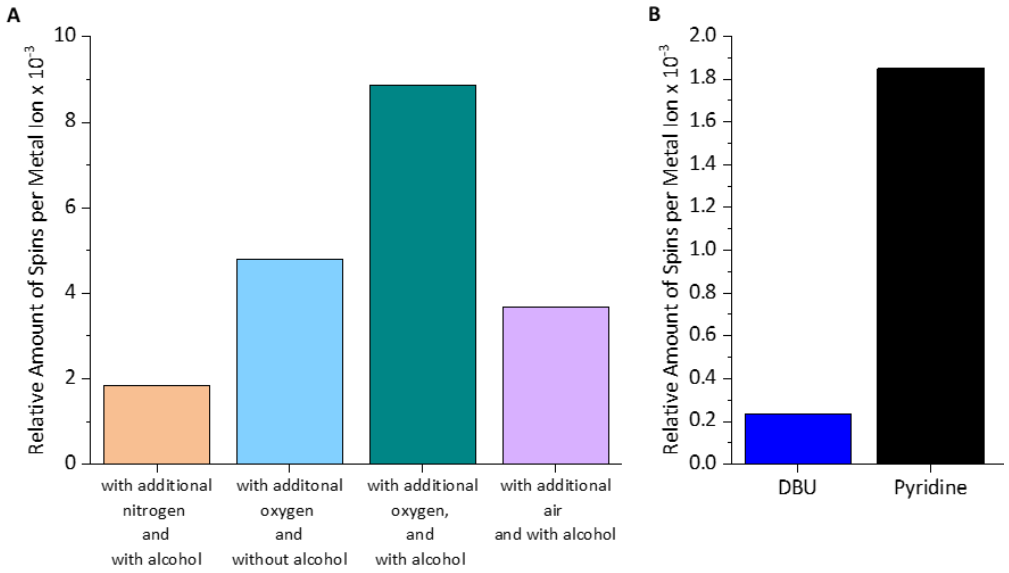

*Figure IV.11: Relative amount of spin per million metal ions for the CW EPR spectra at X-band (9.5 GHz) of (A) ligand **PQQ$_{15\text{-}5}$** and lanthanum(III) triflate under different reaction conditions and (B) ligand **PQQ$_{15\text{-}5}$**, lanthanum(III) triflate, 4-methylbenzyl alcohol and different bases.*

The g value in each case was 2.003 (approximately ± 0.0005). There is a slightly larger amount of radical present when alcohol is added compared to when no alcohol is added. This could suggest that there may be radicals formed as part of the reaction mechanism. However, the organic radical is still present even without alcohol, again showing that PQQ species tend to form radicals readily when exposed to various conditions. There is a greater amount of radical when oxygen is present compared to when it is absent (under nitrogen conditions). This could be due to reoxidation of the ligand by oxygen producing a larger amount of semiquinone radical. This highlights the importance to run control reactions both under inert atmosphere as well as in air or at least consider the impact of radical formation and oxygen on these types of reactions. However, it should be noted that the obtained numbers are only estimations, since these values cannot be calculated exactly due to a small amount of evaporation when gases are bubbled through as well as possible different time points at which the experiments were taken. Every effort was made to minimize these effects.

4. Kinetic Isotope Effect

One of the most essential tools for investigating catalytic mechanisms or providing deeper insights into the transition states in chemical and enzymatic reactions is to measure kinetic isotope effects (KIEs).[294–297] This method is often applied in biological, organic and physical chemistry,[298] and it can be detected by applying different techniques such as liquid scintillation counting, mass spectrometry, nuclear magnetic resonance spectroscopy and polarimetry.[295]

KIEs can be used to interpret which bonds are being broken, formed or rehybridized during the rate determining step of a reaction.[299] Since the KIEs are expressed as the change in the reaction rate when replacing an atom with a heavy isotope, the most common way to investigate isotope effects is by replacing a hydrogen atom with a deuterium in either the substrate or solvent.[294,298,299] Thereby, the KIE values can be calculated from the ratio between the rate constants with deuterated (k_D) and undeuterated (k_H) substrates or solvents according to equation 3.

$$\mathrm{KIE} = \frac{k_\mathrm{H}}{k_\mathrm{D}} \tag{3}$$

It can be distinguished between two types of KIE, primary and secondary, depending on the location of the isotopically labelled atom.[294,296,298,299] A primary KIE occurs when a bond is formed or cleaved to the isotopic atom during the reaction. A secondary KIE on the other hand, arises from isotopic substitution of an atom at position which is not directly involved in bond cleavage or formation.

Hence, the magnitude of the secondary KIEs is usually smaller than primary KIEs.[296] Furthermore, the KIE can also be classified as normal or inverse, whereby the normal describes reactions where the lighter isotope reacts faster than the heavier one ($k_H/k_D > 1$). The inverse KIE occurs when the heavier isotope reacts faster than the lighter one ($k_H/k_D < 1$). If the ratio between k_H and k_D equals 1, it can be concluded that there is no isotope effect and the bond with the isotopic substitution is not involved in the rate determining step of the reaction.[299]

In 2022 Luo *et al.* reported a KIE observed on O–H (KIE = 1.40) and C–H (KIE = 2.19) of benzylic alcohol when studying a catalytic system comprised of the *ortho*-quinone ligand ***o*-Q** and lanthanum(III) triflate.[279] Based on these observations, the authors proposed a proton-coupled hydride transfer instead of stepwise deprotonation and hydride transfer.

In order to gain some insights into the mechanism of the alcohol oxidation reaction discussed in this project, a series of stoichiometric reactions were carried out with benzyl alcohol and benzyl-α,α-d_2 alcohol (Scheme IV.4). The reason for choosing an alcohol with deuterated α position is that on the one hand C–H bonds do not generally undergo exchange in the absence of an external reagent or catalyst (in contrast to N–H and O–H bonds),[297] and on the other hand the hydrogen atoms at this position are being suggested to play a key mechanistic role during the alcohol oxidation reaction in MDH (either for the hydride transfer or for the base-catalyzed proton abstraction).[90]

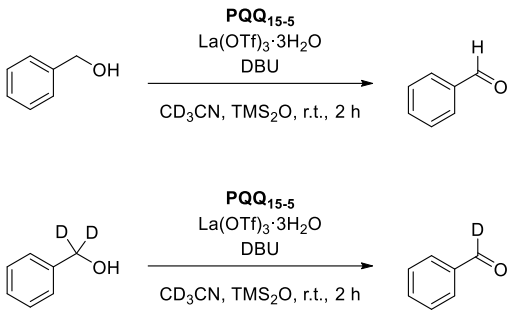

Scheme IV.4: Dehydrogenation reactions of benzyl alcohol (top) and benzyl-α,α-d_2 alcohol (bottom).

Several reactions with alcohols in various concentrations under identical reaction conditions were performed and monitored by ^{1}H NMR. By comparing the initial reaction rates a clear trend was observed - the deuterated alcohol reacted slower than the undeuterated counterpart and a KIE value of 2.61 was determined (Figure IV.12). Thus, an indication was given that a cleavage of a C–H α-hydrogen atom bond is involved in the rate limiting step of the alcohol oxidation reaction.

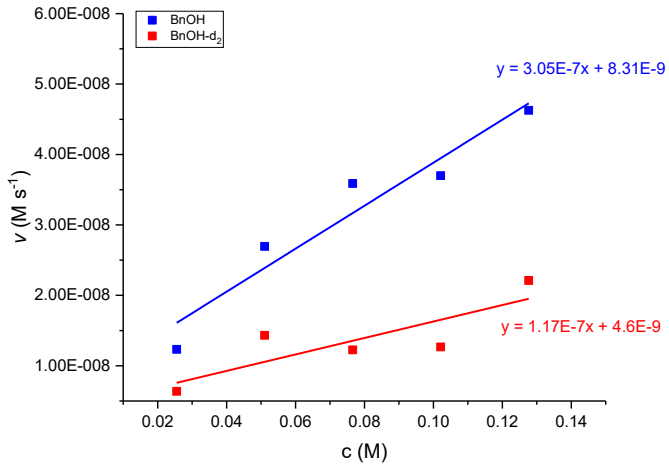

Figure IV.12: Initial rates versus substrate concentration for the reaction of ***PQQ***$_{15\text{-}5}$ *(6.4 mM), lanthanum(III) triflate (12.9 mM) and DBU (12.8 mM) with benzyl alcohol (blue) and benzyl-α,α-d*$_2$ *alcohol (red).*

In order to support or reject the proposed mechanistic pathways, however, a comparison between the experimental and theoretical KIE values should be performed.[300] Furthermore, future KIE analysis should also include experiments with various DBU concentrations, in order to investigate if the change in the base concentration will affect the KIE value obtained in the experiment described above.

5. Investigations with Various PQQ-based Ligands

In the course of this project, the oxidation of 4-methylbenzyl alcohol was investigated using different PQQ-based ligand systems (Scheme IV.5). The reaction progress was monitored *via* ^{1}H NMR and all experiments were performed with DBU as base, which was shown to accelerate the alcohol dehydrogenation.[134,143,144,163,166] Furthermore, hexamethyldisiloxane (TMS_2O) was used as an internal standard. The reaction mixtures were degassed prior to the addition of the base, to remove air oxygen of the system, which could possibly act as a terminal oxidant. All experiments were run parallel in the same day to assure comparable reaction conditions (e.g. same room temperature).

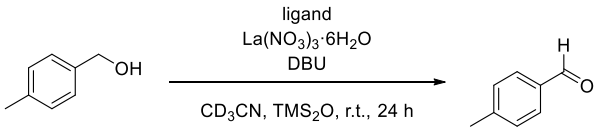

Scheme IV.5: Dehydrogenation reaction of 4-methylbenzyl alcohol to 4-methyl benzaldehyde. The reaction was performed with six different ligands - ***PQQ***$_{15\text{-}5}$*,* ***PQQ***$_{18\text{-}6}$*,* ***PQQ***$_{DEDP}$*,* ***PQQMe***$_2$*, and* ***PQQMe***$_3$*.*

First, a dehydrogenation reaction of 4-methylbenzyl alcohol was performed using **PQQ$_{15\text{-}5}$**, lanthanum(III) nitrate and DBU. The experiment resulted in the successful formation of 4-methyl benzaldehyde in 24% yield after 24 h (Figure IV.13). The yield is close to that observed in the studies discussed in chapter IV.3. for the same system, where a yield of 20% was achieved.[134] When the alcohol oxidation reaction was performed in the presence of **PQQ$_{18\text{-}6}$**, a considerable higher conversion to the respective aldehyde was observed when comparing it to that observed in the experiment with the smaller crown ether ligand. After 24 h, a yield of 50% was calculated for 4-methyl benzaldehyde (Figure IV.13). The results could possibly correlate to the observations made by the UV-Vis experiments, described in chapter III.3. For all dehydrogenation reactions, 2.0 equiv. of La^{3+} were used, however the titration experiment of **PQQ$_{15\text{-}5}$** with La^{3+} showed a saturation upon the addition of 10 to 20 equiv. of metal salt (Figure III.14). In contrast, the UV-Vis absorption spectra of **PQQ$_{18\text{-}6}$** with lanthanum(III) indicated a full complex formation after the addition of 2.0 equiv. of metal salt Figure III.5. Assuming that the La^{3+}-**PQQ$_{15\text{-}5}$** complex was only partly formed, the lower yield of converted alcohol in the ^{1}H NMR experiment could be explained.

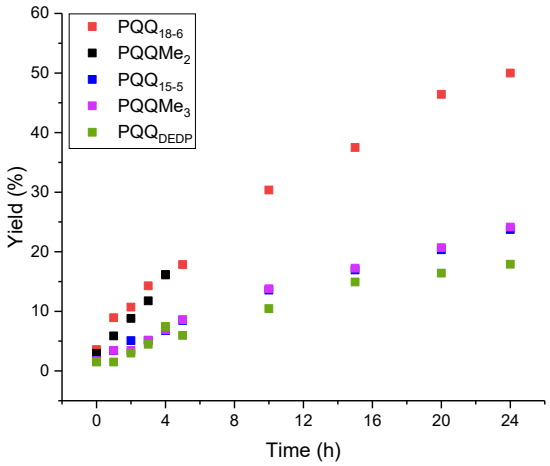

Figure IV.13: Calculated yields of 4-methyl benzaldehyde from the dehydrogenation reactions of 4-methylbenzyl alcohol (25 mM) by different ligands (6.3 mM), lanthanum(III) nitrate (12.5 mM) and DBU (12 mM).

In addition, the ability of the ligands **PQQ$_{DEDP}$** and **PQQMe$_3$** to facilitate the alcohol oxidation in the presence of lanthanum(III) and DBU was examined. Both experiments resulted in a successful aldehyde formation and yields of 18% and 24% respectively were calculated after 24 h (Figure IV.13). However, previous UV-Vis titration experiments showed that the ligands **PQQ$_{DEDP}$** and **PQQMe$_3$** similar to **PQQ$_{15\text{-}5}$** are not fully bound to a complex in the presence of only 2.0 equiv. La^{3+} and much higher metal concentrations are required to reach a saturation (Figure III.16 and Figure III.15). On the other hand, if 10 to 20 equiv. of metal salt are required for the full formation of the La^{3+}-**PQQ$_{15\text{-}5}$** complex and 100 to 150 equiv. for the La^{3+}-**PQQMe$_3$** complex, the achieved yields during the

dehydrogenation experiments are quite similar, suggesting that additional factors should also have an impact on the reaction progress apart from the complex quantity present in the solution.

The conversion of 4-methylbenzyl alcohol was then further studied using **PQQMe$_2$** as a ligand. Similar to **PQQ$_{18\text{-}6}$**, the absorption spectra of **PQQMe$_2$** showed a system saturation after the addition of 2.0 equiv. La^{3+} (Figure III.12). In addition, the dehydrogenation of the alcohol showed a very similar reaction progress as well and a yield of 16% was reached after 4 h from the reaction start. However, during the experiment a precipitation had occurred, which led to signal broadening and made the further spectra analysis unfeasible.

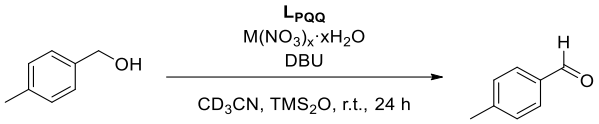

Scheme IV.6: Dehydrogenation reaction of 4-methylbenzyl alcohol to 4-methyl benzaldehyde by **L**$_{PQQ}$ *and DBU in the presence of either* $Ca(NO_3)_2{\cdot}4H_2O$ *or* $La(NO_3)_3{\cdot}6H_2O$.

In the previous chapter II.3. the different pathways for the synthesis of ligand **L**$_{PQQ}$ were discussed. However, the purification of the crude product showed to be challenging and the ^{1}H NMR spectra of the product showed a plenty of additional signals. Considering the ability of PQQ to form addition products with various nucleophiles like water and methanol, it could be assumed that the formation of this species could be the reason for the presence of additional resonance signals in the ^{1}H NMR spectrum of **L**$_{PQQ}$. Moreover, an assumption was made that ligand **L**$_{QQ}$ undergoes self-association processes in solution. Nonetheless, the ability of **L**$_{PQQ}$ to mimic the function of an alcohol dehydrogenase was studied using lanthanum(III) as well as calcium(II) nitrate (Scheme IV.6). Compared to the previous ligands discussed in this study, **L**$_{PQQ}$ showed to be only low soluble in acetonitrile. Even the addition of a metal salt could not enable the formation of a clear solution. However, an alcohol dehydrogenation attempt was started with the intention to investigate qualitatively, if the alcohol conversion would be possible under the given conditions. The recorded spectra showed that even after 1 h after the start of the reaction, 4-methyl benzaldehyde was formed thus confirming that both La^{3+} as well as Ca^{2+} could be used in combination with **L**$_{PQQ}$ as functional models. Nonetheless, the reaction conditions should be optimized in order to enable a quantitative analysis of the product formation. The first step in this direction should be the evaluation of a suitable solvent for the oxidation reaction.

6. Method Development for Monitoring of Alcohol Oxidation

By comparing the results of different reports in the field of modeling the active site chemistry of alcohol dehydrogenases, it becomes apparent that there are more than a few different factors, that impact the processes taking place during enzyme activation and alcohol oxidation.[134,136,144,163,279] Ligand design, charge and size of the metal ions, Lewis acidity as well as counterions are some of those, which have already shown to have an effect on the dehydrogenation reaction outcome in different biomimetic systems. Hence, it is of great importance to further investigate and model the active site environment in the biological counterpart by means of biomimetic studies.[301]

The main goals of the current project are on the one hand, to develop a general standard analytical method for monitoring, examination and comparison of dehydrogenation reactions under different reaction conditions and on the other hand, to find a model system which models as precisely as possible the characteristics of the respective enzyme and thus study more in detail the oxidation mechanism. The search for an accurate model system will include a screening of PQQ based ligands with different geometries and functionalities, some of which were already discussed in chapter II. The screening will aim to investigate the system in connection with alcohol oxidation rates and/or achieved product yields after a certain reaction time. In addition, a metal salt screening of the entire lanthanide series (excluding Pm) should be performed, in order to compare the model system performance with the XoxF-MDH preference for early lanthanides.[118]

In their previous studies on calcium-dependent alcohol dehydrogenases, Itoh and Fukuzumi focused on evaluation of different model systems using UV-Vis spectroscopy.[142–144,163,164] However, the highly fluctuating UV-Vis signatures of the PQQ moieties (due to possible formation of adducts with various nucleophiles) make UV-Vis titrations and data evaluation difficult.[134,136] Recently, we have reported the results of a comprehensive study on a PQQ aza-crown-based model system, whereby ^{1}H NMR was used for monitoring of the alcohol oxidation progress.[134] By applying this spectroscopic technique, we were able to calculate product yields at different reaction times and to compare the impact of different conditions on the reaction outcome. Nevertheless, this method could also set some certain limits. First of all, the progress of reactions with short reaction times (under 3 min) could not be monitored due to the instrument acquisition process. Secondly, reactions taking place in the NMR tubes could not be stirred, which could possibly affect the reaction rates. Thirdly, for NMR experiments deuterated solvents are required which are considerably more expensive than the undeuterated ones. And fourthly, the fact that all spectra should be measured by the NMR facility results in a low number of experiments which can be performed at a time. Therefore, the focus was set on developing a new analytical procedure, which would allow a fast screening of different reaction

conditions and would give us the possibility to design new experiments. GC-MS was employed as the analytical method of choice.

6.1. Experimental Considerations

With a suitable GC-MS substrate/product separation method in hand (see chapter V.3.9.), considerations about the experimental procedure for performing and monitoring of the dehydrogenation reactions were made. For every reaction batch, a ligand stock solution was given in a GC vial and was diluted with acetonitrile. The metal salt was added to the solution and the vial was closed with a cap with a septum. Subsequently the reaction mixture was degassed by using an ultrasonic bath and nitrogen. Finally, degassed alcohol and base solutions were added and the vial was shaken to ensure complete mixing. Subsequently, the vials were given in a thermoshaker and were shaken for a certain reaction time at 28 °C. First it was decided to directly measure the reaction mixture samples without any further purification steps. Thus, it was intended to minimize the errors which could possibly occur from some additional purification steps.

Multiple screenings of the dehydrogenation reaction of 4-methylbenzyl alcohol were performed under variation of the reactant ratios (ligand, metal salt and base). However, an unexpected observation was made as a reaction with **PQQ$_{18\text{-}6}$**, 45 equiv. lutetium(III) nitrate and DBU was performed. The reaction resulted in a conversion of 70% after only 1 h. Initially it was assumed that the increased Lewis acidity of the reaction mixture through the addition of higher amounts of Lu^{3+} could be the reason for the accelerated alcohol conversion and not the nature of the PQQ-Ln complex present in the solution. Nonetheless, previous reports give evidences that reactions performed with Lu^{3+} proceed generally slower (14% after 24 h for the system comprising of **PQQ$_{15\text{-}5}$**, lutetium(III) triflate and DBU in CD_3CN).[134] However, it should be noted that during the GC-MS measurement an injector temperature of 280 °C was used, which in combination with the increased Lewis acidity of the solution and the biomimetic complex present in the mixture could also have an impact on the alcohol oxidation. In order to examine this conjecture, a control reaction was performed under a ligand exclusion and in the presence of lanthanum(III) nitrate. As discussed in our recent publication,[134] both PQQ-ligand and Lewis acid are absolutely required for alcohol oxidation at room temperature. However, the control reaction monitored by the GC-MS resulted in alcohol conversion to the respective aldehyde and gave a yield of 21% after 1 h. This observation was in contradiction with the previous results obtained by NMR. Considering that the previous experiments were performed using lanthanum(III) triflate and the reaction performed on the GC-MS was in the presence of lanthanum(III) nitrate, a second control measurement was conducted.

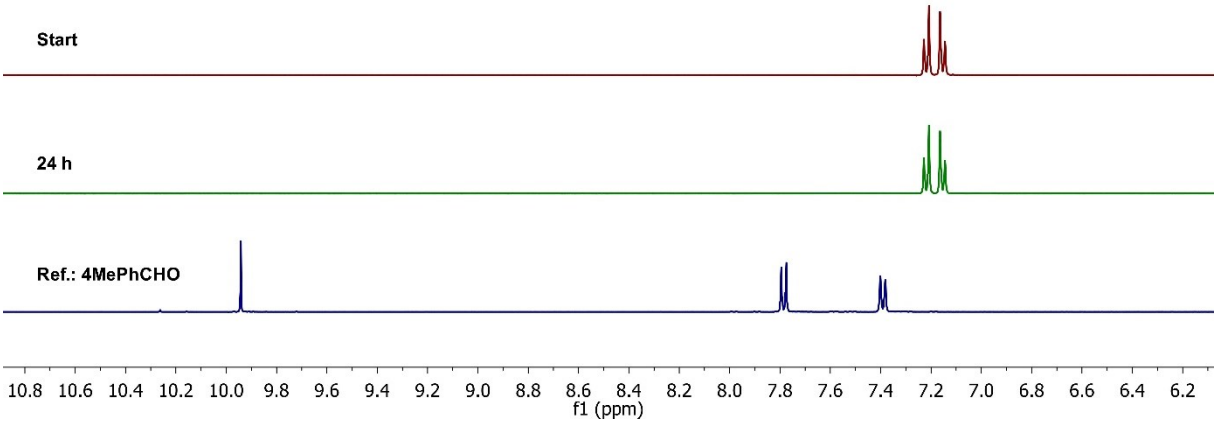

Figure IV.14: ^{1}H NMR spectra of the attempted dehydrogenation reaction of 4-methylbenzyl alcohol (140 mM) by lanthanum(III) nitrate (31 mM) and DBU (5.9 mM) in CD_3CN and a reference spectrum of 4-methyl benzaldehyde.

As shown in Figure IV.14, a dehydrogenation reaction of 4-methylbenzyl alcohol in the presence of lanthanum(III) nitrate and DBU was attempted and monitored by ^{1}H NMR, however, even after 24 h there were no traces of substrate turnover. In both reactions, the one monitored by the GC-MS and the one analyzed by ^{1}H NMR, the same alcohol to metal salt ratios were used and both were conducted in acetonitrile as a solvent (CH_3CN and CD_3CN respectively). The concentrations of both solutions were different, since they had to be adapted to the respective analytical method. Consequently, two assumptions could be made based on the obtained results. The first one suggested that the high injector temperature of the GC-MS (280 °C) could possibly have a promoting effect on the alcohol conversion in combination with a Lewis acid even in the absence of a PQQ-derived ligand. On the other hand, another explanation could be a contamination of the instrument through some PQQ residuals, since all samples were directly injected into the system without initial work-up. These residuals, in combination with the metal salt, could then possibly accelerate the alcohol oxidation. However, the yield of 21% obtained in the first control reaction can be considered as rather high based on previous observations, thus the assumption about the contamination impact on the reaction outcome does not seem plausible. Moreover, an experiment conducted after cleaning the instrument has confirmed that solely a lanthanide(III) nitrate salt is sufficient to promote alcohol conversion during a GC-MS measurement. A further control experiment was performed whereby a solution containing lanthanum(III) nitrate and 4-methylbenzyl alcohol was prepared in acetonitrile. Subsequently, the solution was filtered through a pad of silica and was then subjected to GC-MS measurement. As anticipated no alcohol conversion was observed (Figure VI.36), thus the previous assumptions were confirmed.

In order to avoid contamination of the GC column by the metal salt used for the alcohol oxidation and to interrupt the reaction progress after a defined reaction time, the reaction mixture aliquots collected at certain times should first be worked-up properly. Since all of the reaction components are present in

solution, the metal complexes and residual metal salts cannot be simply removed by filtering through a syringe filter. Thus, a filtration of the reaction mixture through a pad of an absorbent material was considered. TLC showed that with acetonitrile as an eluent system the product/substrate compounds could be easily eluted from the stationary phase (Figure VI.37). The observation was confirmed after filtering a reference mixture of benzyl alcohol and the respective aldehyde through a pad of silica, followed by two additional washing steps with acetonitrile (Figure VI.38, left). An GC-MS analysis of the collected fractions showed that the alcohol and the aldehyde were present only in the first fraction, thus they were eluted only by a single washing step. In addition, C18 silica was also examined as a possible absorbent, however, the product/substrate elution step required very high solvent volumes, which led to the strong dilution of the collected fractions. Removal of the solvent *in vacuo* and a subsequent GC-MS analysis have shown, that the benzaldehyde was not present but evaporated from the system as a result of the rotary evaporation. Thus, the C18 medium was not further examined and the experiments were carried out using normal phase silica. Subsequently, a test reaction was carried out in order to test the method, however, the results showed a lot of fluctuations in the calculated product yields. It should be noted that a small fraction of the solvent could be held back during the washing step of the work-up procedure, which could result in fluctuations in the product concentrations within an experimental series. Furthermore, the sample filtration through the silica proceeds by use of vacuum pump which can also possibly affect the end concentration of the volatile product and solvent in the collected sample.

Therefore, it was examined whether some amount of substrate would be held back on the stationary phase, if an aliquot gets filtered through silica and gets directly injected in the GC-MS without additional washing steps of the stationary phase. Thus, the concentration of the solution would remain constant and the yield of the product would be determined using a conventional calibration curve. In addition, considering the volatile character of the aldehydes, an alternative work-up procedure was tested which involves filtration through a pad of silica filled in a glass pipette using only a pipette bulb to produce pressure (Figure VI.38, right). Hence, solutions of 4-methyl benzaldehyde in different concentrations were prepared and one half of every solution was directly injected in the GC-MS and the other half was filtered through silica prior to injection. As shown in Figure IV.15, in the first four samples the measured aldehyde peak areas from the filtered solutions were almost identical to the peak areas determined for the unfiltered solutions. With increasing concentrations, however, an increasing deviation between the obtained peak area values for every concentration pair was observed. Nonetheless, the measured values were still very close and the deviation can be considered as rather within the error range. As a conclusion, this aliquot work-up procedure is preferred, since preliminary experiments have shown, that the work-up method

involving the use of an internal standard and multiple washing steps of the stationary phase results in greater concentration changes and thus errors in the final values.

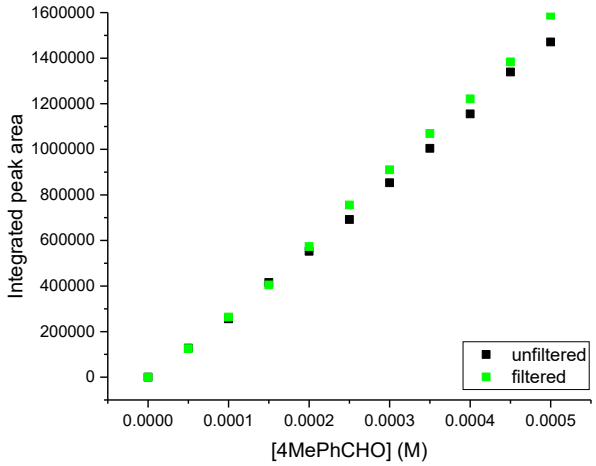

Figure IV.15: Comparison of the measured integrated peak areas of 4-methyl benzaldehyde from different concentrated solutions which were either directly subjected to GC-MS measurement or were first filtered through silica prior to measurement.

With a suitable work-up procedure in hand, again multiple screenings of the dehydrogenation reaction of 4-methylbenzyl alcohol were performed under variation of the reaction conditions. However, once again an unexpected obstacle was encountered and a troubleshooting was required. As the reaction progress was examined under variation of the substrate concentration, the calculated yields (with respect to the ligand) for the reactions performed with higher substrate concentrations (5.0 to 50 equiv.) were over 100% after 24 h (Figure IV.16, left). Since the reactions were performed stoichiometrically (i.e. without additional electron acceptor for the reoxidation of the PQQ moiety), no catalytic turnover was expected. An explanation for the saturation-like progress observed in the last two batches is the high concentration of the aldehyde which goes over the instrument detection limit (see chapter V.3.5.). In order to examine if the yields of over 100% obtained in the GC-MS experiments were caused by the nature of the analytical method or by the reaction conditions, a control reaction was performed and monitored by ^{1}H NMR. Thereby, 22 equiv. of substrate were added to reaction mixture containing **PQQ**$_{18\text{-}6}$, La^{3+} and DBU in CD_3CN. The reaction was performed at room temperature and was monitored over 24 h. As shown in Figure IV.16 on the right, the highest product yield obtained after 24 h was 80% and even a saturation behavior could be observed.

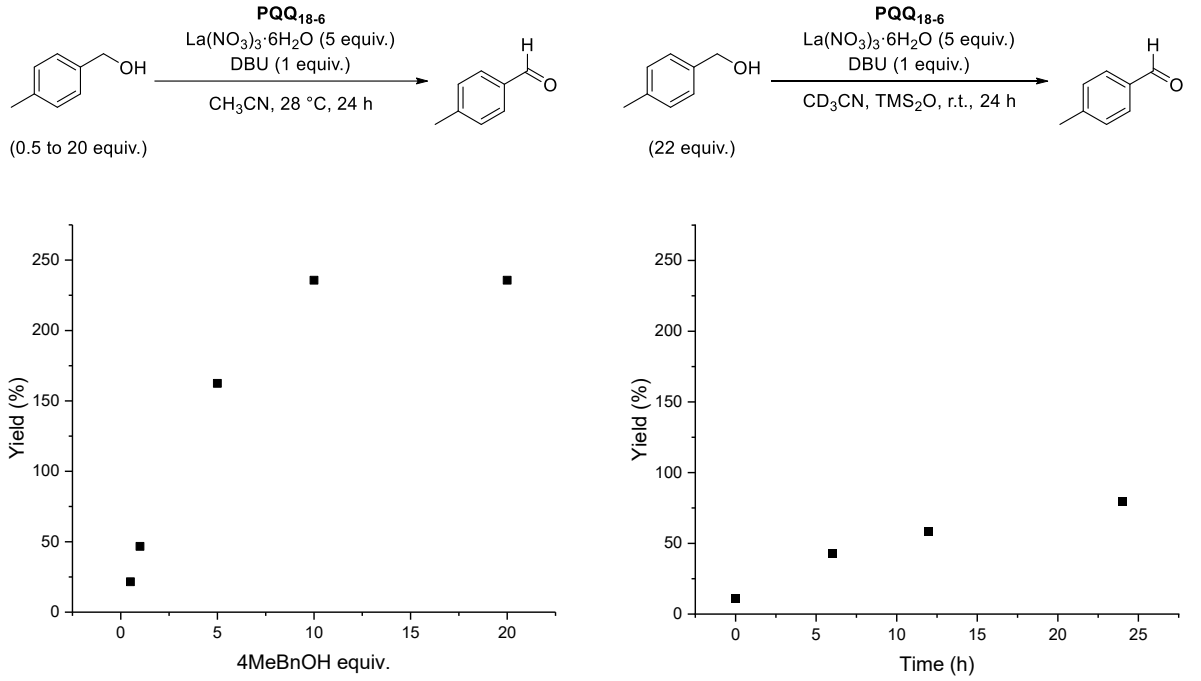

Figure IV.16: Calculated yields of 4-methyl benzaldehyde obtained after 24 h from the dehydrogenation reactions of 4-methylbenzyl alcohol in various concentrations (0.25–10 mM) in the presence of ***PQQ****18-6 (0.5 mM), lanthanum(III) nitrate (2.5 mM) and DBU (0.5 mM) in CH3CN, monitored by GC-MS (left). Calculated yields of 4-methylbenzaldehyde from the dehydrogenation reaction of 4-methylbenzyl alcohol (140 mM) in the presence of* ***PQQ****18-6 (6.3 mM), lanthanum(III) nitrate (31 mM) and DBU (5.9 mM) in CD3CN, monitored by 1H NMR (right).*

Based on these results, two assumptions could be made. The first one regards the different reaction conditions used for the GC-MS experiment. In comparison to the conditions applied for the ^{1}H NMR experiment, the GC-MS reaction solutions were prepared with undeuterated solvent, in much lower concentration and were shaken for 24 h. On the other hand, if solely the reaction conditions were the reason for the unexpected catalytic turnover, the question about the reaction mechanism would still remain open. The conjecture regarding the stoichiometric reaction is that the PQQ moiety gets reduced concurrent to the substrate oxidation and if the quinone form is completely converted to a quinol, the substrate oxidation would be prevented. Hence, the second assumption in regards to the obtained results is also the most plausible one. A preparative mistake could be considered if one assumes that the air oxygen couldn't be removed from the reaction vessel by the degassing procedure applied at the beginning of the experiment. Thereby oxygen could have acted as an oxidant for the PQQ moiety, which would have resulted in catalytic turnover. In order to identify the exact reason for the enhanced conversion of the substrate, a series of control experiments were conducted. Thereby, multiple reaction parameters were varied (Table IV.4).

Table IV.4: Investigated reaction conditions for the dehydrogenation reaction of 4-methylbenzyl alcohol (2.5 mM) in the presence of ***PQQ***$_{18\text{-}6}$ *(0.5 mM), a lanthanum(III) salt (2.5 mM) and DBU (0.5 mM) in either CH_3CN or CD_3CN. The experiments were monitored by GC-MS.*

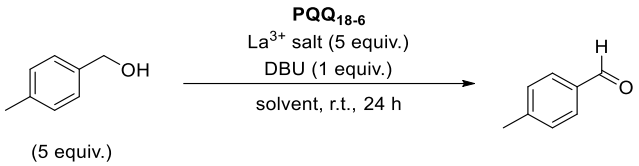

Entry	Reaction conditions					Yield (%)
	Preparation	Degassed	Shaker	Solvent	La^{3+} salt	
1	On air	✓	✓	CH_3CN	NO_3^-	263
2	On air	✓	-	CH_3CN	NO_3^-	227
3	On air	-	✓	CH_3CN	NO_3^-	284
4	On air	✓	✓	CH_3CN	OTf^-	125
5	On air	✓	✓	CD_3CN	NO_3^-	227
6	Glovebox	-	-	CH_3CN	NO_3^-	64
7	Glovebox	-	✓	CH_3CN	NO_3^-	65

As shown in Table IV.4, across all reactions (entries 1 to 5), which were initially prepared in ambient conditions and then subjected to degassing under nitrogen, a substrate conversion exceeding 100% was observed. The experiments prepared in the glovebox (entries 6 and 7), however, gave an aldehyde yield of only 65%. Therefore, based on the obtained results, it could be concluded that in fact residual traces of oxygen persisting in the reaction mixture even after the degassing procedure are responsible for the observed catalytic turnover. Consequently, for a more precise examination of the stochiometric alcohol dehydrogenation reaction, it is prerequisite to prepare the reaction mixture under strict oxygen exclusion in the glovebox.

6.2. Preliminary Reaction Screenings

With a convenient experimental method in hand, the ability of biomimetic complexes to facilitate the oxidation reaction of alcohols to aldehydes under variation of the reaction conditions was examined using GC-MS. First, the formation of 4-methyl benzaldehyde depending on the substrate concentration added in the mixture was examined, whereby the concentrations of the ligand, the metal salt and the base were kept constant and the substrate concentration was varied. Thereby, five different mixtures were subjected to GC-MS measurements 1 h after the reaction start. As shown in Figure IV.17, the obtained aldehyde yields from the first three samples were proportional to the initial

amount of added alcohol. Later, a saturation behavior was observed. Thus, it was shown that the oxidation reaction could not only be affected by changes in the oxidizing agent but it also exhibits a substrate concentration dependence.

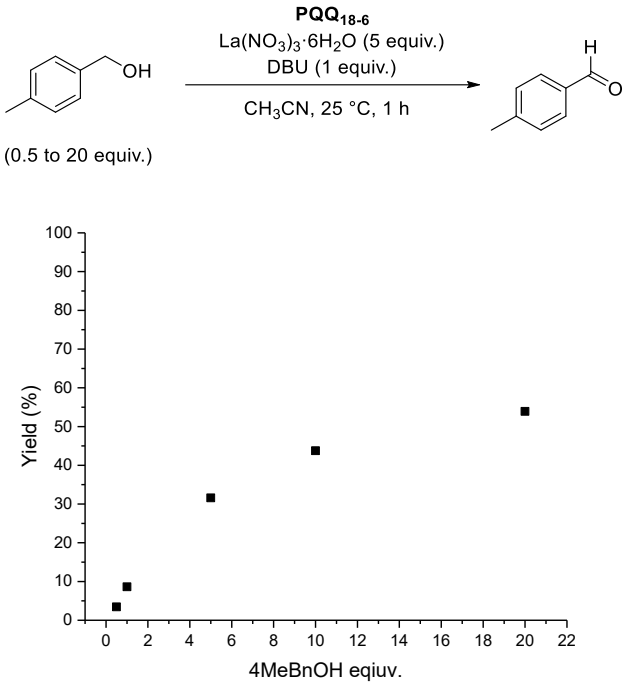

Figure IV.17: Calculated yields of 4-methyl benzaldehyde obtained after 1 h from the dehydrogenation reactions of 4-methylbenzyl alcohol in various concentrations (0.25–10 mM) in the presence of ***PQQ***$_{18\text{-}6}$ *(0.5 mM), lanthanum(III) nitrate (2.5 mM) and DBU (0.5 mM) in* CH_3CN*. The experiments were monitored by GC-MS.*

In addition, dehydrogenation reactions of 4-methylbenzyl alcohol were conducted using either **PQQ**$_{18\text{-}6}$ or **PQQMe**$_2$, lanthanum(III) nitrate in different concentrations and DBU. Reaction aliquots were analyzed after 24 h. As shown in Figure IV.18, after 24 h the reactions performed with **PQQ**$_{18\text{-}6}$ and either 0.5 or 1.0 equiv. La^{3+} resulted in alcohol conversions of 15% and 48%, respectively. An increase of the metal salt concentration led to higher product formation, as confirmed by the results obtained from the experiments with 5.0, 10 and 15 equiv. La^{3+} where after 24 h yields of over 70% were determined. On the one hand, these observations could correlate to the required amount of metal to form a complex with the ligand, on the other hand they could be caused by the increased Lewis acidity of the system. With metal salt concentrations of over 5.0 equiv. present in the reaction mixture, a saturation of the system could be observed. When comparing these results with those obtained with ligand **PQQMe**$_2$ in the system, a similar trend was tracked, namely a saturation dependence with respect to the metal salt concentration. Nevertheless, a markable difference in the obtained yields for both ligands was observed, with almost threefold higher yields for ligand **PQQ**$_{18\text{-}6}$. A short discussion of this observation follows later in this section.

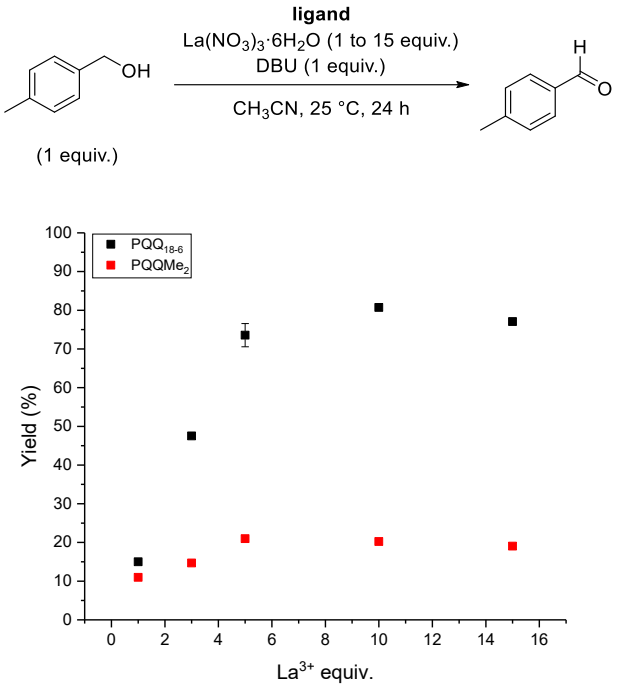

Figure IV.18: Calculated yields of 4-methyl benzaldehyde obtained after 24 h from the dehydrogenation reactions of 4-methylbenzyl alcohol (0.5 mM) in the presence of either ***PQQ*** *18-6 (0.5 mM) or* ***PQQMe*** *2 (0.5 mM), lanthanum(III) nitrate in various concentrations (0.5–7.5 mM) and DBU (0.5 mM) in* CH_3CN*. The experiments were monitored by GC-MS.*

Further, a screening with the entire lanthanide series was conducted with ligand **PQQ**18-6.

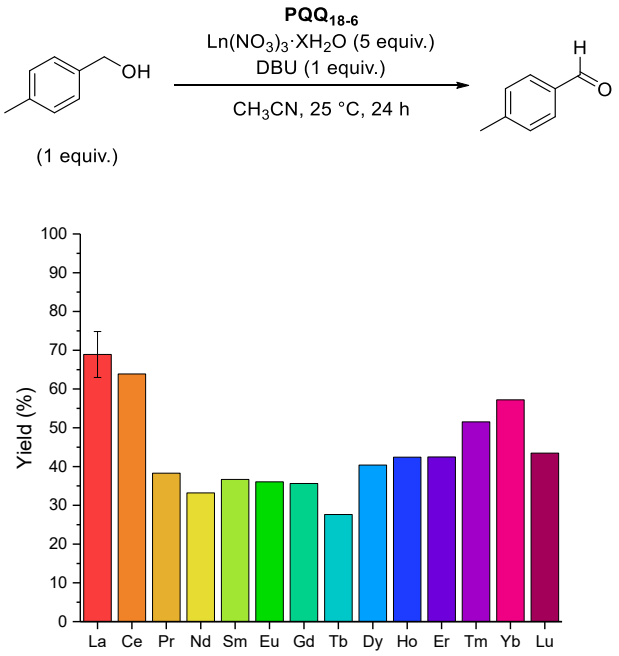

Figure IV.19: Calculated yields of 4-methyl benzaldehyde obtained after 24 h from the dehydrogenation reactions of 4-methylbenzyl alcohol (0.5 mM) in the presence of ***PQQ*** *18-6 (0.5 mM), lanthanide(III) nitrate (2.5 mM; Ln = La to Lu; X = 5, 6) and DBU (0.5 mM) in* CH_3CN*. The experiments were monitored by GC-MS.*

As shown in Figure IV.19, throughout the lanthanide series the ability of the model complexes to accelerate the alcohol oxidation decreases, reaches a bottom, and then slightly increases again. This trend shows a similar progression to this observed in the binding constants for the **PQQ$_{18\text{-}6}$**-Ln complexes in acetonitrile (see chapter III.3.), however, it could also point to a geometry change in the model complexes caused by the lanthanide contraction and thereby changes in the reaction pathway. The specific activity in the enzymatic counterpart decreases gradually from Nd^{3+} to Lu^{3+},[118] thus the model system shows a deviation from this behavior, probably caused by the differences in the coordination environment. The results further underline the significance of fine-tuning the ligand environment in order to construct an accurate biomimetic system.

Prompted by the observed differences in the activity of the **PQQ$_{18\text{-}6}$** based model system compared to MDH, we decided to examine the alcohol dehydrogenation reaction in the presence of different ligands and either La, Gd or Lu. As shown in Figure IV.20, the activities of the **PQQMe$_2$**-Ln complexes follow the same pattern within the lanthanide series as those of the respective **PQQ$_{18\text{-}6}$**-Ln complexes. However, the calculated product yields were much lower with the smaller ligand compared to those obtained with the aza-crown-based one, as already observed in a previous experiment (Figure IV.18). This observation further highlights the importance of the aza-crown moiety for the activity of the biomimetic system and thus for the alcohol oxidation process, by adjusting the metal coordination cavity to the desired PQQ position. Furthermore, if we assume that the alcohol oxidation proceeds through the hemiketal mechanism, those findings would also be supportive of the proposed pushing effect of the aza-crown functionality on the added alcohol moiety to the C-4 quinone carbonyl oxygen of PQQ,[163] thus facilitating the α-proton abstraction (Figure IV.2).

Interestingly, almost identical yields were observed by comparing the results from the oxidation reactions conducted in the presence of **PQQMe$_3$** and the novel PQQ-derivative **P$_{ME}$QQ$_{MEM}$**. The derivative differs from **PQQMe$_3$** only by the substitution of the methyl ester functionality at C-9 through a methyl group, albeit still retaining the ONO pocket for metal coordination, thus we assume that the lanthanide ions coordinate both ligands in a similar fashion. Therefore, in conjunction with the gathered data from the dehydrogenation reactions, one may deduce that alteration in the π-system of the pyridine moiety in PQQ exerts only a negligible influence on the ability of the model complex to oxidize alcohols. Upon analyzing the results obtained for **PQQMe$_3$** and **P$_{ME}$QQ$_{MEM}$**, a further interesting observation was made: the respective Lu-complexes demonstrate an enhanced ability for alcohol oxidation when compared to the La-complexes. This pattern diverges from the trends observed in the **PQQ$_{18\text{-}6}$** and **PQQMe$_2$**-based model systems and deviates from the behavior of the Ln-utilizing bacteria, which show a preference for early lanthanides. It could be assumed that this observation results from changes in the complex stabilities stemming from the use of different ligands, thus influencing the ligand exchange rates for the respective complexes. Lumpe *et al.* made a

hypothesis regarding the alcohol oxidation in MDH,[118] which could also be applied in this scenario. After the formation of a product, the increased stability of the resulting Ln-product complex would render product release and ligand exchange less favorable. Therefore, the results confirm once again that the model complex properties have a huge impact on the alcohol dehydrogenation. Factors such as Lewis acidity of the metal ion, coordination number preferences and stability constants should be considered when selecting complex systems for biomimetic applications.

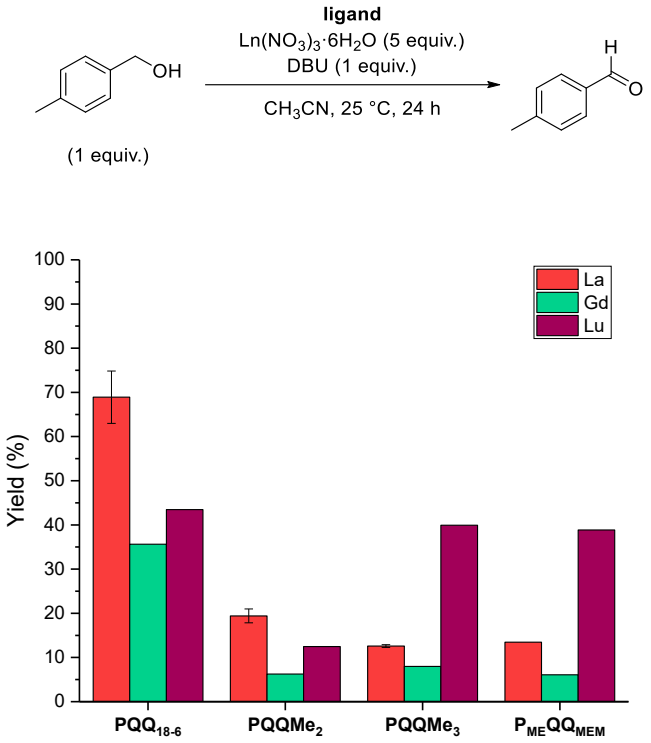

Figure IV.20: Comparison of the calculated yields of 4-methyl benzaldehyde obtained after 24 h from the dehydrogenation reactions of 4-methylbenzyl alcohol (0.5 mM) in the presence of different PQQ-based ligands (0.5 mM), lanthanide(III) nitrate (2.5 mM; Ln = La, Gd, Lu) and DBU (0.5 mM) in CH_3CN. The experiments were monitored by GC-MS.

7. Conclusion

In the course of this project, several synthetic model systems for the active site of quinoprotein alcohol dehydrogenases were evaluated. For the first time, a comparison of biomimetics bearing lanthanides (La^{3+} and Lu^{3+}) and alkaline earth metal ions (Ca^{2+} and Ba^{2+}) was presented and discussed. When using the previously reported PQQMe2-1-aza-15-crown-5 (**$PQQ_{15\text{-}5}$**) ligand platform, which does not account for the negative charges present on MxaF- or XoxF-MDH, the alkaline earth model complexes, in fact, present higher activity and yields in the alcohol dehydrogenation reaction. This highlights the importance of fine-tuning ligand environments in biomimetics. Furthermore, it was observed that the

larger ions were more active than the smaller counterparts (Ba^{2+} > Ca^{2+} and La^{3+} > Lu^{3+}) and this behavior mimics the findings in natural systems, where Ba-MDH had been shown to have a significantly lower activation energy barrier and the early lanthanides were shown to be more effective in turning over substrate in Ln-MDH.[118,302] It was further shown that both counterions and base have some impact on the substrate conversion outcome which is also in line with the results from the CID measurements where it was shown that nitrate counterions are, as expected, more tightly bound than the triflate ions. In addition, a PQQ-based radical was observed under substrate turnover conditions and this warrants further investigation, possibly with pulsed EPR methods and comparison to the natural systems, where a semiquinone radical has been denoted as a stable intermediate.[303]

In addition, a KIE was observed for the oxidation of benzyl alcohol in the presence of **PQQ$_{15\text{-}5}$**, La^{3+} and DBU and based on that an assumption was made that the α-hydrogen atoms are involved in the rate limiting step of the alcohol oxidation reaction.

Furthermore, the alcohol dehydrogenation reaction was examined with different PQQ-based ligands together with La^{3+}. The reactions were monitored *via* ^{1}H NMR and the highest yield was observed for the La^{3+}-**PQQ$_{18\text{-}6}$** system. In addition, NMR experiments were conducted with ligand **L$_{PQQ}$** and it was shown that the ligand is also able to promote the alcohol oxidation reaction of 4-methylbenzyl alcohol in the presence of La^{3+} as well as Ca^{2+}. Unfortunately, the low solubility of the ligand in acetonitrile did not allowed a quantitative monitoring of the alcohol conversion, thus the system could not be yet compared to the rest of the investigated ligands.

Finally, a new method for monitoring of alcohol dehydrogenation reactions was evaluated using GC-MS. Based on some preliminary results, the importance of the separation of the analyte mixture (i.e. substrate and product) from the metal salt containing biomimetic system prior to measurement was demonstrated and a suitable aliquot work-up procedure was proposed. Further it was demonstrated that residual traces of oxygen in the reaction mixture can lead to reoxidation of the PQQ moiety and thus catalytic turnover. Therefore, a glovebox should be used for the investigation of stoichiometric-type reactions. In addition, the oxidation of 4-methylbenzyl alcohol was examined in the presence of different lanthanide nitrates and different PQQ-based ligands and the comparison of the obtained yields showed higher conversions in the reactions with the aza-crown-based ligand. This observation was supportive of the results obtained by ^{1}H NMR. Overall, the GC-MS-based method showed to be a promising alternative to the so far applied ^{1}H NMR and we are confident that in the future, it will give us the possibility to screen more reaction conditions in a shorter time and in a more material saving manner.

V. EXPERIMENTAL SECTION

1. General Considerations

All reactions were carried out with magnetic stirring and, if the reagents were air or moisture sensitive, under a nitrogen atmosphere using standard SCHLENK techniques. Syringes used to transfer anhydrous solvents or reagents were purged with nitrogen prior to use. Reactions were monitored using TLC, ^{1}H NMR or LC-MS. Purified products were dried under high vacuum on a SCHLENK line. Autoclave reactions were performed in a Parr 5500 Series reactor. All reagents were purchased either from commercial sources or the chemical supply of the Ludwig Maximilian University of Munich. Dichloromethane, *iso*-hexane, diethyl ether and chloroform were distilled *via* rotary evaporation prior to use. All other solvents and reagents were used without further purification unless otherwise stated.

Flash column chromatography was performed with the Interchim PuriFlash PF420. Self-Packed columns were used, with Silica gel 60 (40-63 μm) from Merck as stationary phase. As eluent, the solvent mixtures mentioned in the specific experiments were used.

Thin Layer Chromatography (TLC) was performed by using pre-coated aluminum sheets (Silica gel 60, F-254, Merck). The chromatograms were examined under UV light at 254 nm and 365 nm and/or by staining of the TLC plate with vanillin stain (15 g vanillin and 2.5 mL conc. H_2SO_4 in 250 mL ethanol) followed by heating with a heat gun.

2. Analytical Methods

Nuclear Magnetic Resonance (NMR)

^{1}H NMR and ^{13}C NMR spectra were recorded by Brigitte Breitenstein, Dr. Burkhard Krumm or Christine Neumann at the Chemistry Department of the Ludwig Maximilian University of Munich. Unless otherwise stated, measurements were performed at room temperature on Jeol ECP 270 (400 MHz), Jeol ECX 400 (400 MHz) and Bruker Avance III (400 MHz) operating at 400 MHz for proton nuclei and 100 MHz for carbon nuclei. ^{1}H-chemical shifts are reported as δ units in ppm relative to $CDCl_3$ (δ_H = 7.26), DMSO-d_6 (δ_H = 2.50), CD_3CN (δ_H = 1.94), C_6D_6 (δ_H = 7.16), CD_2Cl_2 (δ_H =

5.32), DMF-d_7 (δ_H = 8.03). ^{13}C-chemical shifts are given in δ units in ppm relative to $CDCl_3$ (δ_C = 77.16), DMSO-d_6 (δ_C = 39.52), CD_3CN (δ_C = 118.26), C_6D_6 (δ_C = 128.06), CD_2Cl_2 (δ_C = 53.84), DMF-d_7 (δ_C = 163.15). The following abbreviations were used to characterize signal multiplicities: s (singlet), d (doublet), t (triplet), q (quartet), m (multiplet), br (broad) or combinations thereof. Coupling constants are given in Hertz. The software used for data processing was MNova Version 12.0.1. Two-dimensional correlation spectroscopy (COSY), heterobinuclear multiple quantum correlation (HMQC) and heterobinuclear multiple bond connectivity (HMBC) experiments were used to assign each signal in the spectra.

Mass Spectrometry

Electrospray ionization mass spectrometry (ESI-MS) and electron ionization mass spectrometry (EI-MS) measurements for characterization of organic compounds were carried out by Dr. Werner Spahl, Sonja Kosak or Mariia Palchyk at the Chemistry Department of the Ludwig Maximilian University of Munich. ESI spectra were recorded with a Thermo Finnigan LTQ FT Ultra Fourier Transform Ion Cyclotron Resonance mass spectrometer with acetonitrile/water as the carrier solvent. EI spectra were recorded with a Thermo Q Exactive GC, a Thermo Finnigan MAT 95 or a Jeol MStation mass spectrometer.

Further, mass spectrometry and collision induced dissociation experiments were performed by Dr. Patrick Weis, Alexander Schäfer and Erik K. Schneider at KIT with a LTQ Orbitrap XL (Thermo Scientific) mass spectrometer with helium in the ion trap. The ions were generated with electrospray ionization in positive mode using acetonitrile as solvent. Typical spray conditions were: needle voltage 3 kV, capillary temperature 50 °C.

Ion Mobility Spectrometry and DFT Calculations

Gas phase ion mobility studies were performed by Dr. Patrick Weis, Alexander Schäfer and Erik K. Schneider at KIT on a timsTOF (Bruker) with nitrogen as buffer gas. The experimental collision CCS were compared with predictions based on DFT (density functional theory) combined with trajectory calculations. The DFT calculations were performed with the TURBOMOLE package[247] with the TPSS functional[253] and def2-SVP basis set.[257] Based on the DFT optimized structures theoretical CCS were calculated with the trajectory method as implemented in the IMOS 1.09 package[260,261] using Mulliken partial charges.

GC-MS

GC-MS measurements were performed on an Agilent® 7820 GC equipped with a 30 m x 0.25 mm HP5-MS column (Agilent® 19091S-433UI) coupled to an Agilent® 5977 EI mass spectrometer. The injector temperature was set to 280 °C and the temperature of the ion source to 230 °C.

HPLC

HPLC measurements were performed on an Agilent 1100 SL system (G1313A ALS, G1316A COLCOM, G1316A VWD, G1312A Bin Pump) with an analytical Macherey-Nagel® Nucleodur C18 Isis column (250 x 4.6 mm; 5 μm). Water and acetonitrile were used as eluent components with a flow rate of 0.7 mL/min. The elution was monitored by measuring the absorption at 210 nm.

Elemental Microanalyses

Elemental Microanalyses (C, H, N, S) were performed with an Elementar vario EL by Dr. Bernhard Kempf, Susanne Ebert or Robert Eicher at the Chemistry Department of the Ludwig Maximilian University of Munich.

Melting Point

Melting points were measured on a Büchi M-560 apparatus in open glass capillaries with a temperature gradient of 10 °C/min.

UV-Vis Spectroscopy

UV-Vis Spectroscopy measurements were either conducted with an Agilent Cary 60 UV-Vis with Peltier Element or with an Agilent 8453 Diode Array Spectrophotometer with stirred cuvette holder or with an Epoch 2 Plate Reader from Biotek using either 10 mm quartz suprasil cuvettes from Hellma (total volume of either 1 or 3 mL, path length 1 cm) or a 96-well quartz microplate from Hellma. Measurements under inert atmosphere were conducted using sealable quartz suprasil cuvettes from Hellma (total volume either 1 mL or 3 mL, path length 1 cm) equipped with a stirring bar and a septum.

Luminescence Spectroscopy

Luminescence measurements were performed on a BioTek Synergy H1 Hybrid Microplate Reader. A 96-well quartz microplate from Hellma was used.

FT-Infrared Spectroscopy

FT-IR Spectroscopy was carried out with a Jasco FT/IR-460Plus with ATR Diamond Plate. Spectra Manager Version 2 from JASCO was used for data processing. FT-IR data is reported in absorption frequency (cm^{-1}).

EPR Spectroscopy

EPR measurements were performed using a BRUKER EMXNano Xband (9.5 GHz) spectrometer at room temperature. All 1D CW EPR experiments were conducted using a microwave power of 1.0 mW. Modulation amplitudes and frequencies of 0.01 mT and 100 kHz were used, respectively. A time constant of 1.28 ms and a sweep time of 5 min were also used. CW spectra were processed by Dr. Katherine R. Fisher using MATLAB® and EasySpin® software.[304] To take into account the rapid tumbling of the solutions which were measured, the CW EPR spectra were processed using the garlic function.[304] After spectra were processed using the software, parameters were extracted by fitting the spectra obtained using a non-linear least squares regression model (Nelder/Mead downhill simplex algorithm) where the overall RMSD value for the entire system was minimized to as close to zero as possible. Using the parameters extracted from the recorded spectra, simulated spectra could be produced and compared to the recorded spectra. The amount of spin per metal ion could be obtained by measuring CW EPR spectra, and calculating the double integral of the differential spectra and then using the Xenon software provided by BRUKER to calculate the absolute number of spins which could then be divided by the number of metal ions we knew to be present in the solution.[290]

X-Ray Crystallography

Data collection and structure elucidation was performed by Dr. Peter Mayer at the Chemistry Department of the Ludwig Maximilian University of Munich. The X-ray intensity data were collected on a Bruker D8 Venture TXS system equipped with a multilayer mirror optics monochromator and a Mo Kα rotating-anode X-ray tube (λ = 0.71073 Å). The frames were integrated with the Bruker SAINT software package using a narrow-frame algorithm.[305] Data were corrected for absorption effects using

the Multi-Scan method (SADABS).[306] The structure was solved and refined using the Bruker SHELXTL Software Package.[307]

3. Experimental Procedures

3.1. Synthesis of PQQ Derivatives

***N*-(2-methoxy-5-nitrophenyl)formamide (2)**

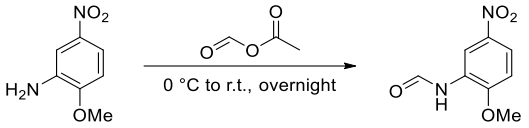

1 **2**: 99%

Adapted from a literature procedure.[1] In a two-necked round-bottomed flask (250 mL) equipped with a KPG-stirrer, acetic anhydride (35.0 mL, 370 mmol, 1.6 equiv.) was cooled to 0 °C. Formic acid (35.0 mL, 928 mmol, 3.9 equiv.) was slowly added, and the mixture was stirred at 0 °C for 1.5 h. 2-Methoxy-5-nitroaniline (**1**) (40.0 g, 238 mmol, 1.0 equiv.) was added in four equal portions over 1 h at 0 °C. The reaction mixture was allowed to warm to room temperature and stirred overnight. The resulting thick yellow paste was diluted with water (850 mL) and stirred until the solid was evenly suspended. The solid was filtered through a glass frit, washed with water, and dried at 60 °C for 3 h and subsequently under high vacuum at room temperature affording **2** (46.3 g, 236 mmol, 99%) as a yellow solid.

^{1}H NMR (400 MHz, DMSO-*d*$_6$): δ / ppm = 10.10 (s, 1H), 9.13 (d, J = 2.9 Hz, 1H), 8.38 (d, J = 1.8 Hz, 1H), 8.03 (dd, J = 9.1 Hz, J = 2.9 Hz, 1H), 7.27 (d, J = 9.1 Hz, 1H), 4.00 (s, 3H).

^{13}C NMR (101 MHz, DMSO-*d*$_6$): δ / ppm = 160.8, 153.5, 140.3, 127.2, 120.3, 114.5, 111.0, 56.8.

HRMS (EI): m/z calc. for [$C_8H_8N_2O$]: 196.0479 $[M]^+$

found: 196.0478.

IR (Diamond-ATR, neat): $\tilde{\nu}$ / cm^{-1} = 3337, 3322, 3108, 3083, 2892, 1694, 1613, 1593, 1532, 1505, 1484, 1459, 1444, 1426, 1331, 1276, 1232, 1183, 1141, 1074, 1014, 942, 894, 863, 819, 807, 748, 728, 705, 668.

m.p.: 194–202 °C.

^{1}H NMR (400 MHz, DMSO-*d*$_6$):

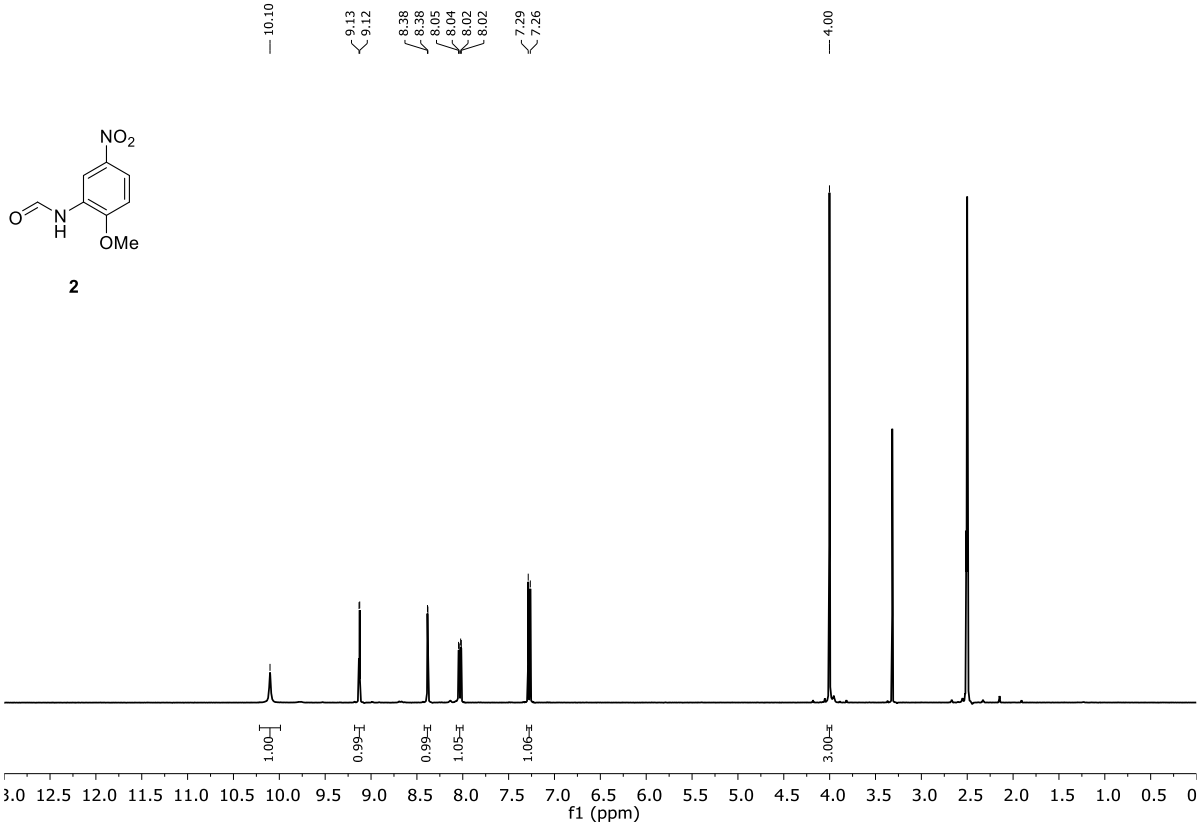

^{13}C NMR (101 MHz, DMSO-*d*$_6$):

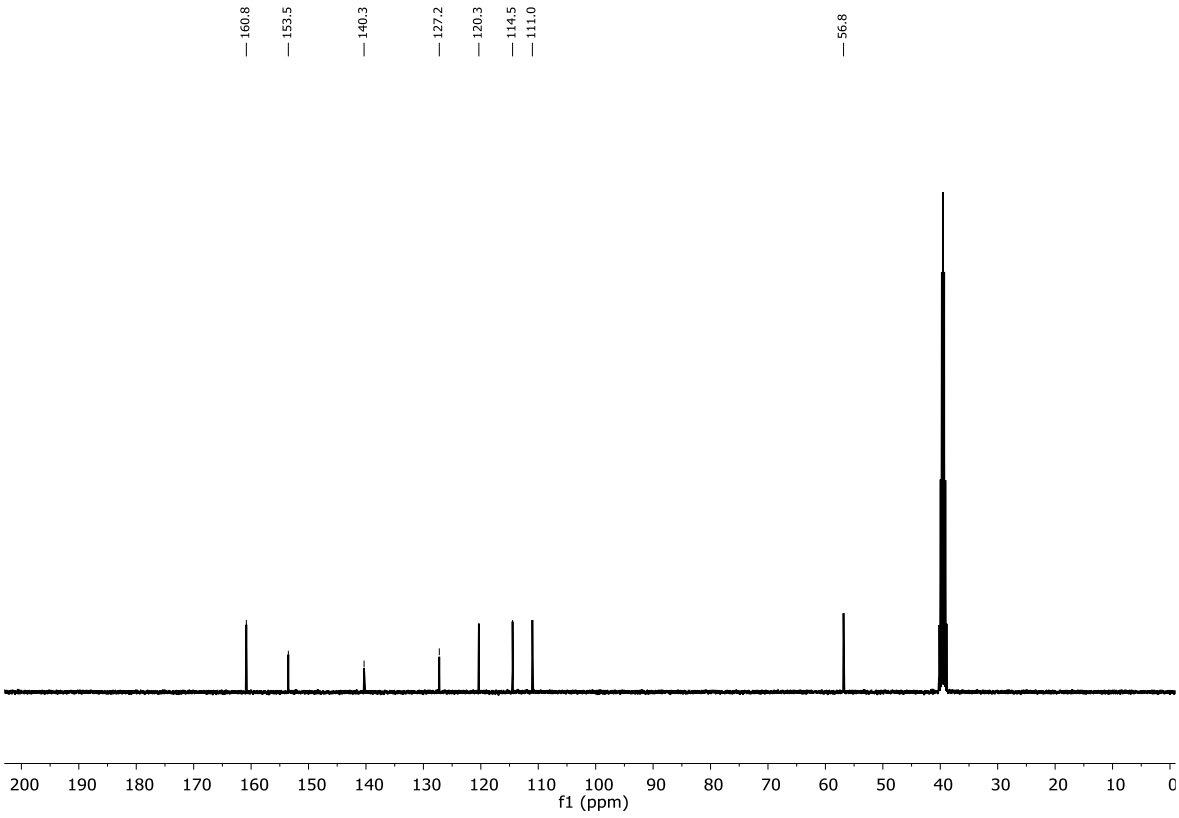

***N*-(5-amino-2-methoxyphenyl)formamide (3)**

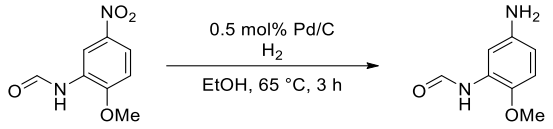

2 **3**: 87%

Adapted from a literature procedure.[1] Pd/C (447 mg, 10 wt.%, 0.5 mol%) was suspended in 80 mL ethanol and combined with **2** (15.0 g, 76.5 mmol, 1.0 equiv.) in an autoclave (300 mL volume). The autoclave reactor was flushed with hydrogen gas three times and then filled with hydrogen gas (7 bar). The reaction mixture was slowly heated to 65 °C and was stirred at this temperature for 3 h. After cooling to room temperature, the suspension was filtered through a pad of Celite under a nitrogen stream. The filter pad was washed with dimethylformamide. The solvent was removed *in vacuo*, and the crude product was triturated with chloroform to yield **3** (11.0 g, 66.5 mmol, 87%) as a beige solid.

^{1}H NMR (400 MHz, DMSO-*d*$_6$): δ / ppm = 9.38 (s, 1H), 8.24 (s, 1H), 7.54 (d, J = 2.7 Hz, 1H), 6.73 (d, J = 8.6 Hz, 1H), 6.25 (dd, J = 8.6 Hz, J = 2.7 Hz, 1H), 4.68 (s, 2H), 3.70 (s, 3H).

^{13}C NMR (101 MHz, DMSO-*d*$_6$): δ / ppm = 159.7, 142.5, 139.9, 127.5, 112.7, 108.9, 107.1, 56.5.

HRMS (EI): m/z calc. for [$C_8H_{10}N_2O_2$]: 166.0737 $[M]^+$

found: 166.0736.

IR (Diamond-ATR, neat): $\tilde{\nu}$ / cm^{-1} = 3391, 3269, 1673, 1598, 1530, 1487, 1457, 1436, 1414, 1294, 1268, 1217, 1175, 1153, 1100, 1025, 863, 795, 743, 668.

m.p.: 150–153 °C.

^{1}H NMR (400 MHz, DMSO-*d*$_6$):

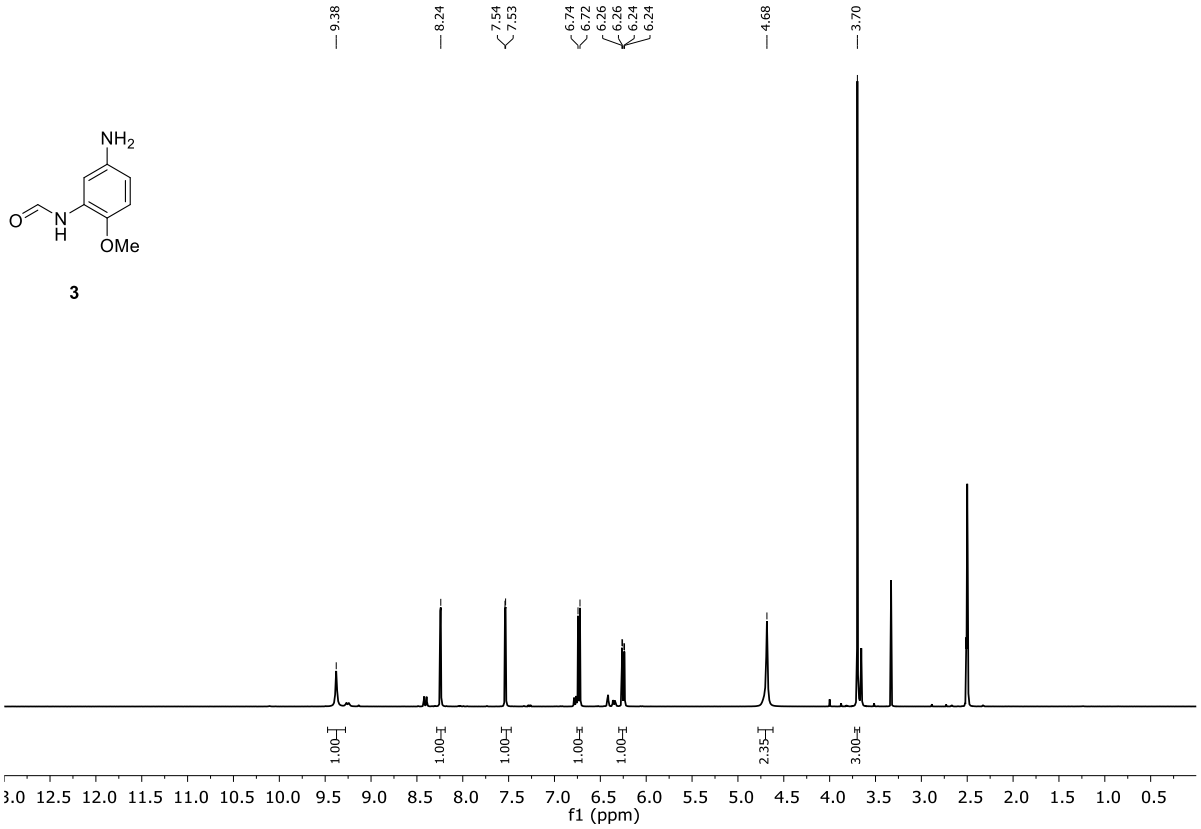

^{13}C NMR (101 MHz, DMSO-*d*$_6$):

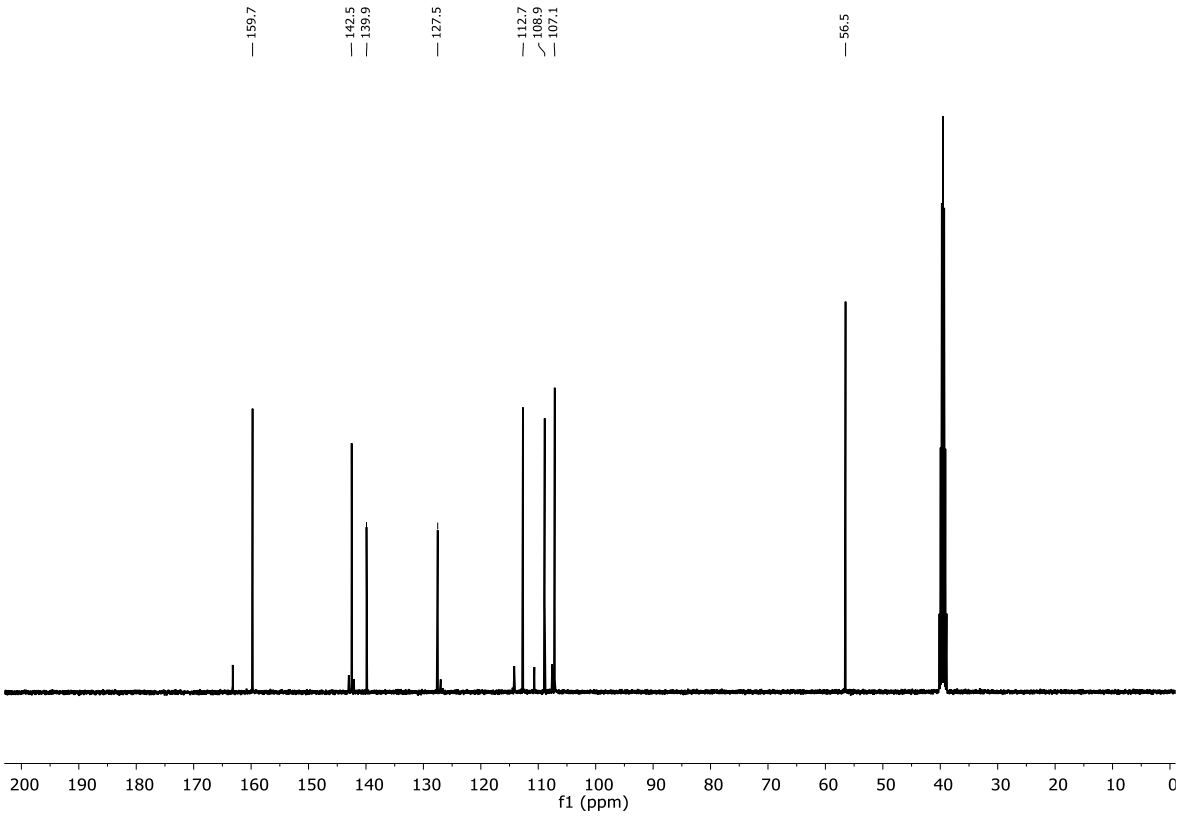

Methyl 2-methyl-3-oxobutanoate (4)

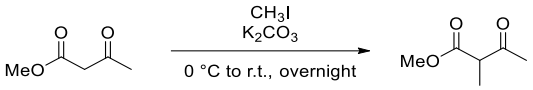

4: 65%

Adapted from a literature procedure.[153] Methyl iodide (12.2 g, 86.1 mmol, 1.0 equiv.) was added to methyl 3-oxobutanoate (10.0 g, 86.1 mmol, 1.0 equiv.) in a round-bottomed flask, and the mixture was cooled to 0 °C. Potassium carbonate (17.9 g, 129 mmol, 1.5 equiv.) was added in portions over 1 h. The reaction mixture was allowed to warm to room temperature and stirred overnight. The thick suspension was diluted with diethyl ether (15 mL) and stirred for 2 h. The reaction mixture was filtered and concentrated *in vacuo*. Subsequent distillation (10.0 mbar, 54 °C) afforded **4** (7.33 g, 56.3 mmol, 65%) as a colorless liquid.

^{1}H NMR (400 MHz, $CDCl_3$): δ / ppm = 3.74 (s, 3H), 3.52 (q, J = 7.2 Hz, 1H), 2.24 (s, 3H), 1.35 (d, J = 7.2 Hz, 3H).

^{13}C NMR (101 MHz, $CDCl_3$): δ / ppm = 203.7, 171.1, 53.6, 52.6, 28.6, 12.9.

HRMS (EI): m/z calc. for $[C_5H_7O_2]$: 99.0411 $[M\text{-}OMe]^+$

found: 99.0411.

IR (Diamond-ATR, neat): $\tilde{\nu}$ / cm^{-1} = 2993, 2955, 1742, 1713, 1454, 1435, 1359, 1329, 1244, 1206, 1152, 1101, 1077, 1051, 988, 956, 859.

^{1}H NMR (400 MHz, $CDCl_3$):

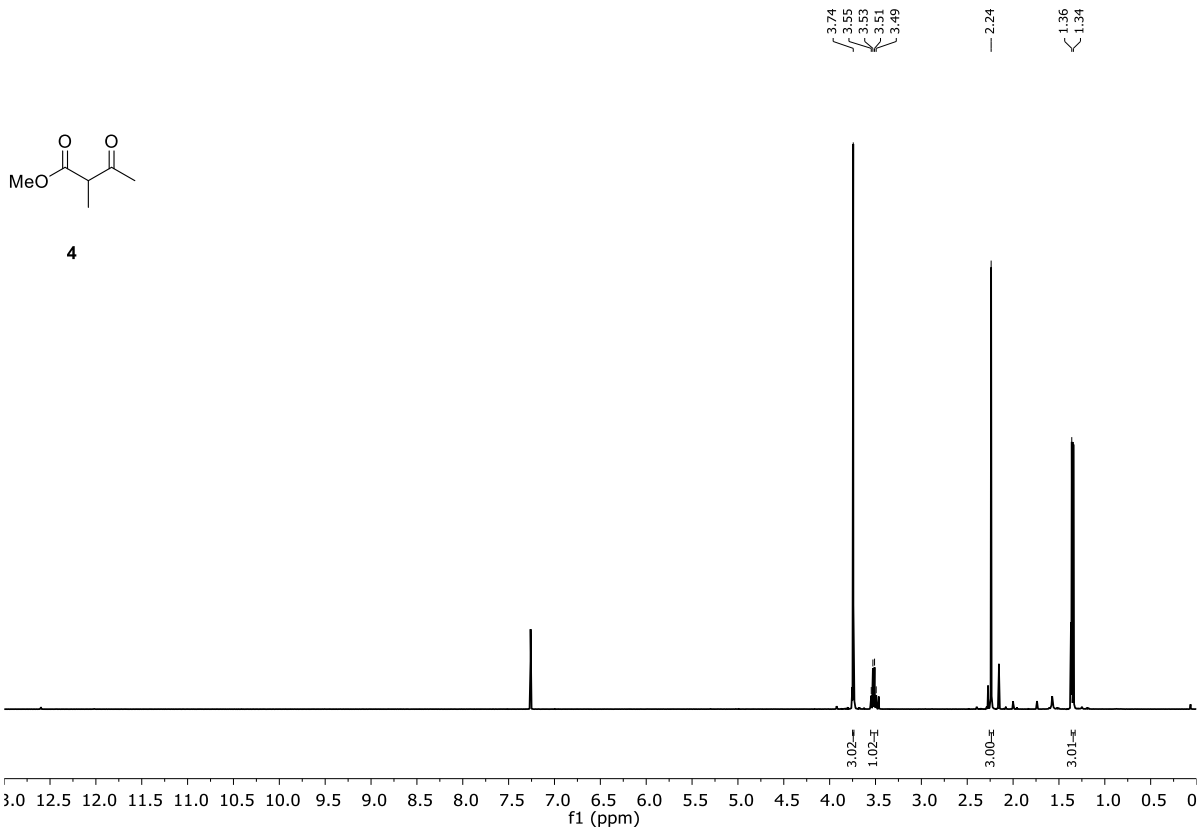

^{13}C NMR (101 MHz, $CDCl_3$):

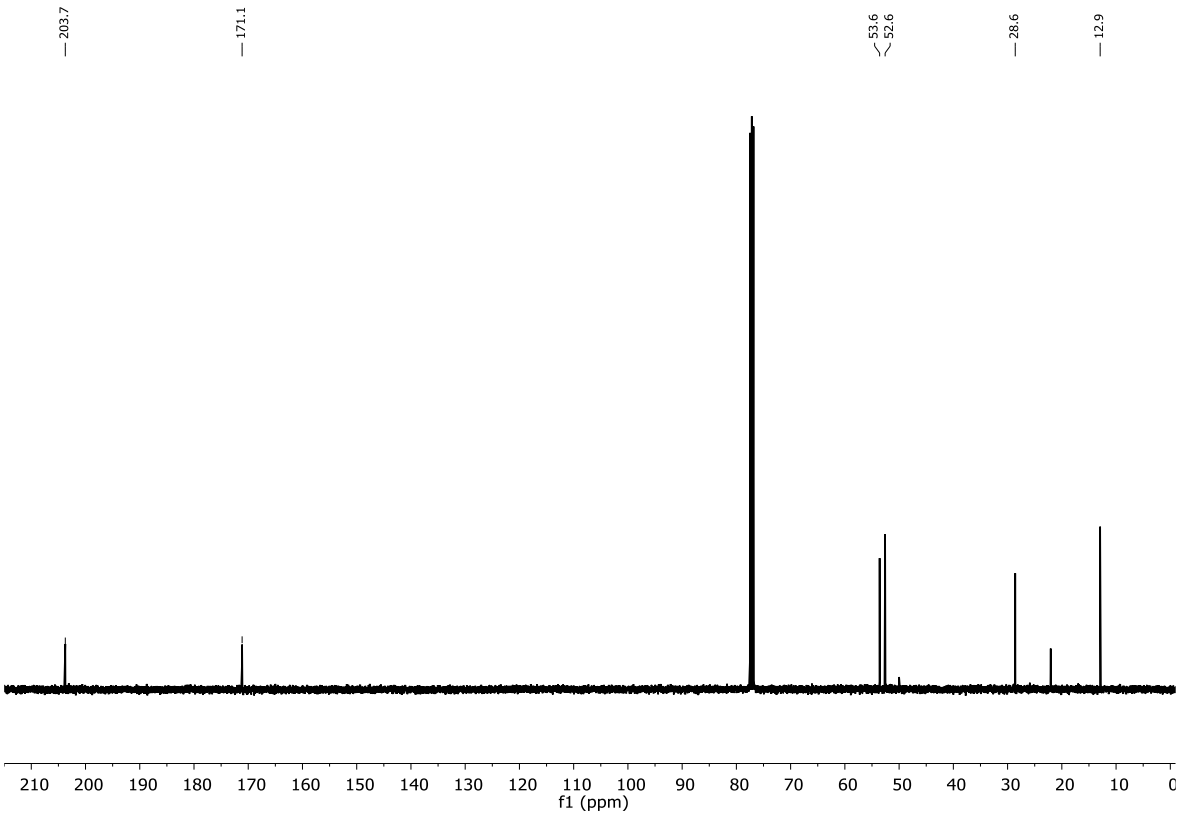

Methyl (*E*)-2-(2-(3-formamido-4-methoxyphenyl)hydrazineylidene) propanoate (5)

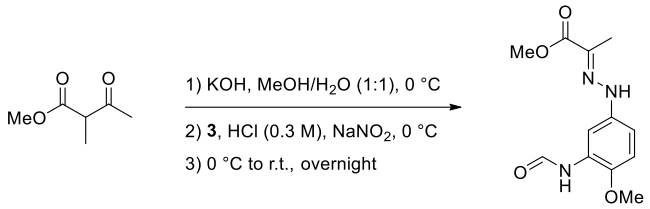

4 **5**: 74%

Adapted from a literature procedure.[1] A solution of **4** (312 mg, 2.4 mmol, 1.2 equiv.) in methanol/water (1:1, 27 mL) was prepared in a round-bottomed flask and cooled to 0 °C. Potassium hydroxide (135 mg, 2.4 mmol, 1.2 equiv.) was added. Compound **3** (332 mg, 2.0 mmol, 1.0 equiv.) was dissolved in 0.3 M hydrochloric acid (13 mL) and cooled to 0 °C. Sodium nitrite (138 mg, 2.0 mmol, 1.0 equiv.) was added, the reaction mixture was briefly stirred and subsequently added to the solution of **4** *via* a transfer cannula. The red reaction mixture was allowed to warm to room temperature and stirred overnight. The precipitate was filtered off, washed with ice-cold ethanol/water (1:1), and dried under high vacuum to afford **5** (392 mg, 1.48 mmol, 74%) as a red solid.

^{1}H NMR (400 MHz, DMSO-*d*$_6$): δ / ppm = 9.77 (s, 1H), 9.60 (s, 1H), 8.30 (d, J = 2.0 Hz, 1H), 8.19 (st, J = 1.4 Hz, 1H), 7.01 (s, 1H), 6.99 (s, 1H), 3.80 (s, 3H), 3.71 (s, 3H), 2.03 (s, 3H).

^{13}C NMR (101 MHz, DMSO-*d*$_6$): δ / ppm = 165.5, 159.9, 143.3, 138.0, 130.3, 127.2, 111.9, 108.7, 107.1, 56.1, 51.6, 11.8.

HRMS (ESI): m/z calc. for [$C_{12}H_{14}N_3O_4$]: 264.0990 $[M-H]^-$

found: 264.0989.

IR (Diamond-ATR, neat): $\tilde{\nu}$ / cm^{-1} = 3371, 3256, 1677, 1591, 1531, 1480, 1443, 1415, 1375, 1320, 1284, 1255, 1199, 1170, 1140, 1095, 1024, 882, 867, 846, 801, 755, 707, 688.

m.p.: 170–179 °C.

This procedure was part of the research internship of Rachel Janßen, conducted under my supervision, and was further optimized during her master thesis and PhD.

^{1}H NMR (400 MHz, DMSO-*d*$_6$):

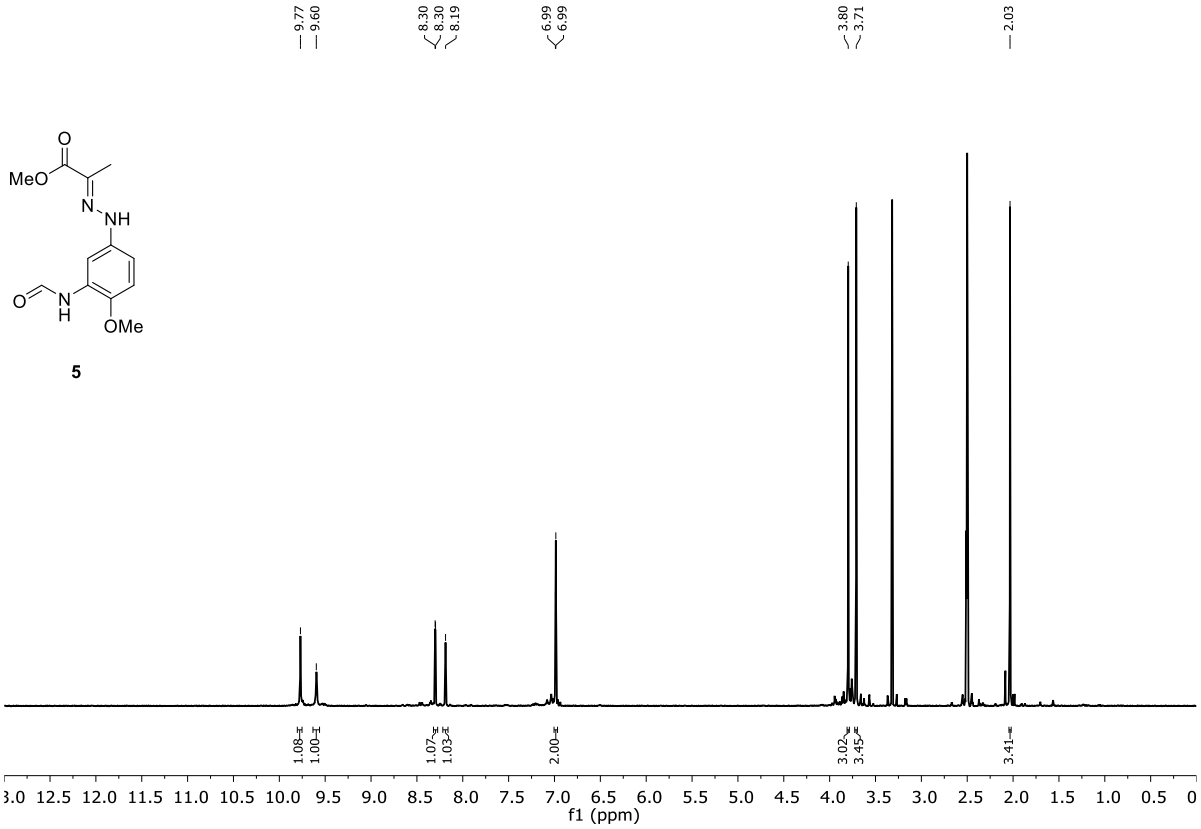

5

^{13}C NMR (101 MHz, DMSO-*d*$_6$):

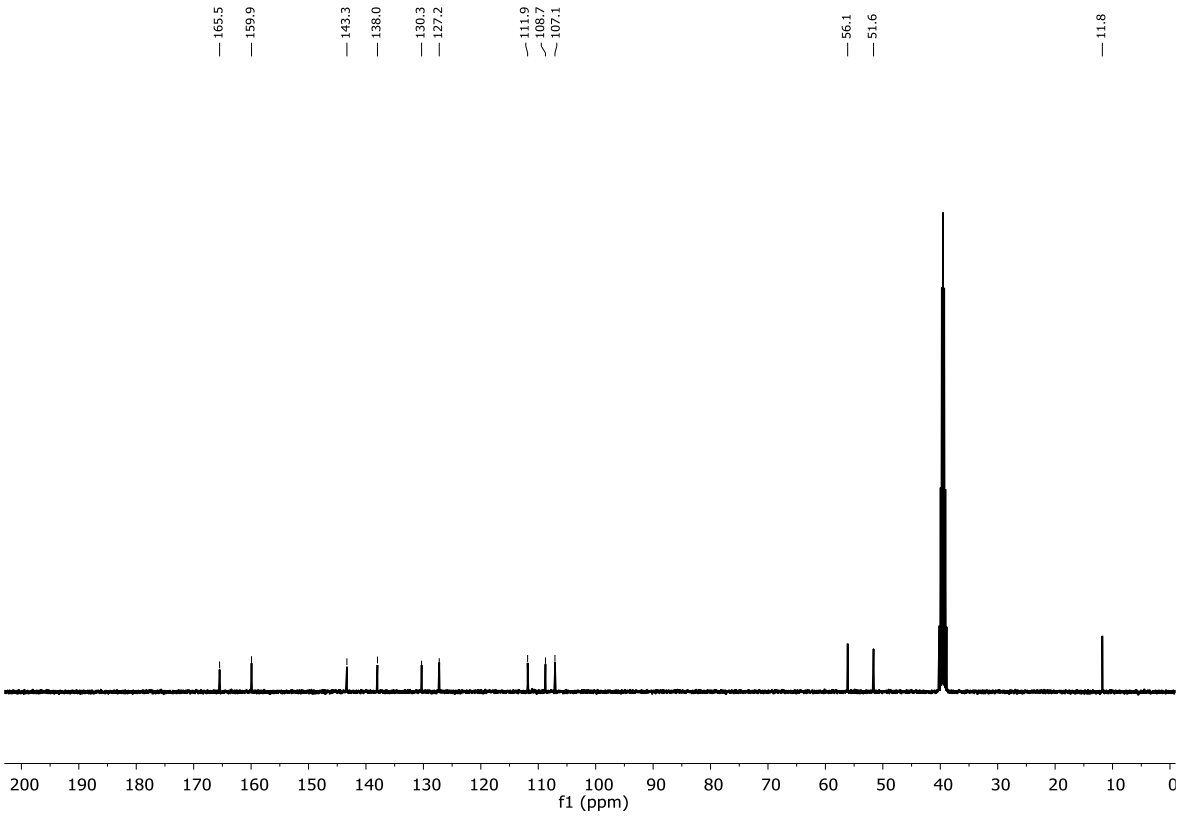

(*E*)-*N*-(2-methoxy-5-(2-(3-oxobutan-2-ylidene)hydrazineyl)phenyl) formamide (6)

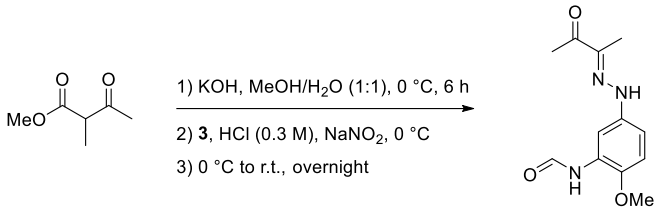

4 **6**: 72%

Adapted from a literature procedure.[1] Keto ester derivative **4** (312 mg, 2.4 mmol, 1.2 equiv.) was dissolved in a mixture of methanol/water (1:1, 15 mL) and cooled to 0 °C in a round-bottomed flask. Potassium hydroxide (135 mg, 2.4 mmol, 1.2 equiv.) was added. The colorless solution was stirred at 0 °C for 6 h and kept in a fridge at 4 °C for 14 h. Aniline derivative **3** (332 mg, 2.0 mmol, 1.0 equiv.) was suspended in 0.3 M hydrochloric acid (13 mL) and cooled to 0 °C. Sodium nitrite (138 mg, 2.0 mmol, 1.0 equiv.) was added to the acidic suspension, and the resulting mixture was added to the alkalic solution *via* a transfer cannula. The red reaction mixture was slowly allowed to warm to room temperature and stirred overnight. The precipitate was filtered off, washed with ice-cold ethanol/water (1:1) and dried under high vacuum to afford **6** (357 mg, 1.43 mmol, 72%) as red solid.

^{1}H NMR (400 MHz, DMSO-d_6): δ / ppm = 9.95 (s, 1H), 9.63 (s, 1H), 8.34 (d, J = 2.5 Hz, 1H), 8.31 (d, J = 1.9 Hz, 1H), 7.05 (dd, J = 8.8 Hz, J = 2.5 Hz, 1H), 7.00 (d, J = 8.9 Hz, 1H), 3.81 (s, 3H), 2.34 (s, 3H), 1.92 (s, 3H).

^{13}C NMR (101 MHz, DMSO-d_6): δ / ppm = 195.8, 160.0, 143.4, 139.6, 137.8, 127.5, 111.9, 108.7, 107.0, 56.1, 23.8, 8.8.

HRMS (ESI): m/z calc. for [$C_{12}H_{14}N_3O_3$]: 248.1041 $[M-H]^-$

found: 248.1042.

IR (Diamond-ATR, neat): $\tilde{\nu}$ / cm^{-1} = 3307, 3234, 2364, 1682, 1662, 1607, 1583, 1539, 1486, 1436, 1415, 1366, 1344, 1315, 1283, 1257, 1215, 1169, 1118, 1032, 946, 887, 797, 744, 725.

m.p.: 206–214 °C.

This procedure was part of the research internship of Rachel Janßen, conducted under my supervision, and was further optimized during her master thesis and PhD.

^{1}H NMR (400 MHz, DMSO-*d*$_6$):

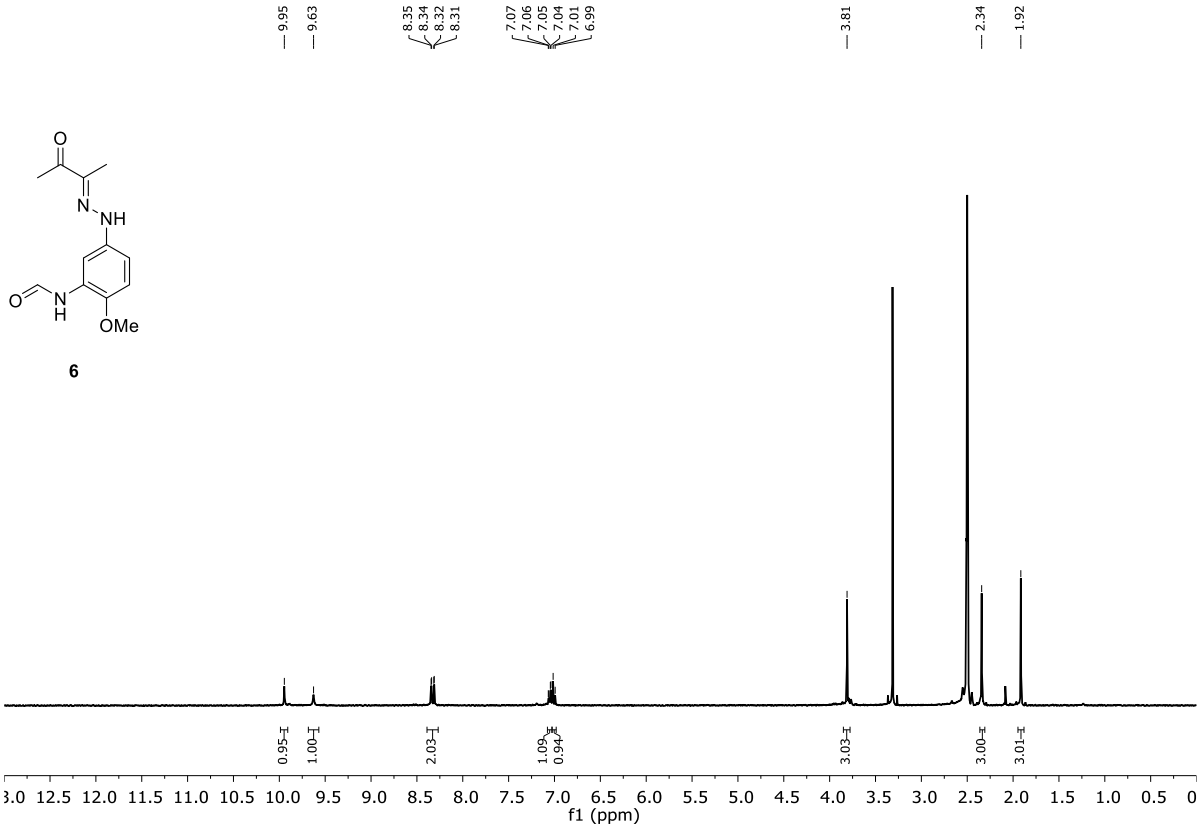

^{13}C NMR (101 MHz, DMSO-*d*$_6$):

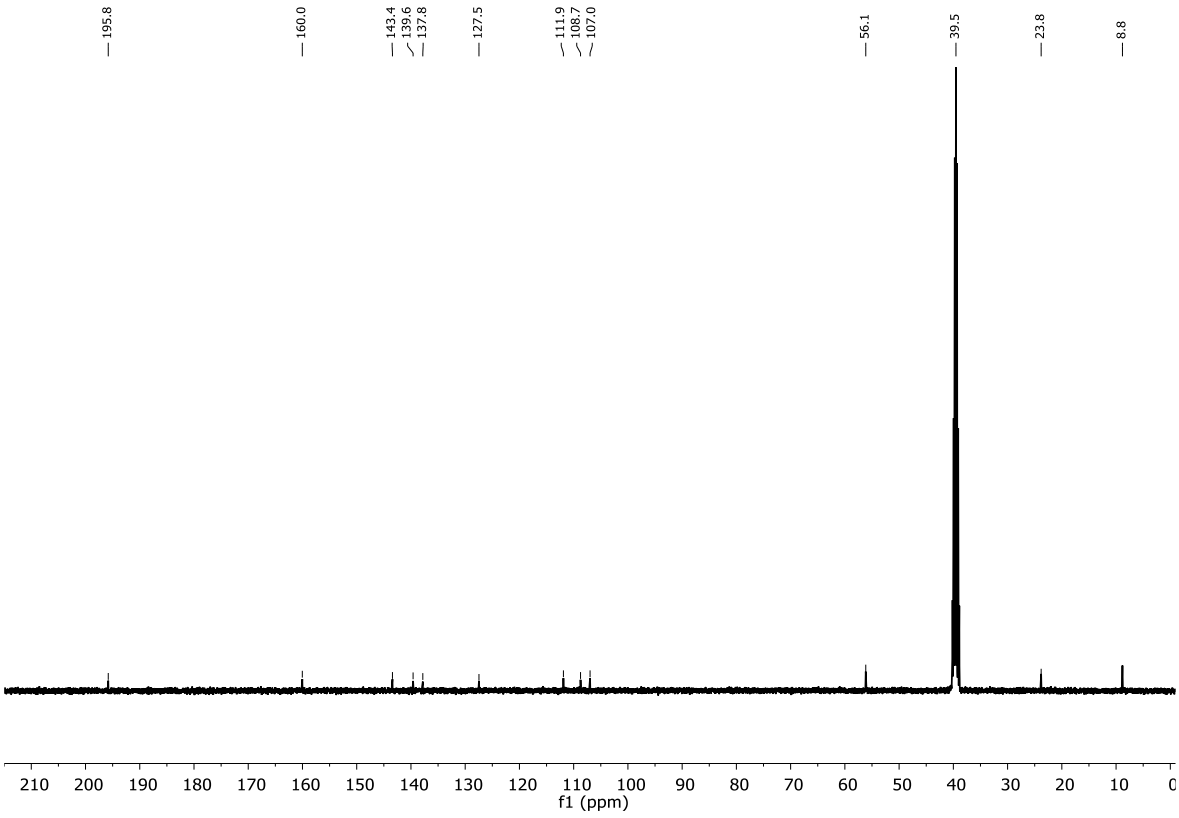

Methyl 6-formamido-5-methoxy-1*H*-indole-2-carboxylate (7)

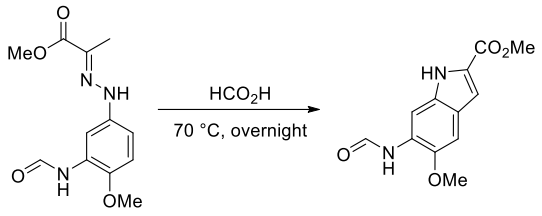

5 **7**: 60%

Adapted from a literature procedure.[1] Hydrazone **5** (591 mg, 2.23 mmol, 1.0 equiv.) was dissolved in 5 mL formic acid in a round-bottomed flask and stirred at 70 °C overnight. The reaction mixture was allowed to cool to room temperature, and the formic acid was removed *in vacuo*. The residue was repeatedly suspended in water (10 mL) and concentrated *in vacuo* (3×). The crude product was triturated with methanol and cooled in the fridge at 4 °C overnight. The solid was filtered off, washed with cold methanol and dried under high vacuum to afford **7** (334 mg, 1.35 mmol, 60%) as an orange solid.

^{1}H NMR (400 MHz, DMSO-d_6): δ / ppm = 11.72 (s, 1H), 9.71 (s, 1H), 8.41 (s, 1H), 8.36 (s, 1H), 7.18 (s, 1H), 7.04 (dd, J = 2.1 Hz, J = 0.7 Hz, 1H), 3.87 (s, 3H), 3.84 (s, 3H).

^{13}C NMR (101 MHz, DMSO-d_6): δ / ppm = 161.5, 160.1, 144.6, 132.2, 126.5, 126.4, 122.1, 107.7, 103.3, 101.6, 55.9, 51.6.

HRMS (ESI): m/z calc. for [$C_{12}H_{11}N_2O_4$]: 247.0724 [M-H]$^-$

found: 247.0724.

IR (Diamond-ATR, neat): $\tilde{\nu}$ / cm^{-1} = 3314, 2696, 2465, 2217, 1670, 1628, 1588, 1537, 1464, 1437, 1396, 1353, 1288, 1215, 1161, 1092, 1020, 994, 938, 904, 866, 833, 794, 759, 724.

m.p.: 209–213 °C.

^{1}H NMR (400 MHz, DMSO-*d*$_6$):

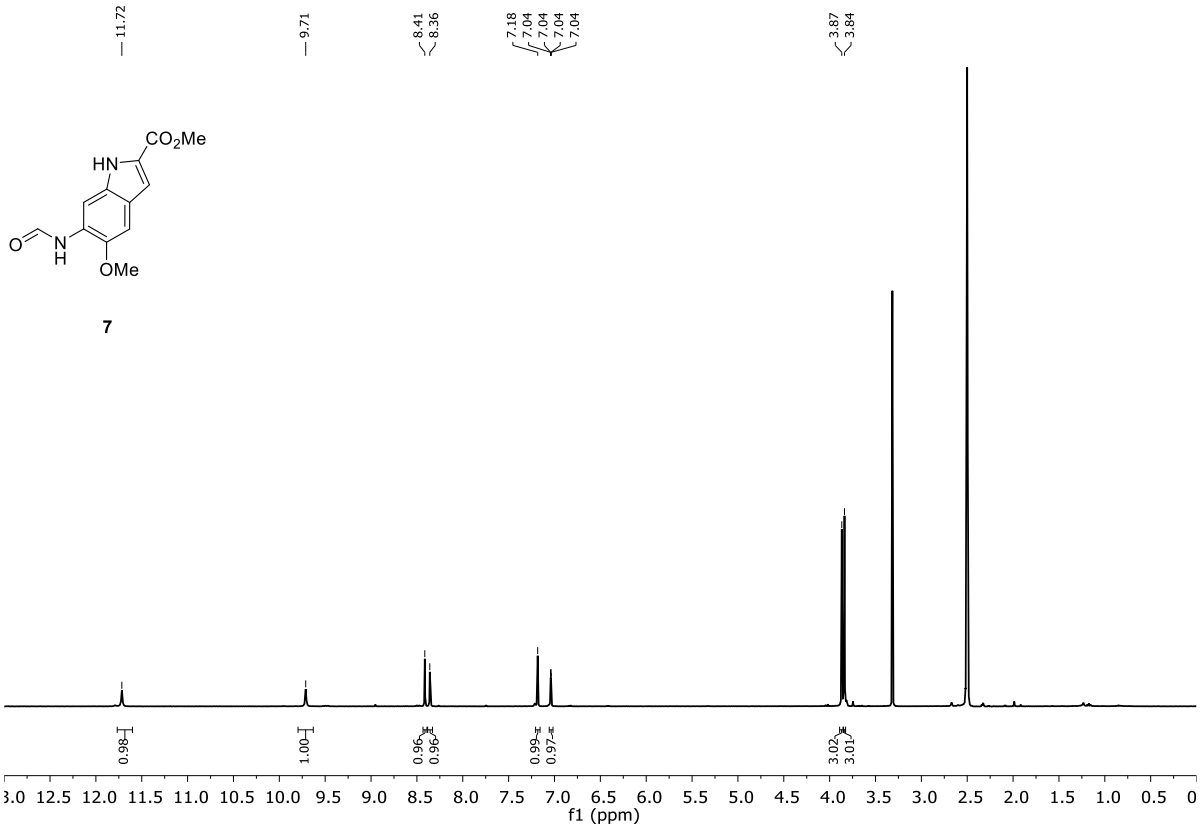

^{13}C NMR (101 MHz, DMSO-*d*$_6$):

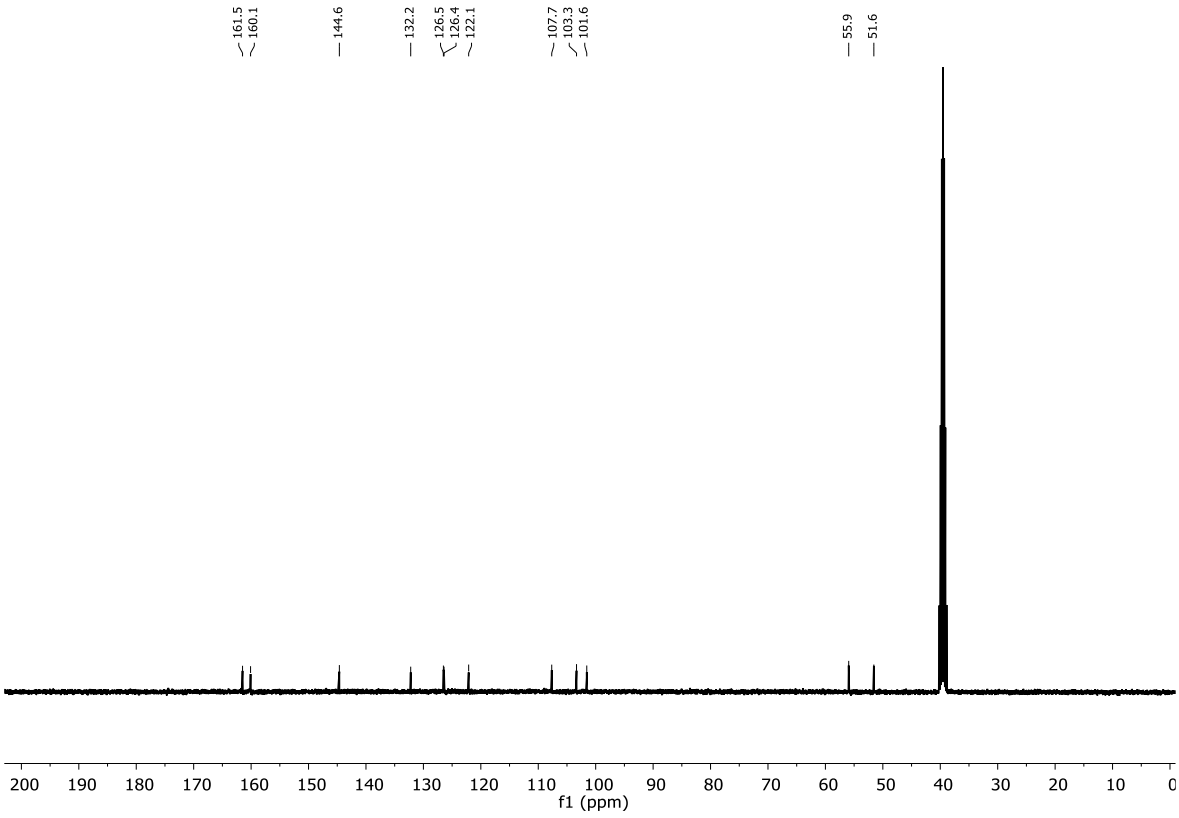

_N_-(2-acetyl-5-methoxy-1_H_-indol-6-yl)formamide (8)

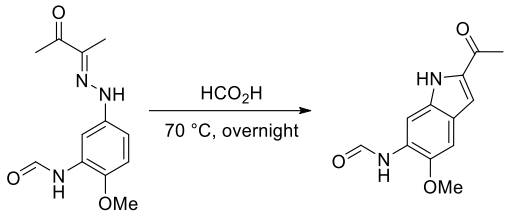

6 **8**: 56%

Adapted from a literature procedure.[1] Hydrazone **6** (470 mg, 1.88 mmol, 1.0 equiv.) was dissolved in 7 mL formic acid in a round-bottomed flask and stirred at 70 °C overnight. The reaction mixture was allowed to cool to room temperature, and the formic acid was removed *in vacuo*. The residue was repeatedly suspended in water (15 mL) and concentrated *in vacuo* (3×). The crude product was triturated with hot methanol (approx. 2 mL) and cooled in an ice-bath. The solid was filtered off, washed with cold methanol, and dried under high vacuum to afford **8** (245 mg, 1.05 mmol, 56%) as a beige solid.

^{1}H NMR (400 MHz, DMSO-d_6): δ / ppm = 11.54 (s, 1H), 9.74 (s, 1H), 8.40 (s, 1H), 8.36 (s, 1H), 7.21 (dd, J = 2.1 Hz, J = 0.7 Hz, 1H), 7.19 (s, 1H), 3.88 (s, 3H), 2.49 (s, 3H).

^{13}C NMR (101 MHz, DMSO-d_6): δ / ppm = 189.0, 160.1, 144.6, 135.6, 132.3, 127.1, 122.3, 109.4, 103.3, 101.9, 56.0, 25.9.

HRMS (ESI): m/z calc. for [$C_{12}H_{11}N_2O_3$]: 231.0775 $[M-H]^-$

found: 231.0774.

IR (Diamond-ATR, neat): $\tilde{\nu}$ / cm^{-1} = 3201, 2329, 1670, 1632, 1584, 1523, 1463, 1416, 1387, 1361, 1280, 1228, 1206, 1155, 1084, 1021, 984, 941, 875, 842, 761, 732.

m.p.: 253–255 °C.

^{1}H NMR (400 MHz, DMSO-*d*$_6$):

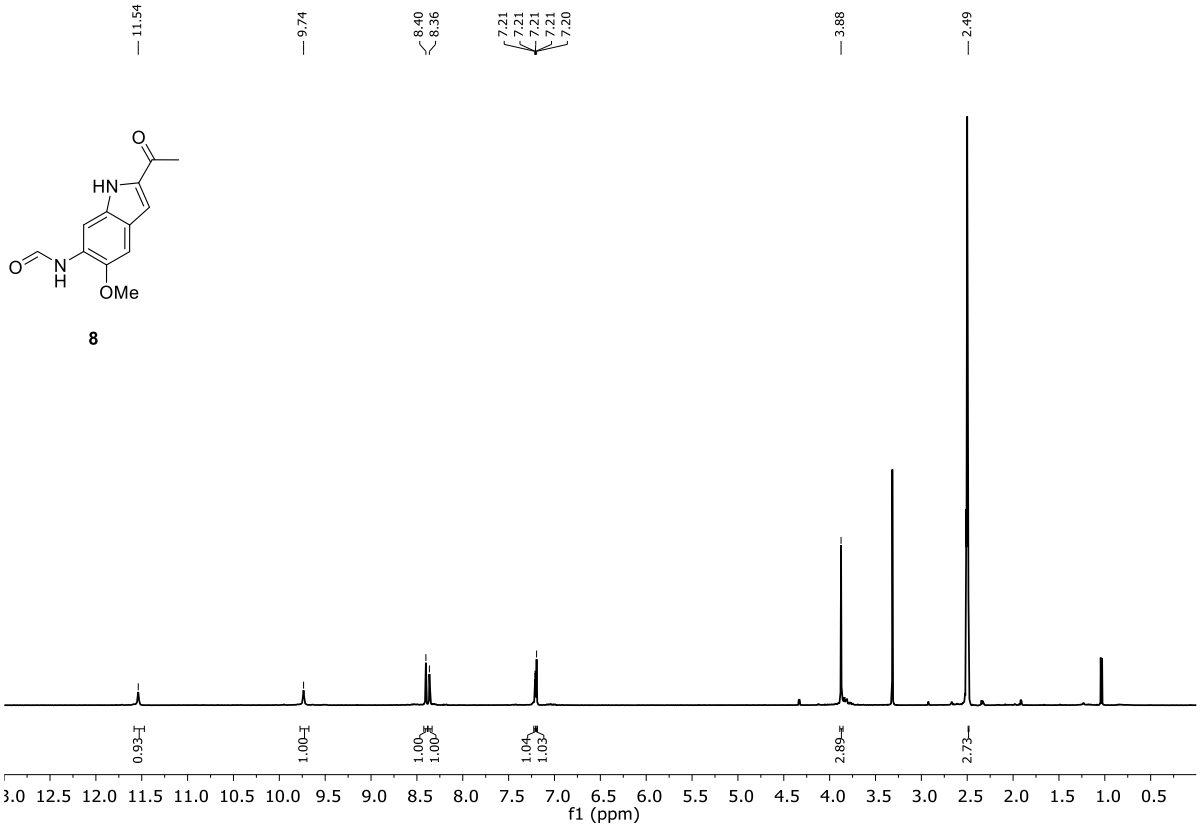

^{13}C NMR (101 MHz, DMSO-*d*$_6$):

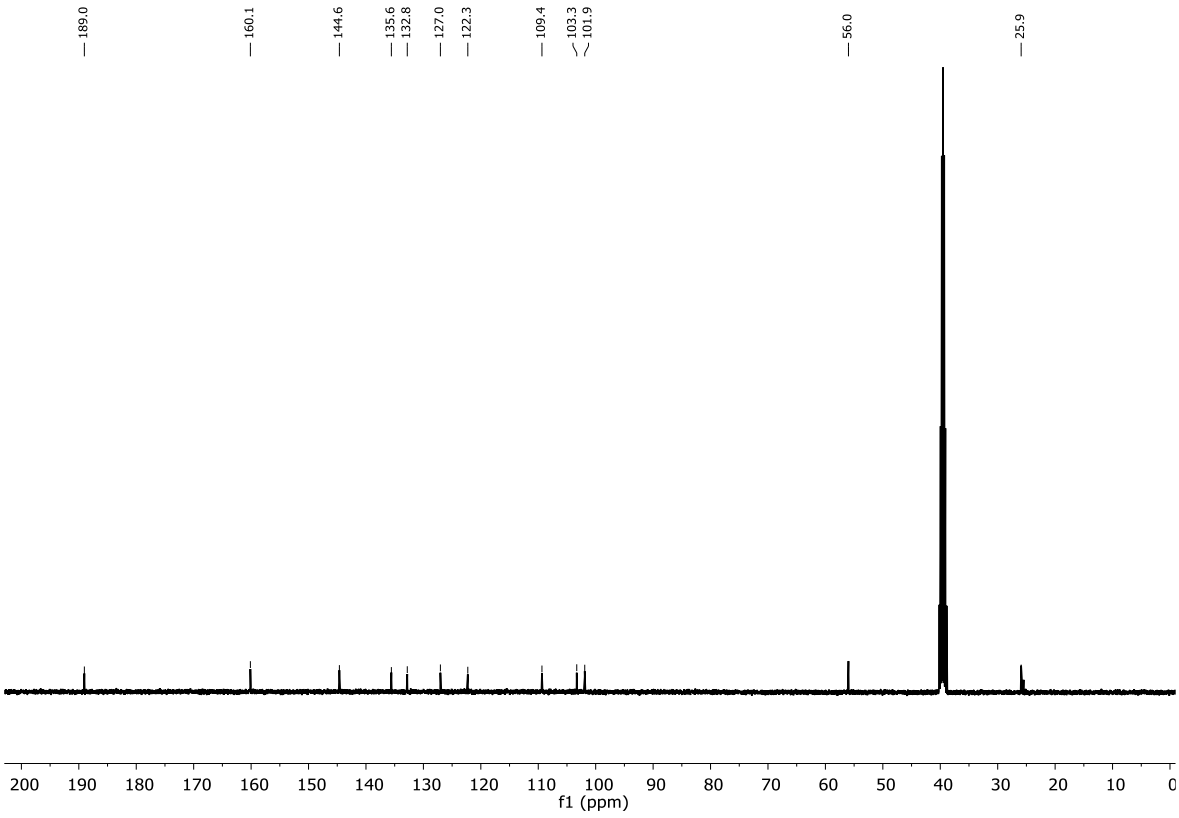

Methyl 6-amino-5-methoxy-1*H*-indole-2-carboxylate (9)

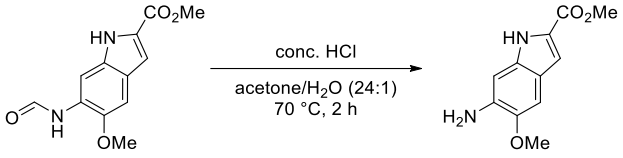

7 **9**: 84%

Adapted from a literature procedure.[1] Concentrated hydrochloric acid (2.67 mL, 32.0 mmol, 3.0 equiv.) was added to a stirred solution of acetone/water (66.7 mL, 96:4) in a round-bottomed flask. Compound **7** (2.65 g, 10.7 mmol, 1.0 equiv.) was added, and the reaction mixture was heated to 70 °C and stirred for 2 h. The precipitate was filtered off and washed with acetone. The solid was taken up in chloroform (120 mL) and aqueous sodium hydroxide (2 M, 120 mL). The aqueous phase was extracted with chloroform (2 × 100 mL), and the combined organic layers were washed with brine and dried over sodium sulfate. The solvent was removed *in vacuo* affording **9** (1.98 g, 9.0 mmol, 84%) as a light-brown solid.

^{1}H NMR (400 MHz, DMSO-*d*$_6$): δ / ppm = 11.17 (s, 1H), 6.92 (dd, J = 2.2 Hz, J = 0.9 Hz, 1H), 6.90 (s, 1H), 6.62 (d, J = 0.7 Hz, 1H), 4.96 (s, 2H), 3.79 (s, 3H), 3.78 (s, 3H).

^{13}C NMR (101 MHz, DMSO-*d*$_6$): δ / ppm = 161.6, 144.5, 138.4, 134.3, 123.1, 117.8, 108.5, 100.8, 94.1, 55.4, 51.1.

HRMS (ESI): m/z calc. for [$C_{11}H_{13}N_2O_3$]: 221.0921 $[M+H]^+$

found: 221.0921.

IR (Diamond-ATR, neat): $\tilde{\nu}$ / cm^{-1} = 3333, 2982, 2941, 2839, 1683, 1635, 1620, 1522, 1504, 1462, 1437, 1364, 1297, 1273, 1211, 1195, 1150, 1107, 1028, 1002, 941, 877, 839, 828, 811, 779, 760, 728, 705, 687, 671, 665, 658.

m.p.: 160–162 °C.

^{1}H NMR (400 MHz, DMSO-*d*$_6$):

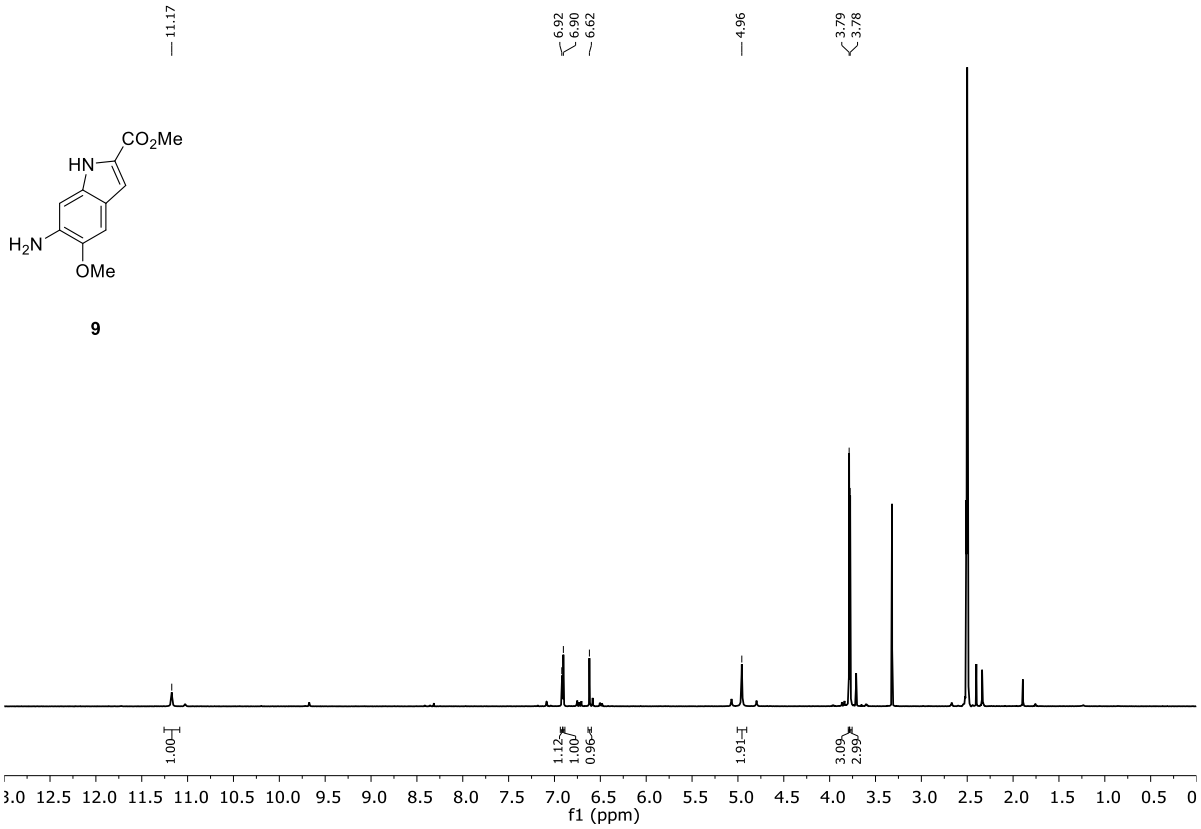

^{13}C NMR (101 MHz, DMSO-*d*$_6$):

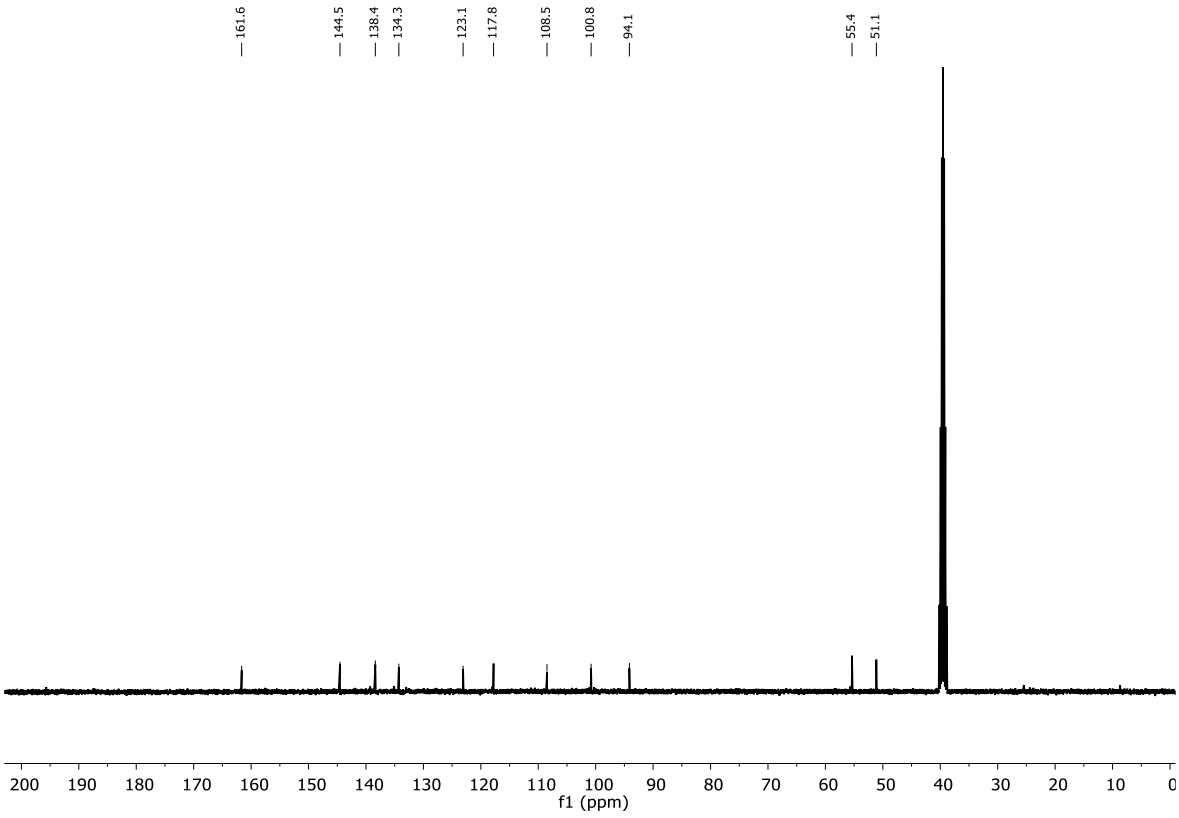

1-(6-Amino-5-methoxy-1*H*-indol-2-yl)ethan-1-one (10)

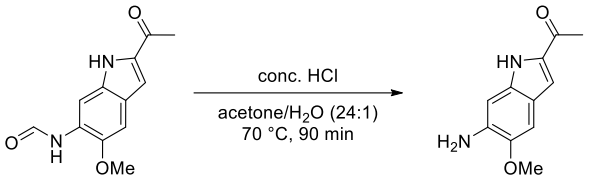

8 **10**: 79%

Adapted from a literature procedure.[1] Concentrated hydrochloric acid (0.22 mL, 2.58 mmol, 3.0 equiv.) was added to a stirred solution of acetone/water (5.38 mL, 96:4) in a round-bottomed flask. Compound **8** (200 mg, 0.86 mmol, 1.0 equiv.) was added, and the reaction mixture was heated to 70 °C and stirred for 90 min. After cooling to room temperature, the solvent was evaporated and the residue was suspended in aqueous sodium hydroxide (2 M, 10 mL) and dichloromethane (10 mL). The biphasic mixture was filtered and the aqueous phase was extracted with dichloromethane (2 × 10 mL). The combined organic layers were washed with brine and dried over sodium sulfate, and the solvent was removed *in vacuo* to afford **10** (139 mg, 0.68 mmol, 79%) as a light-brown solid.

^{1}H NMR (400 MHz, DMSO-*d*$_6$): δ / ppm = 11.02 (s, 1H), 7.08 (dd, J = 2.3 Hz, J = 0.8 Hz, 1H), 6.91 (s, 1H), 6.59 (d, J = 0.6 Hz, 1H), 5.07 (s, 2H), 3.78 (s, 3H), 2.40 (s, 3H).

^{13}C NMR (101 MHz, DMSO-*d*$_6$): δ / ppm = 187.4, 144.6, 139.3, 135.2, 133.0, 118.0, 110.6, 101.1, 93.8, 55.4, 25.4.

HRMS (ESI): m/z calc. for [$C_{11}H_{13}N_2O_2$]: 205.0972 $[M+H]^+$

found: 205.0971.

IR (Diamond-ATR, neat): $\tilde{\nu}$ / cm^{-1} = 3459, 3361, 3294, 2922, 2362, 1679, 1636, 1609, 1520, 1504, 1463, 1353, 1296, 1271, 1209, 1149, 1021, 986, 938, 874, 848.

m.p.: 205–206 °C.

^{1}H NMR (400 MHz, DMSO-*d*$_6$):

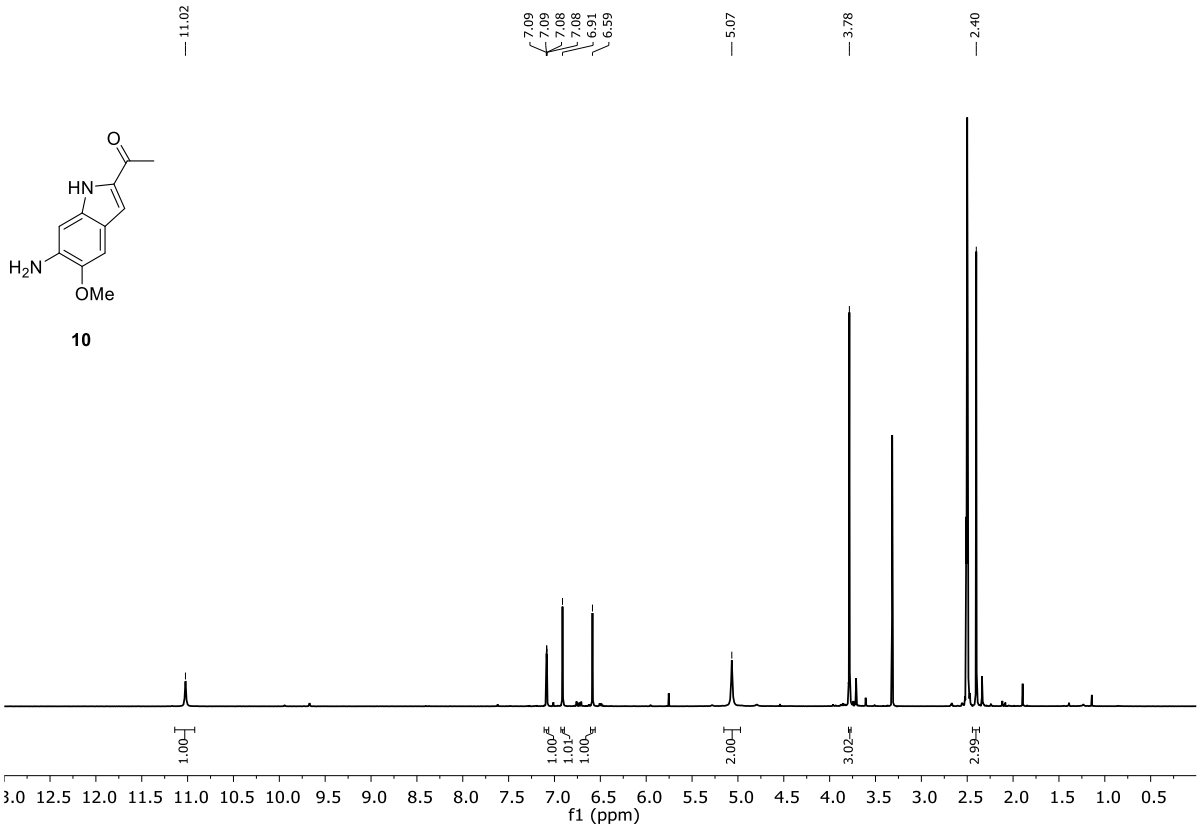

^{13}C NMR (101 MHz, DMSO-*d*$_6$):

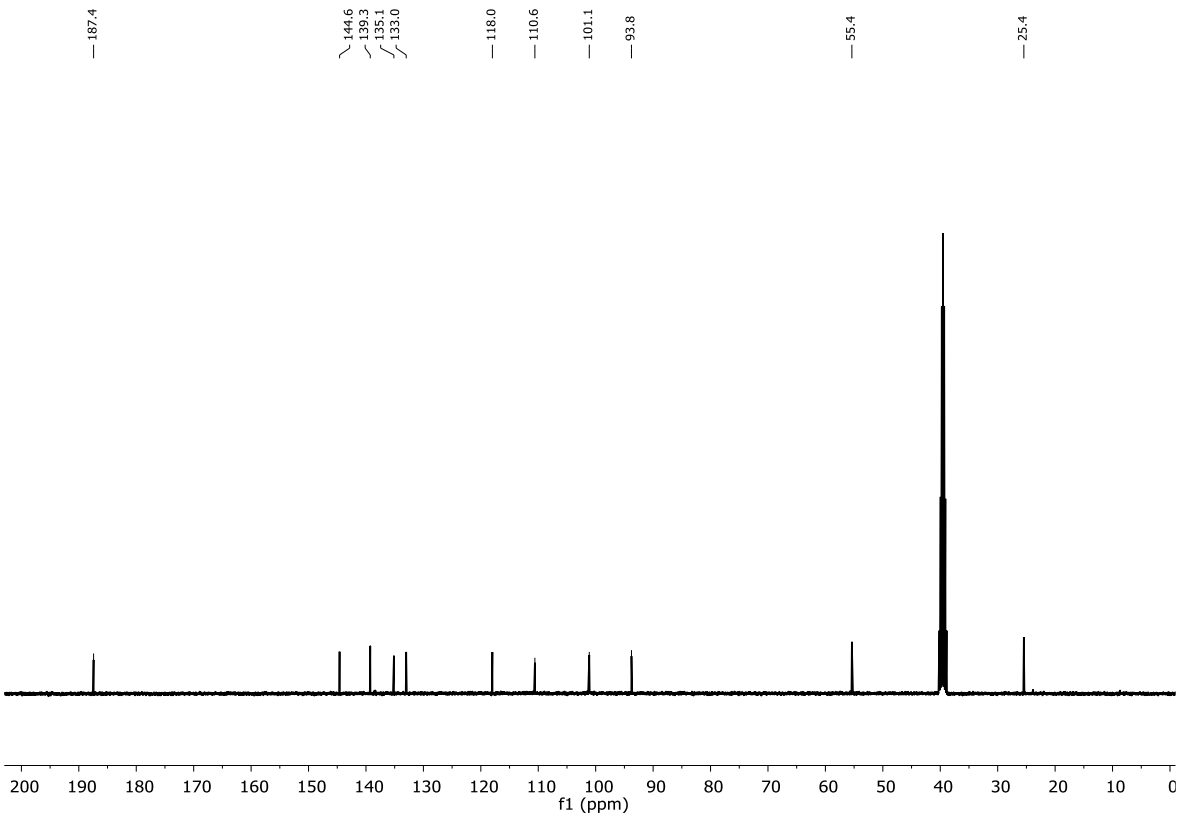

Methyl (*E*)-4-oxopent-2-enoate (12)

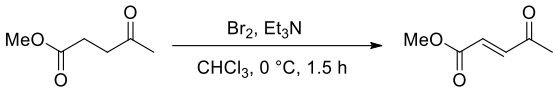

11 **12**: 44%

Adapted from a literature procedure[1] and performed under an inert atmosphere using SCHLENK techniques. Methyl levulinate (**11**) (3.99 g, 30.7 mmol, 1.0 equiv.) was dissolved in dry chloroform (10 mL) in a two-necked round-bottomed flask (100 mL) and cooled to 0 °C. A solution of bromine (1.8 mL, 35.1 mmol, 1.1 equiv.) in dry chloroform (6 mL) was added dropwise. The mixture was stirred at 0 °C for 1 h, allowed to warm to room temperature, and stirred for 30 min until the solution turned from brown to light yellow. Excess hydrogen bromide was removed under nitrogen flow. A solution of triethylamine (14.0 mL, 100 mmol, 3.3 equiv.) in dry chloroform (20 mL) was slowly added, and the reaction mixture was stirred for 30 min. The reaction mixture was washed with water (2 × 40 mL), hydrochloric acid (2 M, 2 × 40 mL), saturated sodium carbonate solution (2 × 40 mL), and brine (1 × 40 mL). The organic phase was carefully concentrated *in vacuo* (not less than 300 mbar). The resulting brown liquid was distilled by slowly heating from 50–130 °C in 10 °C steps under vacuum (8-11 mbar), and the product was collected in a cold trap to afford **12** (1.72 g, 13.4 mmol, 44%) as colorless crystals.

^{1}H NMR (400 MHz, $CDCl_3$): δ / ppm = 7.01 (d, J = 16.1 Hz, 1H), 6.64 (d, J = 16.1 Hz, 1H), 3.81 (s, 3H), 2.35 (s, 3H).

^{13}C NMR (101 MHz, $CDCl_3$): δ / ppm = 197.6, 166.0, 140.2, 131.2, 52.5, 28.3.

HRMS (EI): m/z calc. for $[C_5H_5O_3]$: 113.0233 $[M\text{-}CH_3]^+$

found: 113.0233.

IR (Diamond-ATR, neat): $\tilde{\nu}$ / cm^{-1} = 3061, 3008, 2957, 1719, 1675, 1644, 1456, 1429, 1362, 1316, 1264, 1253, 1197 1180, 1023, 1002, 994, 913, 879, 822, 717.

m.p.: 57–60 °C.

This procedure was part of the research internship of Rachel Janßen, conducted under my supervision, and was further optimized during her master thesis and PhD.

^{1}H NMR (400 MHz, $CDCl_3$):

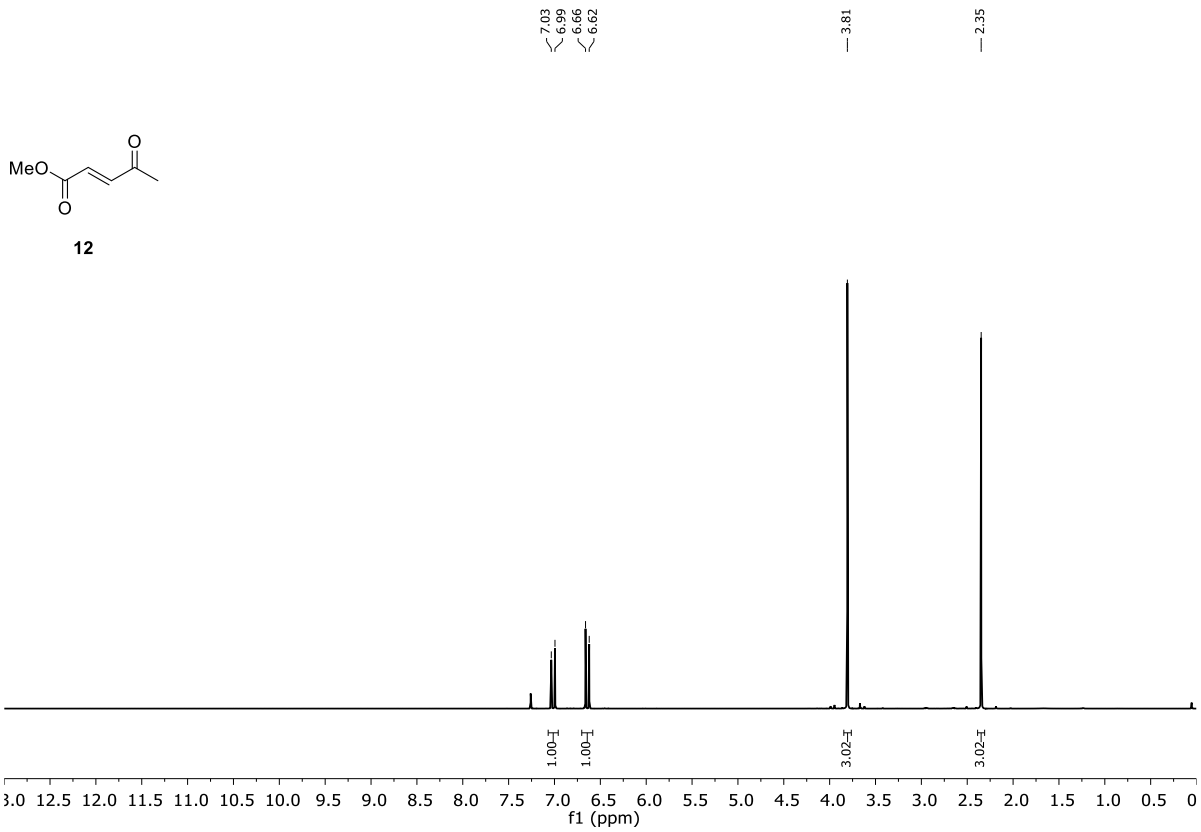

^{13}C NMR (101 MHz, $CDCl_3$):

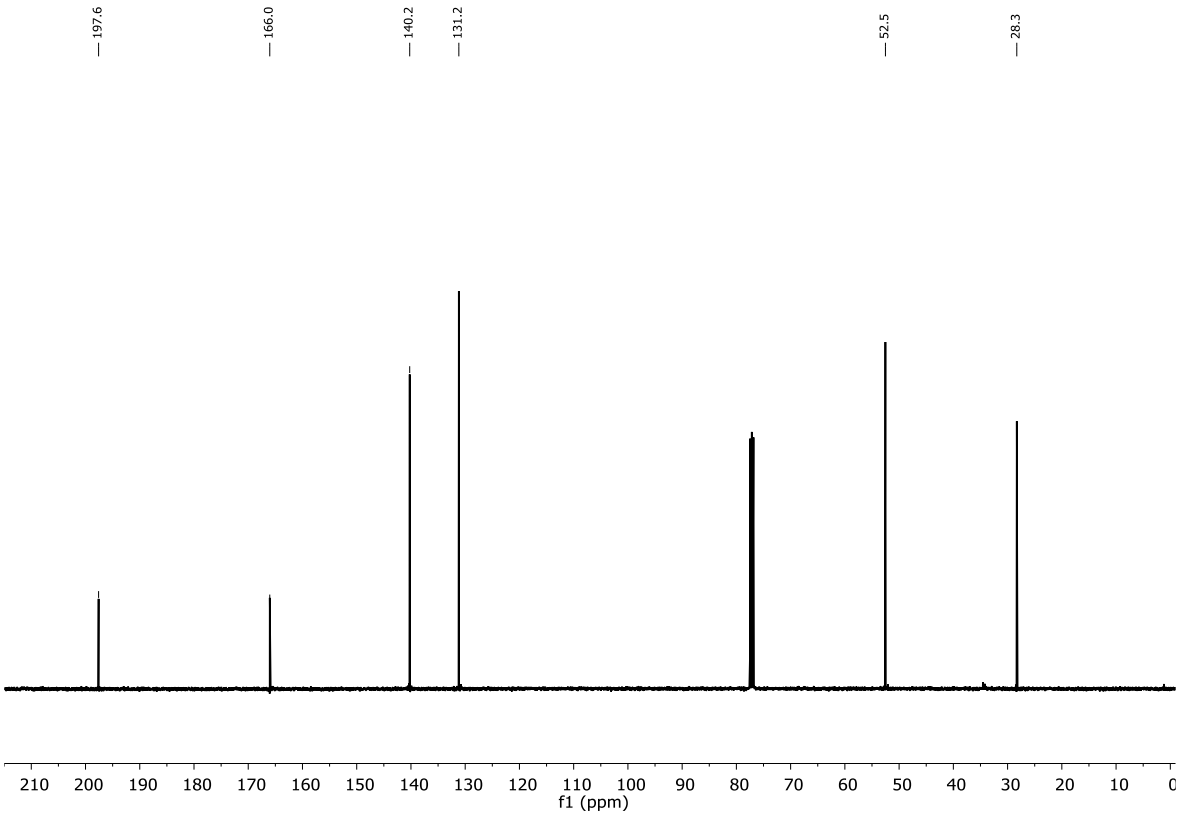

5-Methoxy-2,7-bis(methoxycarbonyl)-9-methylpyrrolo[2,3-*f*]quino-lin-1-ide (13)

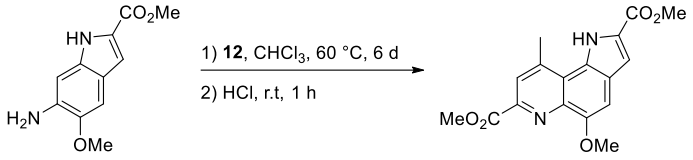

9 **13**: 71%

Adapted from a literature procedure.[1] Compounds **9** (552 mg, 2.5 mmol, 1.0 equiv.) and **12** (353 mg, 2.75 mmol, 1.1 equiv.) were suspended in chloroform (50 mL) in a round-bottomed flask, and the mixture was stirred at 60 °C for 6 d. After the reaction mixture had cooled to room temperature, hydrogen chloride generated *in situ* in a second reaction vessel (by dropping concentrated sulfuric acid on sodium chloride) was bubbled through the reaction mixture for 1 h. The reaction was stirred for 1 h at room temperature and then quenched with saturated sodium carbonate solution (30 mL). The layers were separated, and the aqueous layer was extracted with chloroform (2 × 30 mL). The combined organic layers were dried over sodium sulfate. The solvent was removed *in vacuo*, and the residue was purified by flash column chromatography (5% methanol in dichloromethane, R_f = 0.56) to afford **13** (585 mg, 1.78 mmol, 71%) as a light brown solid.

^{1}H NMR (400 MHz, DMSO-*d*$_6$): δ / ppm = 10.88 (s, 1H), 8.09 (d, J = 0.7 Hz, 1H), 7.47 (s, 1H), 7.39 (d, J = 1.9 Hz, 1H), 3.99 (s, 3H), 3.95 (s, 3H), 3.92 (s, 3H), 3.13 (s, 3H).

^{13}C NMR (101 MHz, DMSO-*d*$_6$): δ / ppm = 165.6, 161.0, 150.9, 144.0, 143.6, 140.1, 128.1, 126.2, 125.3, 122.9, 119.9, 109.7, 102.6, 55.7, 52.4, 52.0, 22.0.

HRMS (ESI): m/z calc. for [$C_{17}H_{15}N_2O_5$]: 327.0986 [M-H]$^-$

found: 327.0988.

IR (Diamond-ATR, neat): $\tilde{\nu}$ / cm^{-1} = 3480, 2953, 1711, 1694, 1648, 1616, 1540, 1507, 1483, 1442, 1431, 1384, 1351, 1294, 1276, 1256, 1205, 1168, 1132, 1102, 1046, 994, 935, 899, 883, 866, 851, 818, 782, 763, 713.

m.p.: 182–192 °C.

This procedure was part of the research internship of Rachel Janßen, conducted under my supervision, and was further optimized during her master thesis and PhD.

^{1}H NMR (400 MHz, DMSO-*d*$_6$):

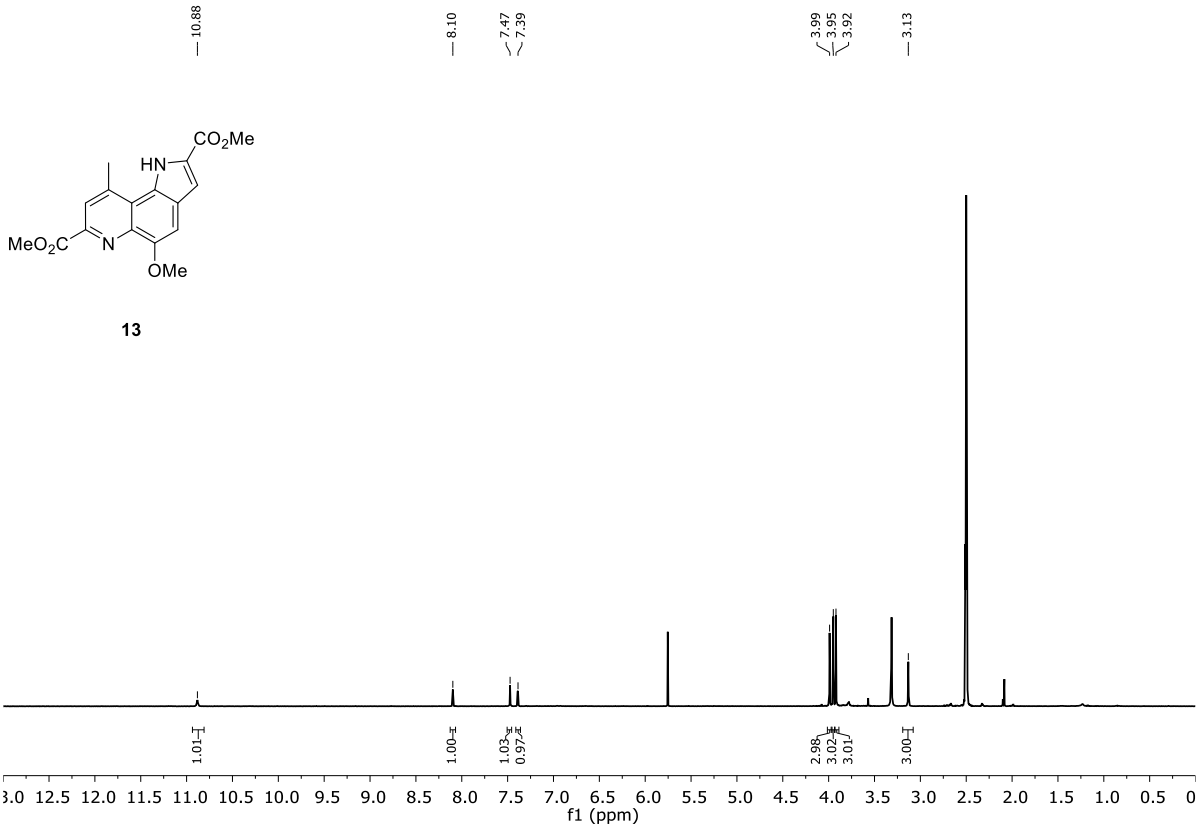

^{13}C NMR (101 MHz, DMSO-*d*$_6$):

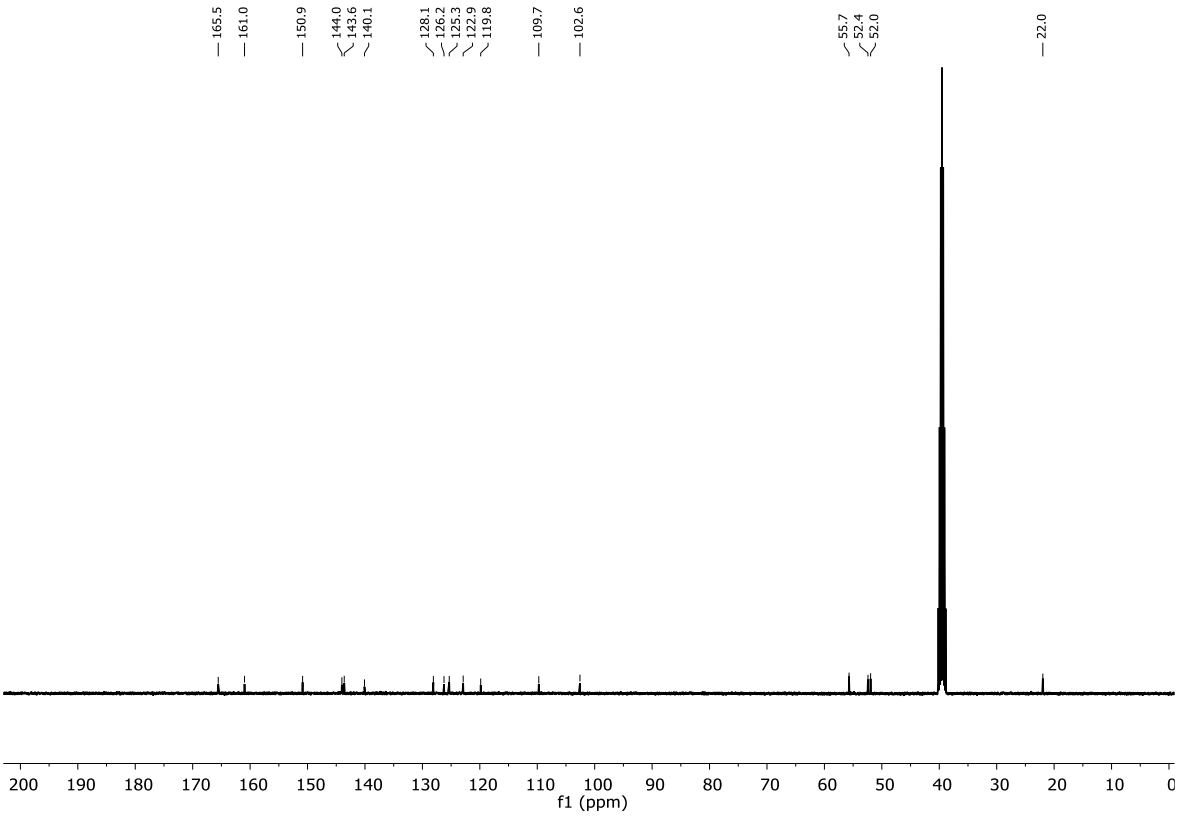

Methyl 2-acetyl-5-methoxy-9-methyl-1*H*-pyrrolo[2,3-*f*]quinoline-7-carboxylate (14)

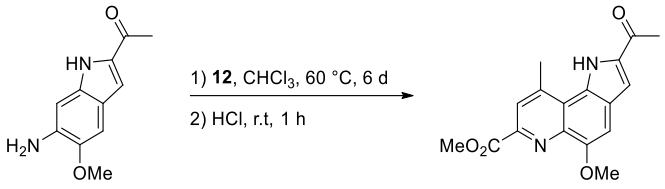

10 **14**: 69%

Adapted from a literature procedure.[1] Compounds **10** (316 mg, 1.55 mmol, 1.0 equiv.) and **12** (218 mg, 1.7 mmol, 1.1 equiv.) were suspended in chloroform (40 mL) in a round-bottomed flask and stirred at 60 °C for 6 d. After the reaction mixture had cooled to room temperature, hydrogen chloride generated *in situ* (by dropping concentrated sulfuric acid on sodium chloride) was bubbled through the reaction mixture for 1 h. The reaction was stirred for 1 h at room temperature and then quenched with saturated sodium carbonate solution (30 mL). The layers were separated, and the aqueous layer was extracted with chloroform (2 × 30 mL). The combined organic layers were dried over sodium sulfate. The solvent was removed *in vacuo*, and the residue was purified by flash column chromatography (2% methanol in dichloromethane, R_f = 0.29) to afford **14** (332 mg, 1.06 mmol, 69%) as a light brown solid.

^{1}H NMR (400 MHz, DMSO-*d*$_6$): δ / ppm = 10.62 (s, 1H), 8.10 (d, J = 0.7 Hz, 1H), 7.57 (d, J = 1.9 Hz, 1H) 7.47 (s, 1H), 4.00 (s, 3H), 3.95 (s, 3H), 3.12 (s, 3H), 2.62 (s, 3H).

^{13}C NMR (101 MHz, DMSO-*d*$_6$): δ / ppm = 189.0, 165.6, 150.9, 144.3, 143.9, 140.5, 136.3, 126.8, 125.5, 123.0, 119.9, 110.9, 102.7, 55.8, 52.5, 26.3, 21.9.

HRMS (ESI): m/z calc. for [$C_{17}H_{15}N_2O_4$]: 311.1037 [M-H]$^-$

found: 311.1039.

IR (Diamond-ATR, neat): $\tilde{\nu}$ / cm^{-1} = 3406, 3133, 2947, 1738, 1721, 1707, 1653, 1639, 1615, 1590, 1538, 1502, 1480, 1436, 1410, 1380, 1371, 1358, 1273, 1257, 1230, 1208, 1156, 1130, 1040, 1006, 984, 942, 909, 897, 881, 852, 782, 767, 687, 668.

m.p.: 236–236 °C.

This procedure was part of the research internship of Rachel Janßen, conducted under my supervision, and was further optimized during her master thesis and PhD.

^{1}H NMR (400 MHz, DMSO-*d*$_6$):

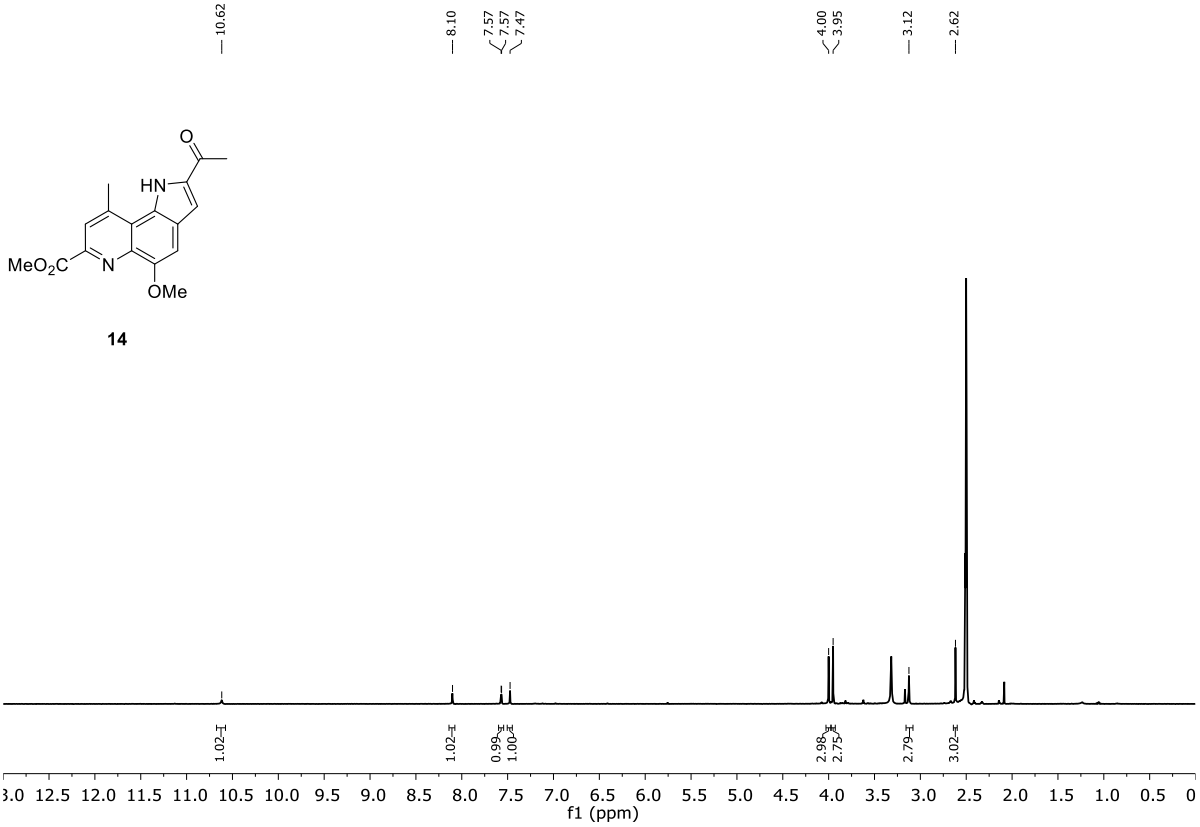

^{13}C NMR (101 MHz, DMSO-*d*$_6$):

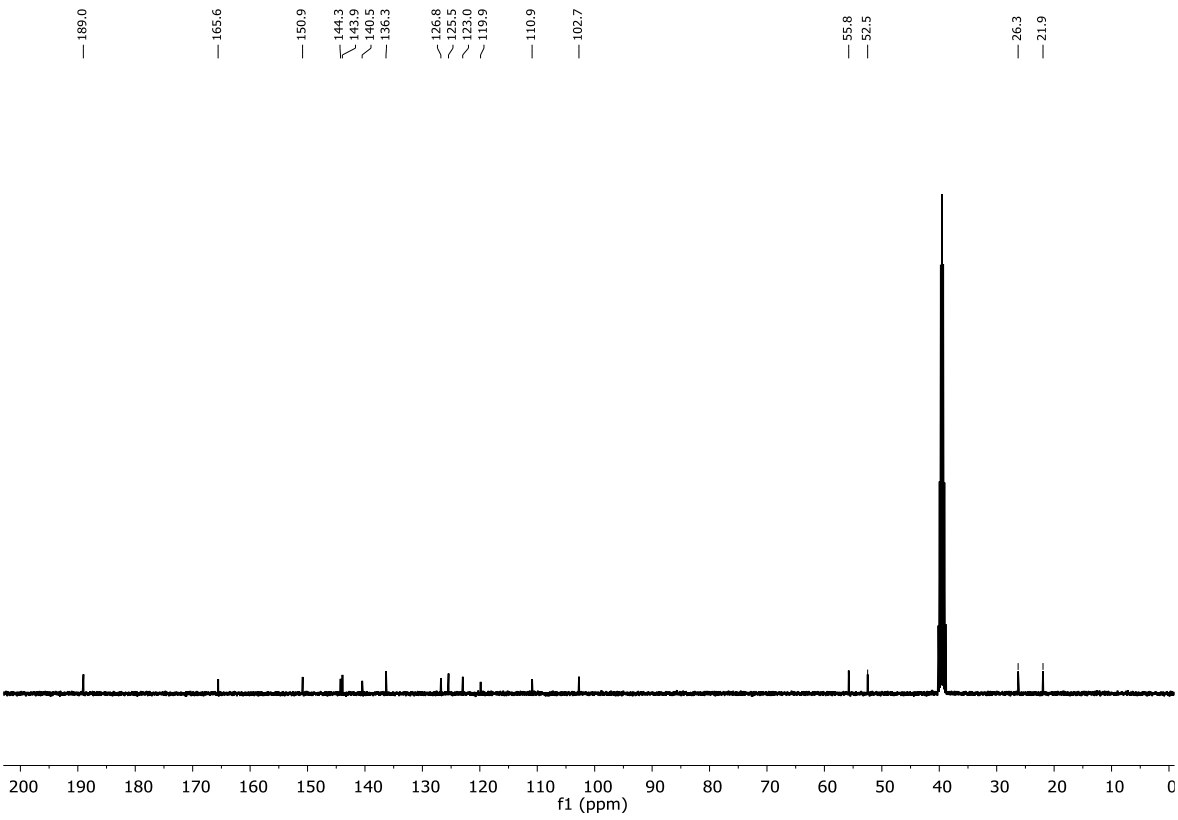

Dimethyl 9-methyl-4,5-dioxo-4,5-dihydro-1*H*-pyrrolo[2,3-*f*]quino-line-2,7-dicarboxylate ($P_{ME}QQ_{MEM}$)

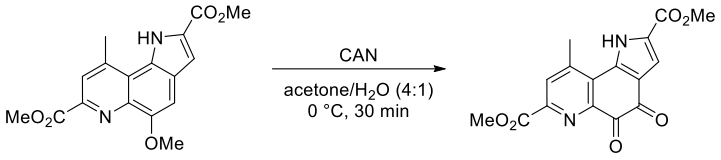

13 $P_{ME}QQ_{MEM}$: 31%

Adapted from a literature procedure.[1] Compound **13** (200 mg, 0.61 mmol, 1.0 equiv.) was suspended in acetonitrile/water (4:1, 6 mL), and the mixture was cooled to 0 °C. A solution of ceric ammonium nitrate (1.34 g, 2.44 mmol, 4.0 equiv.) in acetonitrile/water (4:1, 8 mL) was added, and the reaction mixture was stirred at 0 °C for 30 min. The precipitate was filtered off and washed with water and toluene/ethyl acetate (1:1). The solid was dried at 100 °C for 20 min and subsequently under high vacuum at room temperature to afford $P_{ME}QQ_{MEM}$ (61.2 mg, 0.19 mmol, 31%) as a red solid. R_f = 0.23, 2% methanol in dichloromethane. Crystals suitable for X-ray analysis were grown from dimethylformamide by slow vapor diffusion of diethyl ether.

^{1}H NMR (400 MHz, DMSO-d_6): δ / ppm = 11.44 (s, 1H), 8.15 (s, 1H), 7.30 (d, J = 1.5 Hz, 1H), 3.92 (s, 3H), 3.88 (s, 3H), 2.91 (s, 3H).

^{13}C NMR (101 MHz, DMSO-d_6): δ / ppm = 178.5, 173.7, 164.6, 160.0, 147.1, 145.6, 144.8, 137.2, 130.5, 128.1, 127.4, 123.8, 114.4, 52.7, 52.2, 20.8.

HRMS (ESI): m/z calc. for $[C_{16}H_{11}N_2O_6]$: 327.0623 $[M-H]^-$

found: 327.0624.

IR (Diamond-ATR, neat): $\tilde{\nu}$ / cm^{-1} = 3599, 3515, 3128, 3080, 2970, 1713, 1674, 1613, 1592, 1570, 1497, 1477, 1437, 1403, 1383, 1365, 1316, 1294, 1237, 1202, 1178, 1138, 1072, 1052, 1039, 998, 982, 929 907, 861, 828, 789, 763, 735, 699, 680, 663.

m.p.: 253–256 °C.

X-Ray Crystallographic Data: Crystallographic data have been deposited with the Cambridge Crystallographic Data Centre, CCDC, 12 Union Road, Cambridge CB21EZ, UK. Copies of the data can be obtained free of charge on quoting the depository numbers CCDC-2193479 (https://www.ccdc.cam.ac.uk/structures/).

This procedure was part of the research internship of Rachel Janßen, conducted under my supervision, and was further optimized during her master thesis and PhD.

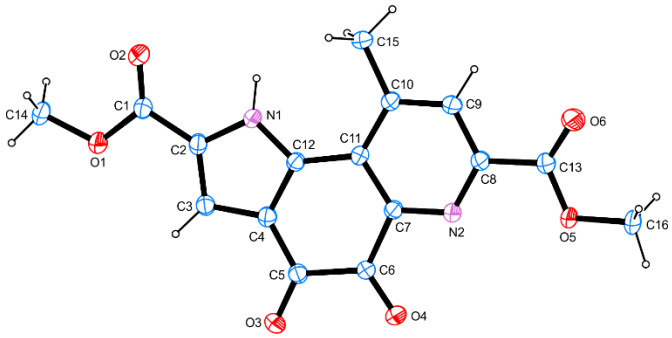

Figure V.1: ORTEP[308] representation of the molecular structure of ***PMEQQMEM****.*

Table V.1: Crystallographic data for ***PMEQQMEM****.*

PMEQQMEM	
net formula	$C_{16}H_{12}N_2O_6$
M_r/g mol^{-1}	328.28
crystal size/mm	0.060 × 0.050 × 0.030
T/K	102.(2)
radiation	MoKα
diffractometer	'Bruker D8 Venture TXS'
crystal system	monoclinic
space group	'C 1 2/c 1'
a/Å	8.5929(5)
b/Å	21.5998(13)
c/Å	15.3761(10)
α/°	90
β/°	105.320(2)
γ/°	90
V/Å^3	2752.5(3)
Z	8
calc. density/g cm^{-3}	1.584
μ/mm^{-1}	0.124
absorption correction	Multi-Scan
transmission factor range	0.93–1.00
refls. measured	26705
R_{int}	0.0483
mean $\sigma(I)/I$	0.0266
θ range	2.632–27.485
observed refls.	2584
x, y (weighting scheme)	0.0419, 4.3094
hydrogen refinement	H(C) constr, H(N) refall
refls in refinement	3158
parameters	224
restraints	0
$R(F_{obs})$	0.0415
$R_w(F^2)$	0.1101
S	1.043
shift/error$_{max}$	0.001
max electron density/e Å^{-3}	0.380
min electron density/e Å^{-3}	−0.441

^{1}H NMR (400 MHz, DMSO-*d*$_6$):

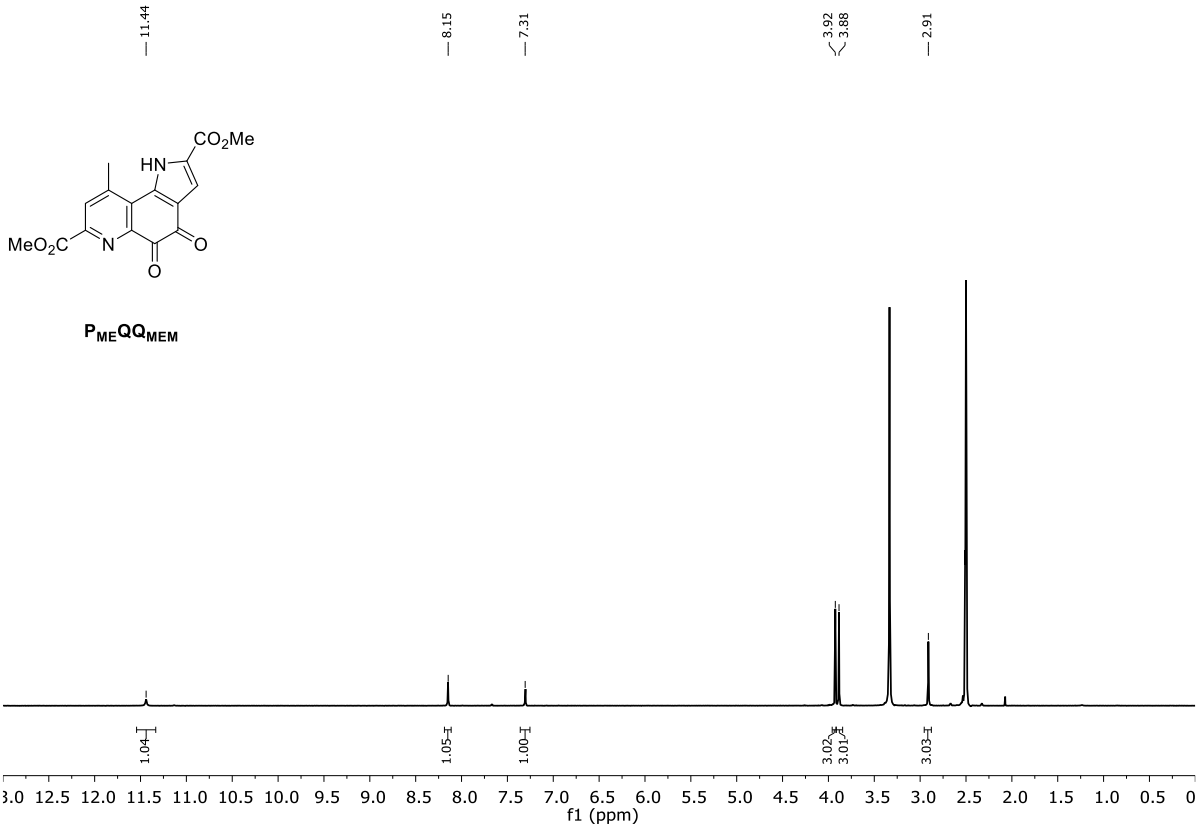

$P_{ME}QQ_{MEM}$

^{13}C NMR (101 MHz, DMSO-*d*$_6$):

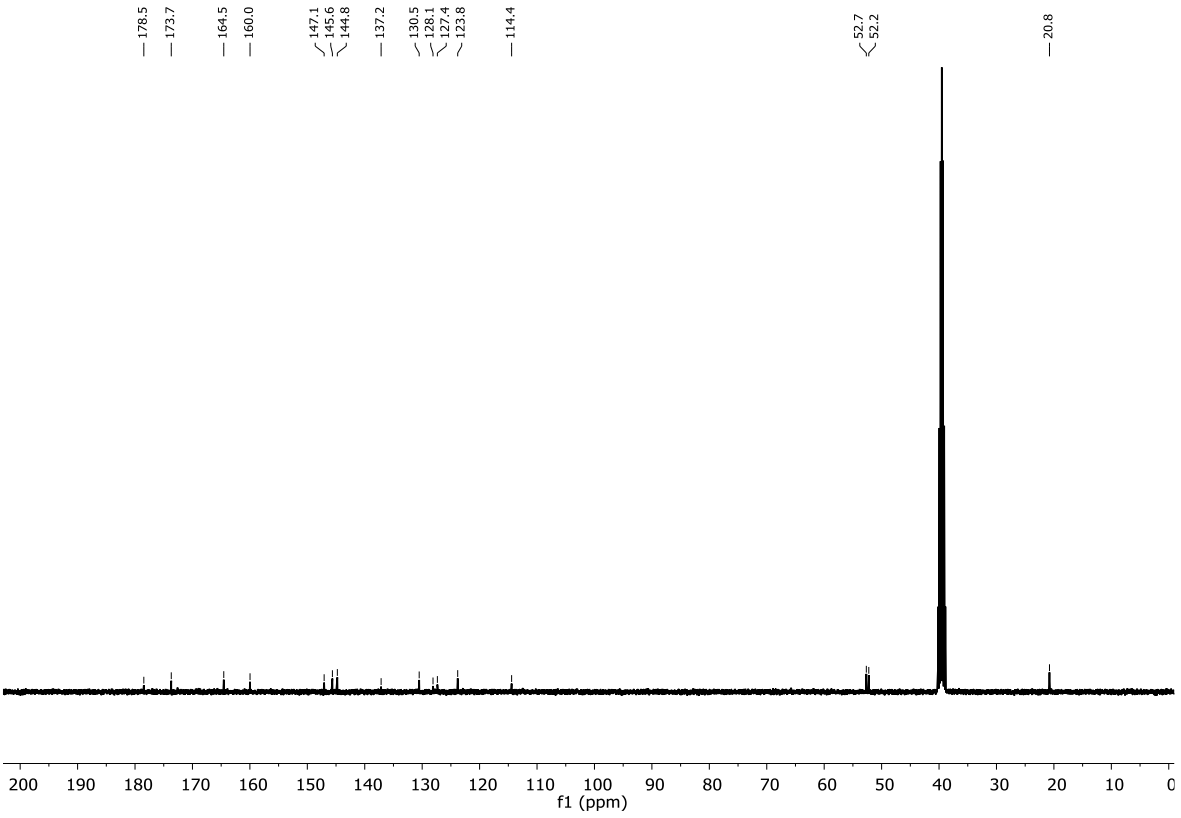

Methyl 2-acetyl-9-methyl-4,5-dioxo-4,5-dihydro-1*H*-pyrrolo[2,3-*f*]quinoline-7-carboxylate (PKQQMEM)

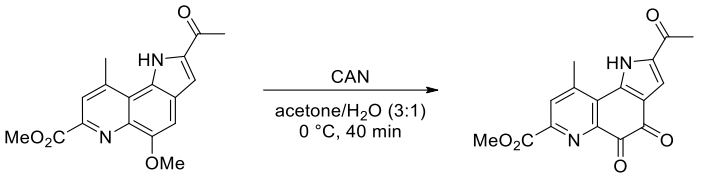

14 **P_KQQ_{MEM}**: 46%

Adapted from a literature procedure.[1] Compound **14** (200 mg, 0.64 mmol, 1.0 equiv.) was suspended in acetonitrile/water (3:1, 5 mL) in a round-bottomed flask, and the mixture was cooled to 0 °C. A solution of ceric ammonium nitrate (1.42 g, 2.56 mmol, 4.0 equiv.) in acetonitrile/water (3:1, 6 mL) was added, and the reaction mixture was stirred at 0 °C for 40 min. The precipitate was filtered off and washed with acetonitrile/water (3:1). The solid was dried at 100 °C for 1 h and subsequently under high vacuum at room temperature to afford **PKQQMEM** (91.7 mg, 0.29 mmol, 46%) as a red solid. R_f = 0.21, 2% methanol in dichloromethane.

^{1}H NMR (400 MHz, DMSO-*d*$_6$): δ / ppm = 11.13 (s, 1H), 8.15 (s, 1H), 7.67 (d, J = 1.9 Hz, 1H), 3.93 (s, 3H), 2.91 (s, 3H), 2.53 (s, 3H).

^{13}C NMR (101 MHz, DMSO-*d*$_6$): δ / ppm = 188.3, 178.5, 173.9, 164.5, 147.3, 145.8, 145.0, 137.7, 135.5, 130.5, 128.0, 123.9, 116.0, 52.7, 26.1, 20.7.

HRMS (ESI): m/z calc. for [$C_{16}H_{11}N_2O_5$]: 311.0673 $[M-H]^-$

found: 311.0674.

IR (Diamond-ATR, neat): $\tilde{\nu}$ / cm^{-1} = 3362, 3114, 3068, 2960, 2925, 2852, 1705, 1658, 1590, 1493, 1447, 1425, 1379, 1354, 1308, 1279, 1236, 1221, 1198, 1146, 1106, 1074, 1036, 1018, 993, 944, 934, 914, 885, 830, 795, 760, 713, 687, 681, 669.

m.p.: 281–285 °C.

This procedure was part of the research internship of Rachel Janßen, conducted under my supervision, and was further optimized during her master thesis and PhD.

^{1}H NMR (400 MHz, DMSO-*d*$_6$):

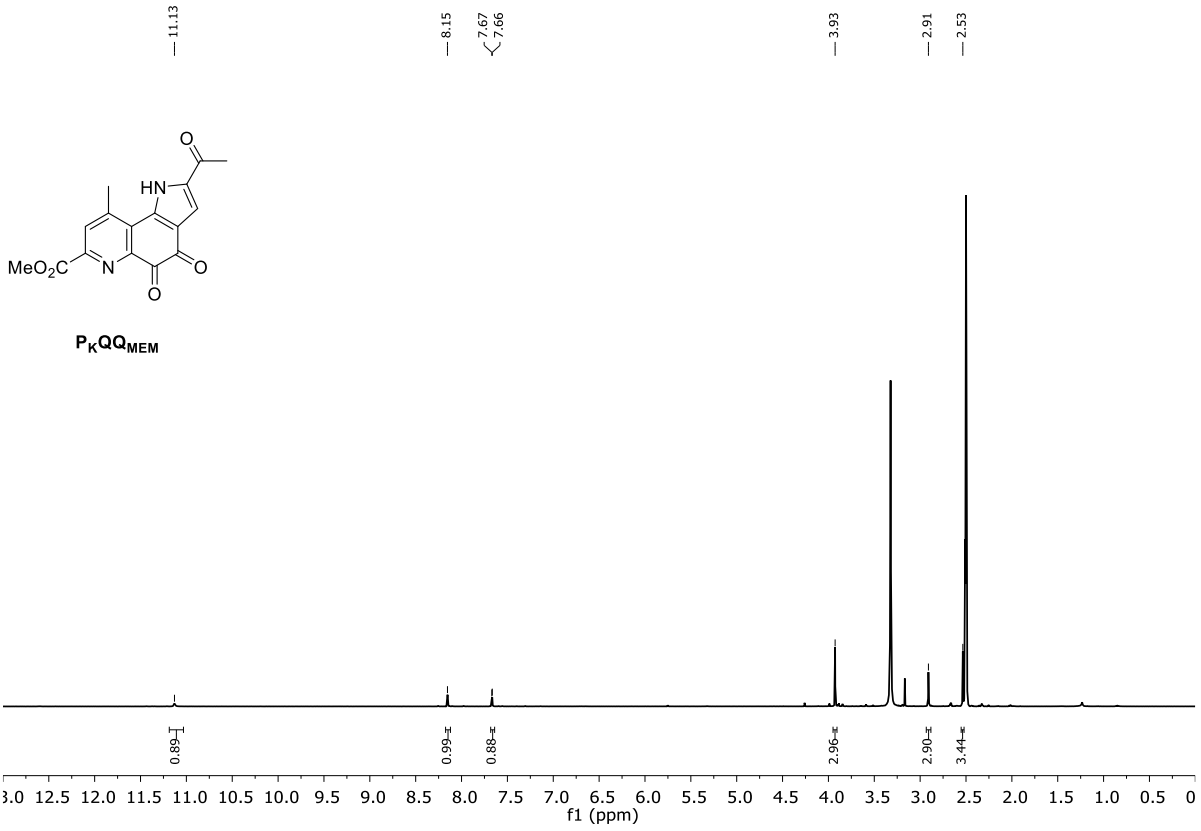

^{13}C NMR (101 MHz, DMSO-*d*$_6$):

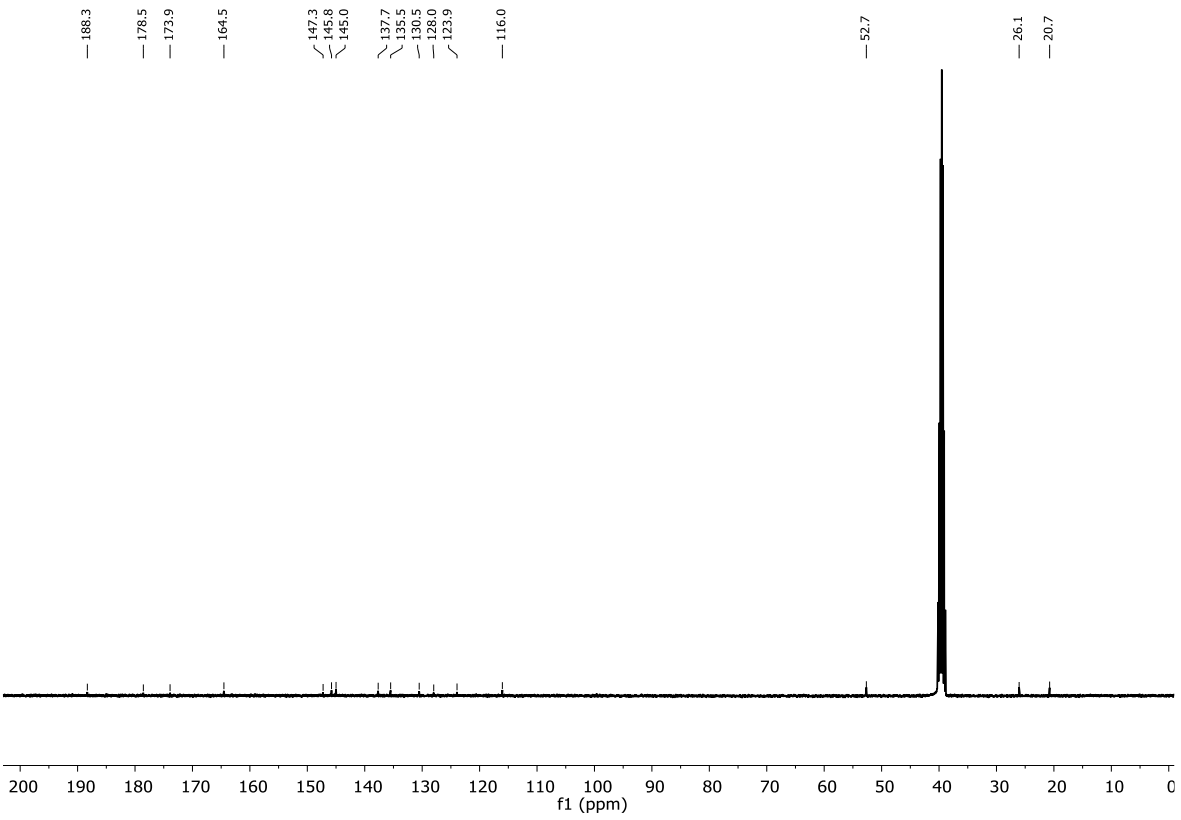

3.2. Synthesis of PQQ Aza-Crown Ligands

Trimethyl 4,5-dioxo-4,5-dihydro-1*H*-pyrrolo[2,3-*f*]quinoline-2,7,9-tricarboxylate (PQQMe$_3$)

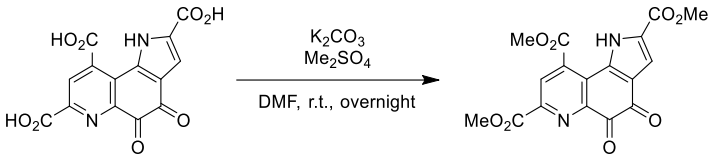

PQQ **PQQMe$_3$**: 91%

Based on procedures, described by Duine *et al.*[168] and Urakami *et al.*[309] in a dry and nitrogen flushed SCHLENK flask, **PQQ** (50.0 mg, 0.151 mmol, 1.0 equiv.) was dissolved in dry DMF (2 mL). Potassium carbonate (523 mg, 3.79 mmol, 25.0 equiv.), which was previously dried under high vacuum at 650 °C (heat gun), was given to the PQQ solution under nitrogen counter-flow. Dimethyl sulfate (1.55 mL, 1.33 g/mL, 16.3 mmol, 108 equiv.) was added, and the mixture was stirred at room temperature and under nitrogen overnight to give a bright orange suspension. In order to completely remove K_2CO_3 residues and to quench the excess of Me_2SO_4, HCl (8 mL 2 M and 1 mL conc.) was added, and the mixture was further stirred for 5 h. The orange precipitate was filtered off, and the residue was washed with water and dried under high vacuum to give pure **PQQMe$_3$** (51 mg, 0.137 mmol, 91%).

^{1}H NMR (400 MHz, DMSO-*d*$_6$): δ / ppm = 12.51 (s, 1H), 8.56 (s, 1H), 7.29 (d, J = 2.1 Hz, 1H), 4.05 (s, 3H), 3.96 (s, 3H), 3.89 (s, 3H).

^{13}C NMR (101 MHz, DMSO-*d*$_6$): δ / ppm = 177.0, 173.3, 166.5, 163.8, 159.8, 148.9, 145.7, 134.2, 133.5, 128.5, 126.6, 126.5, 125.0, 113.8, 54.2, 52.9, 52.4.

HRMS (ESI): m/z calc. for [$C_{17}H_{13}N_2O_8$]: 373.0666 $[M+H]^+$

found: 373.0665.

IR (Diamond-ATR, neat): $\tilde{\nu}$ / cm^{-1} = 3126, 1717, 1679, 1552, 1495, 1429, 1345, 1266, 1200, 1171, 1115, 1075, 995, 953, 923, 900, 834, 807, 783, 769, 754, 733, 720, 689, 672.

Elemental analysis (CHN): % calc. for [$C_{17}H_{12}N_2O_{13}$]: C 54.85, H 3.25, N 7.52

found: C 54.59, H 3.36, N 7.48.

^{1}H NMR (400 MHz, DMSO-d_6):

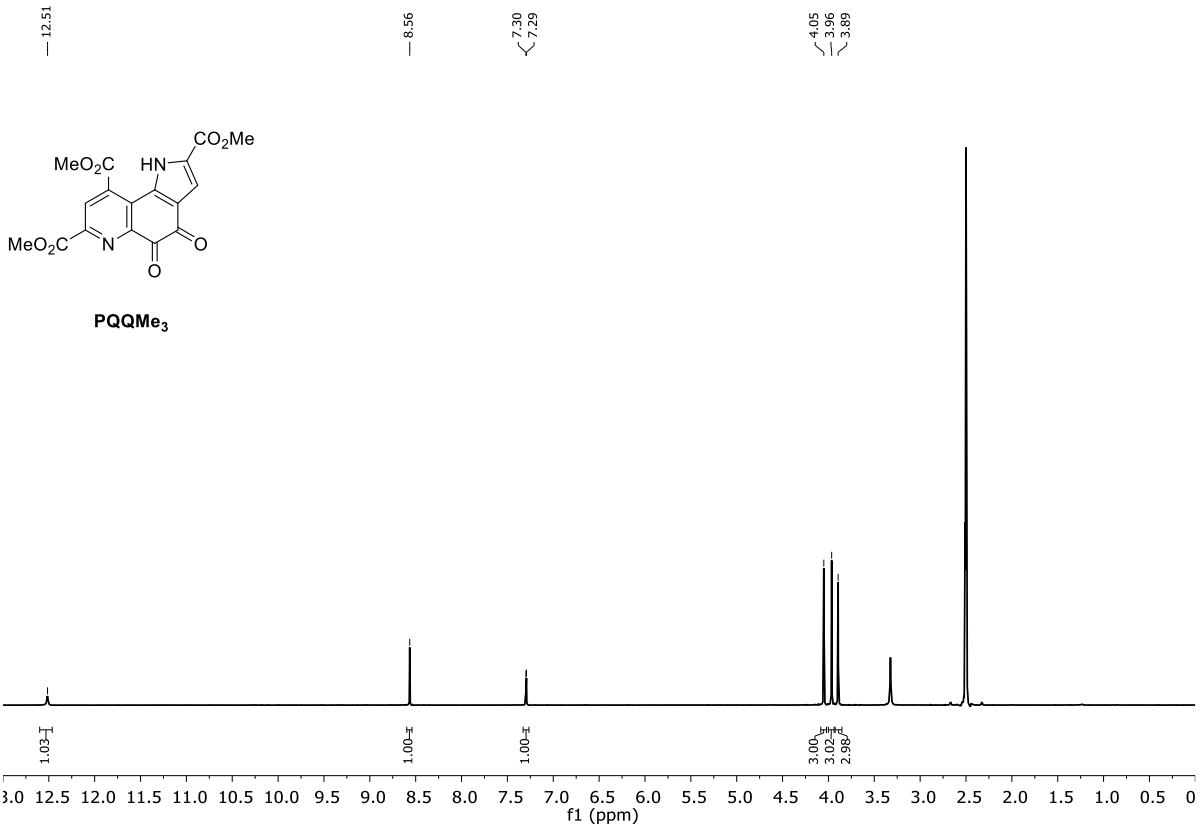

PQQMe$_3$

^{13}C NMR (101 MHz, DMSO-d_6):

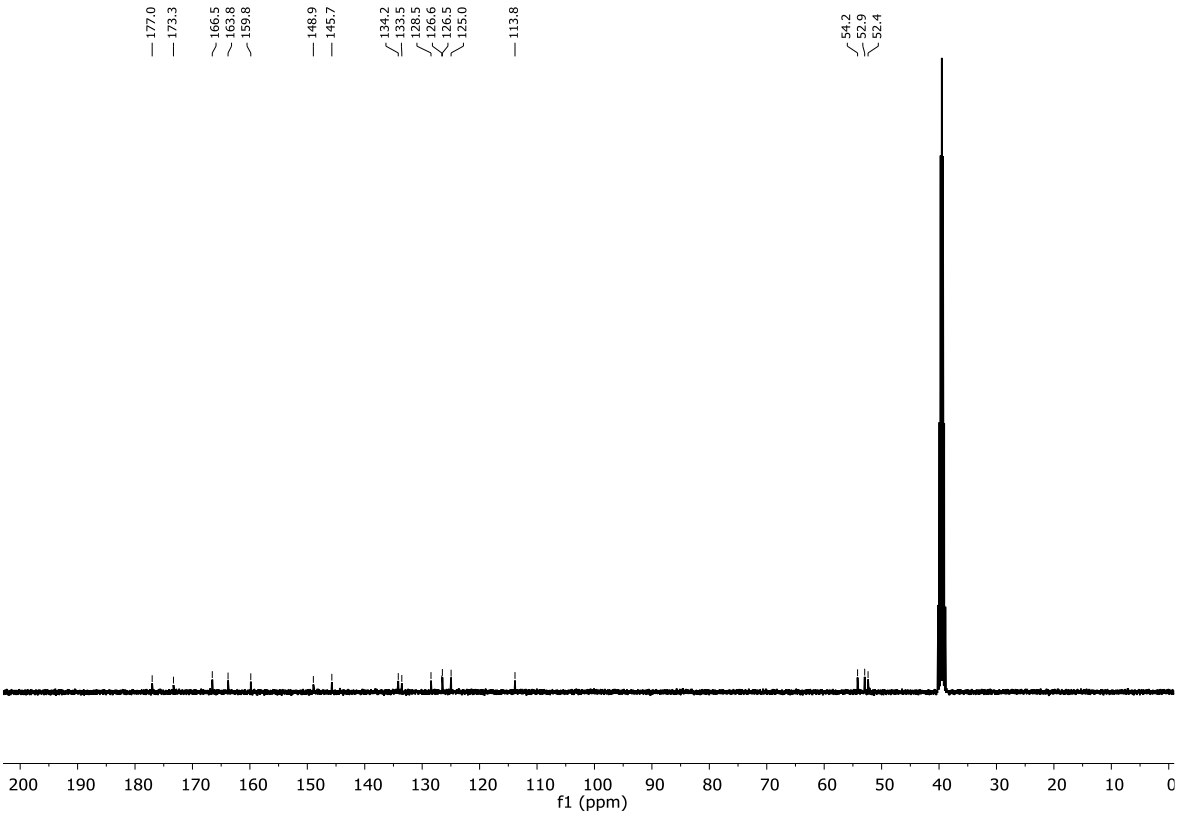

2,9-bis(methoxycarbonyl)-4,5-dioxo-4,5-dihydro-1*H*-pyrrolo[2,3-*f*]quinoline-7-carboxylic acid (PQQMe$_2$)

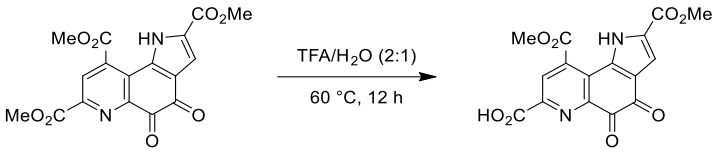

PQQMe$_3$ **PQQMe$_2$**: 92%

PQQMe$_3$ (50 mg, 0.134 mmol) was put into a 10 mL round-bottomed flask, and a 1:2 mixture of H_2O/TFA (2 mL) was added. The dark red solution was stirred at 60 °C for 12 h. After cooling down to room temperature, H_2O (5 mL) was added, which caused immediate precipitation of a dark red solid. The precipitate was filtered off, washed with H_2O, dried first at 100 °C for several hours and then under high vacuum overnight, to afford 44 mg (0.123 mmol, 92%) of **PQQMe$_2$** as a red powder.

^{1}H NMR (400 MHz, DMSO-*d*$_6$): δ / ppm = 12.52 (s, 1H), 8.56 (s, 1H), 7.28 (d, J = 1.4 Hz, 1H), 4.05 (s, 3H), 3.89 (s, 3H).

^{13}C NMR (101 MHz, DMSO-*d*$_6$): δ / ppm = 177.2, 173.4, 166.7, 164.8, 159.9, 148.9, 147.0, 134.1, 133.8, 128.5, 126.4, 126.3, 124.8, 113.8, 54.2, 52.4.

HRMS (ESI): m/z calc. for [$C_{16}H_{11}N_2O_8$]: 359.0512 $[M+H]^+$

found: 359.0510.

IR (Diamond-ATR, neat): $\tilde{\nu}$ / cm^{-1} = 3443, 3101, 1762, 1706, 1675, 1551, 1495, 1435, 1362, 1287, 1240, 1209, 1156, 1133, 1058, 994, 960, 921, 870, 768, 692.

Elemental analysis (CHN): % calc. for [$C_{16}H_{10}N_2O_8 \cdot 1.2H_2O$]: C 50.59, H 3.29, N 7.37

found: C 50.54, H 3.21, N 7.53.

^{1}H NMR (400 MHz, DMSO-*d*$_6$):

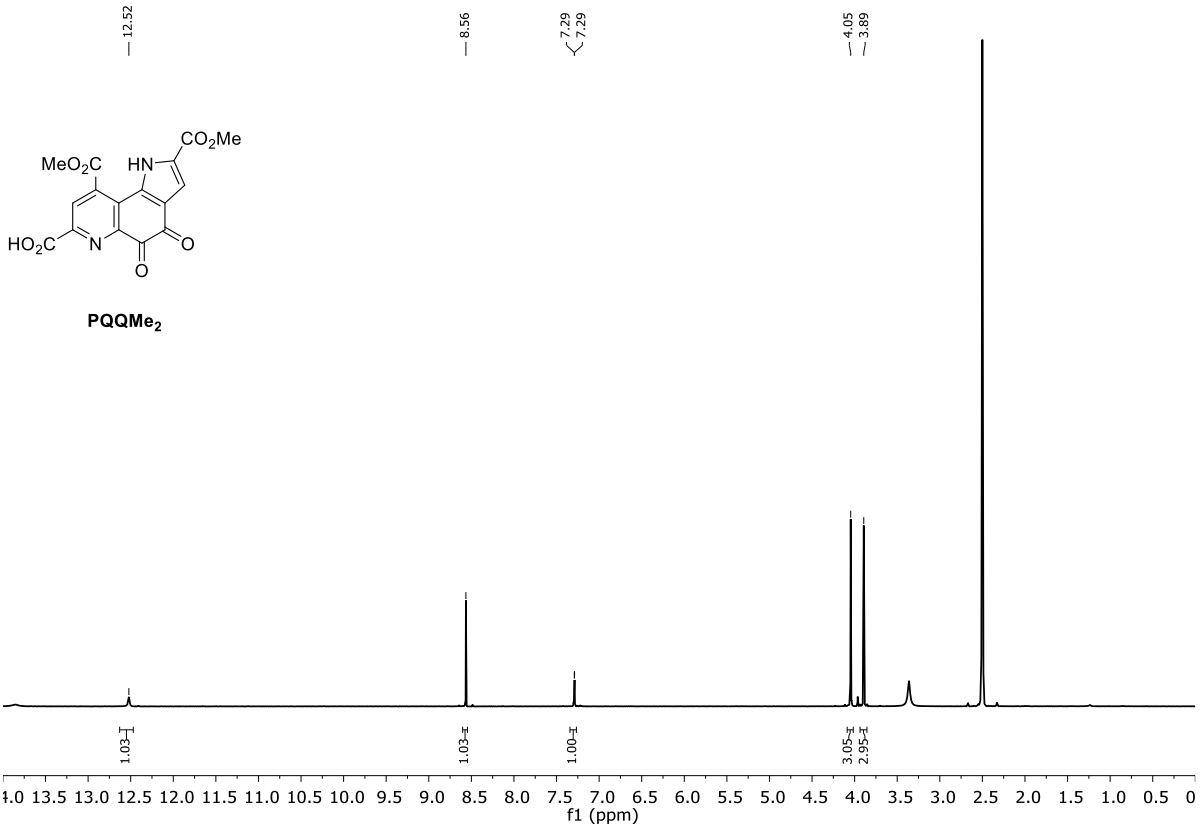

PQQMe$_2$

^{13}C NMR (101 MHz, DMSO-*d*$_6$):

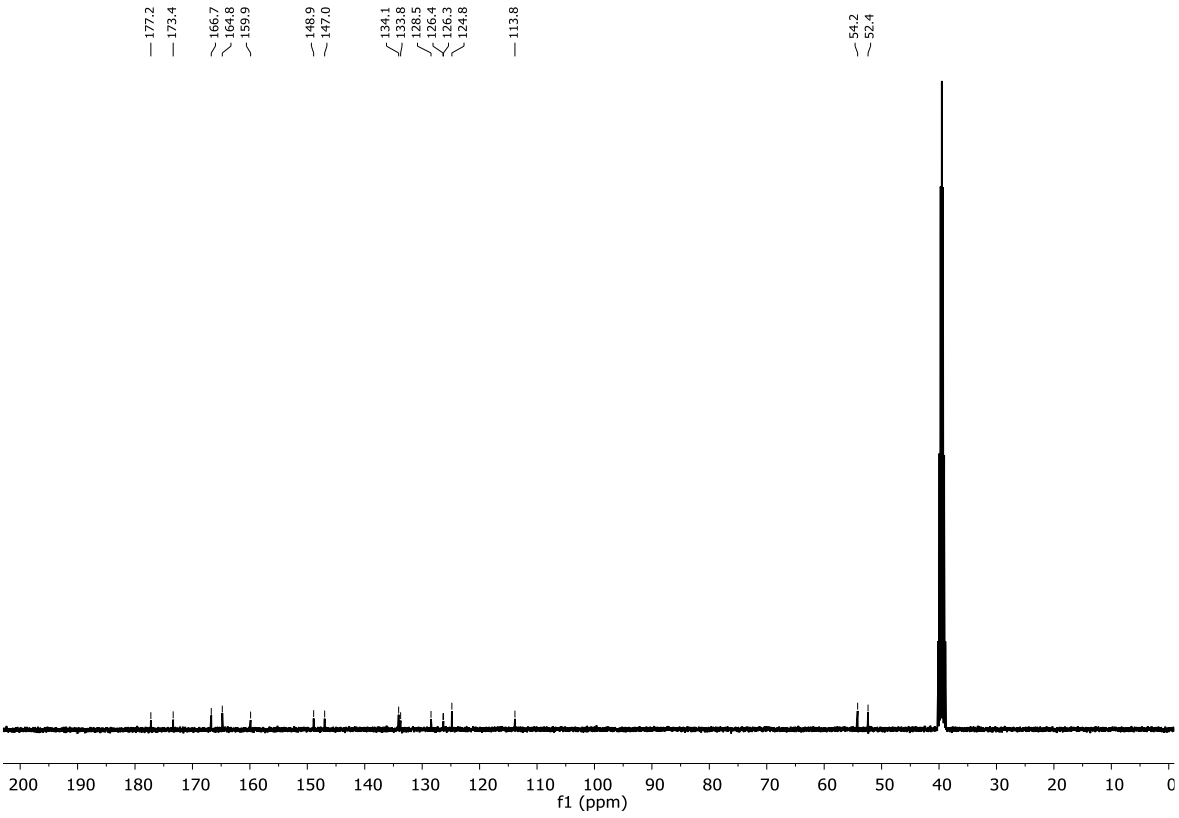

Dimethyl 7-(1,4,7,10-tetraoxa-13-azacyclopentadecane-13-carbonyl)-4,5-dioxo-4,5-dihydro-1*H*-pyrrolo[2,3-*f*]quinoline-2,9-dicarboxylate ($PQQ_{15\text{-}5}$)

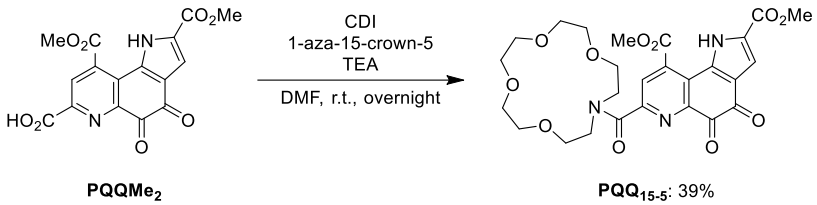

In a dry and nitrogen flushed SCHLENK flask, equipped with a magnetic stirring bar and a septum, **$PQQMe_2$** (101 mg, 0.282 mmol, 1.0 equiv.) and CDI (93.0 mg, 0.573 mmol, 2.0 equiv.) were dissolved in dry DMF (4 mL) and were stirred for 30 min at room temperature. In a second dry and nitrogen flushed flask, 1-aza-15-crown-5 (62.2 mg, 0.284 mmol, 1.0 equiv.) was dissolved in dry DMF (2 mL) and TEA (0.08 mL, 0.726 g/mL, 0.573 mmol, 2.0 equiv.) was added. Subsequently, the amine solution was added to the solution of the activated acid and the reaction mixture was stirred at room temperature overnight. After completion of the reaction, the solvent was removed *in vacuo*. The crude product was suspended in H_2O (20 mL) and extracted with CH_2Cl_2 (3 × 20 mL). The combined organic layers were washed with 1 M HCl (20 mL) and H_2O (20 mL). The solvent was evaporated and the residue was suspended in H_2O (10 mL). The suspension was centrifuged (5 min at 4500 rpm) and the supernatant was removed. The residue was vortex-mixed with H_2O, centrifuged again and lyophilized to give $PQQMe_2$-1-aza-15-crown-5 (**$PQQ_{15\text{-}5}$**, 62.5 mg, 0.112 mmol, 39%) as a brown-red solid.

^{1}H NMR (400 MHz, CD_3CN): δ / ppm = 12.61 (s, 1H), 8.35 (s, 1H), 7.33 (s, 1H), 4.08 (s, 3H), 3.91 (s, 3H), 3.83–3.77 (m, 5H), 3.72–3.71 (m, 2H), 3.62–3.55 (m, 15H).

^{13}C NMR (101 MHz, CD_3CN): δ / ppm = 180.4, 174.4, 168.9, 168.0, 161.2, 155.0, 147.8, 135.6, 135.3, 130.4, 128.2, 126.4, 125.4, 115.0, 71.6, 71.4, 70.9, 70.8, 70.7, 69.1, 55.3, 53.1, 52.2, 50.2.

HRMS (ESI): m/z calc. for $[C_{26}H_{28}N_3O_{11}]$: 558.1729 $[M\text{-}H]^-$

found: 558.1728.

IR (Diamond-ATR, neat): $\tilde{\nu}$ / cm^{-1} = 2920, 2851, 2360, 1713, 1679, 1622, 1575, 1558, 1496, 1475, 1436, 1404, 1346, 1283, 1253, 1227, 1204, 1118, 1070, 1002, 983, 936, 840, 796, 771, 757, 737, 722, 707, 699.

Elemental analysis (CHN): % calc. for $[C_{26}H_{29}N_3O_{11}\cdot 0.04C_3H_7NO]$: C 55.78, H 5.25, N 7.57

found: C 55.75, H 5.34, N 7.49.

This procedure was first investigated by Henning Lumpe, but was further optimized as part of this dissertation.

^{1}H NMR (400 MHz, CD_3CN):

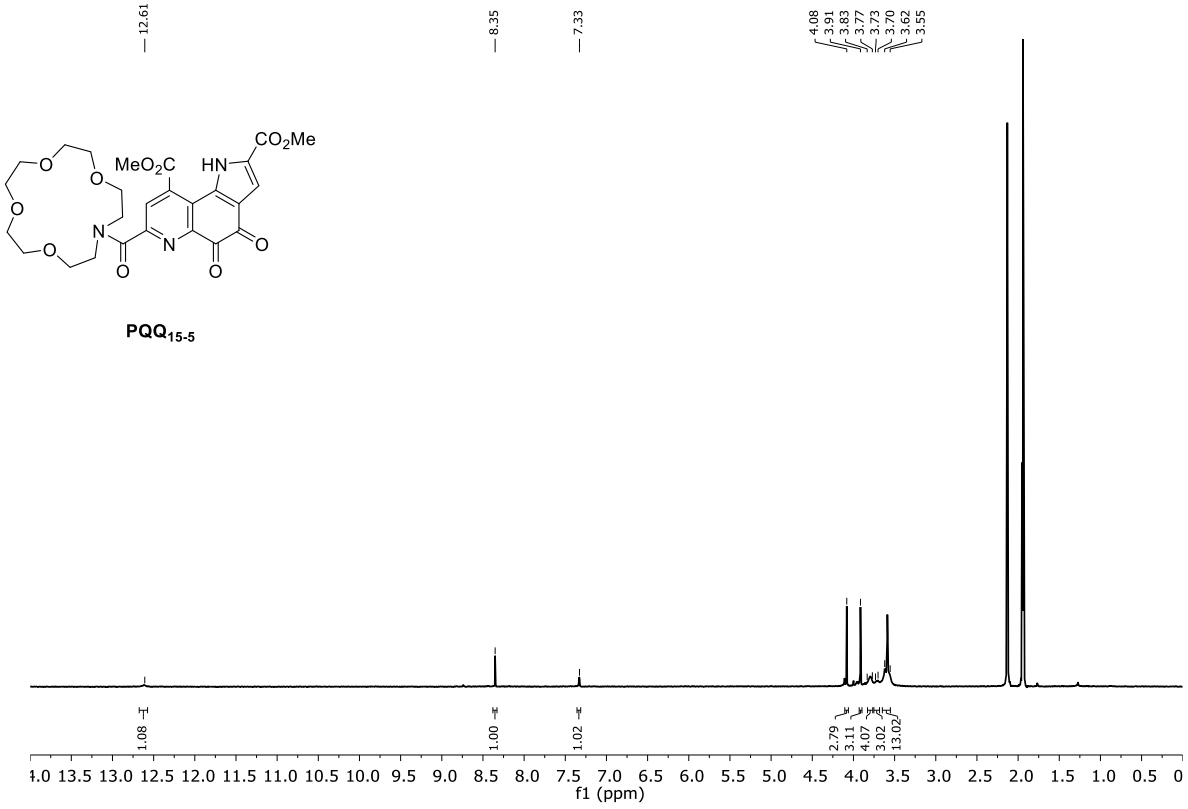

PQQ$_{15\text{-}5}$

^{13}C NMR (101 MHz, CD_3CN):

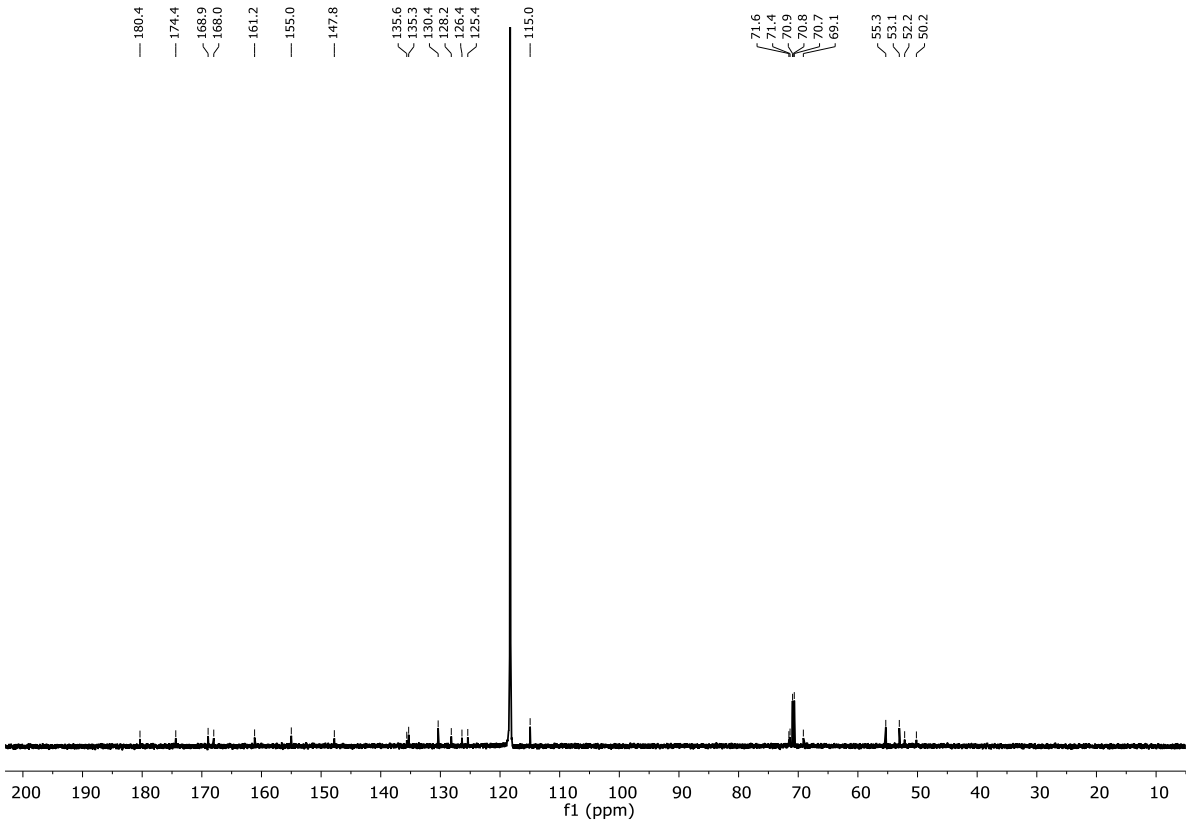

Dimethyl 7-(1,4,7,10,13-pentaoxa-16-azacyclooctadecane-16-carbonyl)-4,5-dioxo-4,5-dihydro-1*H*-pyrrolo[2,3-*f*]quinoline-2,9-dicarboxylate ($PQQ_{18\text{-}6}$)

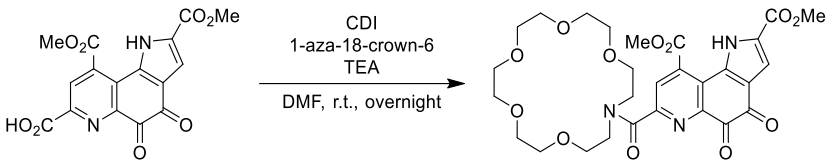

$PQQMe_2$ **$PQQ_{18\text{-}6}$**: 60%

In a dry and nitrogen flushed SCHLENK flask, equipped with a magnetic stirring bar and a septum, **$PQQMe_2$** (102.6 mg, 0.286 mmol, 1.0 equiv.) and CDI (58.5 mg, 0.361 mmol, 1.3 equiv.) were dissolved in dry DMF (5 mL). In a second dry and nitrogen flushed flask, 1-aza-18-crown-6 (92.0 mg, 0.349 mmol, 1.2 equiv.) was dissolved in dry DMF (1 mL) and TEA (0.1 mL, 0.726 g/mL, 0.717 mmol, 2.5 equiv.) was added. Subsequently, the amine solution was added to the solution of the activated acid and the reaction mixture was stirred at room temperature overnight. After completion of the reaction, the solvent was removed *in vacuo* and the residue was dried under high vacuum. The received solid was dissolved in H_2O (40 mL) and extracted with DCM (3 × 20 mL). The combined organic layers were washed with brine and dried over sodium sulfate. The crude product was dissolved in H_2O (10 mL), lyophilized and dried under high vacuum to give PQQMe2-aza-18-crown-6 (**$PQQ_{18\text{-}6}$**, 103 mg, 0.171 mmol, 60%) as a brown solid. R_f = 0.32, 5% methanol in dichloromethane.

^{1}H NMR (400 MHz, CD_3CN): δ / ppm = 12.61 (s, 1H), 8.35 (s, 1H), 7.32 (s, 1H), 4.08 (s, 3H), 3.91 (s, 3H), 3.79–3.51 (m, 24H).

^{13}C NMR (101 MHz, CD_3CN): δ / ppm = 180.4, 174.4, 168.9, 167.9, 161.2, 154.9, 147.8, 135.7, 135.4, 130.4, 128.2, 126.4, 125.4, 115.0, 71.3, 71.2, 71.2, 71.1, 71.1, 71.0, 70.5, 69.5, 55.3, 53.1, 50.6, 48.0.

HRMS (ESI): m/z calc. for [$C_{28}H_{32}N_3O_{12}$]: 602.1991 [M-H]$^-$

found: 602.1991.

IR (Diamond-ATR, neat): $\tilde{\nu}$ / cm^{-1} = 2867, 1713, 1681, 1626, 1495, 1471, 1433, 1406, 1351, 1237, 1204, 1096, 1001, 934, 835, 791, 767, 731, 709, 672, 658.

Elemental analysis (CHN): % calc. for [$C_{28}H_{33}N_3O_{12}\cdot 0.82H_2O$]: C 54.41, H 5.67, N 6.80

found: C 54.39, H 5.65, N 6.80.

This procedure was first investigated by Henning Lumpe, but was further optimized as part of this dissertation.

^{1}H NMR (400 MHz, CD_3CN):

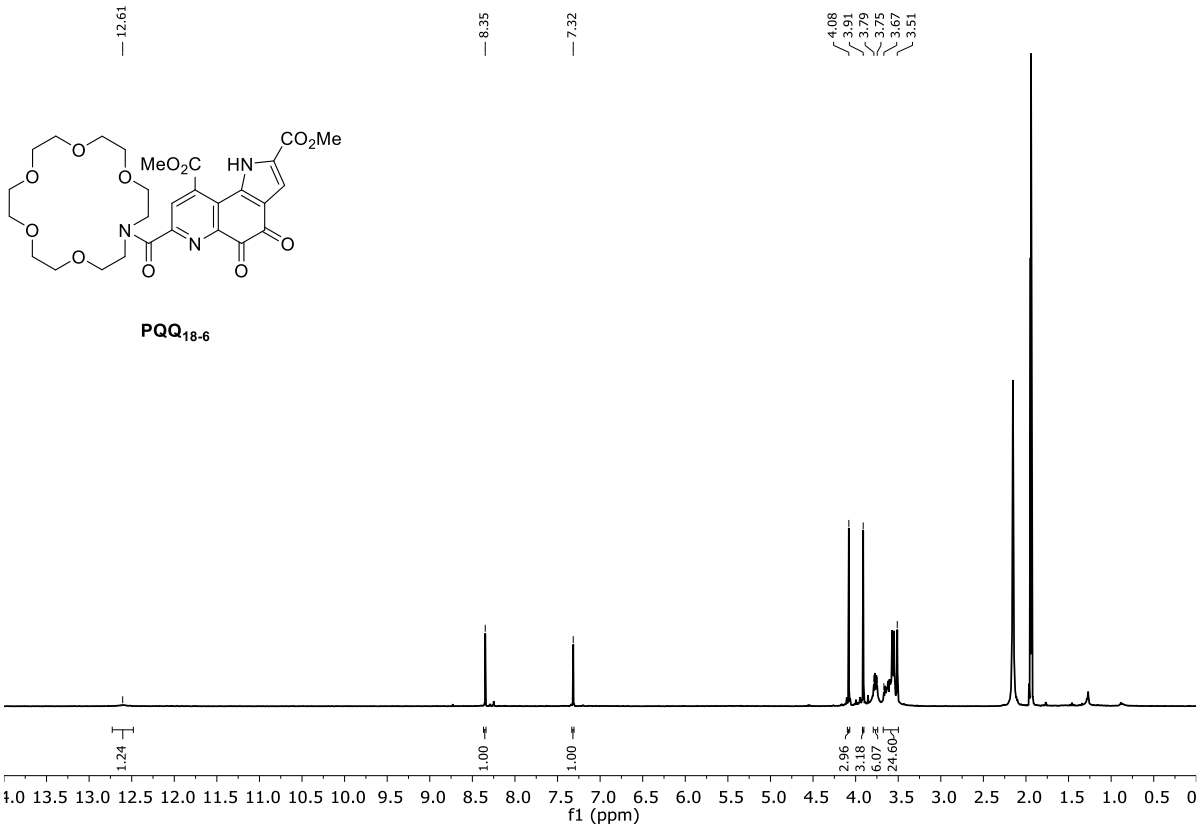

^{13}C NMR (101 MHz, CD_3CN):

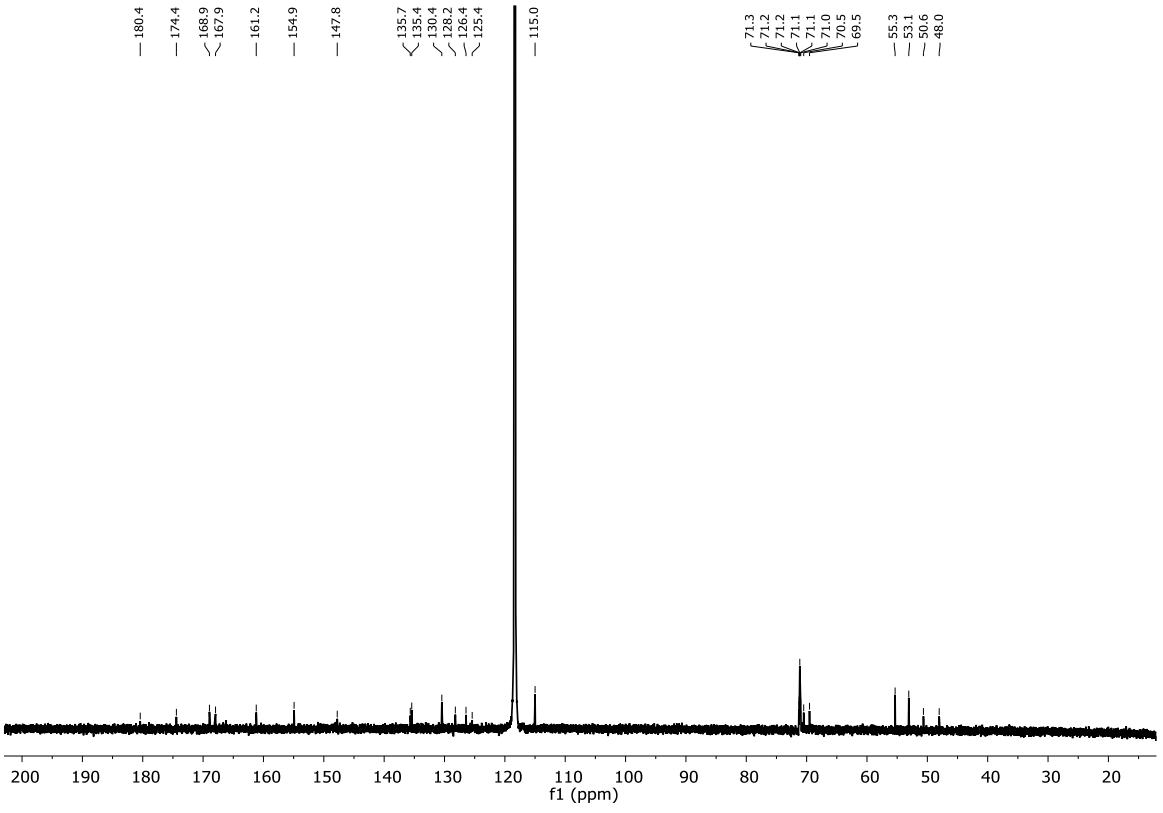

3.3. Synthesis of Ligand L_{PQQ}

2-bromo-*N*,*N*-dicyclohexylacetamide (22)

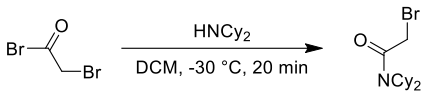

22: 49%

According to a literature procedure,[310] dicyclohexylamine (12.5 g, 68.9 mmol, 2.0 equiv.) was dissolved in 50 mL DCM under a nitrogen atmosphere and the solution was cooled to -30 °C. 2-bromoacetyl bromide (6.95 g, 34.4 mmol, 1.0 equiv.) was added dropwise to the stirring solution at a rate which maintained the reaction temperature below -10 °C. While adding 2-bromoacetyl bromide, a colorless solid precipitated. After stirring for another 20 min at -30 °C, the reaction was allowed to warm up to room temperature. The suspension was diluted with 50 mL DCM and the reaction was quenched with 2 M HCl (60 mL). The mixture was filtered on a glass frit to remove the suspended solids and the biphasic mixture was separated. The organic phase was washed with 2 M HCl (20 mL) and brine, dried over sodium sulfate and the solvent was removed *in vacuo*. The crude product was recrystallized from cyclohexane (30 mL) and dried under reduced pressure to afford **22** (5.09 g, 16.8 mmol, 49%) as colorless needles.

^{1}H NMR (400 MHz, $CDCl_3$): δ / ppm = 3.80 (s, 2H), 3.44 (br, 1H), 2.93 (br, 1H), 2.40 (br, 2H), 1.86-1.06 (m, 18H).

^{13}C NMR (101 MHz, $CDCl_3$): δ / ppm = 165.7, 59.7, 56.6, 31.2, 29.6, 29.2, 26.6, 26.0, 25.4, 25.3.

HRMS (ESI): m/z calc. for $[C_{14}H_{25}BrNO]$: 302.1114 $[M+H]^+$

found: 302.1115.

IR (Diamond-ATR, neat): $\tilde{\nu}$ / cm^{-1} = 2931, 2857, 1633, 1470, 1454, 1445, 1371, 1317, 1269, 1246, 1218, 1180, 1130, 1112, 1054, 1000, 897, 685.

^{1}H NMR (400 MHz, $CDCl_3$):

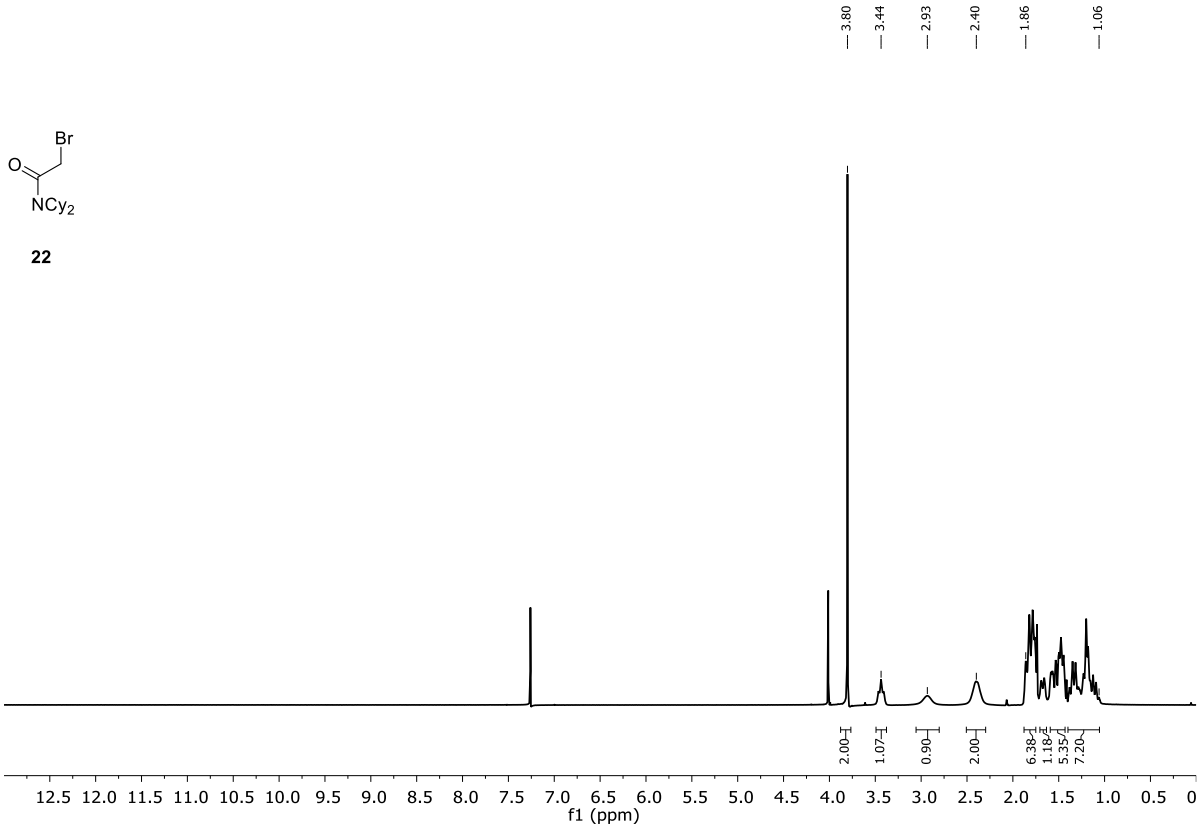

^{13}C NMR (101 MHz, $CDCl_3$):

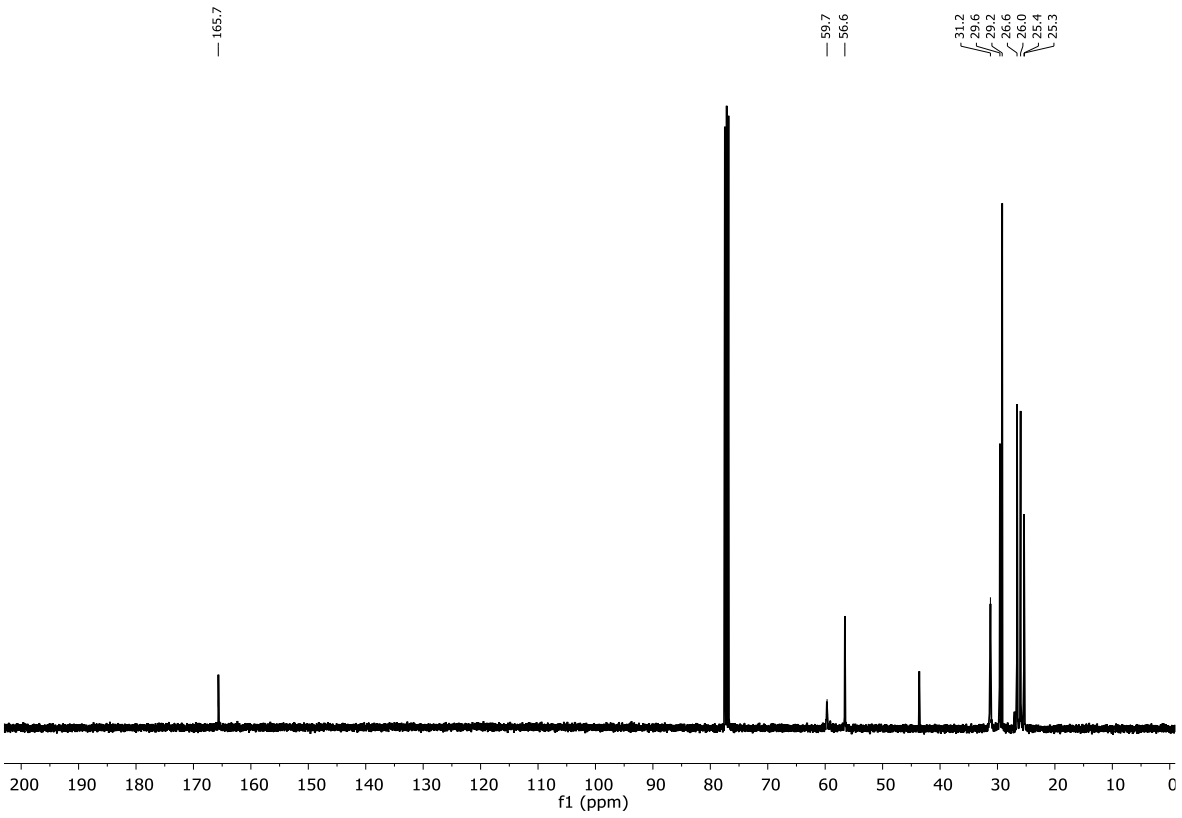

2,2'-(benzylazanediyl)bis(*N*,*N*-dicyclohexylacetamide) (23)

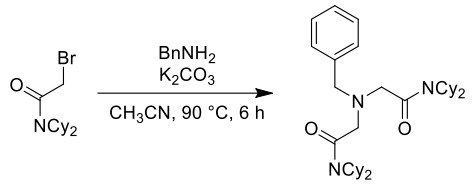

22 **23**: 79%

According to a literature procedure,[311] to a stirred solution of **22** (7.91 g, 26.2 mmol, 2.0 equiv.) in acetonitrile (27 mL), benzylamine (1.4 g, 13.1 mmol, 1.0 equiv.) and potassium carbonate (4.7 g, 34.0 mmol, 2.6 equiv.) were added. The suspension was stirred under reflux for 6 h and after completion of the reaction, the hot mixture was filtered, and the filtrate was left to cool down to room temperature overnight. Subsequently, the product was collected on a glass frit and dried under reduced pressure to give **23** (5.66 g, 10.3 mmol, 79%) as colorless needles.

^{1}H NMR (400 MHz, $CDCl_3$): δ / ppm = 7.41 (d, J = 7.0 Hz, 2H), 7.29 (t, J = 7.2 Hz, 2H), 7.22 (t, J = 7.3 Hz, 1H), 3.95 (s, 2H), 3.45 (s, 4H), 2.86 (br, 2H), 2.49 (br, 4H), 1.74-1.02 (m, 38H).

^{13}C NMR (101 MHz, $CDCl_3$): δ / ppm = 169.9, 139.5, 129.5, 128.3, 127.1, 59.3, 56.8, 56.2, 56.0, 31.4, 30.3, 26.8, 25.9, 25.5, 25.4, 24.9.

HRMS (ESI): m/z calc. for $[C_{35}H_{56}N_3O_2]$: 550.4367 $[M+H]^+$

found: 550.4363.

IR (Diamond-ATR, neat): $\tilde{\nu}$ / cm^{-1} = 2923, 2849, 2358, 1634, 1425, 1365, 1299, 1265, 1238, 1183, 1140, 1043, 995, 893, 833, 806, 753, 703, 665.

^{1}H NMR (400 MHz, $CDCl_3$):

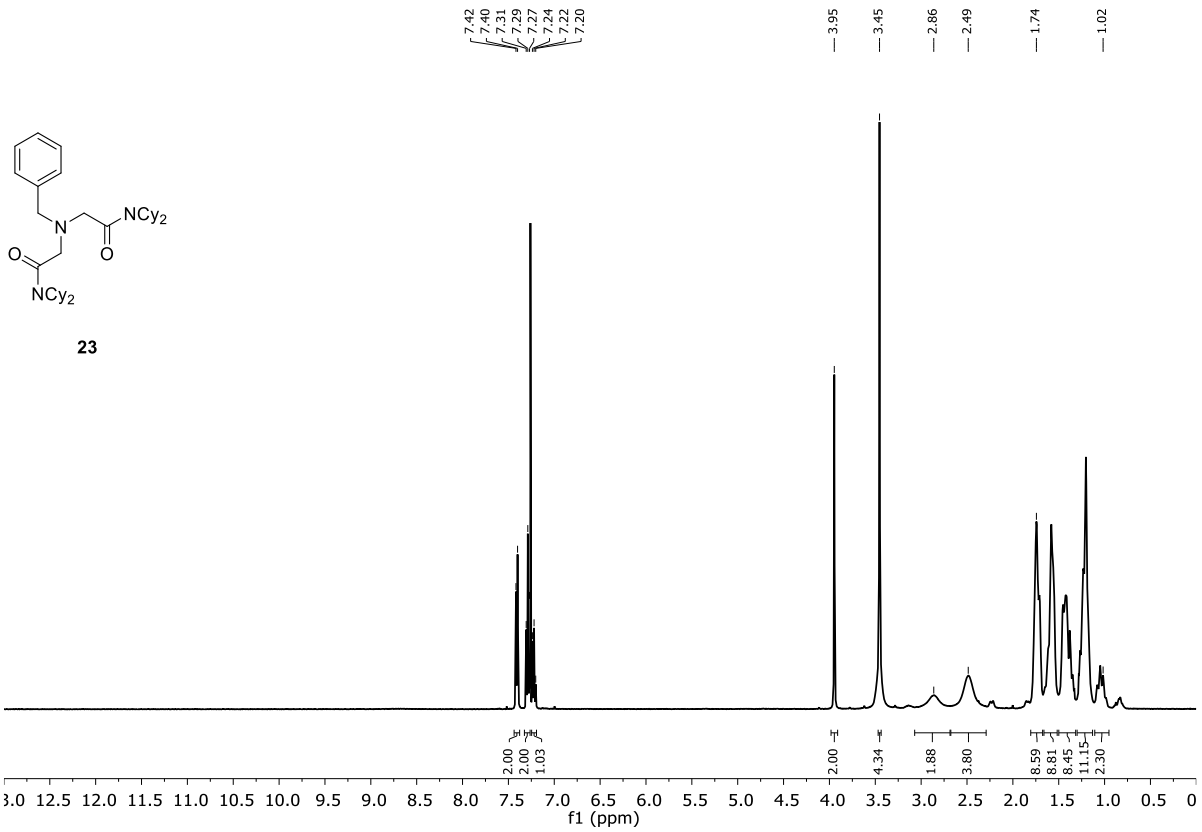

^{13}C NMR (101 MHz, $CDCl_3$):

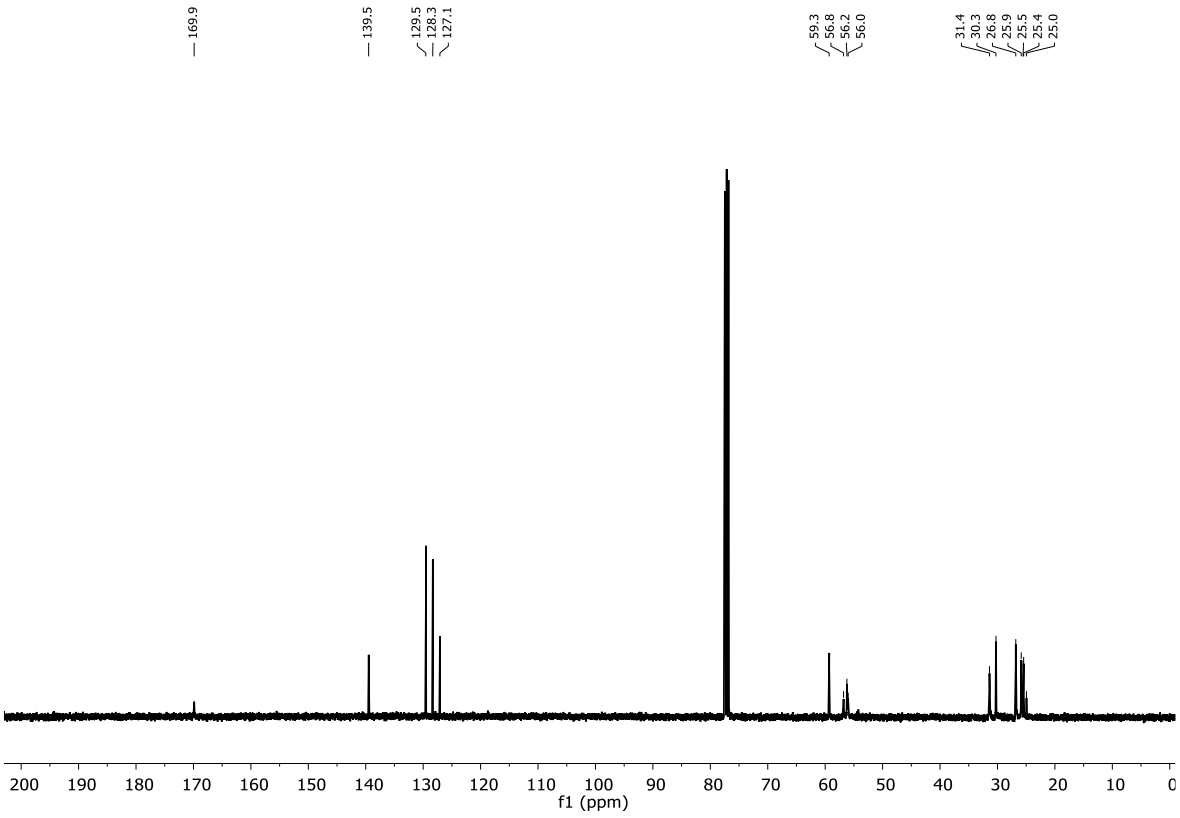

2,2'-azanediylbis(*N*,*N*-dicyclohexylacetamide) (24)

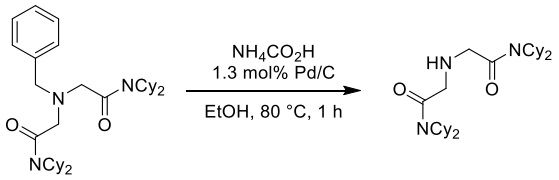

23 **24**: 97%

According to a literature procedure,[166] **23** (3.54 g, 6.43 mmol, 1.0 equiv.) was suspended in 10 mL EtOH and ammonium formate (4.58 g, 72.6 mmol, 11.3 equiv.) was added. The reaction mixture was heated to 80 °C and Pd/C (89.0 mg, 10 wt. %, 0.084 mmol, 1.3 mol%) was added, which initiated gas evolution. The mixture was stirred for 1 h and after completion of the reaction, the suspension was filtered through a pad of Celite. H_2O was added to the filtrate and a colorless solid precipitated. The precipitate was filtered off and dried under high vacuum to afford **24** (2.88 g, 6.27 mmol, 97%) as a colorless solid.

^{1}H NMR (400 MHz, $CDCl_3$): δ / ppm = 3.42 (s, 4H), 3.34 (br, 2H), 2.92 (br, 2H), 2.43 (br, 4H), 1.81-1.06 (m, 36H). NH not observed.

^{13}C NMR (101 MHz, $CDCl_3$): δ / ppm = 169.8, 56.6, 56.1, 51.6, 31.4, 30.2, 26.8, 26.1, 25.5, 25.4.

HRMS (ESI): m/z calc. for $[C_{28}H_{50}N_3O_2]$: 460.3898 $[M+H]^+$

found: 460.3894.

IR (Diamond-ATR, neat): $\tilde{\nu}$ / cm^{-1} = 2924, 2849, 1643, 1425, 1363, 1298, 1265, 1237, 1185, 1140, 1097, 1052, 998, 893, 860, 833, 807, 752, 703, 679, 665.

^{1}H NMR (400 MHz, $CDCl_3$):

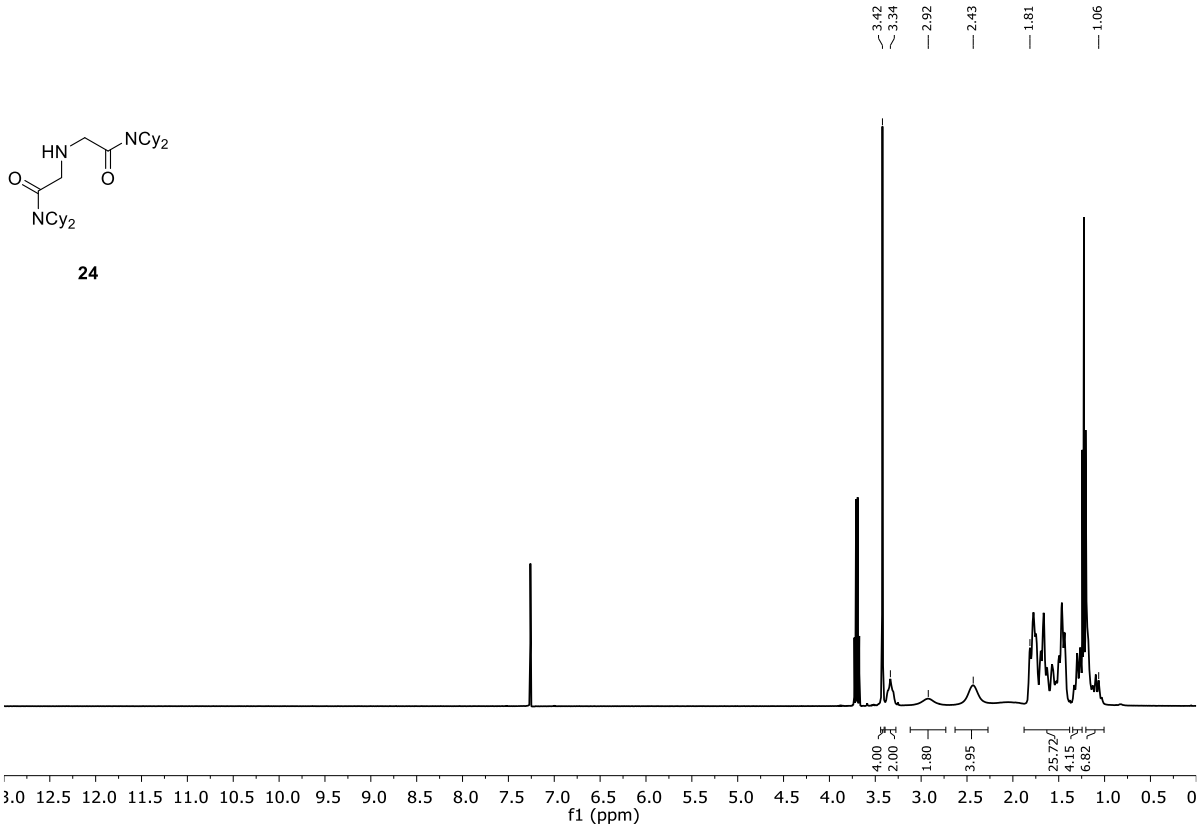

^{13}C NMR (101 MHz, $CDCl_3$):

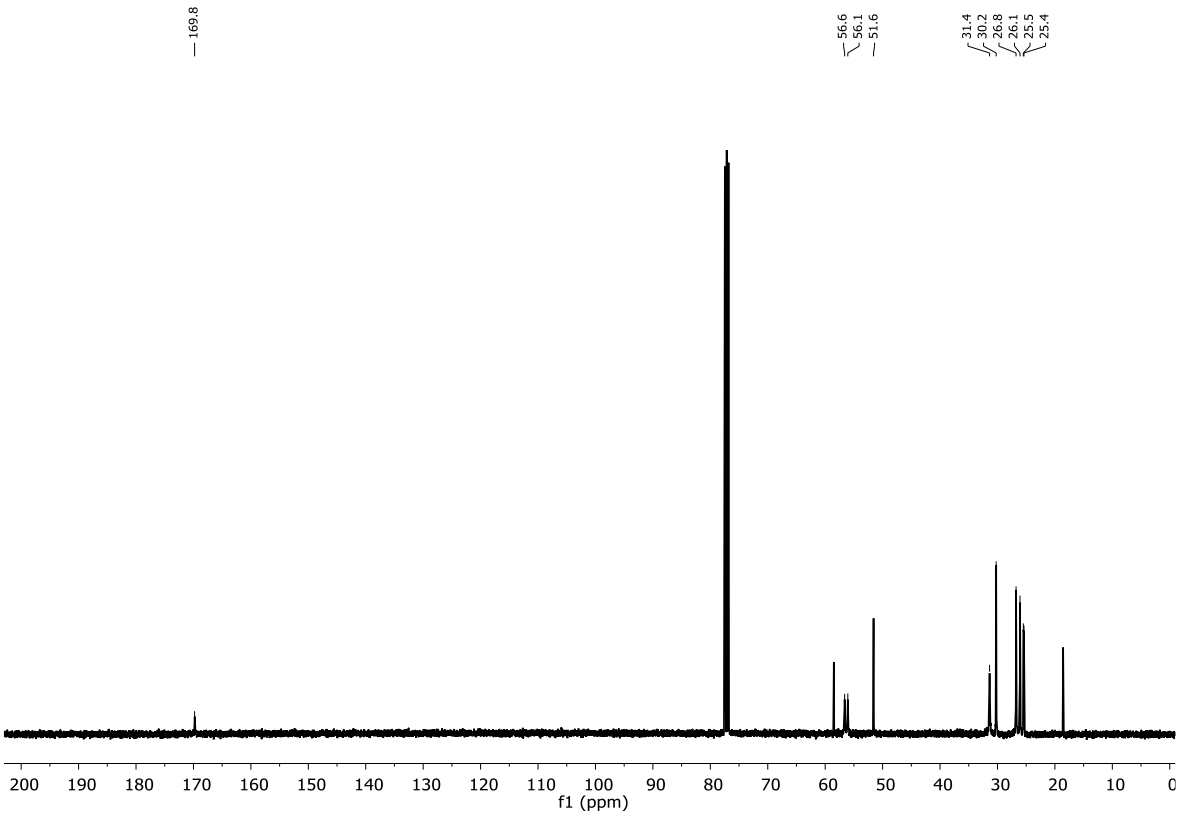

2,2'-((2-nitrophenyl)azanediyl)bis(*N*,*N*-dicyclohexylacetamide) (25)

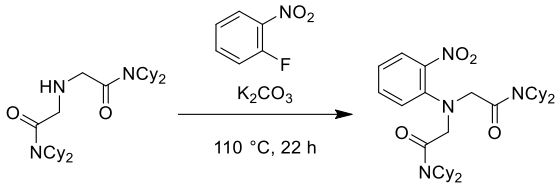

24 **25:** 50%

According to a literature procedure,[166] **24** (1.48 g, 3.21 mmol, 1.2 equiv.) and potassium carbonate (0.666 g, 4.82 mmol, 1.8 equiv.) were pestled and charged in a pear-shaped flask. 1-fluoro-2-nitrobenzene (0.378 g, 2.68 mmol, 1.0 equiv.) was added, and the reaction mixture was heated to 110 °C and stirred for 22 h. After cooling to room temperature, the orange residue was diluted in 30 mL diethyl ether and was filtered on a glass frit. 2 M HCl (18 mL) was added to the filtrate to precipitate any remaining starting amine. The biphasic mixture was filtered on a glass frit and subsequently both phases were separated. The organic phase was washed with brine and dried over sodium sulfate. The solvent was evaporated and the crude product was recrystallized from boiling hexane to yield **25** (0.783 g, 1.35 mmol, 50%) as a yellow solid.

^{1}H NMR (400 MHz, $CDCl_3$): δ / ppm = 7.70 (dd, J = 8.1 Hz, J = 1.6 Hz, 1H), 7.33 (ddd, J = 8.7 Hz, J = 7.0 Hz, J = 1.7 Hz, 1H), 6.82-6.78 (m, 2H), 4.19 (s, 4H), 3.29 (br, 2H), 2.98 (br, 2H), 2.49 (br, 4H), 1.83-1.47 (m, 24H), 1.30-1.04 (m, 12H).

^{13}C NMR (101 MHz, $CDCl_3$): δ / ppm = 167.9, 145.1, 139.2, 133.4, 126.9, 119.0, 118.8, 57.2, 56.5, 55.6, 31.3, 30.2, 26.8, 26.0, 25.6, 25.4.

HRMS (ESI): m/z calc. for $[C_{34}H_{52}N_4NaO_4]$: 603.3886 $[M+Na]^+$

found: 603.3876.

IR (Diamond-ATR, neat): $\tilde{\nu}$ / cm^{-1} = 2930, 2850, 1744, 1627, 1599, 1565, 1512, 1452, 1322, 1271, 1240, 1204, 1171, 1137, 1051, 993, 933, 892, 855, 784, 750, 723, 695, 674, 664.

^{1}H NMR (400 MHz, $CDCl_3$):

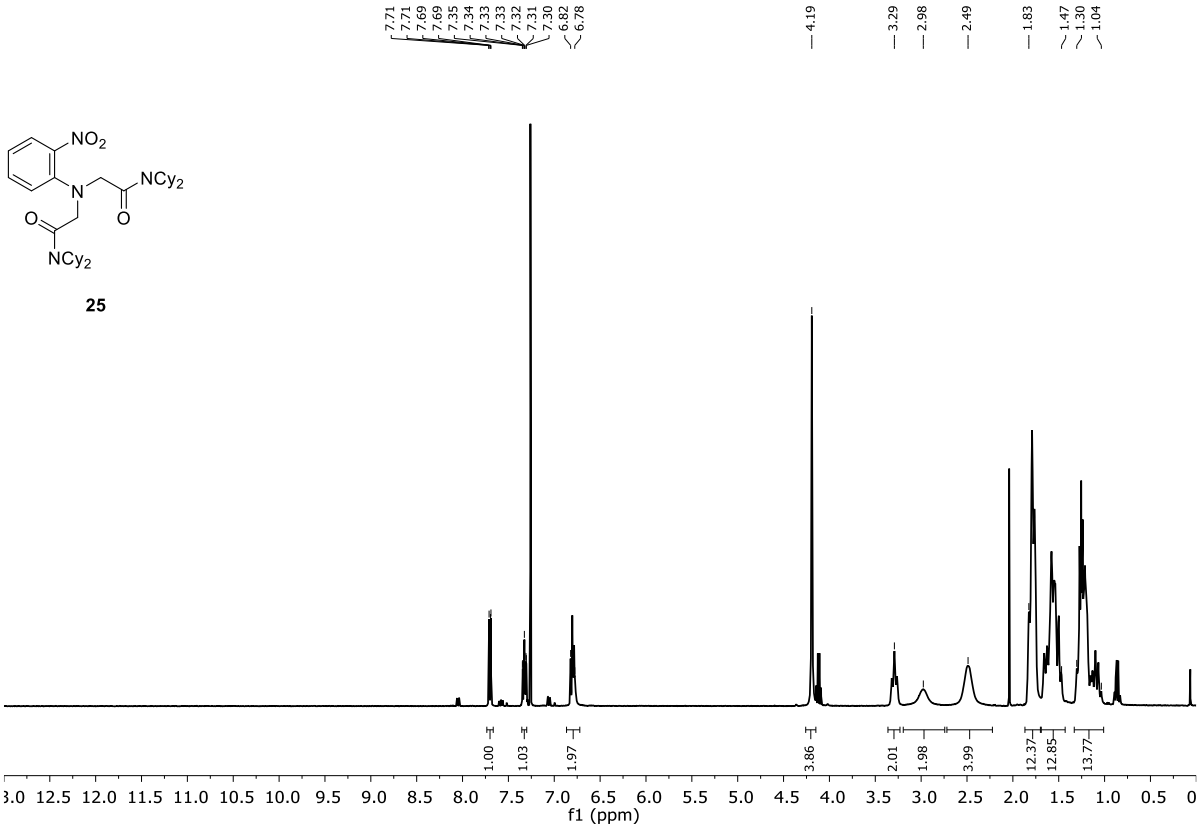

^{13}C NMR (101 MHz, $CDCl_3$):

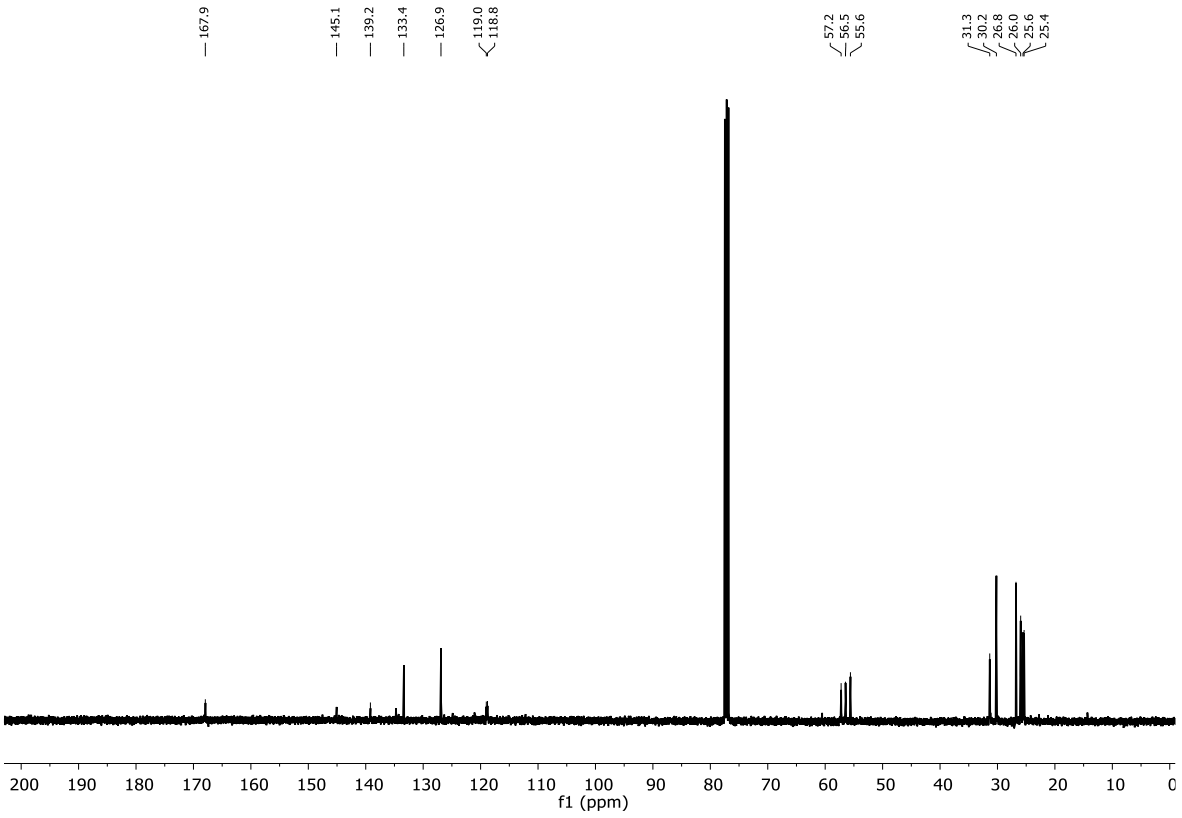

2,2'-((2-aminophenyl)azanediyl)bis(*N*,*N*-dicyclohexylacetamide) (19)

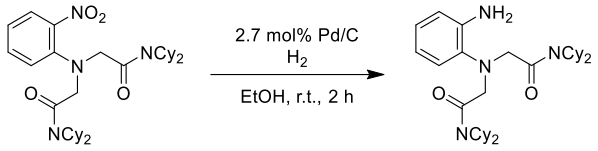

25 **19**: 80%

A round-bottomed flask equipped with a magnetic stirring bar and a septum was charged with **25** (200 mg, 0.344 mmol, 1.0 equiv.), 5 mL EtOH and Pd/C (10.0 mg, 10 wt. %, 0.009 mmol, 2.7 mol%). Nitrogen was bubbled through the reaction mixture for 5 min. Subsequently, hydrogen gas was bubbled through the suspension for 15 min and the reaction was stirred at room temperature for 2 h under a hydrogen atmosphere (hydrogen filled balloon). The suspension was then filtered through a pad of Celite and was washed with hexane. The solvent was removed *in vacuo* and the crude product was purified by flash column chromatography (2% methanol in dichloromethane, R_f = 0.64) to afford **19** (151 mg, 0.274 mmol, 80%) as a pale-yellow solid.

^{1}H NMR (400 MHz, C_6D_6): δ / ppm = 7.63 (dd, J = 7.8 Hz, J = 1.4 Hz, 1H), 6.93 (td, J = 7.6 Hz, J = 1.4 Hz, 1H), 6.80 (td, J = 7.6 Hz, J = 1.5 Hz, 1H), 6.50 (dd, J = 7.8 Hz, J = 1.5 Hz, 1H), 4.53 (br, 2H), 4.04 (s, 4H), 3.57 (br, 2H), 2.85 (br, 5H), 1.76-1.73 (m, 4H), 1.51-1.06 (m, 33H).

^{13}C NMR (101 MHz, C_6D_6): δ / ppm = 169.6, 143.8, 138.5, 125.2, 124.2, 118.0, 115.2, 57.2, 56.6, 56.1, 31.7, 30.5, 27.1, 26.0, 25.6.

HRMS (ESI): m/z calc. for $[C_{34}H_{55}N_4O_2]$: 551.4320 $[M+H]^+$

found: 551.4313.

IR (Diamond-ATR, neat): $\tilde{\nu}$ / cm^{-1} = 2922, 2851, 1638, 1502, 1441, 1299, 1265, 1238, 1184, 1126, 995, 894, 742, 690, 663.

^{1}H NMR (400 MHz, C_6D_6):

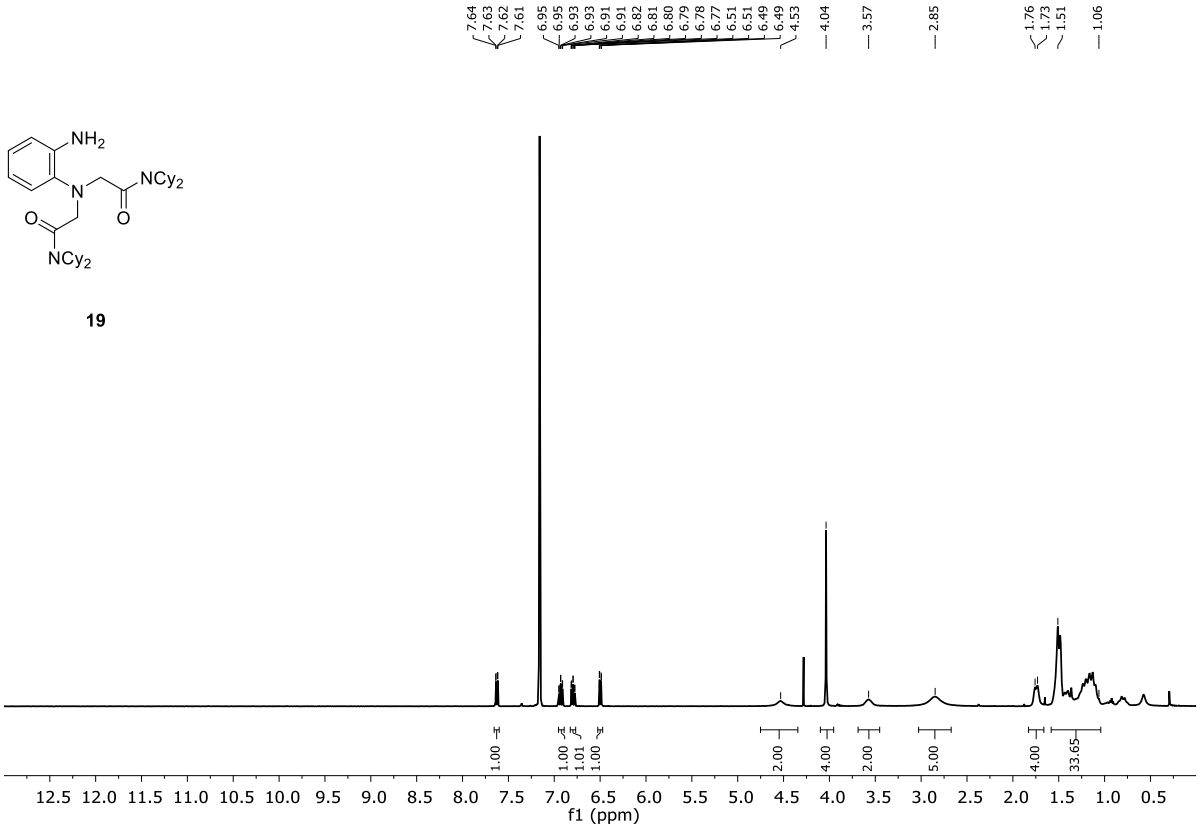

^{13}C NMR (101 MHz, C_6D_6):

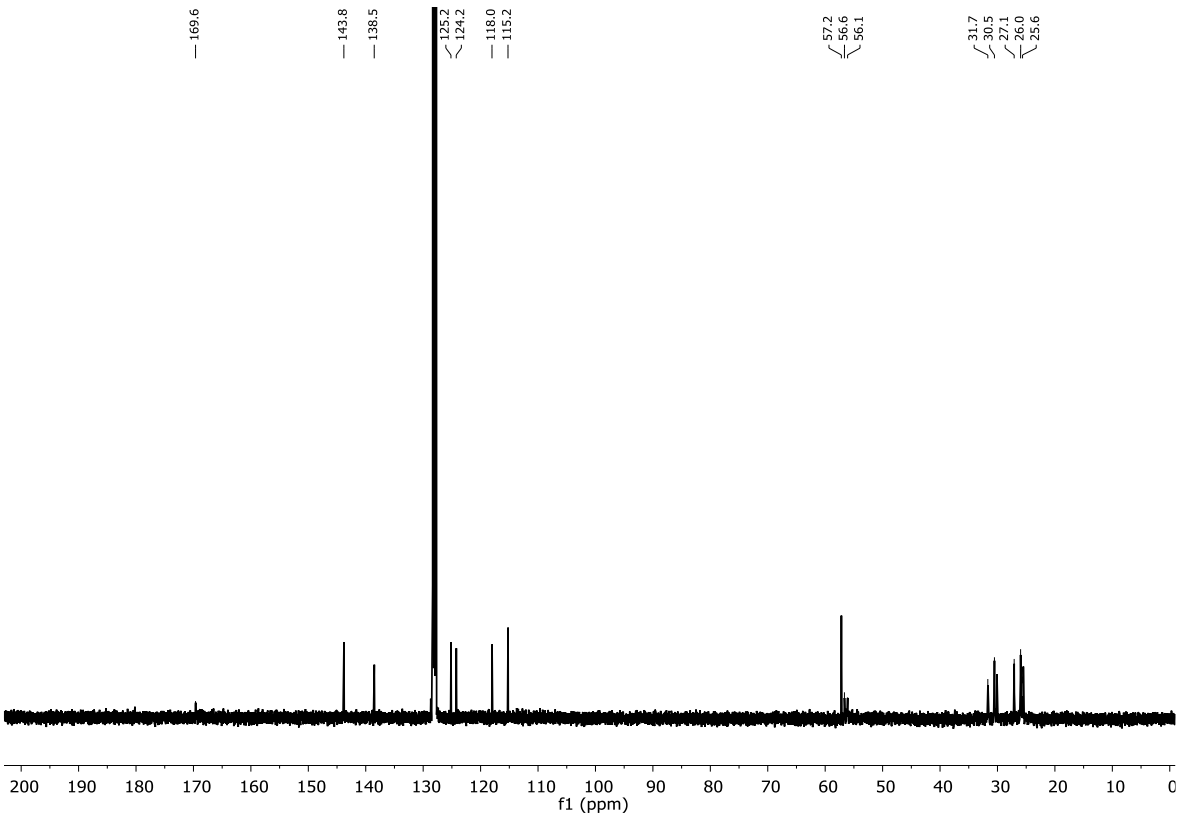

5-methoxy-2,9-bis(methoxycarbonyl)-1*H*-pyrrolo[2,3-*f*]quinoline-7-carboxylic acid (16)

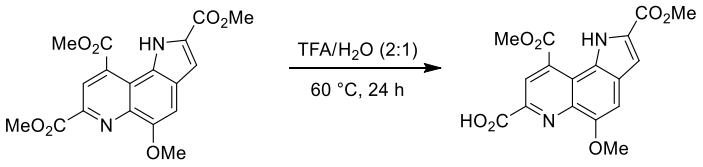

15 **16**: 52%

According to a literature procedure,[169] the trimethyl ester **15** (92.3 mg, 0.248 mmol) was dissolved in 1 mL TFA/H_2O (2:1), and the reaction mixture was heated at 60 °C for 24 h. After cooling down to room temperature, the reaction mixture was diluted with 5 mL H_2O. The brown precipitate was filtered off and washed with H_2O. The product was dried under high vacuum to give **16** (46 mg, 0.128 mmol, 52%) as a brown solid.

^{1}H NMR (400 MHz, DMSO-*d*$_6$): δ / ppm = 12.00 (s, 1H), 8.69 (s, 1H), 7.56 (s, 1H), 7.31 (s, 1H), 4.11 (s, 3H), 4.01 (s, 3H), 3.93 (s, 3H).

The ^{1}H NMR spectrum is shown on page 164.

The ^{13}C NMR signals could not be distinguished from background noise.

HRMS (ESI): m/z calc. for $[C_{17}H_{15}N_2O_7]$: 359.0874 $[M+H]^+$

found: 359.0874.

IR (Diamond-ATR, neat): $\tilde{\nu}$ / cm^{-1} = 3307, 2963, 2924, 2850, 1710, 1614, 1504, 1436, 1371, 1325, 1249, 1201, 1149, 1007, 899, 851, 819, 805, 760, 741, 704.

Dimethyl 7-((2-(bis(2-(dicyclohexylamino)-2-oxoethyl)amino)phenyl)carbamoyl)-4,5-dioxo-4,5-dihydro-1H-pyrrolo[2,3-f]quinoline-2,9-dicarboxylate (L_{PQQ})

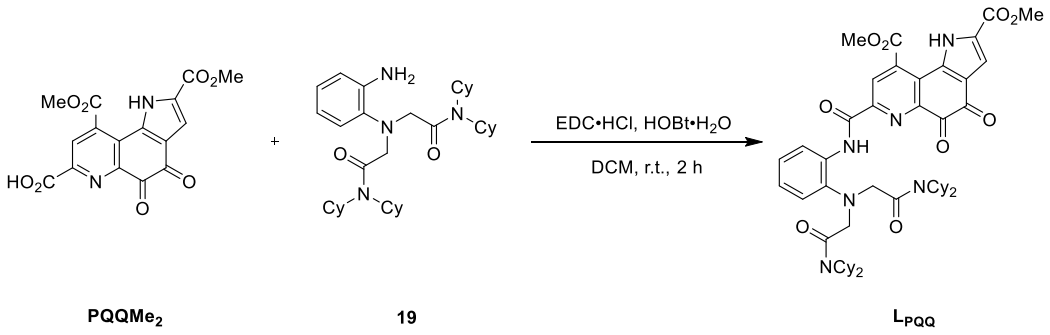

$PQQMe_2$ **19** **L_{PQQ}**

In a dry and nitrogen flushed SCHLENK flask, equipped with a magnetic stirring bar and a septum, **$PQQMe_2$** (19.8 mg, 0.055 mmol, 1.0 equiv.) was suspended in dry DCM (3 mL). EDC·HCl (16.4 mg, 0.086 mmol, 1.6 equiv.) and HOBt·H_2O (13.0 mg, 0.085 mmol, 1.5 equiv.) were added, and the reaction mixture was stirred at room temperature for 10 min. Subsequently, **19** (30.4 mg, 0.055 mmol, 1.0 equiv.) was added, and the reaction mixture was stirred at room temperature for 2 h. After completion of the reaction 10 mL H_2O were added and the aqueous phase was extracted with DCM (2 x 10 mL). The combined organic layers were washed with brine, dried over sodium sulfate and the solvent was removed *in vacuo*. The crude product was purified by flash column chromatography (10% *iso*-hexane in diethyl ether, R_f = 0.45) and dried under high vacuum to yield **L_{PQQ}** (27.5 mg, 56%) as pale-yellow solid.

Crystals suitable for X-ray analysis were grown from dichloromethane by slow vapor diffusion of diethyl ether at room temperature.

^{1}H NMR (400 MHz, CD_2Cl_2): δ / ppm = 12.68 (s, 1H), 11.83 (s, 1H), 8.78 (s, 1H), 8.44 (d, 1H), 7.53 (d, 1H), 7.43 (d, 1H), 7.22 (t, 1H), 7.13 (t, 1H), 6.48 (br, 2H), 4.15 (s, 3H), 4.00 (s, 4H), 3.95 (s, 3H), 3.26 (br, 2H), 2.86 (br, 2H), 2.14 (br, 4H), 1.73-0.98 (m, 34H).

Due to either a decomposition of the product or formation of additional products, no clear ^{13}C NMR spectrum or 2D spectra could be obtained.

HRMS (ESI): m/z calc. for [$C_{50}H_{61}N_6O_9$]: 889.4506 [M-H]$^-$

found: 889.4495.

IR (Diamond-ATR, neat): $\tilde{\nu}$ / cm^{-1} = 3257, 2929, 2853, 2164, 1715, 1694, 1634, 1585, 1516, 1454, 1435, 1412, 1334, 1304, 1230, 1190, 1144, 1126, 1048, 995, 940, 894, 860, 834, 806, 792, 759, 724, 697, 677.

^{1}H NMR (400 MHz, CD_2Cl_2):

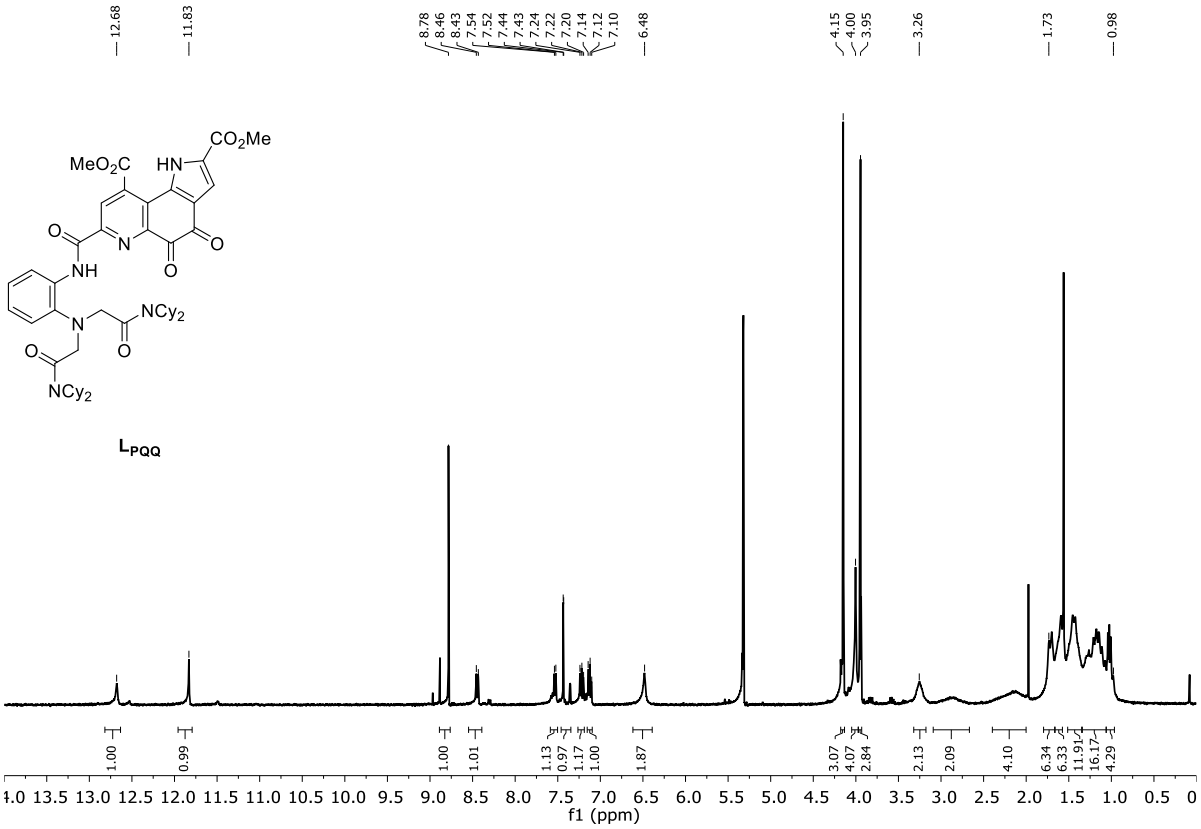

X-Ray Crystallographic Data:

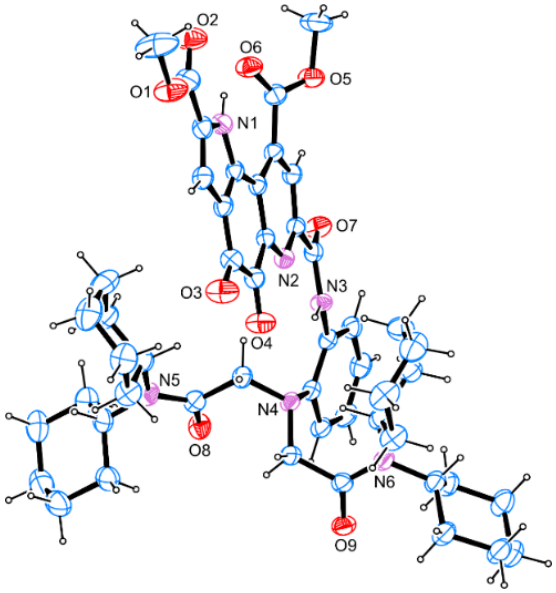

Figure V.2: ORTEP[308] representation of the molecular structure of **L**$_{PQQ}$.

Table V.2: : Crystallographic data for ***L*****PQQ**.

LPQQ	
net formula	$C_{50}H_{62}N_6O_9$
M_r/g mol^{-1}	891.05
crystal size/mm	0.110 × 0.100 × 0.090
T/K	109.(2)
radiation	MoKα
diffractometer	'Bruker D8 Venture TXS'
crystal system	monoclinic
space group	'P 1 21/c 1'
a/Å	11.6736(5)
b/Å	22.5625(9)
c/Å	18.3016(8)
α/°	90
β/°	101.404(2)
γ/°	90
V/Å^3	4725.2(3)
Z	4
calc. density/g cm^{-3}	1.253
μ/mm^{-1}	0.087
absorption correction	Multi-Scan
transmission factor range	0.93–0.99
refls. measured	60791
R_{int}	0.0504
mean $\sigma(I)/I$	0.0326
θ range	2.901–25.350
observed refls.	6579
x, y (weighting scheme)	0.0516, 6.6841
hydrogen refinement	mixed
refls in refinement	8634
parameters	593
restraints	0
$R(F_{obs})$	0.0606
$R_w(F^2)$	0.1608
S	1.059
shift/error$_{max}$	0.001
max electron density/e Å^{-3}	1.237
min electron density/e Å^{-3}	−0.253

3.4. Synthesis of further PQQ-based Ligands

Dimethyl 7-(bis(3-ethoxy-3-oxopropyl)carbamoyl)-4,5-dioxo-4,5-dihydro-1*H*-pyrrolo[2,3-*f*]quinoline -2,9-dicarboxylate (PQQ_{DEDP})

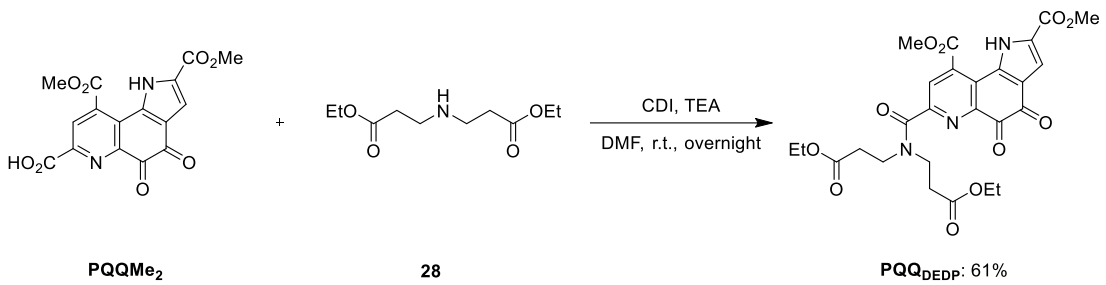

In a dry and nitrogen flushed SCHLENK flask, equipped with a magnetic stirring bar and a septum, **$PQQMe_2$** (20.0 mg, 0.056 mmol, 1.0 equiv.) and CDI (11.0 mg, 0.068 mmol, 1.2 equiv.) were dissolved in dry DMF (2.5 mL). Diethyl 3,3'-azanediyldipropionate (**28**) (12.0 mg, 0.055 mmol, 1.0 equiv.) and TEA (11.3 mg, 0.112 mmol, 2.0 equiv.) were added to the solution, and the reaction mixture was stirred at room temperature overnight. After completion of the reaction, the solvent was removed *in vacuo* and the residue was suspended in 10 mL H_2O and was stirred at room temperature overnight. The suspension was centrifuged (10 min at 4500 rpm) and the supernatant was removed. The residue was vortex-mixed with H_2O, centrifuged again and lyophilized to give **PQQ_{DEDP}** (17.0 mg, 0.034 mmol, 61%) as an orange solid. R_f = 0.3, 2% methanol in dichloromethane.

^{1}H NMR (400 MHz, DMF-d_7): δ / ppm = 12.70 (s, 1H), 8.45 (s, 1H), 7.32 (s, 1H), 4.16 (s, 3H), 4.15 (q, J = 7.1 Hz, 2H), 4.09 (q, J = 7.1 Hz, 2H), 3.96 (s, 3H), 3.84–3.79 (m, 4H), 3.11 (t, J = 7.3 Hz, 2H), 2.81 (t, J = 7.3 Hz, 2H), 1.25 (t, J = 7.1 Hz, 3H), 1.21 (t, J = 7.1 Hz, 3H).

^{13}C NMR (101 MHz, DMF-d_7): δ / ppm = 178.4, 173.8, 171.9, 171.8, 167.9, 166.7, 160.5, 152.8, 147.5, 134.9, 134.8, 129.3, 127.1, 125.8, 125.2, 114.2, 60.5, 60.3, 54.4, 52.2, 45.9, 43.4, 34.0, 32.3, 14.1.

HRMS (ESI): m/z calc. for [$C_{26}H_{26}N_3O_{11}$]: 556.1573 [M-H]$^-$

found: 556.1573.

IR (Diamond-ATR, neat): $\tilde{\nu}$ / cm^{-1} = 2970, 1716, 1683, 1626, 1497, 1473, 1432, 1382, 1314, 1279, 1257, 1225, 1183, 1152, 1115, 1029, 1012, 1000, 952, 928, 862, 832, 781, 762, 737, 698, 664, 657.

^{1}H NMR (400 MHz, DMF-d_7):

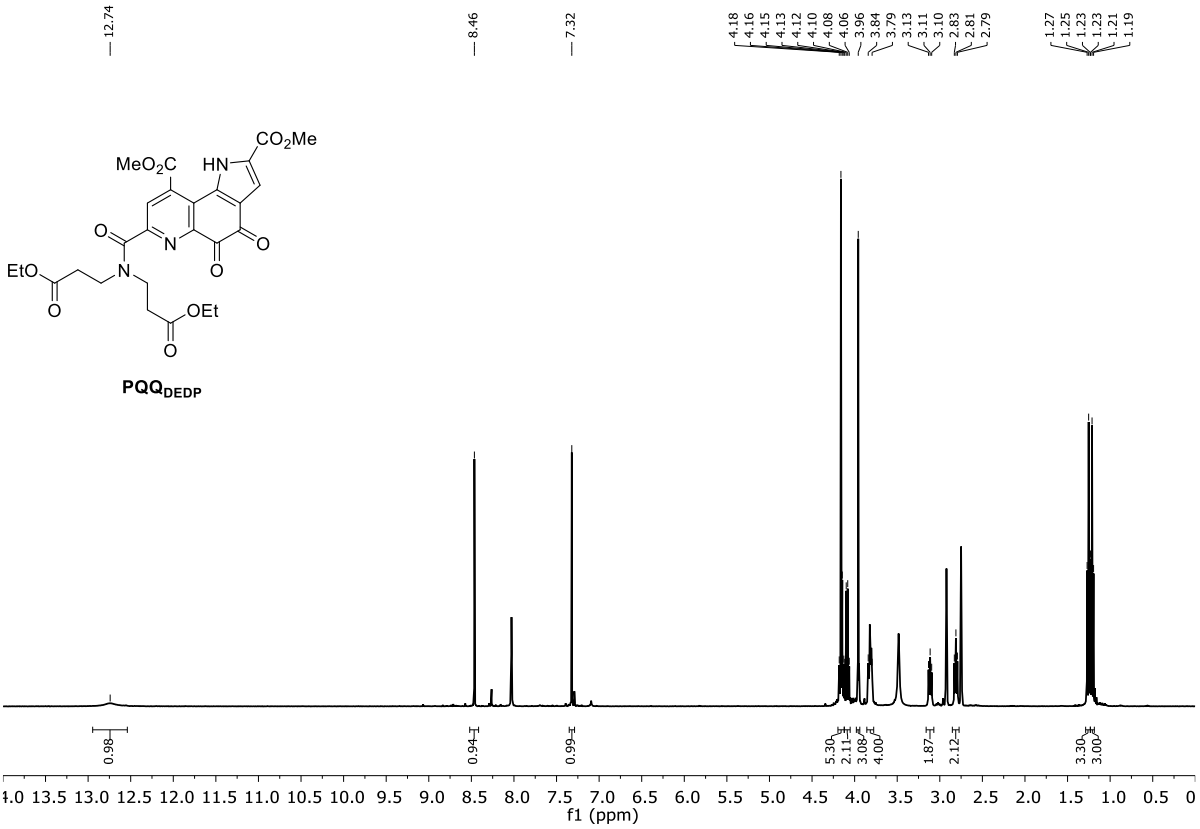

^{13}C NMR (101 MHz, DMF-d_7):

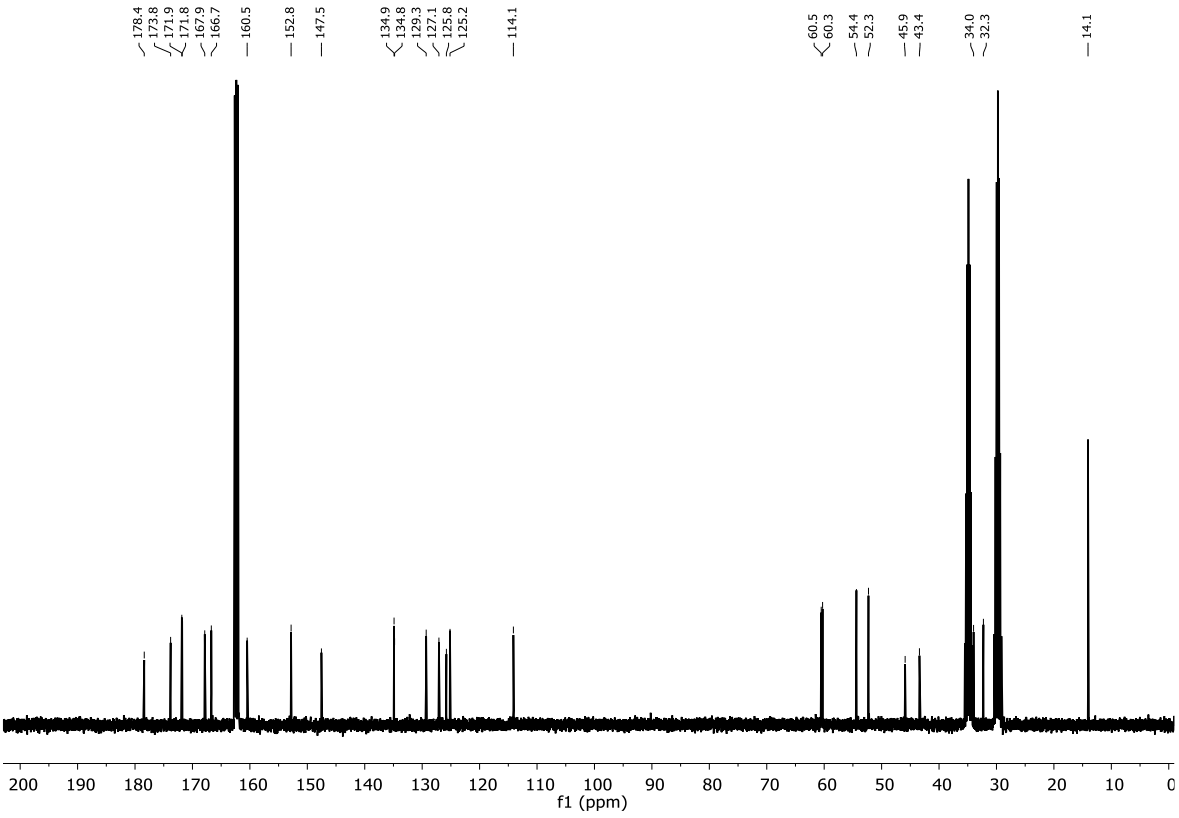

3,3'-((2,9-bis(methoxycarbonyl)-4,5-dioxo-4,5-dihydro-1*H*-pyrrolo[2,3-*f*]quinoline-7-carbonyl)azanediyl)dipropionic acid (29)

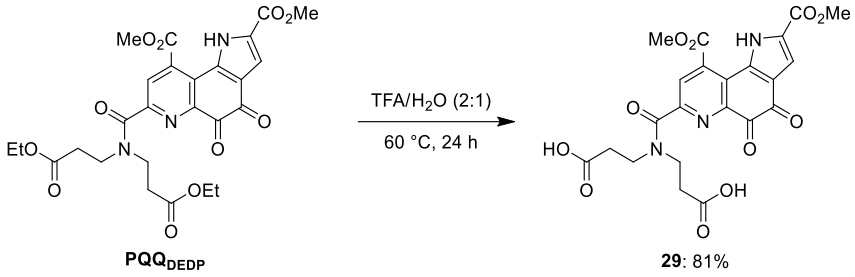

PQQ$_{DEDP}$ (20.7 mg, 0.037 mmol) was dissolved in 1 mL TFA/H_2O (2:1) and the reaction mixture was heated at 60 °C for 24 h. After cooling down to room temperature, the reaction mixture was diluted with 5 mL H_2O. The aqueous phase was extracted with dichloromethane (2 × 100 mL), and the combined organic layers were washed with brine and dried over sodium sulfate. The solvent was removed *in vacuo* affording **29** (15 mg, 0.03 mmol, 81%) as a red-brown solid.

^{1}H NMR (400 MHz, DMSO-*d*$_6$): δ / ppm = 12.46 (s, 1H), 8.26 (s, 1H), 7.27 (s, 1H), 4.04 (s, 3H), 3.89 (s, 3H), 3.65 (t, J = 7.3 Hz, 2H), 3.59 (t, J = 7.4 Hz, 2H), 2.83 (t, J = 7.4 Hz, 2H), 2.63 (t, J = 7.3 Hz, 2H).

HRMS (ESI): m/z calc. for [$C_{22}H_{18}N_3O_{11}$]: 500.0947 [M-H]$^-$

found: 500.0951.

The ^{13}C NMR signals could not be distinguished from background noise. Due to the limited amount of product no further characterization was performed.

^{1}H NMR (400 MHz, DMSO-*d*$_6$):

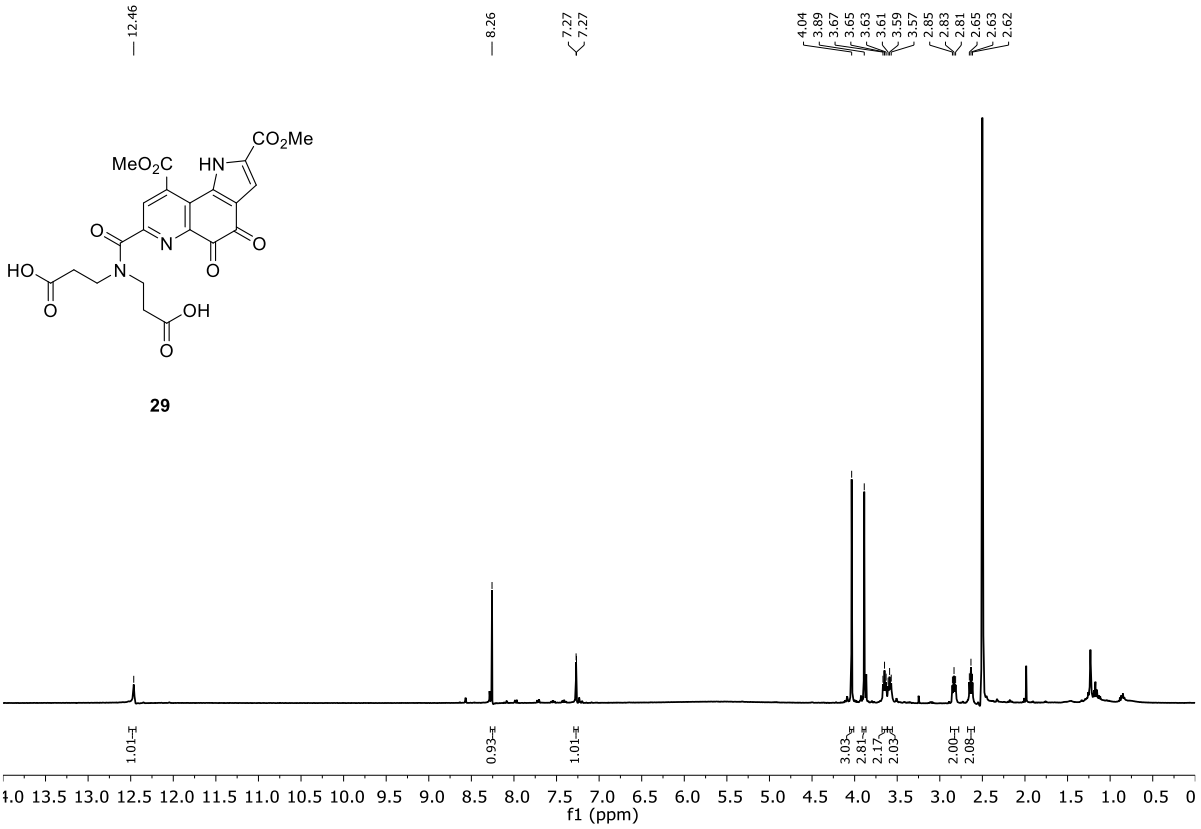

29

^{1}H NMR (400 MHz, DMSO-*d*$_6$):

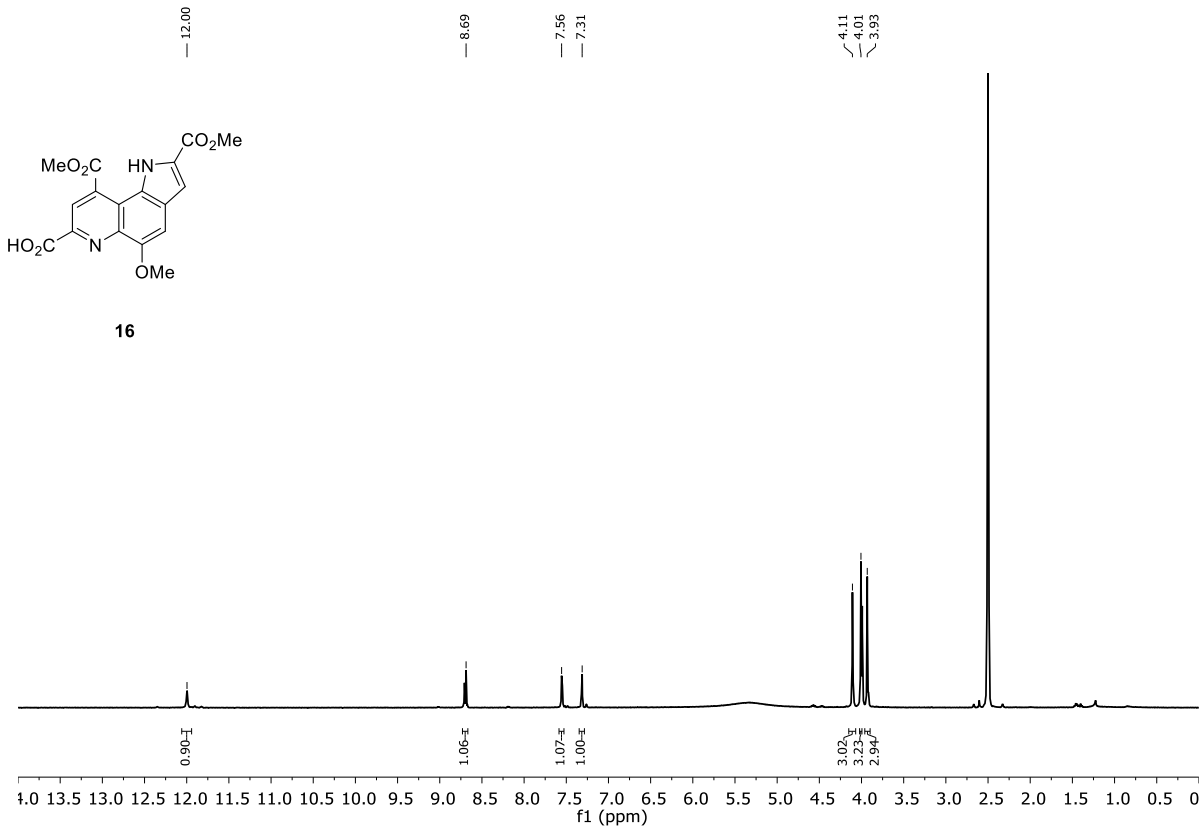

16

4,5-dihydroxy-2,9-bis(methoxycarbonyl)-1H-pyrrolo[2,3-f]quinoline-7-carboxylic acid ($PQQMe_2H_2$)

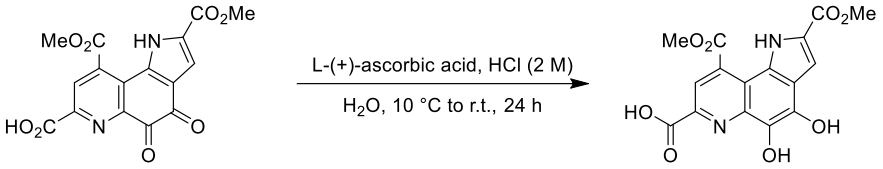

$PQQMe_2$ **$PQQMe_2H_2$**: 65%

A round bottom flask, equipped with a magnetic stirring bar, was charged with L-(+)-ascorbic acid (370 mg, 2.1 mmol, 18.1 equiv.) and dissolved in H_2O (12 mL). The pH value was set to 2 with HCl (2 M). **$PQQMe_2$** (41.7 mg, 0.116 mmol, 1.0 equiv.) was suspended in H_2O (16 mL) and it was added dropwise over 1 h to the solution of the acid at 10 °C. After the addition was completed, the solution was allowed to warm up to room temperature and stirred overnight. Subsequently, the precipitated solid was centrifuged (4500 rpm, 5 min) and washed with diluted HCl (2 M). The crude product was dried under high vacuum to give **$PQQMe_2H_2$** (28 mg, 0.07 mmol, 65%) as a red-brown solid.

^{1}H NMR (400 MHz, DMSO-d_6): δ / ppm = 13.17 (s, 1H), 12.13 (s, 1H), 10.21 (s, 1H), 9.26 (s, 1H), 8.55 (s, 1H), 7.42 (d, J = 2.4 Hz, 1H), 4.11 (s, 3H), 3.94 (s, 3H).

^{13}C NMR (101 MHz, DMSO-d_6): δ / ppm = 168.0, 164.8, 160.7, 142.3, 140.6, 137.6, 132.7, 131.0, 126.5, 123.3, 122.8, 118.8, 110.4, 105.7, 54.0, 52.2.

IR (Diamond-ATR, neat): $\tilde{\nu}$ / cm^{-1} = 3277, 1710, 1638, 1582, 1521, 1473, 1436, 1403, 1209, 1162, 1112, 998, 971, 941, 886, 840, 798, 756, 730, 712, 687, 682, 660, 654.

Elemental analysis (CHN): % calc. for [$C_{28}H_{33}N_3O_{12}$·0.82H_2O]: C 48.71, H 4.04, N 7.10

found: C 48.38, H 3.70, N 7.36.

A reoxidation of the product was observed in HRMS (ESI).

This procedure was part of the bachelor thesis of Sophia Glocker, conducted under my supervision.

^{1}H NMR (400 MHz, DMSO-*d*$_6$):

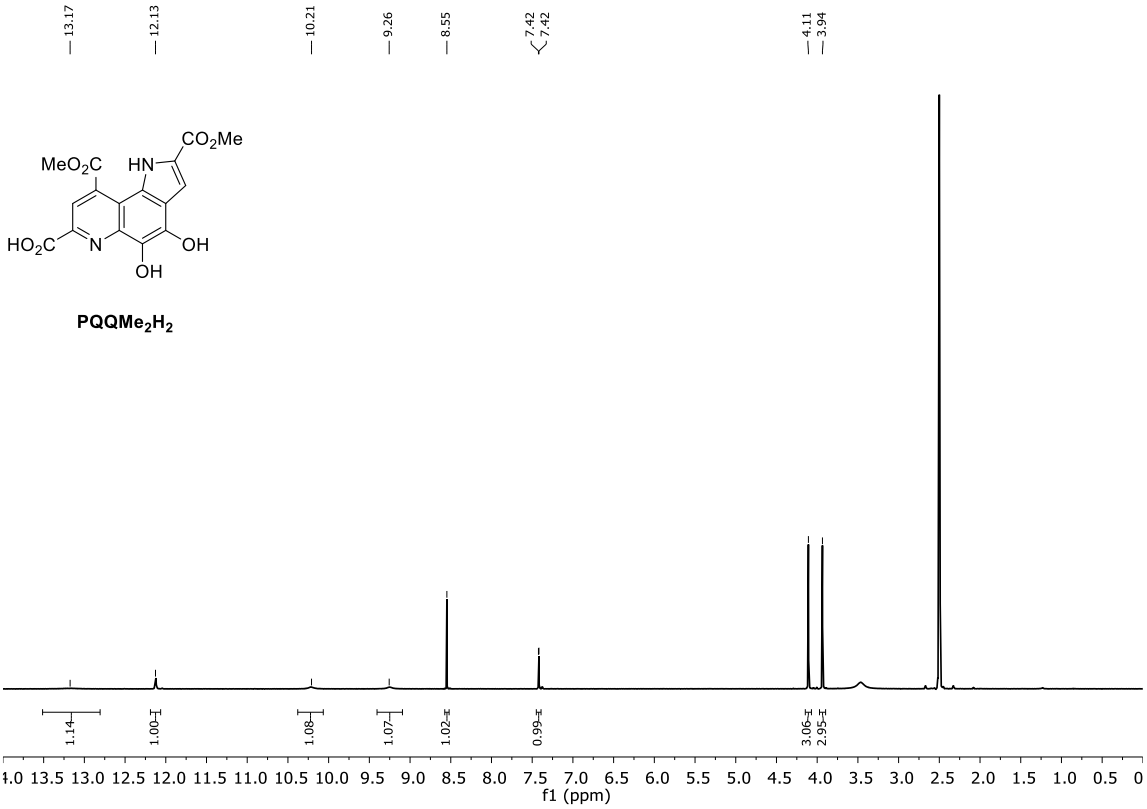

^{13}C NMR (101 MHz, DMSO-*d*$_6$):

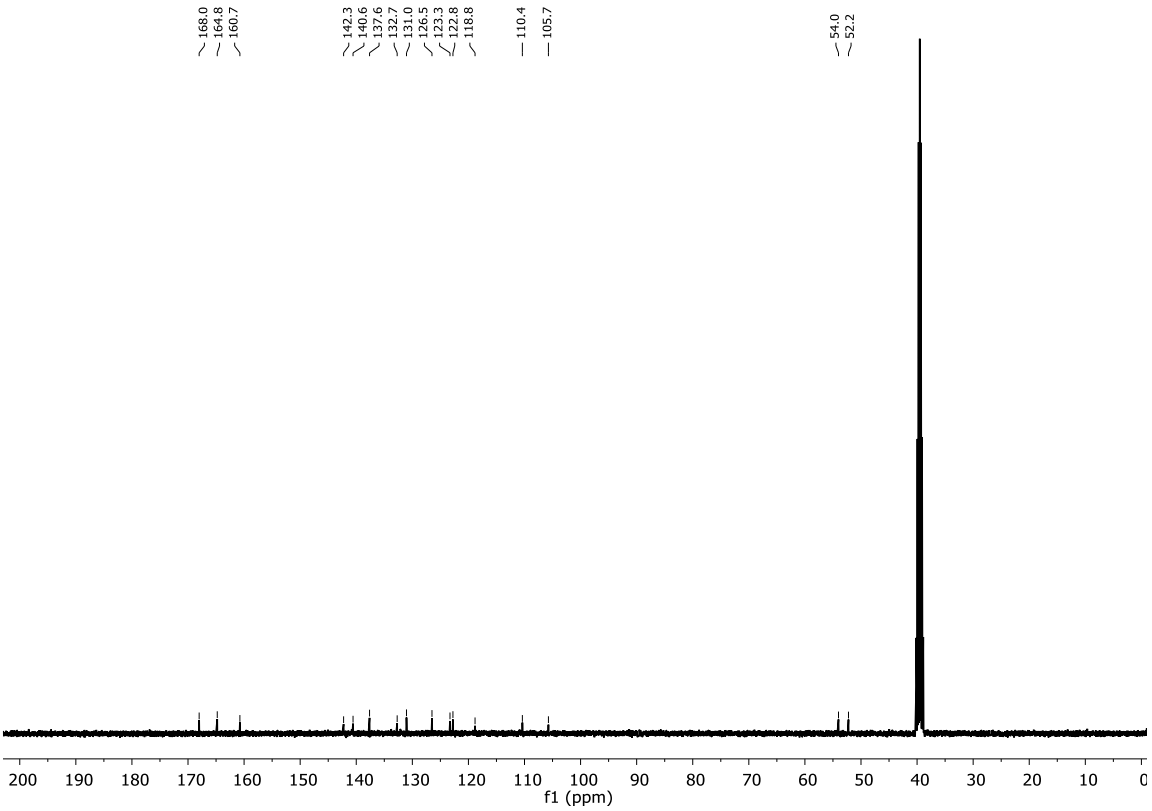

Dimethyl 4,5-dioxo-7-((3,14,25-trihydroxy-2,10,13,21,24-pentaoxo-3,9,14,20,25-pentaaza-triacontan-30-yl)carbamoyl)-4,5-dihydro-1*H*-pyrrolo[2,3-*f*]quinoline-2,9-dicarboxylate (PQQ$_{DFO}$)

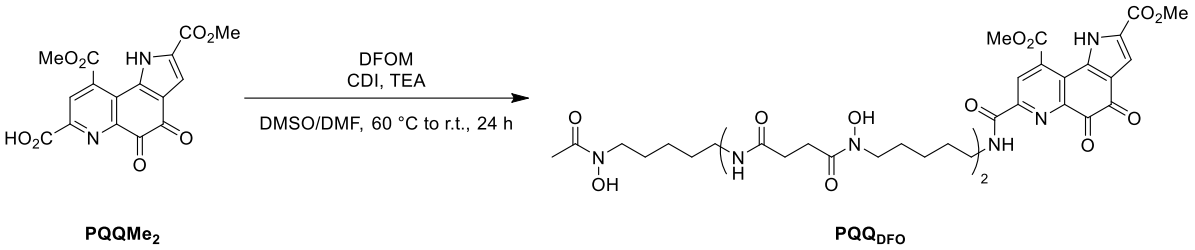

In a dry and nitrogen flushed SCHLENK flask, equipped with a magnetic stirring bar and a septum, **PQQMe$_2$** (16.4 mg, 0.05 mmol, 1.0 equiv.) and CDI (8.9 mg, 0.05 mmol, 1.2 equiv.) were dissolved in 2 mL dry DMF and were stirred at 60 °C for 1 h. Subsequently, the activated acid was added dropwise to a solution of DFO mesylate (30.0 mg, 0.05 mmol, 1.0 equiv.) and TEA (18.5 mg, 0.18 mmol, 4.0 equiv.) in 2 mL dry DMSO/DMF, which was also stirred at 60 °C for 1 h under a nitrogen atmosphere. The reaction mixture was stirred at room temperature overnight. After completion of the reaction, the solvent was evaporated to give a brown solid crude mixture containing **PQQ$_{DFO}$** as verified by HRMS. Due to impurities present in the crude mixture, the exact yield of pure product could not be determined.

HRMS (ESI): m/z calc. for [$C_{41}H_{57}N_8O_{15}$]: 901.3938 $[M-H]^+$

found: 901.3963.

Obtained ^{1}H NMR spectra were not clear enough to identify desired product.

This procedure was part of the bachelor thesis of Jonas Weiser, conducted under my supervision. As this project was not further continued, no additional analytical characterization was conducted.

3.5. Experimental Procedures to Subchapter III.3.

Method of continuous variation:

Stock solutions of **PQQ$_{18\text{-}6}$** (0.05 mM) and $La(NO_3)_3 \cdot 6H_2O$ (0.05 mM) were each prepared in acetonitrile. The UV-Vis measurements were conducted in a quartz suprasil cuvette (1000 µL), whereby 11 solutions containing **PQQ$_{18\text{-}6}$** and La^{3+} in different ratios were analyzed. Each sample included x µL **PQQ$_{18\text{-}6}$** (x = 1000; 900; 800; …; 0) and y µL La^{3+} (y = 1000 − x).

Mole ratio method:

Stock solutions of **PQQ$_{18\text{-}6}$** (0.1 mM) and $La(NO_3)_3 \cdot 6H_2O$ (0.1 mM) were each prepared in acetonitrile. The UV-Vis measurements were conducted in a quartz suprasil cuvette (1000 µL), whereby 15 solutions containing **PQQ$_{18\text{-}6}$** and La^{3+} in different ratios were analyzed. Each sample included x µL **PQQ$_{18\text{-}6}$** (x = 500; 400; 300; 250; 200; 180; 160; …; 20; 0), 100 µL La^{3+} and y µL acetonitrile (y = 900 − x).

General procedure: UV-Vis titration experiments (0 to 5.0 equiv. Ln^{3+})

Stock solutions of a ligand (0.0015 M) and a metal salt (0.015 M) were each prepared in acetonitrile. 100 µL of the ligand stock solution were given in a quartz suprasil cuvette (3000 µL) and were diluted with 2850 µL acetonitrile. The metal salt was added stepwise to the solution (0.1 equiv. per 1 µL added) and absorption spectra were measured.

General procedure: UV-Vis titration experiments (0 to 10 equiv. Ln^{3+})

Stock solutions of a ligand (0.0015 M) and a metal salt (0.03 M) were each prepared in acetonitrile. 100 µL of the ligand stock solution were given in a quartz suprasil cuvette (3000 µL) and were diluted with 2850 µL acetonitrile. The metal salt was added stepwise to the solution (0.5 equiv. per 2.5 µL added) and absorption spectra were measured.

General procedure: UV-Vis titration experiments (0 to 300 equiv. Ln^{3+})

Stock solutions of a ligand (0.0015 M) and a metal salt (0.375 M) were each prepared in acetonitrile. 100 µL of the ligand stock solution were given in a quartz suprasil cuvette (3000 µL) and were diluted with 2780 µL acetonitrile. The metal salt was added stepwise to the solution (10 equiv. per 4 µL added) and absorption spectra were measured.

UV-Vis titration experiment with L_{PQQ} (0 to 10 equiv. La^{3+})

A stock solution of **L_{PQQ}** (0.00029 M) and a stock solution of $La(NO_3)_3 \cdot 6H_2O$ (0.03 M) were prepared in acetonitrile/DMF (7% DMF) and in acetonitrile respectively. 520 μL of the ligand stock solution were given in a quartz suprasil cuvette (3000 μL) and were diluted with 2430 μL acetonitrile. The metal salt was added stepwise to the solution (0.5 equiv. per 2.5 μL added) and absorption spectra were measured.

TRF measurements:

Stock solutions of a ligand (0.001 M) and $Eu(NO_3)_3 \cdot 6H_2O$ (0.025 M) were each prepared in acetonitrile. 100 μL of the ligand stock solution were given in a 96-well quartz microplate from Hellma and were diluted with 96 μL acetonitrile. 4 μL of the Eu^{3+} stock solution were added and a TRF spectrum was measured.

Stock solutions including the ligands **L_{PQQ}** and **P_KQQ_{MEM}** were prepared by adding 1.0 equiv. of $Eu(NO_3)_3 \cdot 6H_2O$ to the suspension of the respective ligand (0.001 M) in acetonitrile. 100 μL of the Eu^{3+}-ligand stock solution were given in a 96-well quartz microplate from Hellma and were diluted with 100 μL acetonitrile, and a TRF spectrum was measured.

3.6. Experimental Procedures to Subchapter IV.3.

Dehydrogenation reactions: PQQMe$_2$-1-aza-15-crown-5 (**$PQQ_{15\text{-}5}$**; 6.5 mM, 1.0 equiv.) was placed in a sealable NMR tube with a septum and was dissolved in CD_3CN (0.55 mL). TMS_2O (1.0 equiv.) was added and a ^1H NMR spectrum was recorded. Then, a metal salt (2.0 equiv.) was added and a second spectrum was recorded. After addition of 4-methylbenzyl alcohol (4.0 equiv.), a third ^1H NMR was measured. Subsequently the reaction mixture was degassed by using an ultrasonic bath, high vacuum and nitrogen. Finally, degassed base (2.0 equiv.) was added, the tube was shaken to ensure complete mixing and a ^1H NMR spectrum was recorded as quickly as possible. The reaction was then monitored by recording spectra every 10 min (for 1 h), then every hour (for 4 h), then every 5 h (for 15 h). The final spectrum was recorded after 24 h after the start of the reaction. The reactions were run in duplicate, in the case of barium in triplicate, the points in Figure IV.5 reflect the mean ± SEM. The yields were calculated based on the amount of ligand **$PQQ_{15\text{-}5}$**. The metal salts used were $Ba(OTf)_2$, $Ca(OTf)_2 \cdot H_2O$, $Ln(OTf)_3 \cdot 3H_2O$ (Ln = La, Eu and Lu) and $La(NO_3)_3 \cdot 6H_2O$ and the bases used were DBU, 2,6-lutidine and pyridine.

The reactions involving the absence of one of the components were performed following the same experimental procedure by skipping the corresponding addition step. The reaction monitoring was then performed by recording spectra in bigger time intervals.

EPR experiments: The concentration of ligand **PQQ$_{15\text{-}5}$** was 25 mM in acetonitrile. Depending on the nature of the experiment, the amount of metal salt if added was 2.0 equiv., the amount of 4-methylbenzyl alcohol if added was 4.0 equiv. and the amount of DBU if added was 2.0 equiv. The metal salts used were $Ba(OTf)_2$, $Ca(OTf)_2{\cdot}H_2O$ and $Ln(OTf)_3{\cdot}3H_2O$ (Ln = La, Eu and Lu).

3.7. Experimental Procedure to Subchapter IV.4.

PQQMe$_2$-1-aza-15-crown-5 (**PQQ$_{15\text{-}5}$**; 6.4 mM, 1.0 equiv.) was placed in a sealable NMR tube with a septum and was dissolved in CD_3CN (0.56 mL). TMS_2O (1.0 equiv) and $La(OTf)_3{\cdot}3H_2O$ (2.0 equiv.) were added, and the reaction mixture was degassed by using an ultrasonic bath, high vacuum and nitrogen. Subsequently degassed alcohol (0 to 20 equiv.) and degassed DBU (2.0 equiv.) were added, the tube was shaken to ensure complete mixing and a ^{1}H NMR spectrum was recorded as quickly as possible. The reaction was then monitored by recording spectra continuously for 2 h. The yields were calculated based on the amount of ligand **PQQ$_{15\text{-}5}$**. The alcohols used were benzyl alcohol and benzyl-α,α-d$_2$ alcohol.

3.8. Experimental Procedure to Subchapter IV.5.

A ligand (6.3 mM, 1.0 equiv.) was placed in a sealable NMR tube with a septum and was dissolved in CD_3CN (0.57 mL). TMS_2O (1.0 equiv.) was added and a ^{1}H NMR spectrum was recorded. Then, a metal salt (either $La(NO_3)_3{\cdot}6H_2O$ or $Ca(NO_3)_2{\cdot}4H_2O$, 2.0 equiv.) and 4-methylbenzyl alcohol (4.0 equiv.) were added and a second ^{1}H NMR was measured. Subsequently the reaction mixture was degassed by using an ultrasonic bath, high vacuum and nitrogen. Finally, degassed DBU (2.0 equiv.) was added, the tube was shaken to ensure complete mixing and a ^{1}H NMR spectrum was recorded as quickly as possible. The reaction was then monitored by recording spectra every hour (for 5 h), then every five hours (for 15 h). The final spectrum was recorded after 24 h after the start of the reaction. The yields were calculated based on the amount of the respective ligand.

3.9. Experimental Procedures to Subchapter IV.6.

GC-MS Separation Method

By using reference alcohol and aldehyde samples, a GC-MS method was evaluated aiming the elution of both compounds with different retention times. The samples were syringe filtered (PTFE, 0.45 µm) and injected onto an Agilent® 7820 GC (1 µL in a 1:1 split mode) equipped with a 30 m x 0.25 mm HP5-MS column (Agilent® 19091S-433UI) coupled to an Agilent® 5977 EI mass spectrometer. The injector temperature was set to 280 °C and the temperature of the ion source to 230 °C. The initial oven temperature was 80 °C, held there for 1 min, and subsequently it was ramped to 160 °C at 20 °C/min. Mass spectra were recorded in scan mode between 1.6–400 m/z.

As shown in Figure V.3, the applied method enabled the separation of the two different compounds with retention times of 3.999 min for 4-methyl benzaldehyde and 4.364 min for 4-methylbenzyl alcohol.

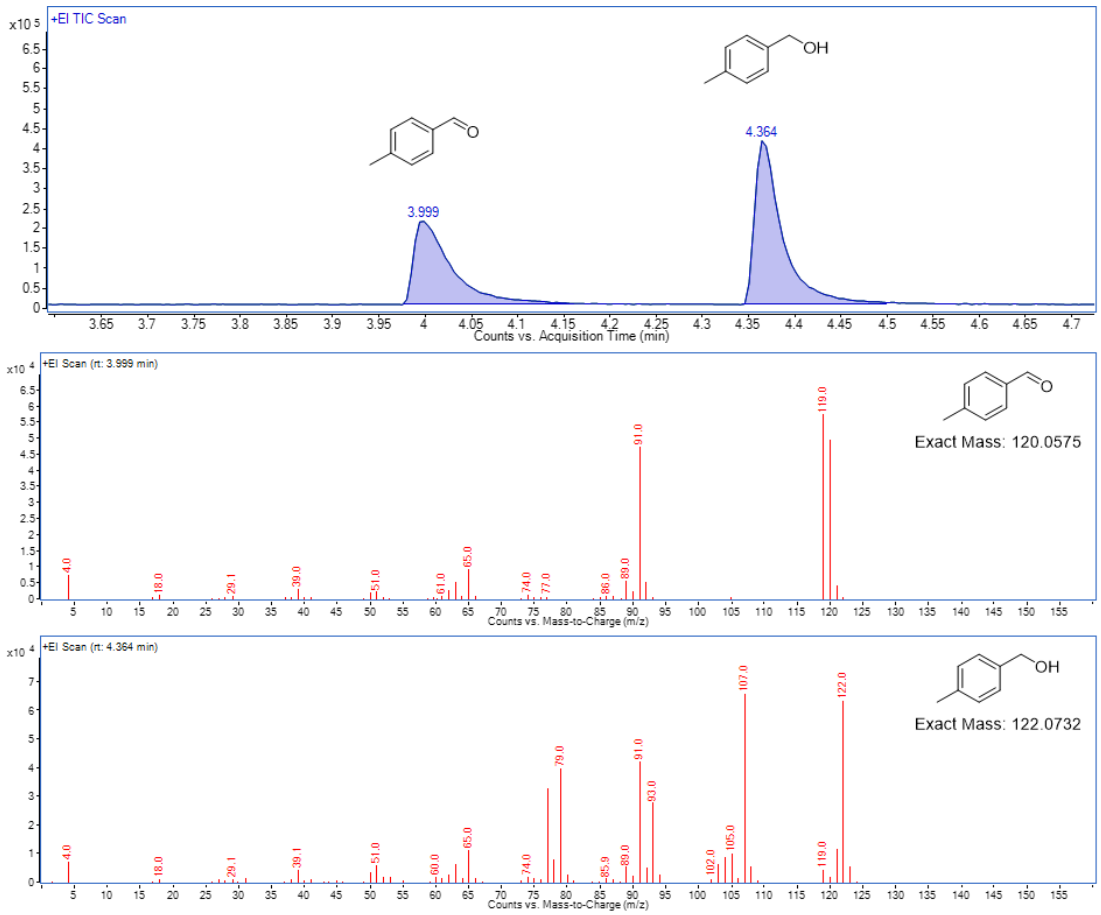

Figure V.3: GC-MS reference traces of 4-methyl benzaldehyde and 4-methylbenzyl alcohol (upper spectrum). EI mass spectra (lower spectra) recorded at t_R = 4.399 min (4-methyl benzaldehyde) and t_R = 4.364 min (4-methylbenzyl alcohol).

Calibration Measurements

To quantify the concentration of 4-methyl benzaldehyde from obtained GC-MS chromatograms, calibration measurements were conducted. Hence, several solutions of different concentration were prepared and were subjected to GC-MS measurements with the method described in the subchapter above. The peak areas were plotted against the concentration as amount of substance per volume. The resulting calibration line is shown in Figure V.4 (right). As shown in Figure V.4 on the left, higher aldehyde concentrations (over 0.001 M) go over the instrument detection limit, thus for future experiments the concentration range should be kept up to 0.0005 M.

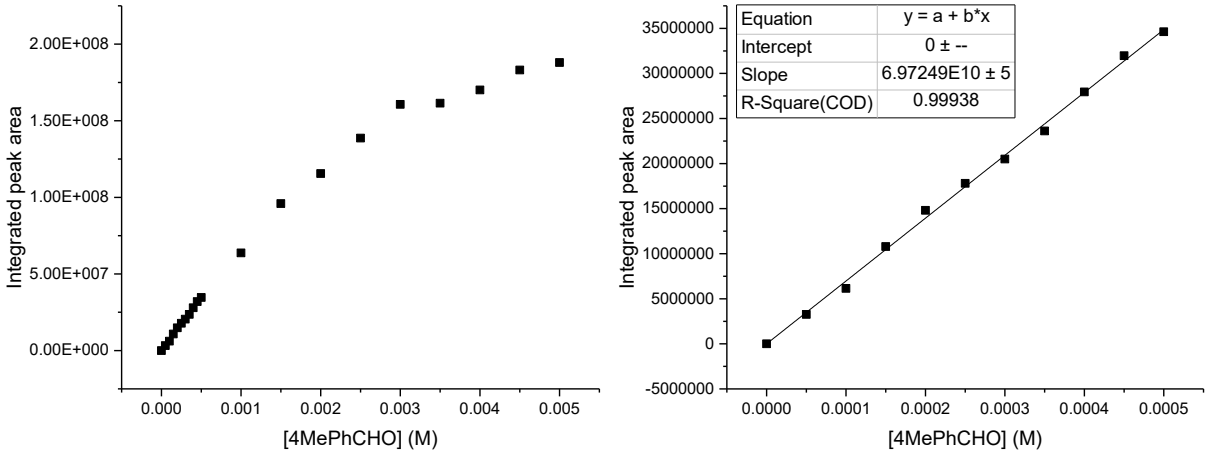

Figure V.4: Plot of the 4-methyl benzaldehyde concentration vs. the integrated peak area obtained by GC-MS analysis (left). Calibration line plot of 4-methyl benzaldehyde (right).

Control reaction: alcohol dehydrogenation attempt under ligand exclusion:

Stock solutions of $La(NO_3)_3 \cdot 6H_2O$ (1.79 M) and 4-methylbenzyl alcohol (7.97 M) were each prepared in CD_3CN.

550 µL CD_3CN were placed in a sealable NMR tube with a septum and 0.76 µL TMS_2O (1.0 equiv.) were added as internal standard and a ^1H NMR spectrum was recorded. Then, the metal salt (10 µL, 5.0 equiv.) and 4-methylbenzyl alcohol (10 µL, 22 equiv.) were added and the reaction mixture was degassed by using an ultrasonic bath, high vacuum and nitrogen. Finally, degassed DBU (0.5 µL, 0.93 equiv.) was added, the tube was shaken to ensure complete mixing and a ^1H NMR spectrum was recorded as quickly as possible. A second spectrum was recorded after 24 h.

Test of aliquot work-up procedure:

Solutions of 4-methyl benzaldehyde were prepared in different concentrations (0 to 0.5 M) in acetonitrile. 0.5 mL from each solution were directly subjected to GC-MS measurement. Further 0.5 mL from the same solution were first filtered through a glass pipette filled with silica (approx. 220 mg) and then through a syringe filter prior to the GC-MS injection.

Preliminary alcohol dehydrogenation experiments under variation of the alcohol concentration:

A solution of **PQQ$_{18\text{-}6}$** (0.5 mM, 1.0 equiv.) and $La(NO_3)_3 \cdot 6H_2O$ (5.0 equiv.) was prepared in an Eppendorf tube in CH_3CN. Subsequently 4-methylbenzyl alcohol (0.5 to 20 equiv.) and DBU (1.0 equiv.) were added. The reaction mixture (total volume 1.0 mL) was immediately transferred to a GC vial, closed with a cap with a septum and subsequently degassed by using an ultrasonic bath under a nitrogen flow. The vial was wrapped with Parafilm® and placed in a thermoshaker (28 °C). After 24 h the reaction mixture (0.5 mL) was filtered through a glass pipette filled with silica (approx. 220 mg), then through a syringe filter and finally was subjected to GC-MS measurement.

The yield percentages were calculated based on the amount of the ligand.

Control reaction: alcohol dehydrogenation reaction in the presence of high alcohol concentration:

Stock solutions of **PQQ$_{18\text{-}6}$** (0.0065 M), $La(NO_3)_3 \cdot 6H_2O$ (1.79 M) and 4-methylbenzyl alcohol (7.97 M) were each prepared in CD_3CN.

550 µL of the **PQQ$_{18\text{-}6}$** (1.0 equiv.) stock solution were placed in a sealable NMR tube with a septum. 0.76 µL TMS_2O (1.0 equiv.) were added as internal standard and a ^1H NMR spectrum was recorded. Then, the metal salt (10 µL, 5.0 equiv.) and 4-methylbenzyl alcohol (10 µL, 22 equiv.) were added and the reaction mixture was degassed by using an ultrasonic bath, high vacuum and nitrogen. Finally, degassed DBU (0.5 µL, 0.93 equiv.) was added, the tube was shaken to ensure complete mixing and a ^1H NMR spectrum was recorded as quickly as possible. The reaction was then monitored by recording spectra after 6, 12 and 24 h.

General procedure for the investigated alcohol dehydrogenation experiments under variation of the reaction conditions:

The sample was either prepared on air or in a glovebox. A solution of **PQQ$_{18\text{-}6}$** (0.5 mM, 1.0 equiv.) and a La^{3+} salt (5.0 equiv.) was prepared in an Eppendorf tube in either CH_3CN or CD_3CN. Subsequently 4-methylbenzyl alcohol (5.0 equiv.) and DBU (1.0 equiv.) were added. The reaction mixture (total

volume 1.0 mL) was immediately transferred to a GC vial, closed with a cap with a septum and subsequently degassed (unless otherwise stated) by using an ultrasonic bath under a nitrogen flow. The vial was wrapped with Parafilm® and placed in a thermoshaker (28 °C, unless otherwise stated). After 24 h the reaction mixture (0.5 mL) was filtered through a glass pipette filled with silica (approx. 220 mg), then through a syringe filter and finally was subjected to GC-MS measurement.

The yield percentages were calculated based on the amount of the ligand.

General procedure for the reaction screenings described in subchapter IV.6.2.:

All samples were prepared in a glovebox. A solution of a ligand (0.5 mM, 1.0 equiv.) and a metal salt (1.0 to 15 equiv.) was prepared in an Eppendorf tube in CH_3CN. Subsequently 4-methylbenzyl alcohol (0.5 to 20 equiv.) and DBU (1.0 equiv.) were added. The reaction mixture (total volume 1.0 mL) was immediately transferred to a GC vial, closed with a cap with a septum, and the vial was wrapped with Parafilm®. After either 1 or 24 h the reaction mixture (0.5 mL) was filtered through a glass pipette filled with silica (approx. 220 mg), then through a syringe filter and finally was subjected to GC-MS measurement.

The yield percentages were calculated based on the amount of the ligand.

VI. APPENDIX

1. Crystallization Experiments

1.1. Crystallization attempts with ligand L_{PQQ}

In order to investigate the coordination ability of the ligand **L_{PQQ}**, crystallization experiments were performed. DMF was used as a solvent, since both ligand and metal salt are soluble in it.

Experiment A: **L_{PQQ}** (2.9 mg, 3.25 μmol, 1.0 equiv.), $La(NO_3)_3 \cdot 6H_2O$ (1.55 mg, 3.58 μmol, 1.1 equiv.), TEA (0.26 mg, 6.5 μmol, 2.0 equiv.), DMF (400 μL), vapor diffusion with acetone.

Experiment B: **L_{PQQ}** (2.3 mg, 2.58 μmol, 1.0 equiv.), $La(NO_3)_3 \cdot 6H_2O$ (1.23 mg, 2.84 μmol, 1.1 equiv.), TEA (0.522 mg, 5.16 μmol, 2.0 equiv.), DMF (400 μL), vapor diffusion with diethyl ether.

Unfortunately, the crystallization experiments A and B did not yield any crystals. A further attempt to obtain crystals from a **L_{PQQ}**-La^{3+} complex was performed, following the procedure described below.

Experiment C: **L_{PQQ}** (11.0 mg, 12.3 μmol, 1.0 equiv.) and $La(NO_3)_3 \cdot 6H_2O$ (5.5 mg, 12.7 μmol, 1.0 equiv.) were dissolved in 2 mL acetonitrile. The reaction mixture was stirred under reflux for 15 min, whereby the solution became turbid upon increasing the temperature. Subsequently, five drops of DMF were added to the hot reaction mixture and the resulting clear solution was allowed to slowly cool down to room temperature. The reaction mixture was refrigerated at -20 °C for 5 days. Since no crystals were formed, the solution was concentrated *in vacuo* and a vapor diffusion with diethyl ether was performed. Unfortunately, the crystallization experiment failed to accomplish.

1.2. Crystallization attempts with $PQQMe_2$

In order to examine the coordination chemistry of **$PQQMe_2$** with lanthanide ions, several crystallization attempts were conducted. First, the solubility of an acetonitrile solution of **$PQQMe_2$** and Ln^{3+} was analyzed in different solvents (Table VI.1). The addition of *tert*-butyl methyl ether (TBME), dichloromethane (DCM) and water to the complex solutions resulted in the formation of red precipitations, hence these solvents were considered as suitable precipitants for vapor diffusion experiments. Thus, with every solvent three different crystallization batches were prepared using either lanthanum(III), gadolinium(III) or lutetium(III) nitrate as metal salt for the complex formation.

The vapor diffusion experiments including TBME and DCM resulted in the precipitation of red solids. All three batches including water as precipitant, however, yielded small red crystals. Unfortunately, the crystals were too low scattering for an X-ray measurement, hence they could not be analyzed. The further attempts to improve the quality of the crystals were not successful.

Table VI.1: Solubility examination. ***PQQMe*$_2$** *(1 mg, 0.003 mmol) was suspended in acetonitrile (200 µL). 1.0 equiv. of $Ln(NO_3)_3 \cdot 6H_2O$ (Ln: La, Gd, Lu) was added to the ligand, resulting in an immediate color change from orange to dark-red. The mixture was centrifuged and 10 µL of the supernatant were placed in a GC vial and 100 µL of solvent were added.*

Solvent	Observation
TBME	red precipitation
DCM	red precipitation
H_2O	red precipitation
$CHCl_3$	solution
1,4-dioxane	solution
THF	solution

As part of her Bachelor thesis performed under my supervision, Sophia Glocker conducted several crystallization attempts in order to investigate the coordination chemistry of **PQQMe$_2$** with La^{3+}. Thereby, two different crystallization methods were applied: vapor diffusion using either diisopropyl ether (DIPE) or tetrahydrofuran (THF) and slow evaporation. All stock solutions were prepared in DMF and the experiments were conducted at room temperature. As shown in the batches with lanthanum(III) triflate led to the formation of orange needle-shaped crystals, which were unfortunately not suitable for X-ray analysis. The slow solvent evaporation of the solutions containing lanthanum(III) nitrate and lanthanum(III) perchlorate resulted in precipitation of orange solids. Interestingly, the experiments including lanthanum(III) chloride gave green brown slurry mixtures. The formation of some radicals was assumed as the most likely explanation of the observed color change. Future experiments should concentrate on improving the crystallization conditions of the setting up including lanthanum(III) triflate since this batch already led to the formation of needles.

Table VI.2: List of crystallization attempts and respective observations.

La^{3+} salt	La^{3+}:$PQQMe_2$ ratio	Method	Observation
$LaCl_3 \cdot 7H_2O$	2.0	vapor diffusion (DIPE)	green-brown slurry mixture
$LaCl_3 \cdot 7H_2O$	2.0	vapor diffusion (THF)	green-brown slurry mixture
$LaCl_3 \cdot 7H_2O$	1.9	slow evaporation	green-brown slurry mixture
$La(NO_3)_3 \cdot 6H_2O$	2.3	vapor diffusion (DIPE)	-
$La(NO_3)_3 \cdot 6H_2O$	2.4	slow evaporation	orange solid
$La(OTf)_3 \cdot 2H_2O$	2.4	vapor diffusion (DIPE)	orange needle-shaped crystals
$La(OTf)_3 \cdot 2H_2O$	2.4	vapor diffusion (THF)	orange needle-shaped crystals
$La(OTf)_3 \cdot 2H_2O$	2.5	slow evaporation	orange needle-shaped crystals
$La(ClO_4)_3 \cdot 6H_2O$	2.3	vapor diffusion (DIPE)	-
$La(ClO_4)_3 \cdot 6H_2O$	2.1	slow evaporation	orange solid

1.3. Crystallization attempts with $PQQ_{15\text{-}5}$ and $PQQ_{18\text{-}6}$

In order to investigate the coordination ability of ligands **$PQQ_{15\text{-}5}$** and **$PQQ_{18\text{-}6}$** towards lanthanum(III) and europium(III), crystallization experiments were performed (Table VI.3). All ligand and metal salt stock solutions were prepared in Milli-Q water. The crystallization samples were mixed in ligand to metal ratios of 1:10 and 1:20 and were stored either at 4 °C or at room temperature. Unfortunately, the crystallization attempt at room temperature was not successful, since the gradual evaporation of the solvent led to the formation of a slurry mixture. The batches stored at low temperature have still not yielded any crystals.

*Table VI.3: Crystallization attempts performed with ligands **$PQQ_{15\text{-}5}$** and **$PQQ_{18\text{-}6}$** and various lanthanide salts in water.*

Salt	Total volume (mL)	$[M^{3+}]$ (mM)	[Ligand] (mM)	Equiv. ligand	Equiv. M^{3+}	Temperature (°C)
$LaCl_3 \cdot 7H_2O$	4.5	8.44	0.844	1	10	4
$La(NO_3)_3 \cdot 6H_2O$	4.7	8.51	0.849	1	10	4
$La(OTf)_3 \cdot 2H_2O$	1.38	5.8	0.606	1	10	4
$La(ClO_4)_3 \cdot 6H_2O$	1.9	6.84	0.7	1	10	4
$La(OAc)_3 \cdot 1.5H_2O$	1.9	7.11	0.7	1	10	4
$EuCl_3 \cdot 6H_2O$	1.8	6.94	0.686	1	10	4
$Eu(NO_3)_3 \cdot 6H_2O$	2.1	7.14	0.724	1	10	4
$LaCl_3 \cdot 7H_2O$	4.5	8.44	0.836	1	10	4
$La(NO_3)_3 \cdot 6H_2O$	4.8	8.33	0.842	1	10	4

Salt	Total volume (mL)	[M3+] (mM)	[Ligand] (mM)	Equiv. ligand	Equiv. M3+	Temperature (°C)
$La(OTf)_3 \cdot 2H_2O$	1.4	5.71	0.604	1	9	4
$La(ClO_4)_3 \cdot 6H_2O$	1.9	6.84	0.693	1	10	4
$La(OAc)_3 \cdot 1.5H_2O$	1.9	7.11	0.693	1	10	4
$EuCl_3 \cdot 6H_2O$	1.8	6.94	0.679	1	10	4
$Eu(NO_3)_3 \cdot 6H_2O$	2.1	7.14	0.716	1	10	4
$LaCl_3 \cdot 7H_2O$	1.93	14.0	0.704	1	20	4
$La(NO_3)_3 \cdot 6H_2O$	1.53	12.7	0.64	1	20	4
$La(OTf)_3 \cdot 2H_2O$	1.01	8.89	0.481	1	19	4
$La(ClO_4)_3 \cdot 6H_2O$	1.12	10.3	0.525	1	20	4
$La(OAc)_3 \cdot 1.5H_2O$	2.46	15.2	0.757	1	20	4
$EuCl_3 \cdot 6H_2O$	2.76	15.6	0.778	1	20	4
$Eu(NO_3)_3 \cdot 6H_2O$	2.73	15.6	0.776	1	20	4
$LaCl_3 \cdot 7H_2O$	1.95	13.8	0.699	1	20	4
$La(NO_3)_3 \cdot 6H_2O$	1.54	12.7	0.635	1	20	4
$La(OTf)_3 \cdot 2H_2O$	1.02	8.85	0.478	1	19	4
$La(ClO_4)_3 \cdot 6H_2O$	1.12	10.2	0.522	1	20	4
$La(OAc)_3 \cdot 1.5H_2O$	2.48	15.1	0.75	1	20	4
$EuCl_3 \cdot 6H_2O$	2.79	15.4	0.772	1	20	4
$Eu(NO_3)_3 \cdot 6H_2O$	2.75	15.5	0.769	1	20	4
$LaCl_3 \cdot 7H_2O$	3.01	7.97	0.792	1	10	25
$La(NO_3)_3 \cdot 6H_2O$	1.69	6.81	0.669	1	10	25
$La(OTf)_3 \cdot 2H_2O$	1.51	5.96	0.635	1	9	25
$La(ClO_4)_3 \cdot 6H_2O$	1.48	6.44	0.628	1	10	25
$La(OAc)_3 \cdot 1.5H_2O$	2.14	7.24	0.728	1	10	25
$EuCl_3 \cdot 6H_2O$	2.21	7.24	0.735	1	10	25
$Eu(NO_3)_3 \cdot 6H_2O$	2.95	7.97	0.789	1	10	25
$LaCl_3 \cdot 7H_2O$	3.04	7.9	0.785	1	10	25
$La(NO_3)_3 \cdot 6H_2O$	1.7	6.77	0.664	1	10	25
$La(OTf)_3 \cdot 2H_2O$	1.52	5.92	0.631	1	9	25
$La(ClO_4)_3 \cdot 6H_2O$	1.49	6.4	0.624	1	10	25
$La(OAc)_3 \cdot 1.5H_2O$	2.16	7.18	0.722	1	10	25
$EuCl_3 \cdot 6H_2O$	2.23	7.18	0.729	1	10	25
$Eu(NO_3)_3 \cdot 6H_2O$	2.98	7.89	0.782	1	10	25

In addition, numerous crystallization attempts were performed using the reaction mixtures from already finished experiments whereby various techniques like vapor and layered diffusion, conducted through variation of the solvents, storage temperatures, solution concentrations and ligand to metal ratios were applied. Unfortunately, all attempts were unsuccessful. Moreover, an experiment was carried out based on the gel crystallization technique (Figure II.6).

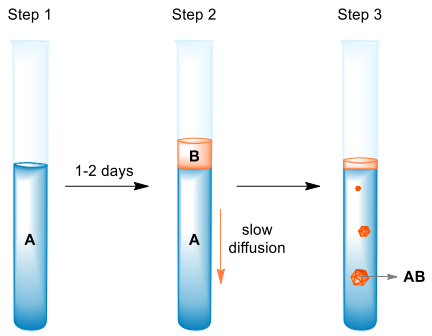

Figure VI.1: Gel crystallization technique. The procedure begins with the preparation of a gel containing compound A. Subsequently, the gel should be overlayered with a solution containing compound B, which will slowly diffuse through the gel, reacting with component A to give crystals with a AB composition.

Sodium metasilicate, also known as sodium water glass, was chosen as a gel medium. First, a solution of Na_2SiO_3 (1.0 g, 8.19 mmol) in 8.6 mL water was prepared by stirring and heating to approx. 80 °C for 10 min. After cooling down to room temperature, the solution was filtered through a syringe filter and 2 mL acetic acid (0.88 M) were given to the mixture. Subsequently, the pH of the mixture was set to 3 using pure acetic acid (100%). Under vigorous stirring, 1.33 g (5.38 mmol) $CeCl_3 \cdot 7H_2O$ were added. The resulting solution was immediately transferred into several test tubes and was stored overnight at room temperature until the gel solidified. On the next day, solutions of both PQQ crown ether ligands **PQQ$_{15\text{-}5}$** (0.015 g, 0.027 mmol in 0.5 mL H_2O) and **PQQ$_{18\text{-}6}$** (0.02 g, 0.033 mmol in 0.5 mL H_2O) were prepared and layered above the gel. The test tubes were closed with Parafilm® and were stored over several weeks at room temperature at a vibration-free space. Unfortunately, the crystallization attempt did not yield any crystals.

2. Interaction of $PQQ_{15\text{-}5}$ with Lanthanide and Alkaline Earth Metal Salts

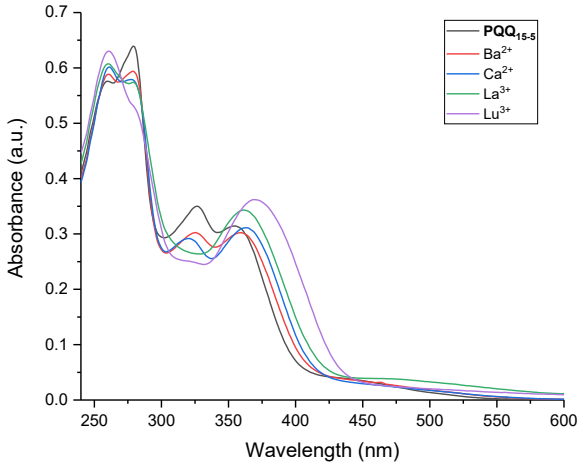

Figure VI.2: Absorption change of ***PQQ****$_{15\text{-}5}$ (0.025 mM) upon addition of 2.0 equiv. metal triflate in acetonitrile at room temperature. The metal salts used were $Ba(OTf)_2$, $Ca(OTf)_2{\cdot}H_2O$ and $Ln(OTf)_3{\cdot}3H_2O$ (Ln = La, and Lu).*

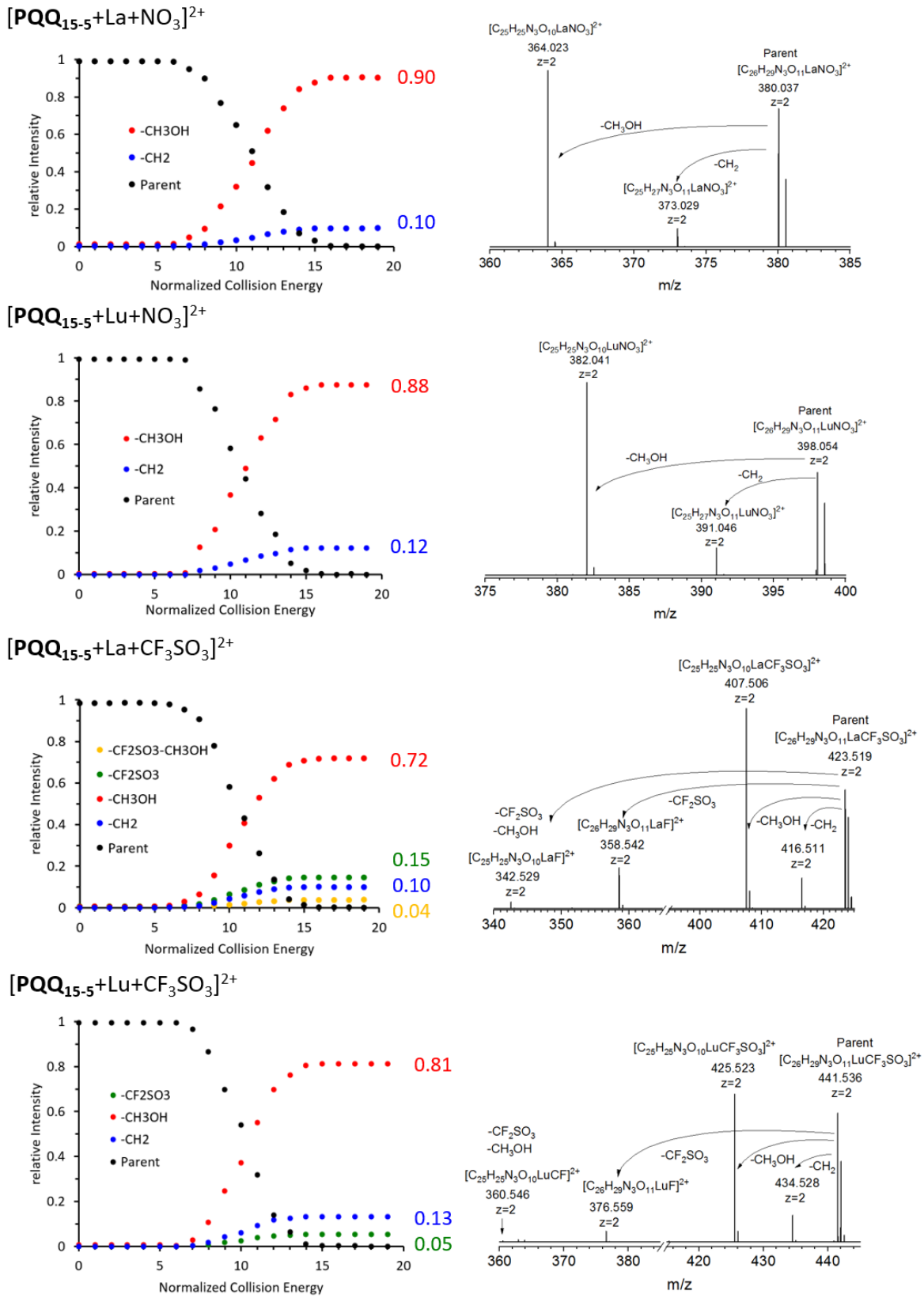

*Figure VI.3: Collision induced dissociation of [**PQQ**$_{15\text{-}5}$+Ln+X]$^{2+}$, Ln = La, Lu; X = NO_3, CF_3SO_3. Left: Relative ion intensities (as obtained by integrating the respective mass spectra) as function of the excitation energy in instrument specific units of "normalized collision energy". Right: Typical fragmentation mass spectra at medium excitation energies (10-11 NCE). The dominant channel is always loss of (neutral) CH_3OH. For Y = CF_3SO_3 loss of (neutral) CF_2SO_3 is observed as well.*

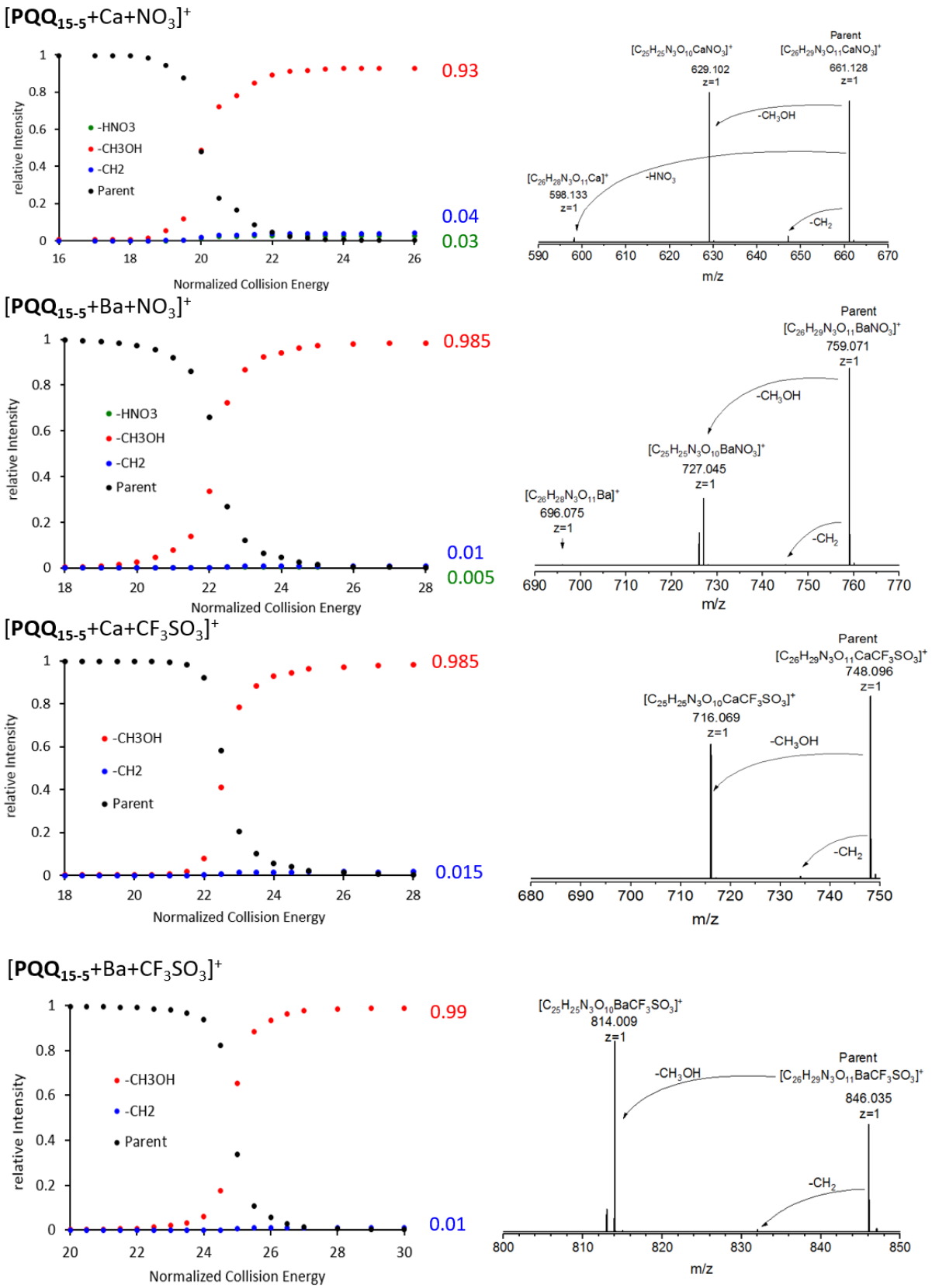

*Figure VI.4: Collision induced dissociation of [**PQQ**15-5+M+X]+, M = Ba, Ca; X = NO3, CF3SO3. Left: Relative ion intensities (as obtained by integrating the respective mass spectra) as function of the excitation energy in instrument specific units of "normalized collision energy". Right: Typical fragmentation mass spectra at medium excitation energies (20-22 NCE). The dominant channel is always loss of (neutral) CH3OH.*

3. Spectroscopic Studies with PQQ Derivatives and Lanthanide Salts

3.1. UV-Vis Titrations of $PQQ_{18\text{-}6}$ with Different Lanthanide(III) Salts

The first La^{3+}-containing reagent investigated for its interaction with ligand **$PQQ_{18\text{-}6}$** was the complex compound $LaCl_3 \cdot 2LiCl$ (see chapter VI.0.2. for more details about the preparation of the reagent). This reagent offers the benefit of being non-aqueous character, however, it is only available as a THF solution. Nonetheless, a metal titration was conducted and despite the reasonable titration curve obtained through the measurement (Figure VI.5), a solid precipitation during the titration with larger quantities of the reagent led to an interference of the measurement and only poor spectroscopic data could be obtained.

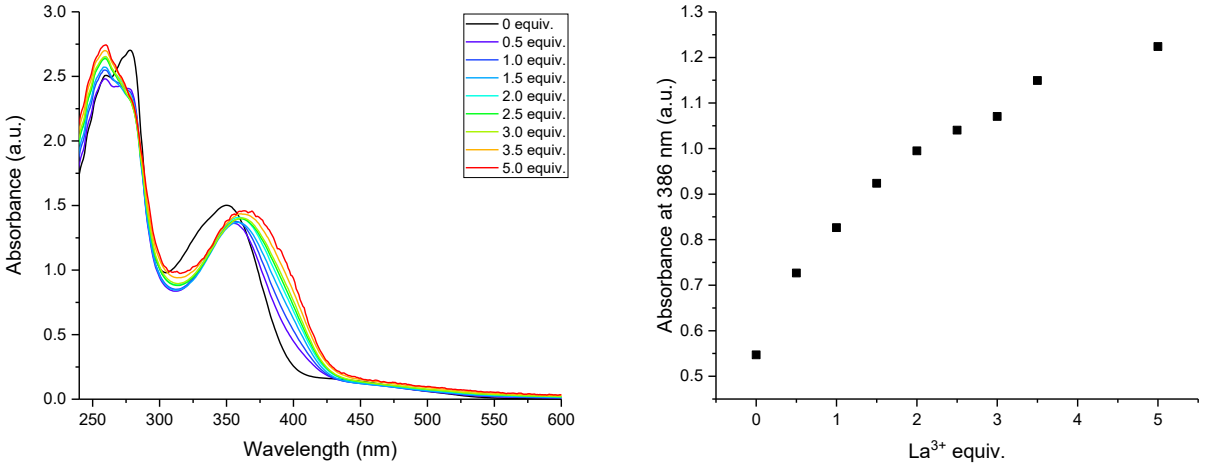

*Figure VI.5: Spectrophotometric titration of **$PQQ_{18\text{-}6}$** (0.25 mM) with increasing amounts of $LaCl_3 \cdot 2LiCl$ (0 to 1.25 mM) in acetonitrile (left) and plot of the absorption change at 386 nm vs. the La^{3+} equivalents added to the ligand (right). Each solution had a constant total volume of 200 µL. The measurements were conducted with an Epoch 2 Plate Reader from Biotek in a 96-well quartz microplate from Hellma.*

UV-Vis Spectroscopy measurements were either conducted with an Agilent Cary 60 UV-Vis with Peltier Element or with an Agilent 8453 Diode Array Spectrophotometer with stirred cuvette holder or with an Epoch 2 Plate Reader from Biotek using either 10 mm quartz suprasil cuvettes from Hellma (total volume of either 1 or 3 mL, path length 1 cm) or a 96-well quartz microplate from Hellma. Measurements under inert atmosphere were conducted using sealable quartz suprasil cuvettes from Hellma (total volume either 1 mL or 3 mL, path length 1 cm) equipped with a stirring bar and a septum.

Furthermore, the interaction between **$PQQ_{18\text{-}6}$** and lanthanum(III) perchlorate was examined and the stepwise titration of the salt resulted in a red shift of the ligand's absorption band at 350 nm (Figure VI.6). The corresponding plot of the absorbance at 386 nm versus the added La^{3+} equivalents revealed

saturation of the complex after the addition of 5.0 equiv. La^{3+}. Unfortunately, the limitation with the lanthanide(III) perchlorates lies in their limited availability from commercial sources, as only lanthanum(III) perchlorate is commercially accessible. This posed a challenge for conducting the aimed metal screenings in this project.

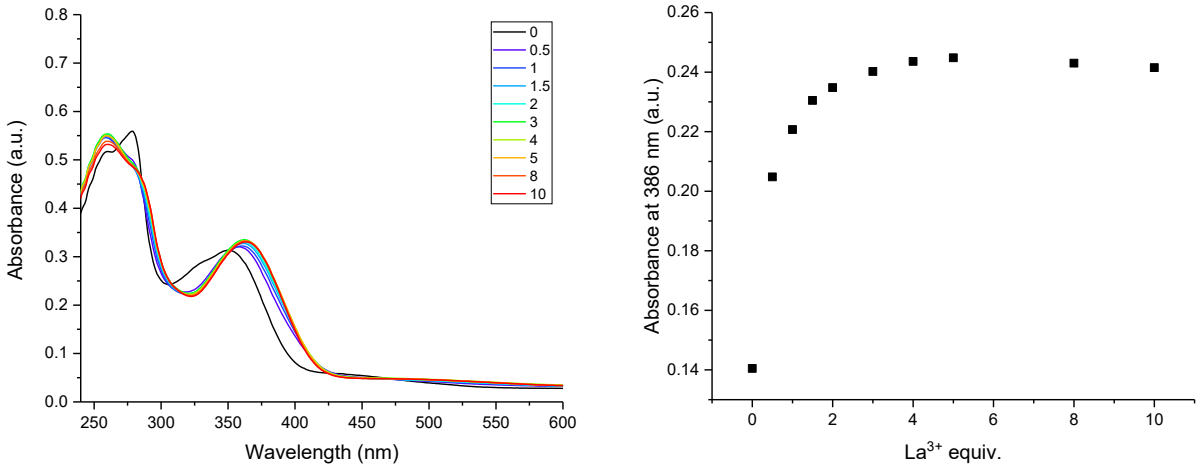

Figure VI.6: Spectrophotometric titration of ***PQQ***$_{18\text{-}6}$ *(0.05 mM) with increasing amounts of* $La(ClO_4)_3 \cdot 6H_2O$ *(0 to 0.5 mM) in acetonitrile (left) and plot of the absorption change at 386 nm vs. the* La^{3+} *equivalents added to the ligand (right). Each solution had a constant total volume of 200 µL. The measurements were conducted with an Epoch 2 Plate Reader from Biotek in a 96-well quartz microplate from Hellma.*

To identify appropriate metal salts for the intended screenings, spectrophotometric titrations were performed using lanthanum(III) chloride (Figure VI.7) and lanthanum(III) triflate (Figure VI.8). Due to the poor solubility of the salts in neat acetonitrile, however, the measurements were performed in solvent systems containing mixtures of acetonitrile with either water and THF, respectively. However, the obtained results from the measurements with the chloride suggested problems with the proper dissociation of the metal salt in the ligand solution due to the higher water content in the solution. The problem associated with the use of the triflate was the volatile character of THF which made the UV-Vis data prone to errors.

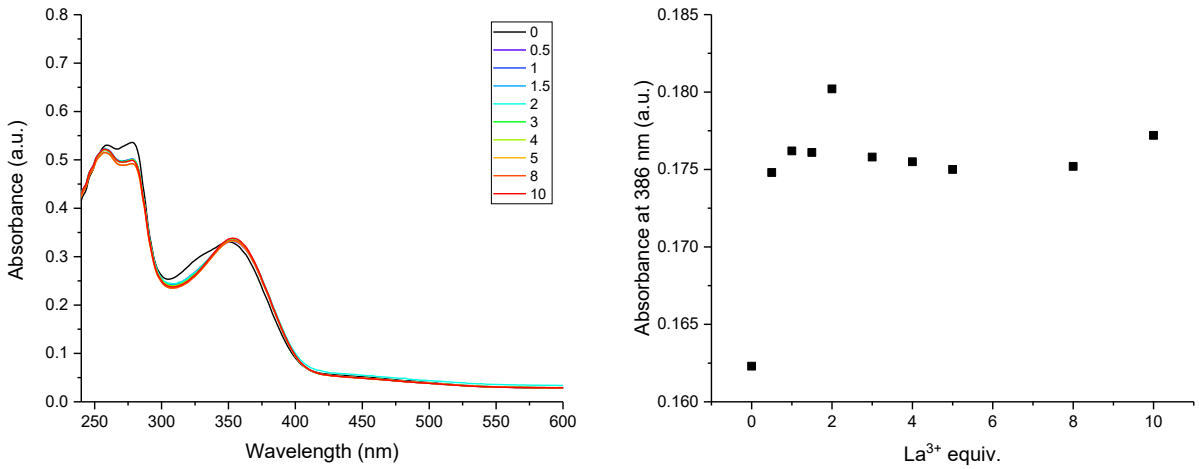

Figure VI.7: Spectrophotometric titration of ***PQQ***$_{18\text{-}6}$ *(0.05 mM) with increasing amounts of* $LaCl_3 \cdot 7H_2O$ *(0 to 0.5 mM) in acetonitrile and 23%* H_2O *(left) and plot of the absorption change at 386 nm vs. the* La^{3+} *equivalents added to the ligand (right). Each solution had a constant total volume of 200 µL. The measurements were conducted with an Epoch 2 Plate Reader from Biotek in a 96-well quartz microplate from Hellma.*

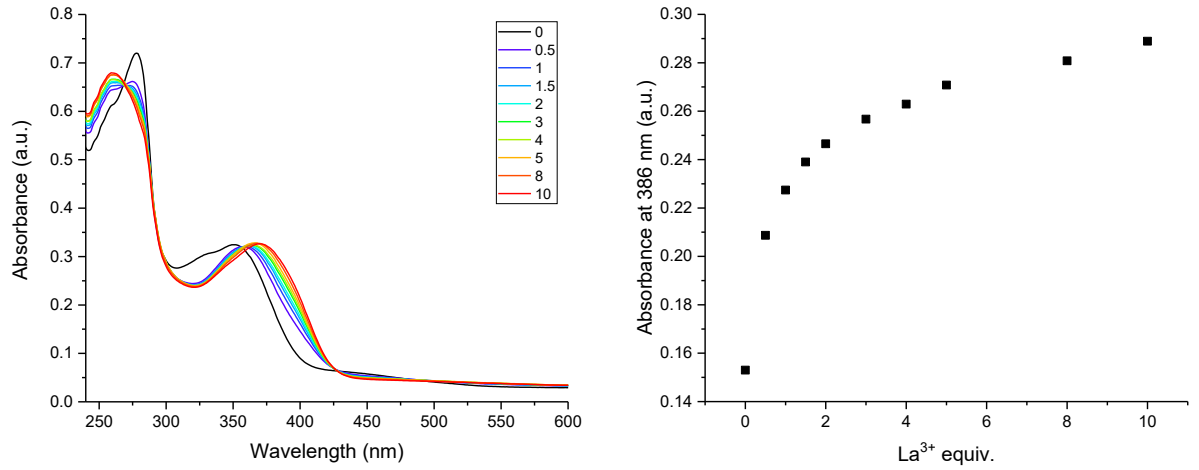

Figure VI.8: Spectrophotometric titration of ***PQQ***$_{18\text{-}6}$ *(0.05 mM) with increasing amounts of* $La(OTf)_3 \cdot 2H_2O$ *(0 to 0.5 mM) in acetonitrile and 19% THF (left) and plot of the absorption change at 386 nm vs. the* La^{3+} *equivalents added to the ligand (right). Each solution had a constant total volume of 200 µL. The measurements were conducted with an Epoch 2 Plate Reader from Biotek in a 96-well quartz microplate from Hellma.*

3.2. Preliminary UV-Vis Experiments

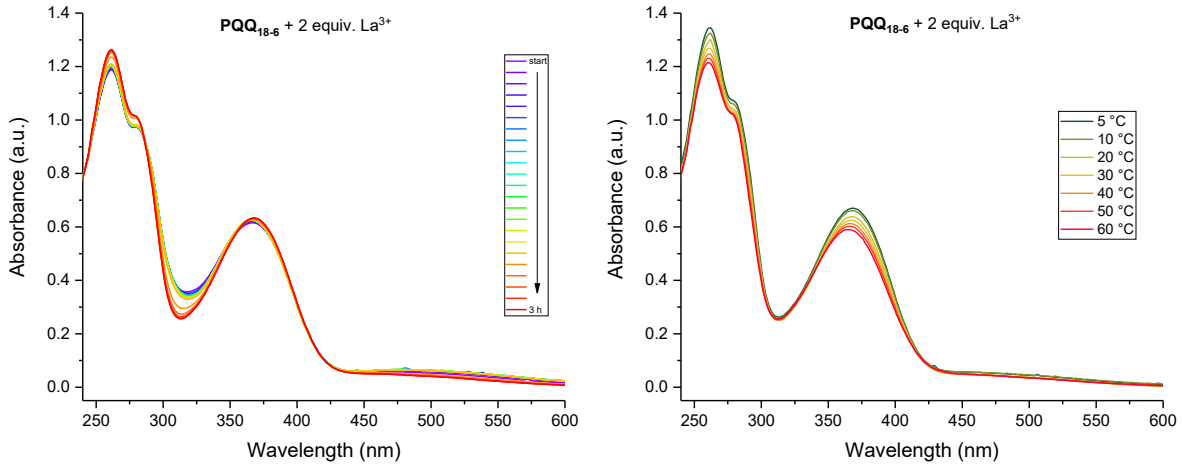

Figure VI.9: Spectrophotometric analysis of freshly prepared solution of ***PQQ***$_{18\text{-}6}$ *together with* $La(NO_3)_3{\cdot}6H_2O$ *(2.0 equiv.) in acetonitrile at 25 °C (left) and 1 day old solution of* ***PQQ***$_{18\text{-}6}$ *together with* $La(NO_3)_3{\cdot}6H_2O$ *(2.0 equiv.) in acetonitrile during temperature increase from 5 °C to 60 °C (right).*

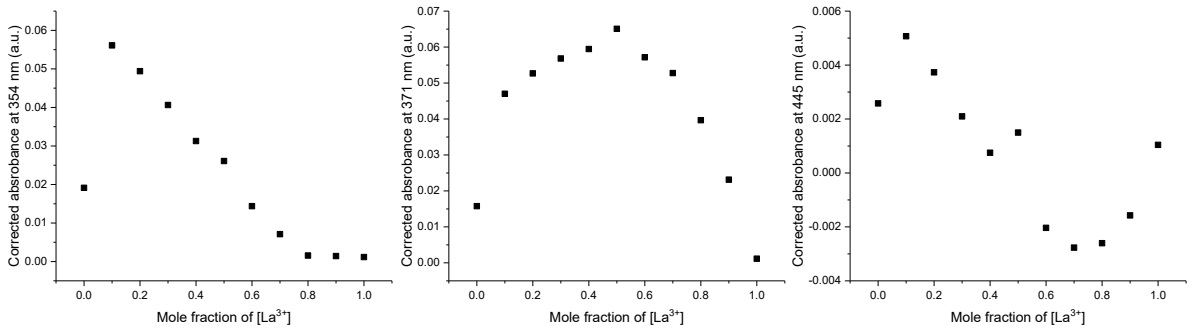

Figure VI.10: Job plot of the corrected absorbance at 354 nm (left), 371 nm (middle) and 445 nm (right) vs. the mole fraction of $[La^{3+}]$*. Data collected from the spectrophotometric analysis of the* ***PQQ***$_{18\text{-}6}$*-to-*La^{3+} *molar ratio by the method of continuous variation.*

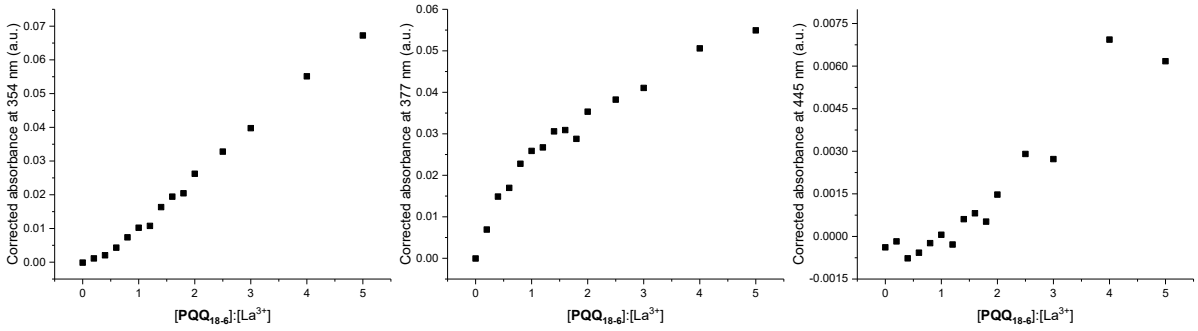

Figure VI.11: Plot of the corrected absorbance at 354 nm (left), 377 nm (middle) and 445 nm (right) vs. the $[$***PQQ***$_{18\text{-}6}]$*:*$[La^{3+}]$ *mole ratio. Data collected from the spectrophotometric analysis for determination of the PQQ18-6 -*La^{3+} *complex stoichiometry by the mole ratio method.*

3.3. UV-Vis Titrations and Evaluation of Binding Constants

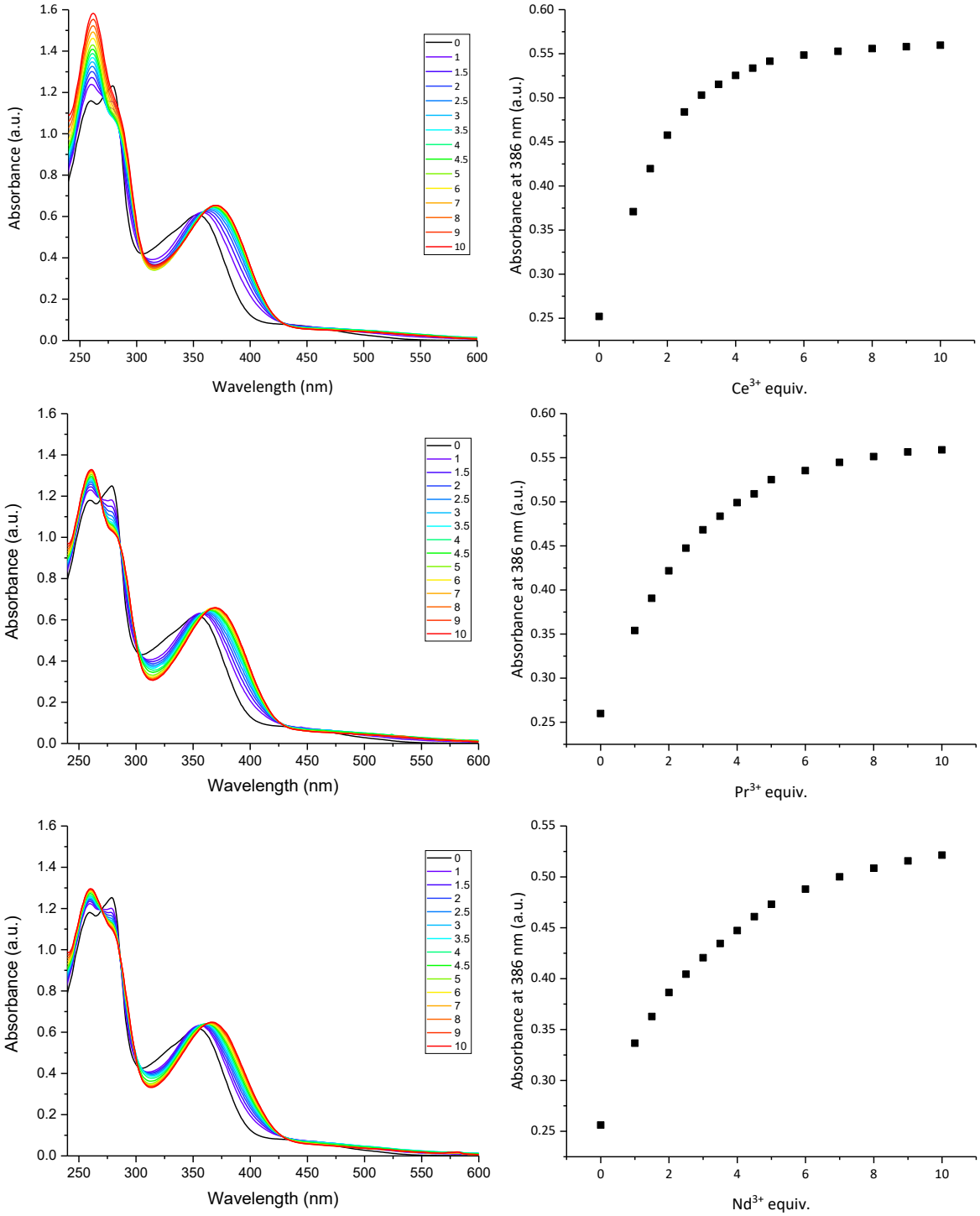

Figure VI.12: Titrations of ***PQQ***$_{18\text{-}6}$ *with increasing amounts of* $Ln(NO_3)_3 \cdot XH_2O$ *(Ln = Ce, Pr, Nd; X = 5 for Pr, 6 for Ce and Nd) in acetonitrile at 25 °C (left) and plot of the absorption change at 386 nm vs. the* Ln^{3+} *equivalents added to the ligand (right).*

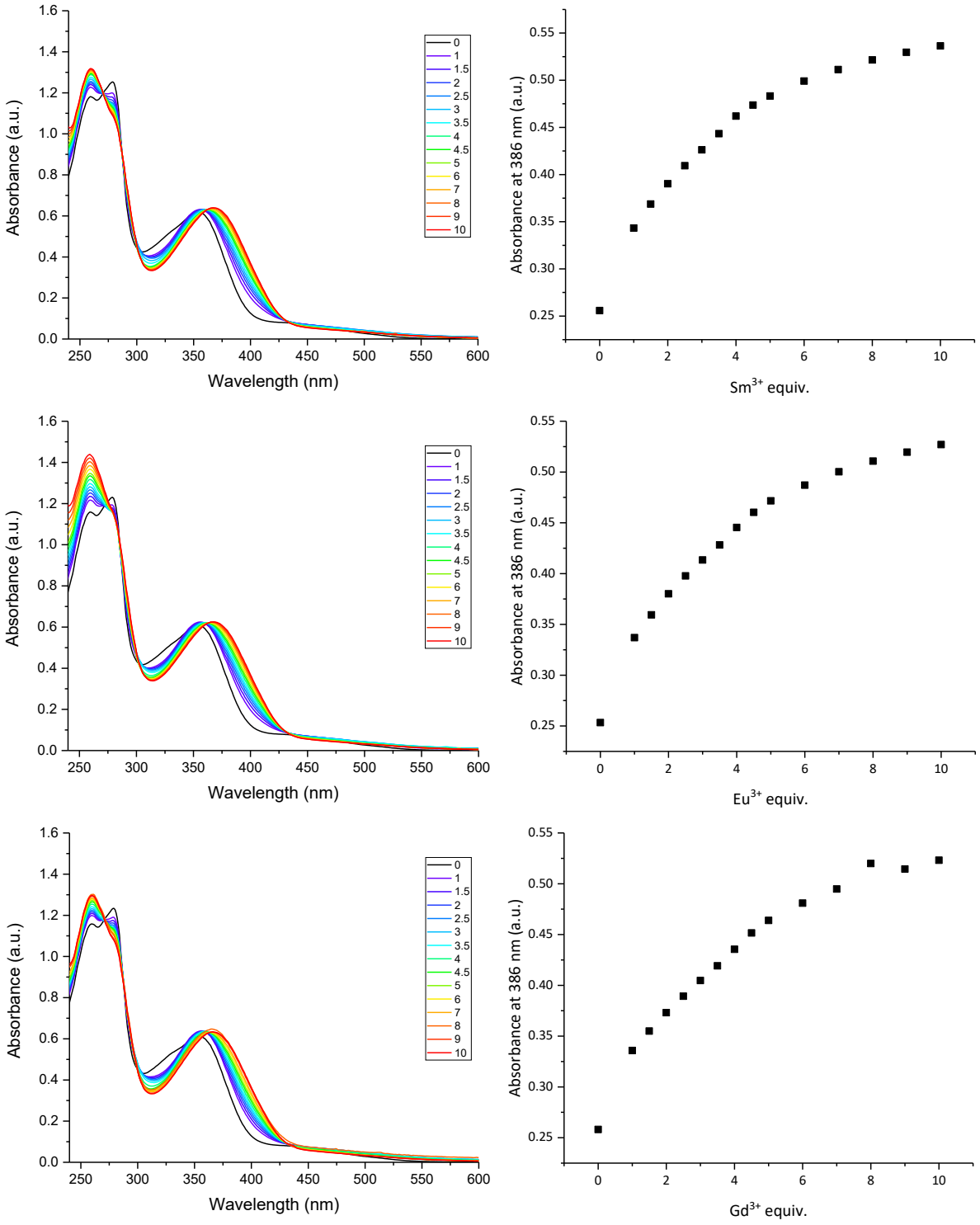

Figure VI.13: Titrations of ***PQQ***$_{18\text{-}6}$ *with increasing amounts of* $Ln(NO_3)_3{\cdot}6H_2O$ *(Ln = Sm, Eu, Gd) in acetonitrile at 25 °C (left) and plot of the absorption change at 386 nm vs. the* Ln^{3+} *equivalents added to the ligand (right).*

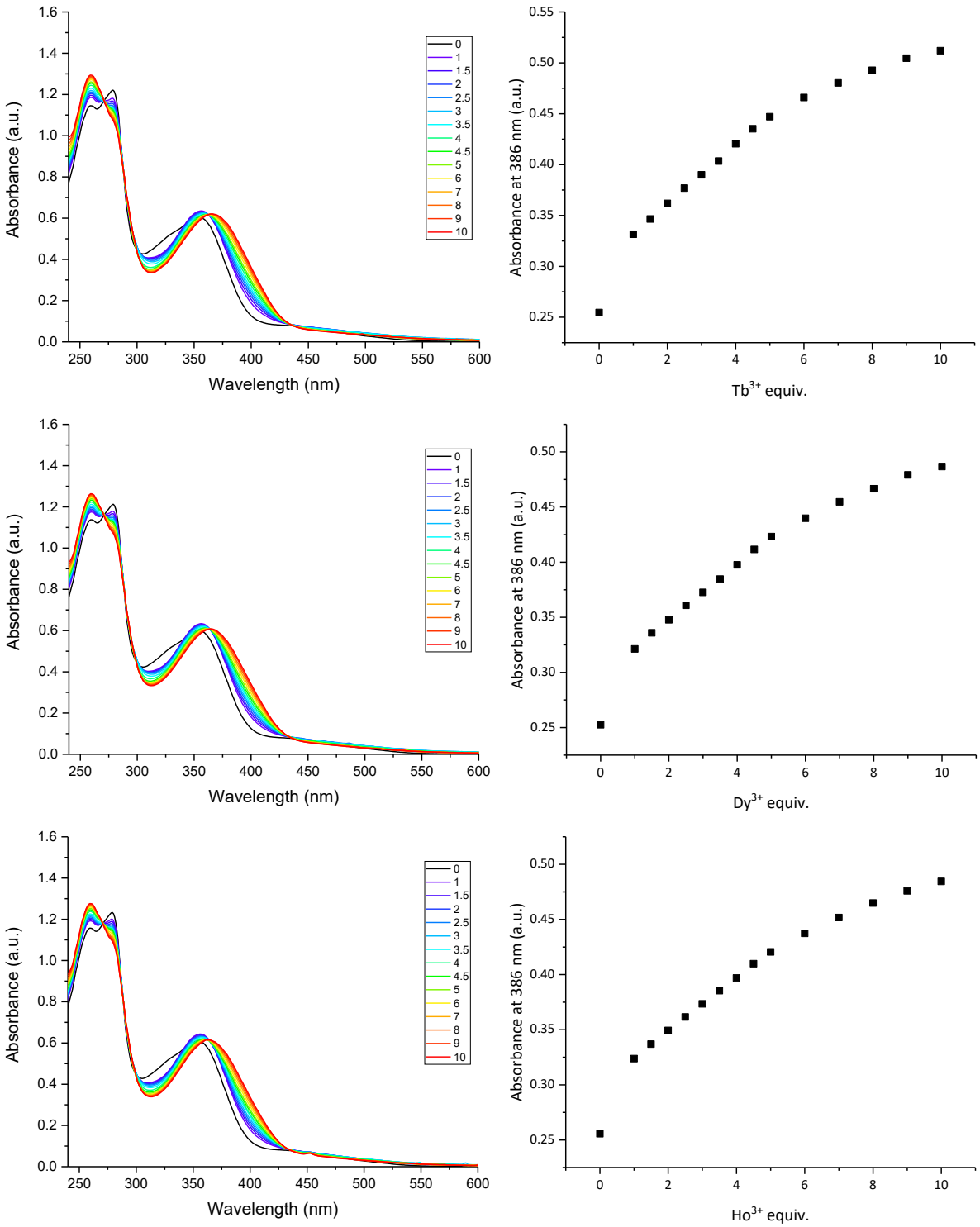

Figure VI.14: Titrations of ***PQQ***$_{18\text{-}6}$ *with increasing amounts of* $Ln(NO_3)_3 \cdot XH_2O$ *(Ln = Tb, Dy, Ho; X = 5 for Dy and Ho, 6 for Tb) in acetonitrile at 25 °C (left) and plot of the absorption change at 386 nm vs. the* Ln^{3+} *equivalents added to the ligand (right).*

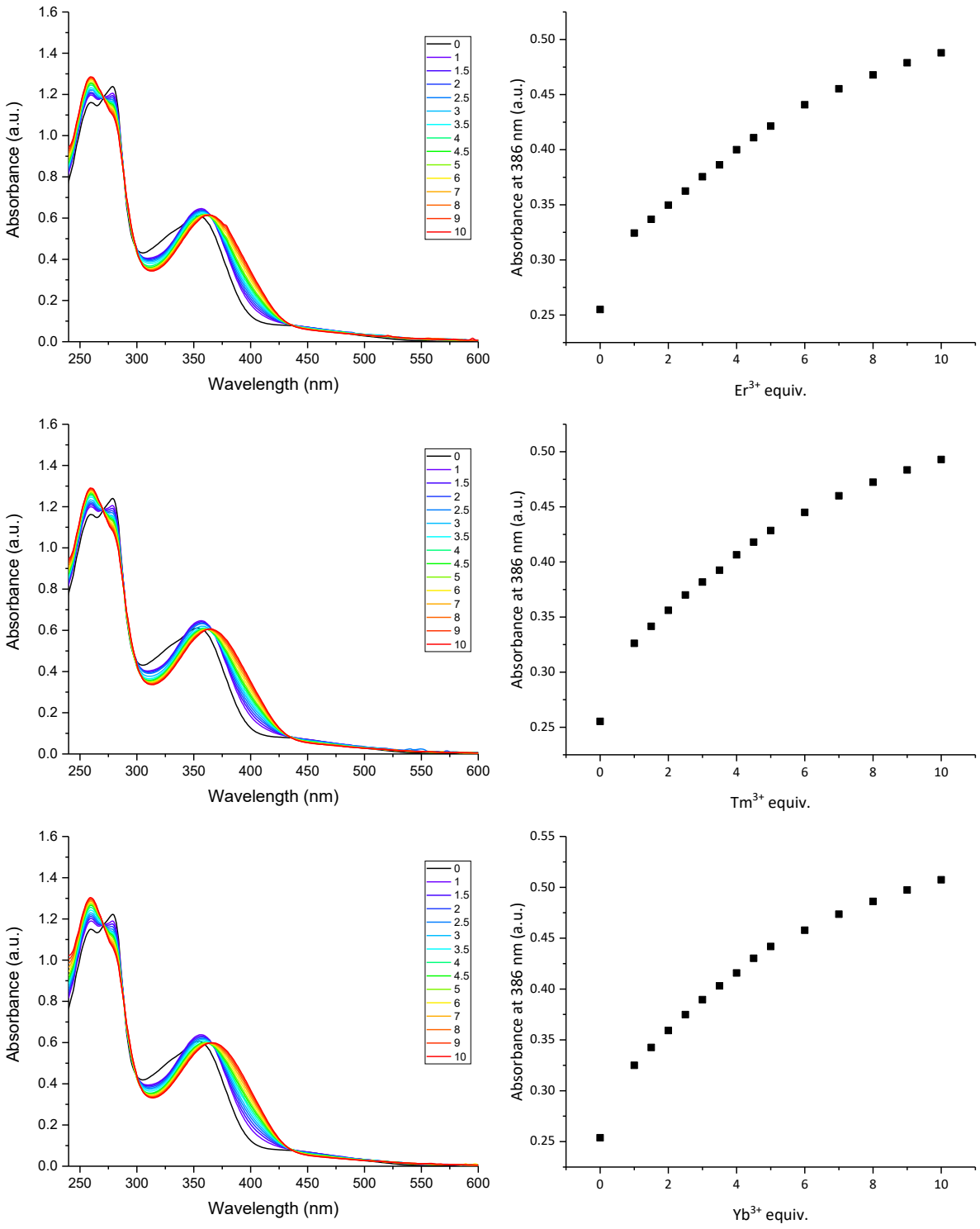

Figure VI.15: Titrations of ***PQQ****18-6 with increasing amounts of* $Ln(NO_3)_3 \cdot 5H_2O$ *(Ln = Er, Tm, Yb) in acetonitrile at 25 °C (left) and plot of the absorption change at 386 nm vs. the* Ln^{3+} *equivalents added to the ligand (right).*

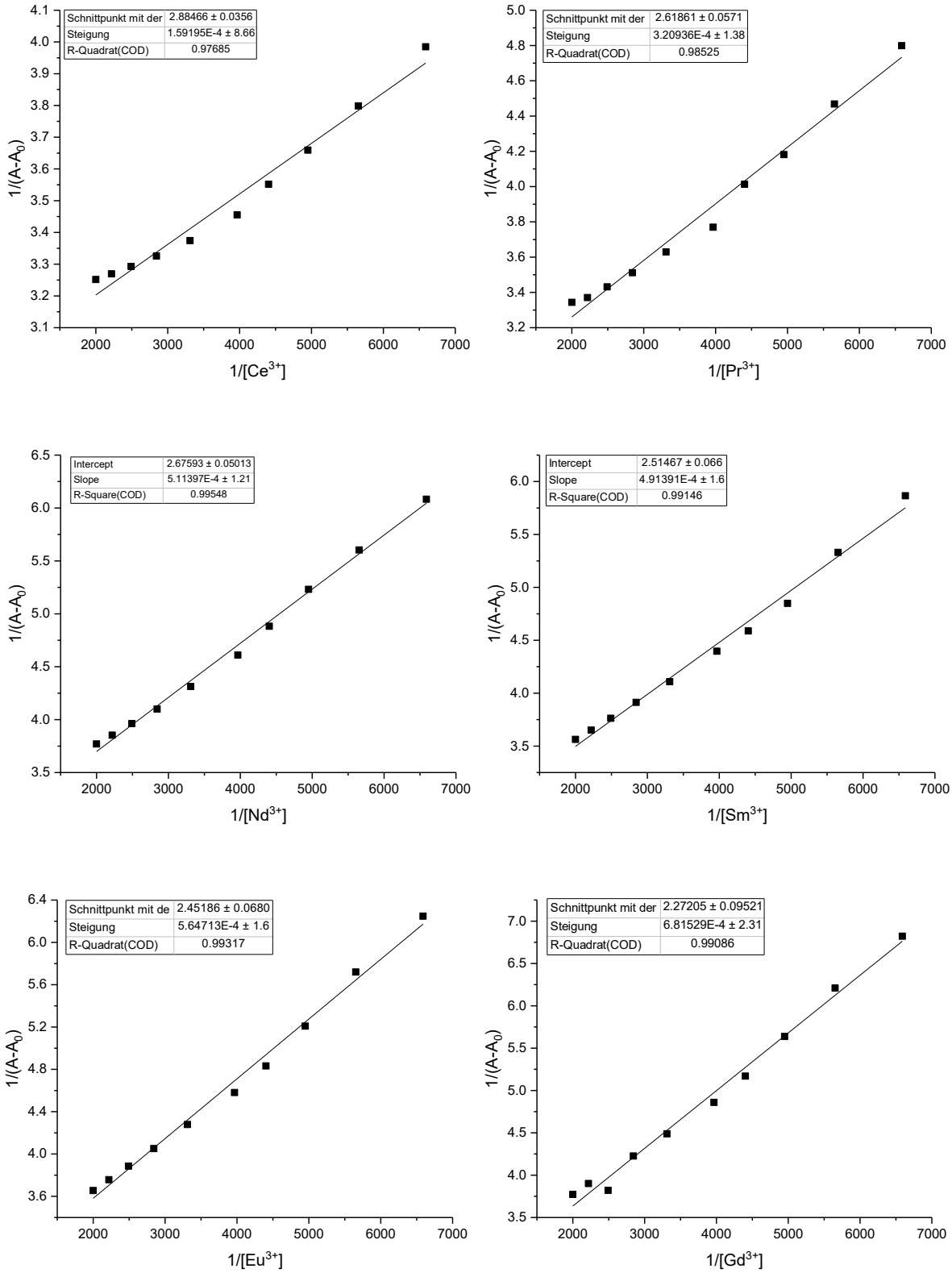

Figure VI.16: Benesi-Hildebrand plots of $1/(A-A_0)$ versus $1/[Ln^{3+}]$ for determination of binding constants K for ***PQQ*****$_{18\text{-}6}$** *complexes (Ln: Ce, Pr, Nd, Sm, Eu, Gd). The Ln^{3+} concentrations used for the plot were from 0.00015 to 0.0005 M (3.0 to 10 equiv.).*

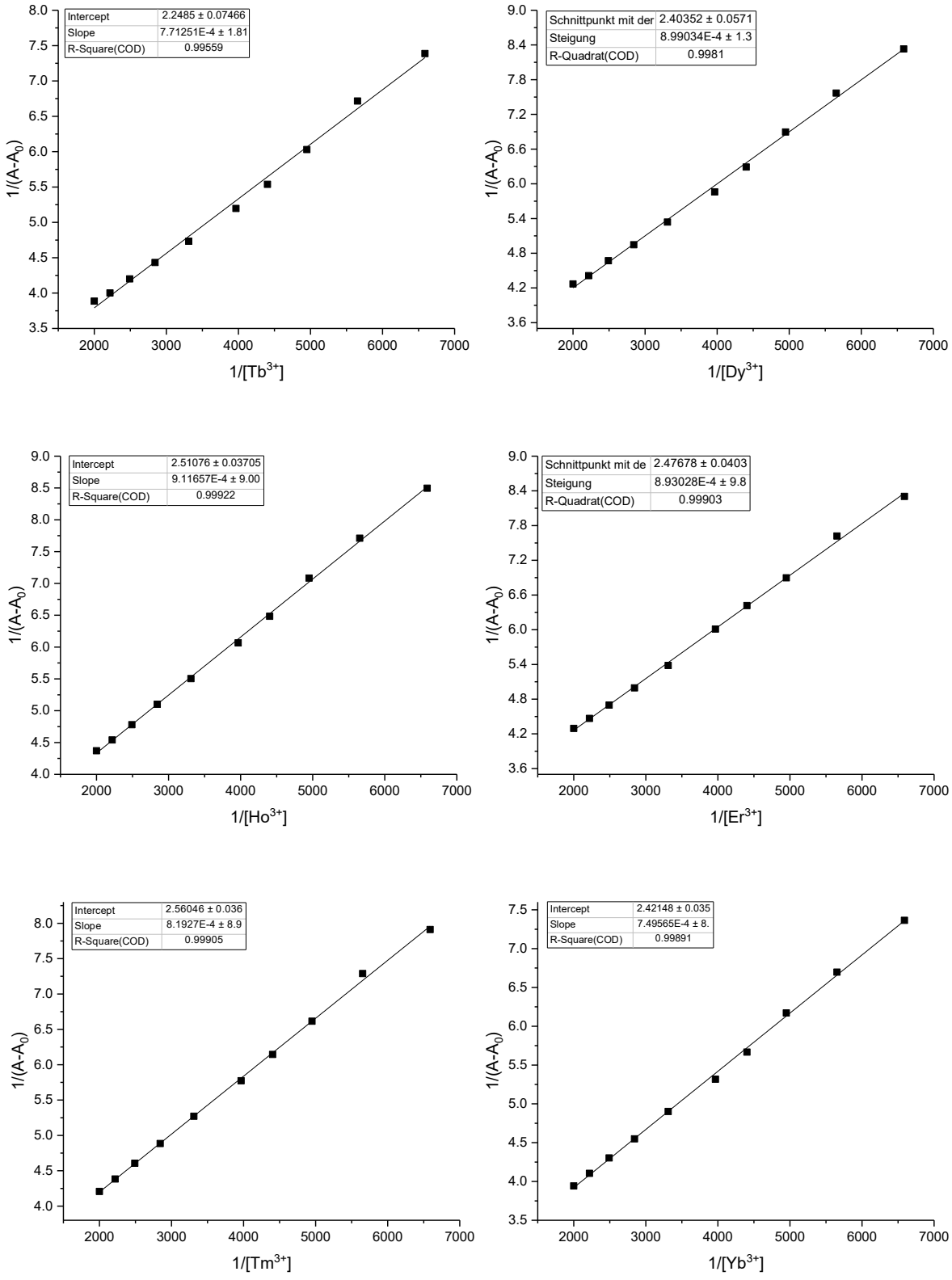

Figure VI.17: Benesi-Hildebrand plots of $1/(A-A_0)$ versus $1/[Ln^{3+}]$ for determination of binding constants K for ***PQQ*****$_{18\text{-}6}$** *complexes (Ln: Tb, Dy, Ho, Er, Tm, Yb). The Ln^{3+} concentrations used for the plot were from 0.00015 to 0.0005 M (3.0 to 10 equiv.).*

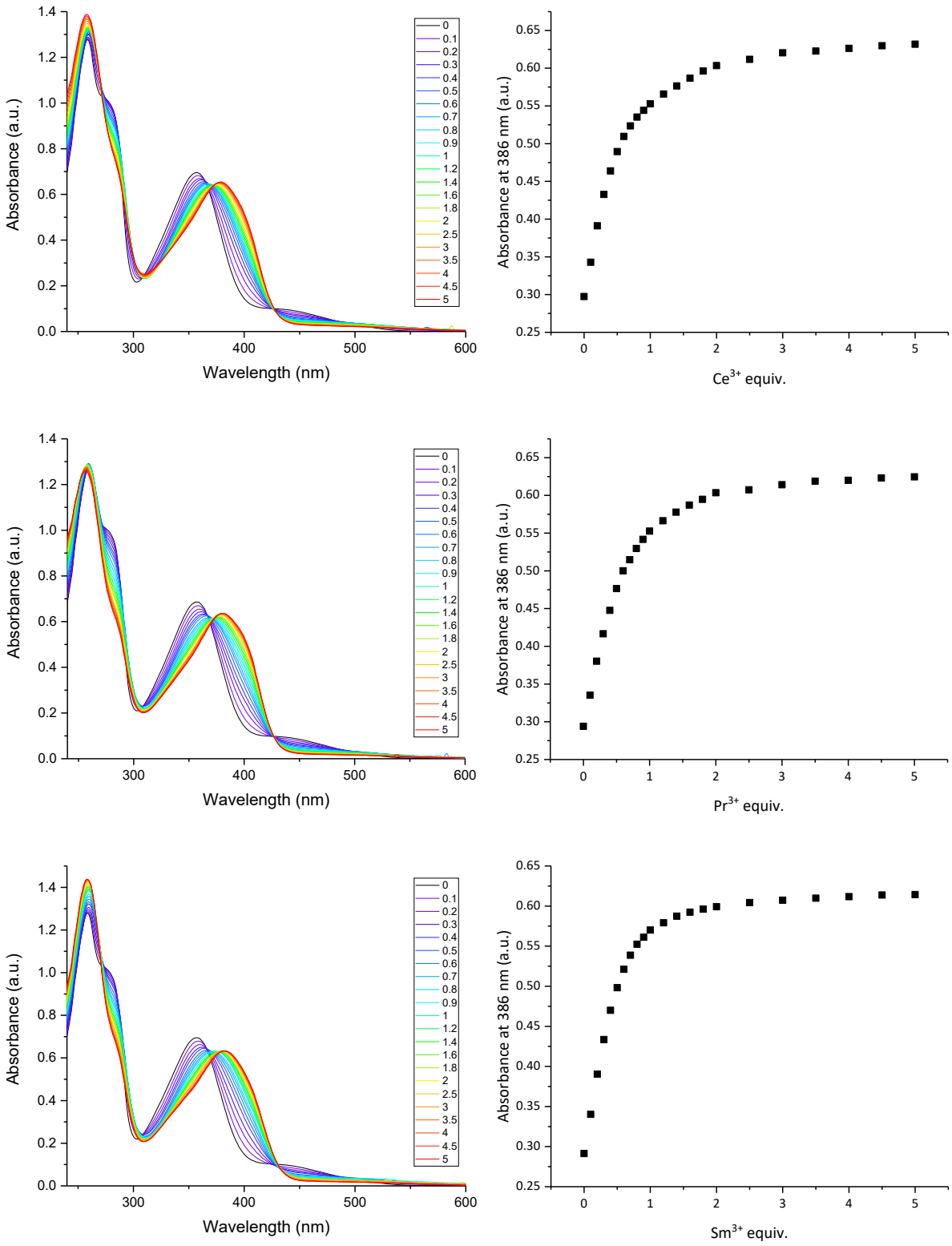

*Figure VI.18: Titrations of **PQQMe**$_2$ with increasing amounts of $Ln(NO_3)_3 \cdot XH_2O$ (Ln = Ce, Pr, Sm; X = 5 for Pr, 6 for Ce and Sm) in acetonitrile at 25 °C (left) and plot of the absorption change at 386 nm vs. the Ln^{3+} equivalents added to the ligand (right).*

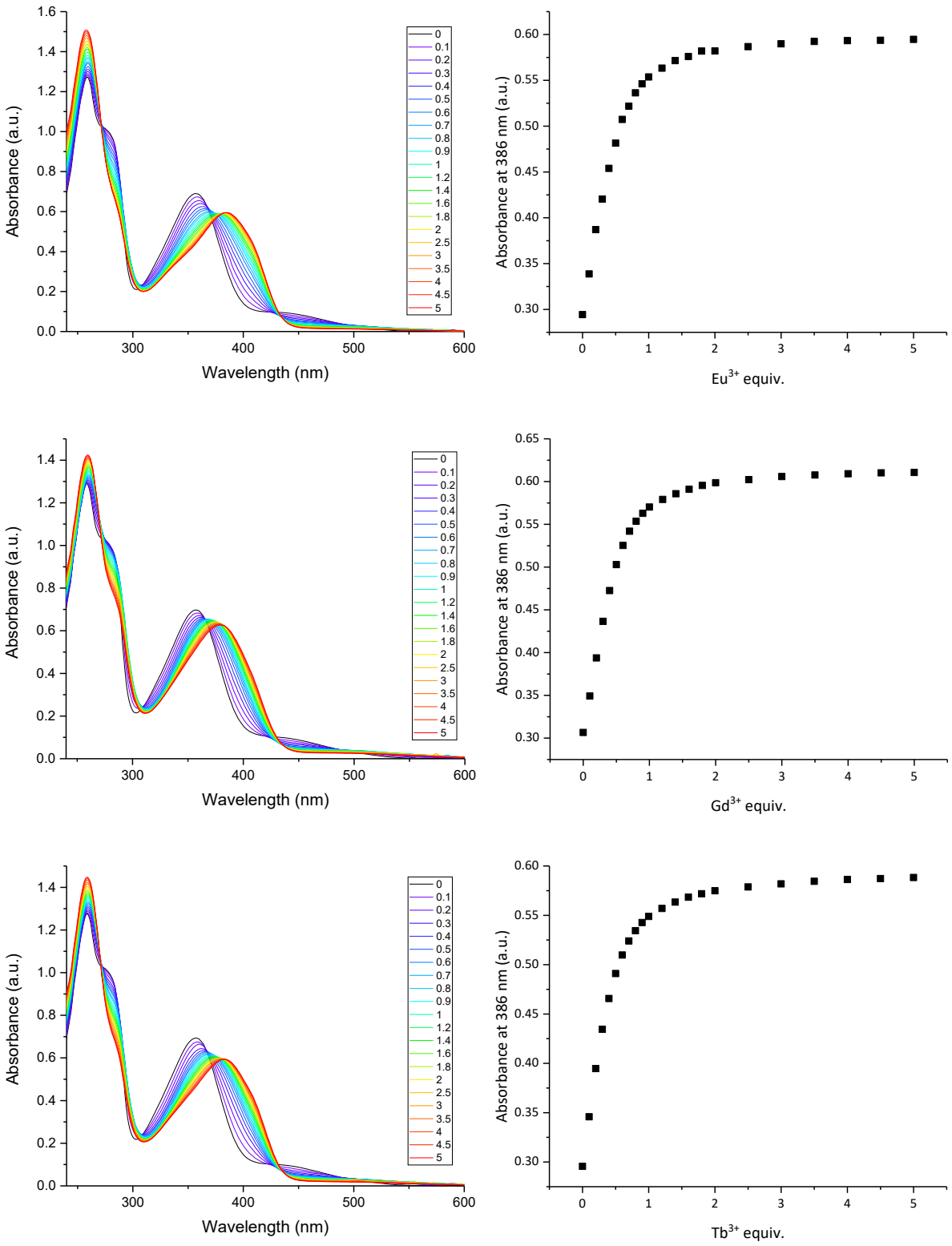

*Figure VI.19: Titrations of **PQQMe**$_2$ with increasing amounts of $Ln(NO_3)_3 \cdot 6H_2O$ (Ln = Eu, Gd, Tb) in acetonitrile at 25 °C (left) and plot of the absorption change at 386 nm vs. the Ln^{3+} equivalents added to the ligand (right).*

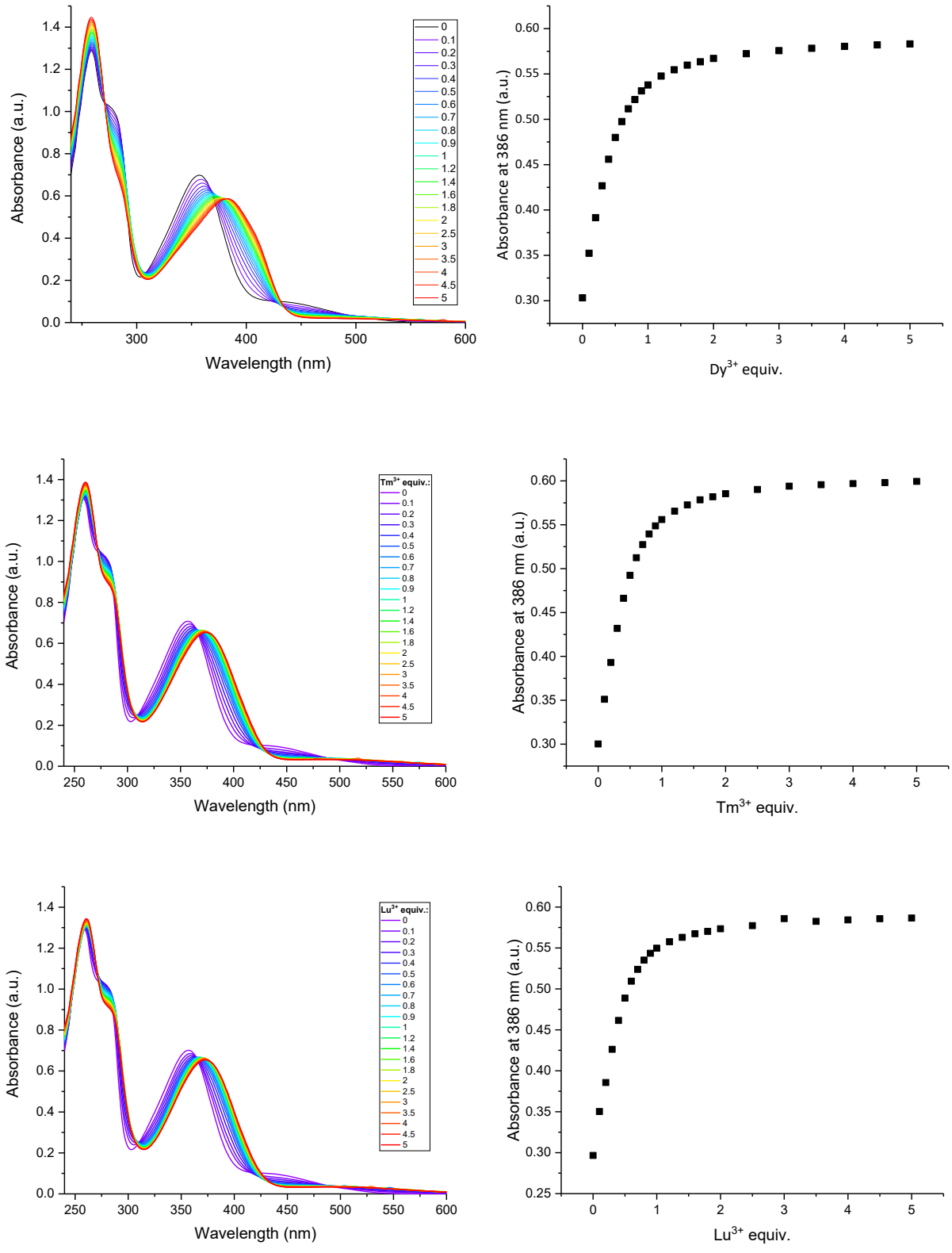

Figure VI.20: Titrations of ***PQQMe2*** *with increasing amounts of $Ln(NO_3)_3 \cdot XH_2O$ (Ln = Dy, Tm, Lu; X = 5 for Dy and Tm, 6 for Lu) in acetonitrile at 25 °C (left) and plot of the absorption change at 386 nm vs. the Ln^{3+} equivalents added to the ligand (right).*

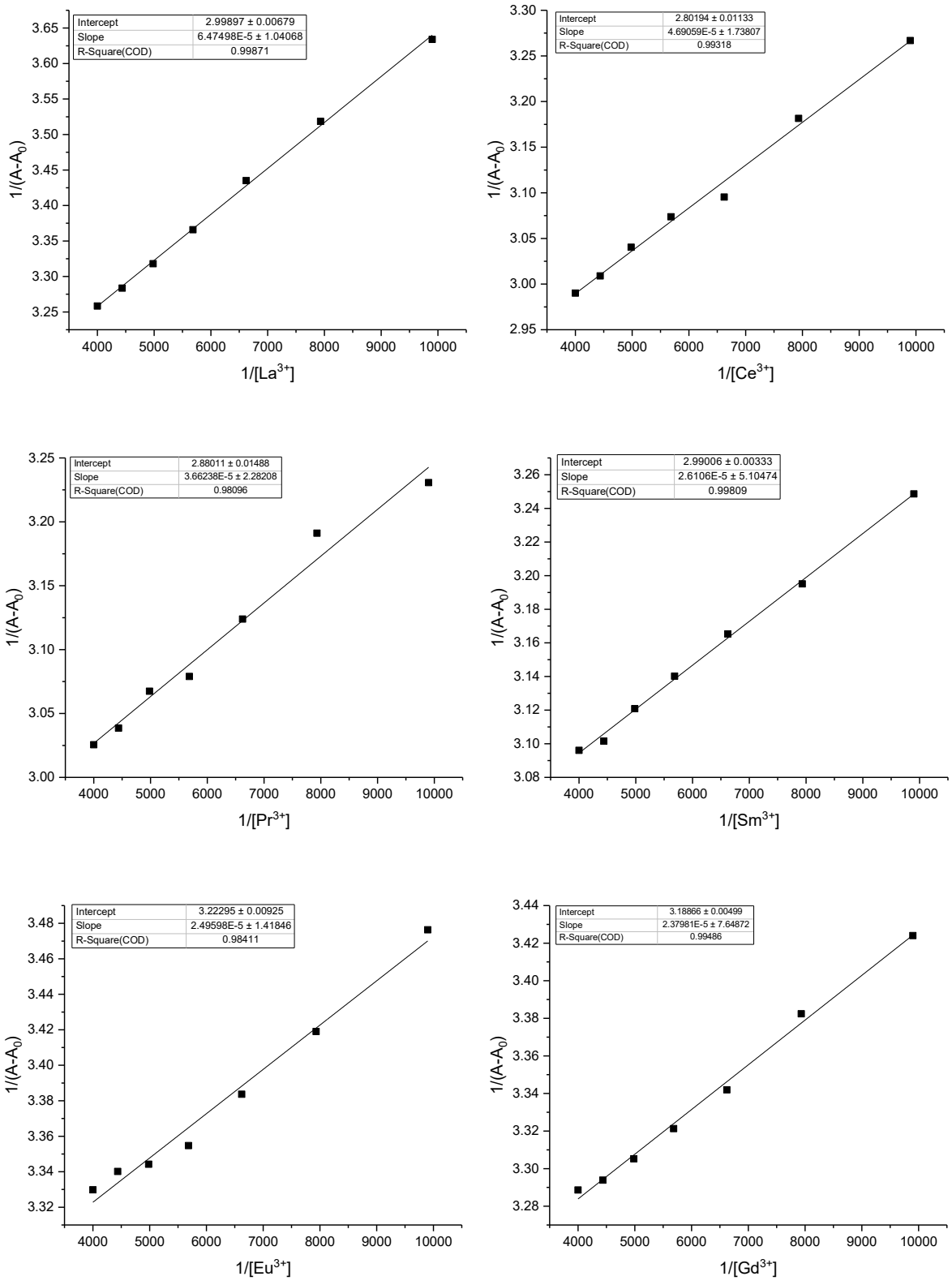

*Figure VI.21: Benesi-Hildebrand plots of $1/(A-A_0)$ versus $1/[Ln^{3+}]$ for determination of binding constants K for **PQQMe**$_2$ complexes (Ln: La, Ce, Pr, Sm, Eu, Gd). The Ln^{3+} concentrations used for the plot were from 0.0001 to 0.00025 M (2.0 to 5.0 equiv.).*

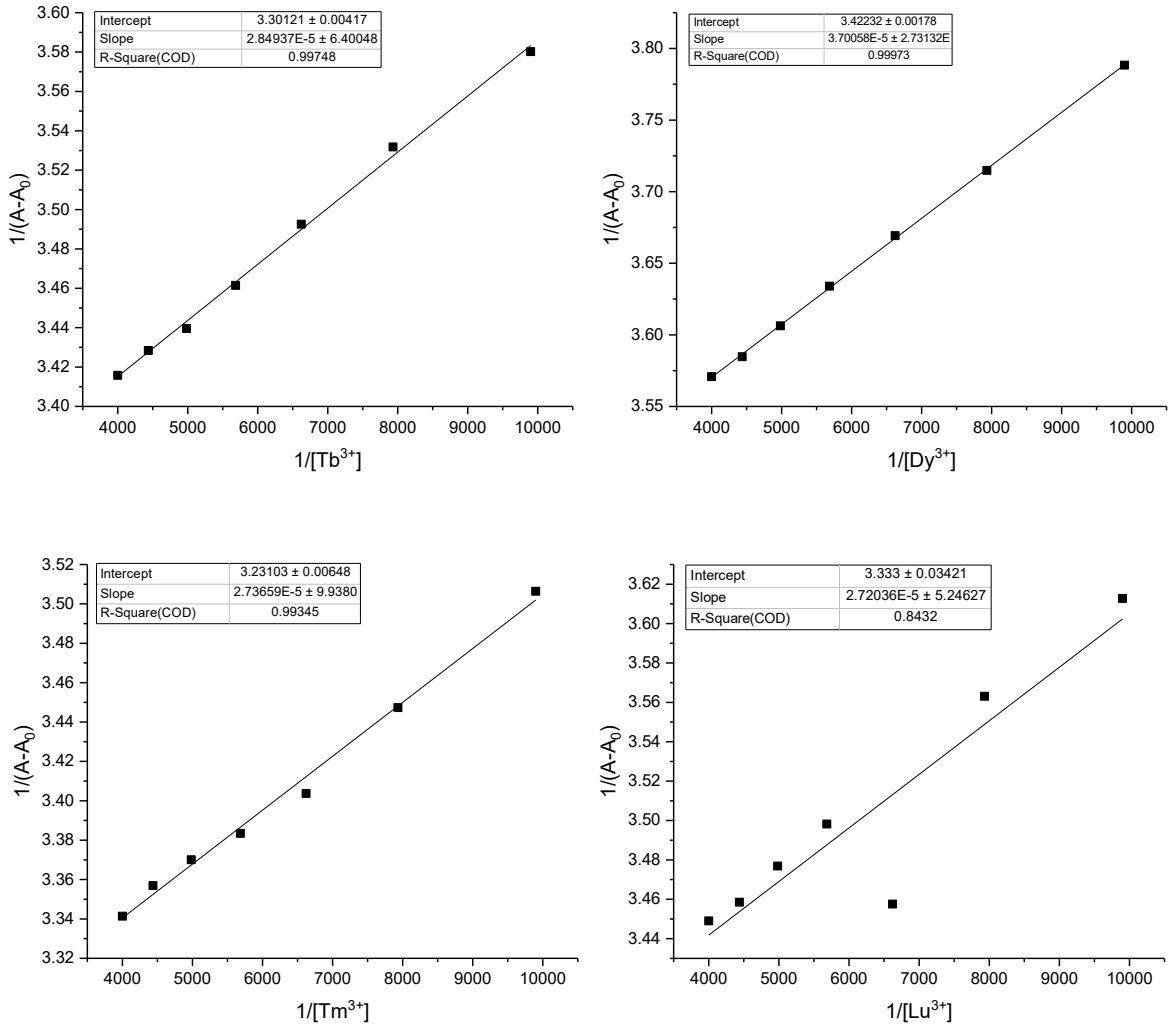

*Figure VI.22: Benesi-Hildebrand plots of $1/(A-A_0)$ versus $1/[Ln^{3+}]$ for determination of binding constants K for **PQQMe**$_2$ complexes (Ln: Tb, Dy, Tm, Lu). The Ln^{3+} concentrations used for the plot were from 0.0001 to 0.00025 M (2.0 to 5.0 equiv.).*

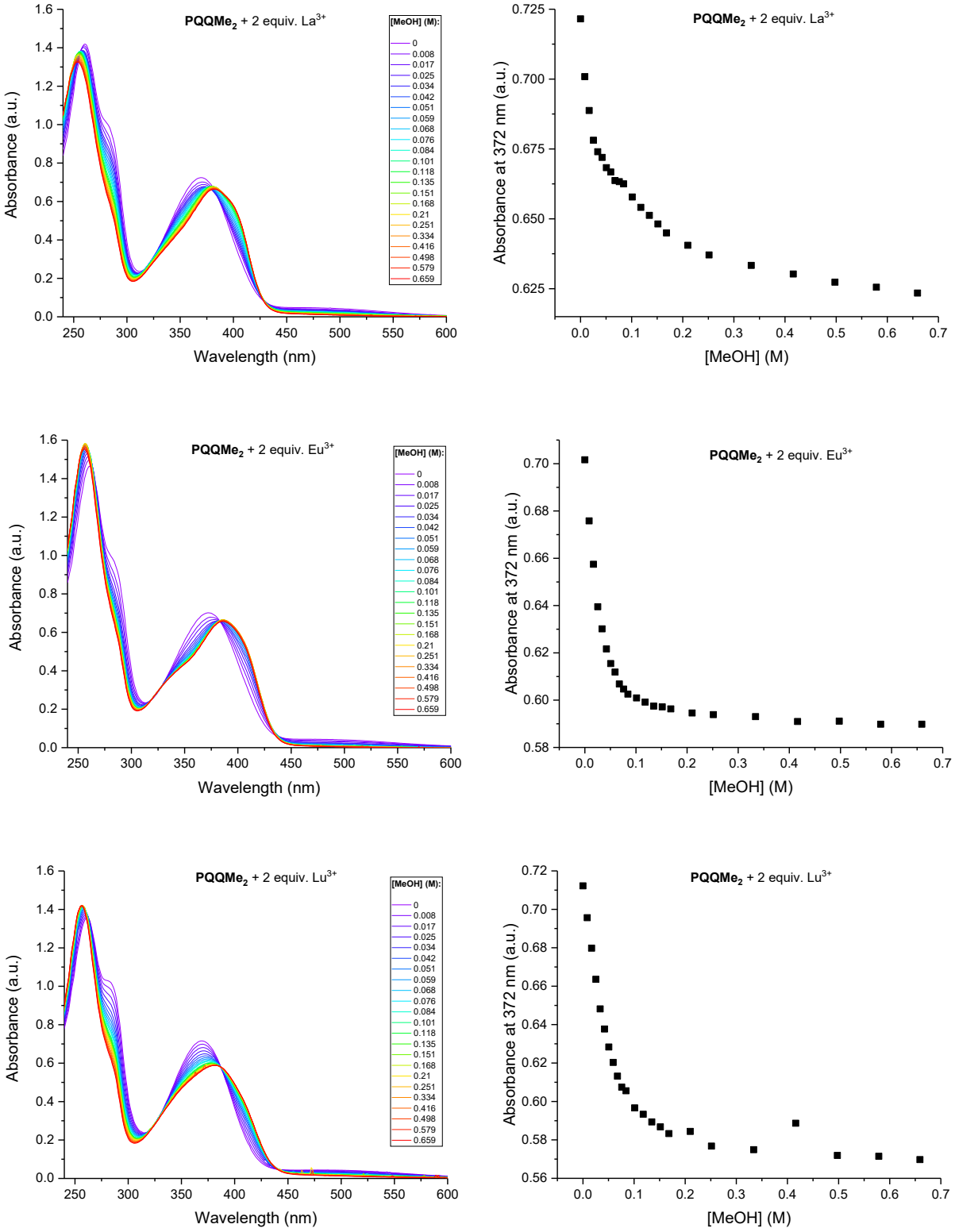

*Figure VI.23: Titrations of **PQQMe**$_2$ (0.00005 M) with increasing amounts of methanol (0.00846 to 0.65918 M) in the presence of 2.0 equiv. $Ln(NO_3)_3 \cdot 6H_2O$ (0.0001 M; Ln = La, Eu, Lu) in acetonitrile at 25 °C (left) and plot of the absorption change at 372 nm vs. the methanol concentration added to the complex solution (right).*

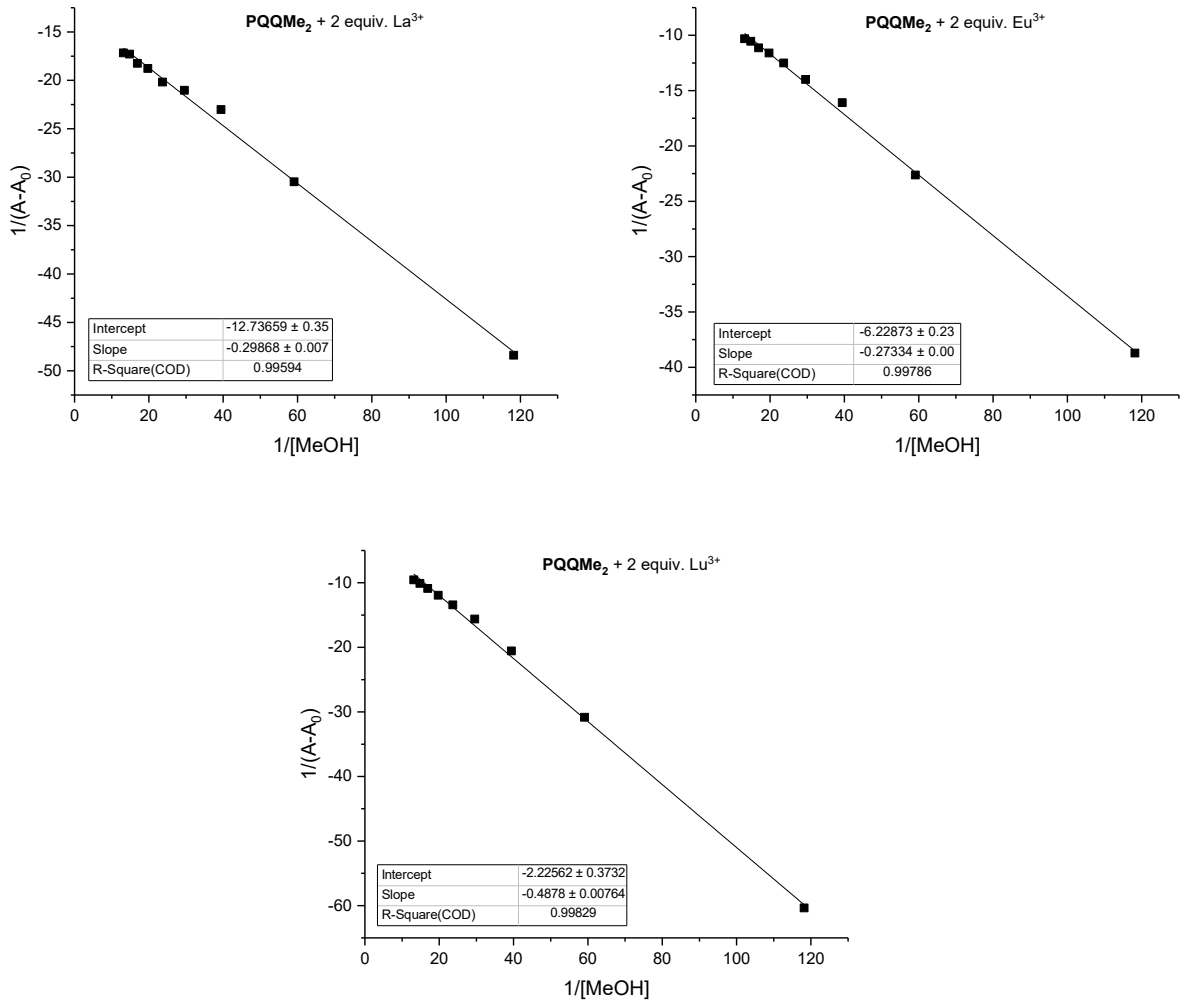

Figure VI.24: Benesi-Hildebrand plots of 1/(A-A₀) versus 1/[MeOH] for the titration of ***PQQMe₂*** *in the presence of* $Ln(NO_3)_3 \cdot 6H_2O$ *(Ln = La, Eu, Lu) with methanol in acetonitrile at 25 °C. The methanol concentrations used for the plot were from 0.008 to 0.076 M.*

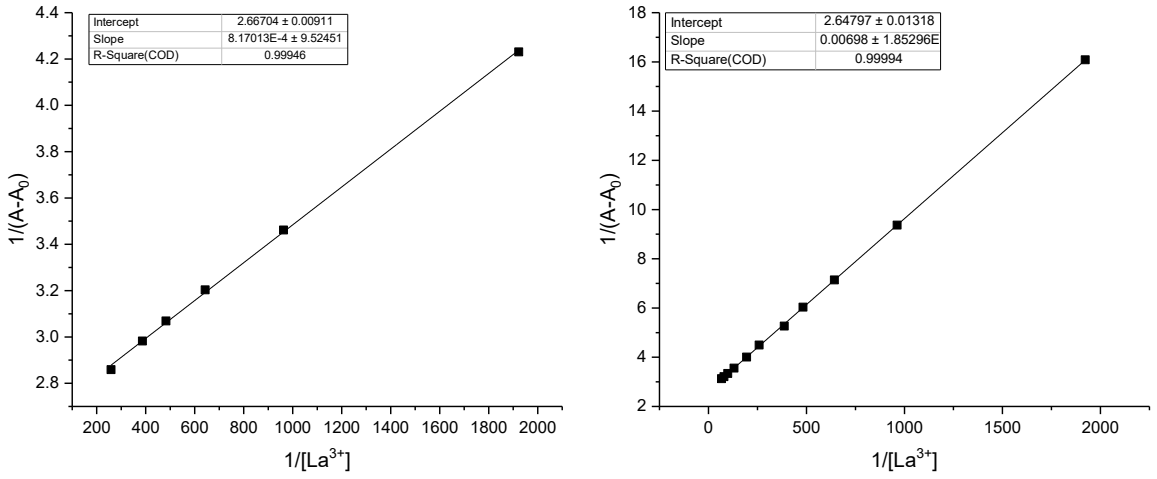

Figure VI.25: **:** *Benesi-Hildebrand plots of 1/(A-A₀) versus 1/[La³⁺] for determination of binding constants K for* ***PQQ*****₁₅₋₅** *(left) and* ***PQQMe*****₃** *(right). The La³⁺ concentrations used for the plots were from 0.0005 to 0.0039 M (10 to 75 equiv.) for* ***PQQ*****₁₅₋₅** *and 0.0005 to 0.015 M (10 to 300 equiv.) for* ***PQQMe*****₃**.

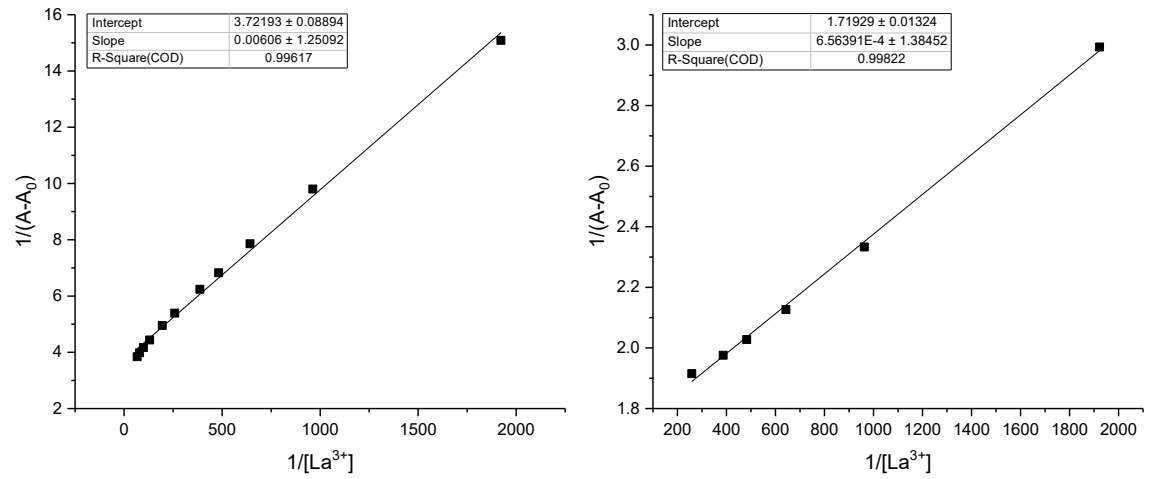

Figure VI.26: Benesi-Hildebrand plots of 1/(A-A₀) versus 1/[La³⁺] for determination of binding constants K for ***PQQ*****DEDP** *(left) and* ***PMEQQ*****MEM** *(right). The La³⁺ concentrations used for the plots were from 0.0005 to 0.015 M (10 to 300 equiv.) for* ***PQQ*****DEDP** *and 0.0005 to 0.0039 M (10 to 75 equiv.) for* ***PMEQQ*****MEM**.

4. Anhydrous Metal Salts

4.1. Tetrahydrofuran Complexes of Lanthanide Nitrates

Given PQQ's propensity for formation of water adducts,[180] Almuth Schmid undertook an endeavor to synthesize anhydrous lanthanide salts as part of her bachelor thesis, conducted under my supervision. In 2006 Niemeyer reported a procedure for the preparation of $Ln(NO_3)_3(THF)_x$ complexes.[312] Multiple efforts were made to replicate the synthesis of the corresponding lanthanum(III) complex by following the exact experimental steps outlined in the original publication (Scheme VI.1). Thereby, lanthanum(III) nitrate hexahydrate was stirred in the presence of trimethyl orthoformate to replace the coordinated water molecules by methanol. Following this, the solvent was removed *in vacuo* and THF was introduced under ice-cooling conditions. The reaction mixture was stirred for 3 h at room temperature and the solvent was subsequently evaporated. The last two steps were repeated twice. Unfortunately, the elemental microanalysis of the resulting crude products from all attempts (Table VI.4) revealed a significant deviation between the calculated values for the desired complex and the actual results. The presence of carbon in the crude products suggested that a water exchange has occurred. Nevertheless, the minimal carbon content suggested either a partial exchange or the presence of a mixture of the desired product and a partially THF-substituted salt.

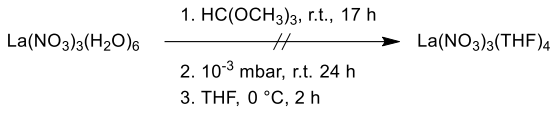

Scheme VI.1: Attempted conversion of lanthanum(III) nitrate hexahydrate to the respective tetrahydrofuran solvate.

Table VI.4: Results from the elemental analysis of the crude products, obtained after the attempted synthesis of $La(NO_3)_3(THF)_4$.

	N	C	H
$La(NO_3)_3(H_2O)_6$	9.70	-	2.79
$La(NO_3)_3(THF)_4$	**6.85**	**31.33**	**5.26**
crude product 1	10.33	10.60	1.83
crude product 2	10.19	10.25	2.01
crude product 3	10.04	10.99	2.04
crude product 4	9.81	10.79	2.57
crude product 5	8.17	17.34	3.59

4.2. $LnCl_3 \cdot 2LiCl$

The experimental studies on PQQ derived compounds often require the use of anhydrous conditions, since the PQQ moiety can form additional products with water. However, often the commercially available lanthanide perchlorates, nitrates, triflates and halides contain water, which could possibly interfere the measurements. An alternative was found in the easy-to-prepare solutions of $LnCl_3 \cdot 2LiCl$ (Ln = La, Ce, Nd) in THF reported by Knochel and coworkers.[313] The Ln^{3+} concentration given by the authors, however, refers to the assumption that the starting reagents undergo a full conversion to the respective $LnCl_3 \cdot 2LiCl$ species. Yet the spectroscopic studies on lanthanide complexes require the knowledge of the exact metal ion content. Hence, a complexometric titration assay with Eriochrome Black T (EBT) as indicator was developed in order to determine the lanthanide concentration of anhydrous $LnCl_3 \cdot 2LiCl$ THF solutions.

EBT is a commercially available azo dye and well-known metal complexing agent that is used in complexometric titrations of alkaline earth and lanthanide elements (Scheme VI.2).[314,315] UV-Vis titration experiments suggested that EBT forms 1:1 binary complexes with lanthanide ions.[315,316]

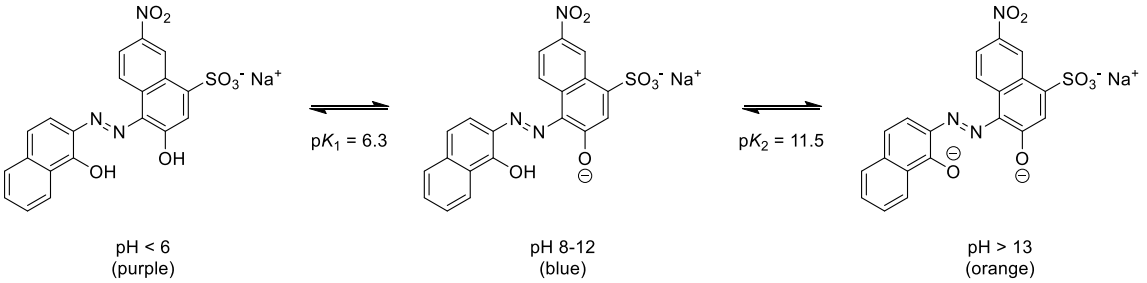

Scheme VI.2: Molecular structure of Eriochrome Black T. Depending on the pH of the solution, it exists as three different colored species.[315]

A stock solution of EBT (0.4 mM) was prepared in CAPS buffer (38 mM, pH 10.45). An important note is that the EBT solution cannot be stored overnight and should be freshly prepared prior to use. $LaCl_3 \cdot 7H_2O$ and LiCl were dissolved in water to obtain a stock solution with a known La^{3+} concentration of 0.4 mM. An Epoch 2 Plate Reader from Biotek was used with a 96 well quartz microplate from Hellma. The titrations were performed under maintaining a constant volume of 200 μL in a well and a constant water to THF ratio (Table VI.5, Figure VI.27).

Table VI.5: Titration of Eriochrome Black T (0.4 mM stock solution in aqueous 38 mM CAPS buffer with pH 10.45) with increasing amount of $LaCl_3 \cdot 7H_2O$ and LiCl (0.4 mM stock solution in water).

V (EBT) (µL)	V (THF) (µL)	V ($LaCl_3 \cdot 7H_2O$, LiCl) (µL)	V (H_2O) (µL)
100	50	0	50
100	50	5	45
100	50	10	40
100	50	15	35
100	50	20	30
100	50	25	25
100	50	30	20
100	50	35	15
100	50	40	10
100	50	45	5
100	50	50	0

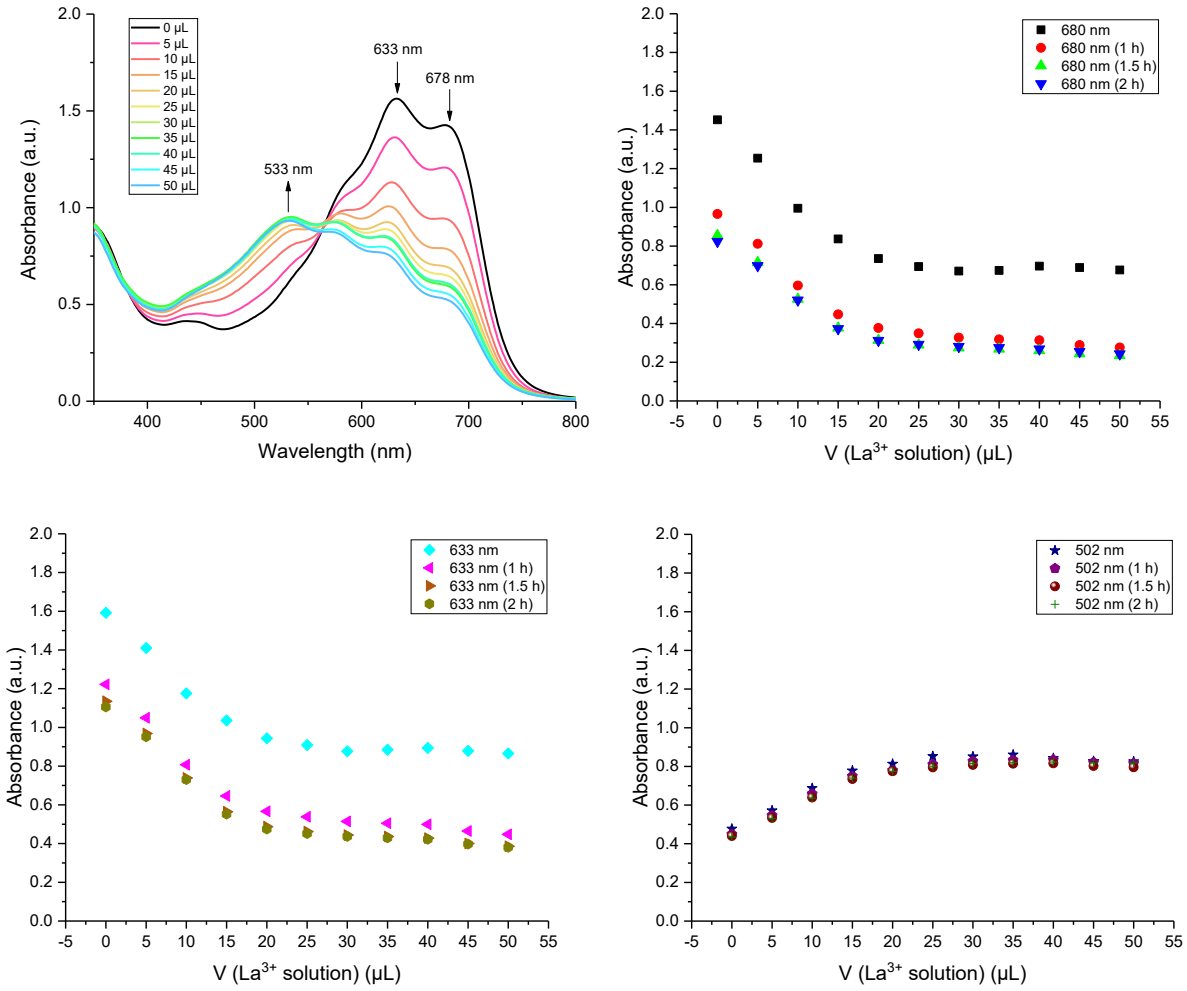

Figure VI.27: UV-Vis spectra of Eriochrome Black T (0.2 mM solution in aqueous CAPS buffer) with consecutive addition of $LaCl_3 \cdot 7H_2O$/LiCl solution (0.01 mM to 0.1 mM) in water and THF. Plots of the absorption change at three different wavelengths against the added volume of metal salt solution.

The UV-Vis spectrum of EBT is shown in Figure VI.27 with absorbance maxima at 633 and 678 nm. After consecutive addition of the $LaCl_3 \cdot 7H_2O$/LiCl solution, an absorption decrease of the two maxima was observed and an absorption increase at 533 nm. The plots of the absorption change at 680, 633 and 502 nm show a complex saturation after the addition of 15 µL (30 µM) La^{3+}. Furthermore, it was shown that the obtained spectra, measured right after the preparation of the samples, differ in comparison to the spectra measured after 2 h. As shown in Figure VI.27, only the absorption at 502 nm does not change drastically over the time. In order to avoid large standard deviations, the absorbance values at 502 nm were thus used for the fit of a calibration line for determination of the lanthanum(III) content of a solution of unknown concentration (Figure VI.28).

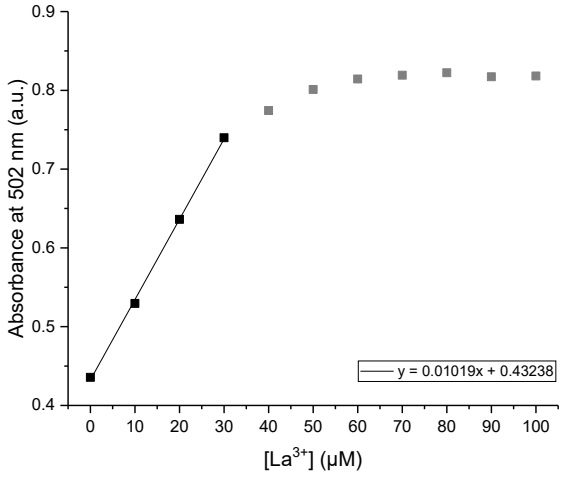

Figure VI.28: Calibration line for the relation between La^{3+} concentration and the absorption change of EBT at 502 nm. Saturation occurred after a La^{3+} concentration of 30 µM. Values above that concentration were not considered for the calibration line.

In order to test the accuracy of the concentration determination method, a $LaCl_3 \cdot 2LiCl$ solution (supplier concentration specification 0.6 M) purchased by Sigma Aldrich was examined as a "sample of unknown concentration". A stock solution was prepared by a 1000-fold dilution of the purchased solution with THF. The UV-Vis titration was performed similar to the procedure described above (Figure VI.29, Table VI.6).

Table VI.6: Titration of Eriochrome Black T (0.4 mM stock solution in aqueous 38 mM CAPS buffer with pH 10.45) with THF solution of $LaCl_3 \cdot 2LiCl$.

V (EBT) (µL)	V (H_2O) (µL)	V ($LaCl_3 \cdot 2LiCl$) (µL)	V (THF) (µL)
100	50	0	50
100	50	5	45
100	50	10	40
100	50	15	35
100	50	20	30
100	50	25	25
100	50	30	20
100	50	35	15
100	50	40	10
100	50	45	5
100	50	50	0

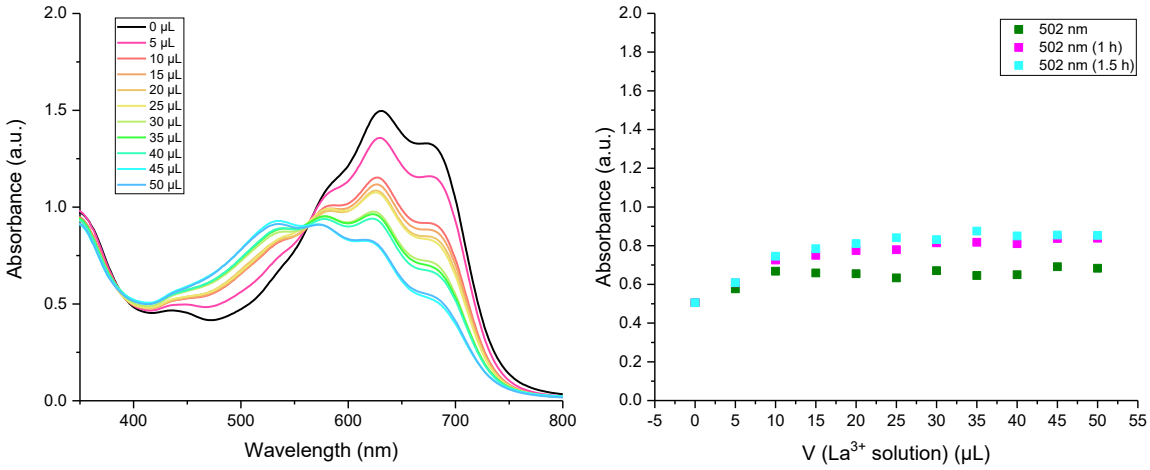

Figure VI.29: UV-Vis spectra of Eriochrome Black T (0.2 mM solution in aqueous CAPS buffer) with consecutive addition of $LaCl_3 \cdot 2LiCl$ solution of unknown concentration in water and THF (left). Plot of the absorption change at 502 nm against the added volume of metal salt solution (right).

On the basis of the obtained UV-Vis data from the titration with the La^{3+} and the calibration curve equitation determined from the plot at Figure VI.28, the concentration of the $LaCl_3 \cdot 2LiCl$ THF stock solution was calculated to be 0.59 mM with a standard deviation of 0.12 mM (Table VI.7). Regarding the supplier concentration specification and the calculated value from the experiment, the developed EBT assay can be considered as a reliable method for metal content determination of lanthanum(III) solutions.

Table VI.7: Concentration determination of a $LaCl_3 \cdot 2LiCl$ stock solution.

Solution with known $[La^{3+}]$		**Solution with unknown $[La^{3+}]$**			
$[La^{3+}]$ (μM)	A_{502} (a.u.)	V (μL)	A_{502} (a.u.)	Conc. in 200 μL well (μM)	Conc. of stock solution (mM)
0	0.4356	-	-	-	-
10	0.5295	5	0.6091	17.34	0.6937
20	0.6362	10	0.7453	30.71	0.6142
30	0.7398	15	0.7841	34.52	0.4602
					Ø 0.5894

5. Gas Phase Characterization of Lanthanide Complexes

5.1. OH- vs. NH distance variation C9-N1

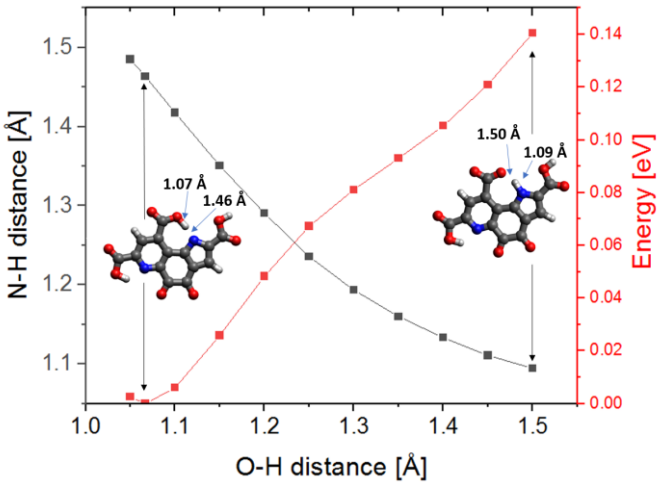

Figure VI.30: Geometry-restricted DFT calculation. The O-H distance of the carboxylic function at C9 is stepwise increased, all remaining geometry parameters are optimized. As a consequence, the N1-H distance decreases and the relative energy increases. This indicates that in gas phase the N1-H function is deprotonated more easily than the neighboring C9-COOH group.

5.2. OH- vs. NH distance variation C7-N6

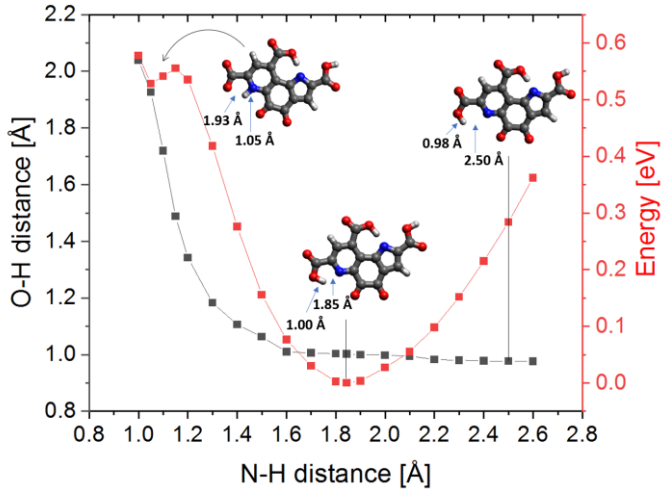

Figure VI.31: Geometry-restricted DFT calculation. The N6-H distance is stepwise varied, all remaining geometry parameters are optimized. The structure lowest in energy is characterized by a protonated carboxylic function at C7 and a hydrogen bridge to N6 (N-H distance 1.85 Å). Reducing the N6-H distance leads to a proton transfer from the COOH group to N6, the energy increases by ca. 0.55 eV. Increasing N6-Hthe distance breaks the hydrogen bond and increases the energy by ca. 0.3 eV.

5.3. Mobilograms of $[PQQ_{15\text{-}5}+H]^+$-variation of trapping parameters

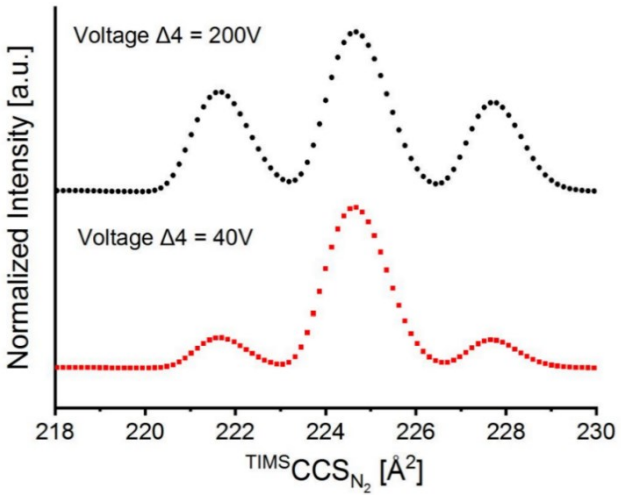

*Figure VI.32: Mobilograms of [**PQQ**$_{15\text{-}5}$+H]$^+$, variation of trapping parameters. The voltage "Δ4" corresponds to the potential difference between accumulation trap and funnel 1 in of the instrument. As a rule of thumb, the ion internal energy increases with that voltage. With increasing energy the peak intensities become more similar.*

5.4. Temperature-dependent ^{1}H NMR measurements of ligand $PQQ_{15\text{-}5}$

The measurements were performed in CD_3CN (0.009 M) at different temperatures (from - 41 °C to 60 °C) with a Jeol ECX 400 (400 MHz) NMR Spectrometer. ^{1}H-chemical shifts are reported in δ units relative to CD_3CN (δ_H = 1.94 ppm). The software used for data processing was MNova Version 12.0.1.

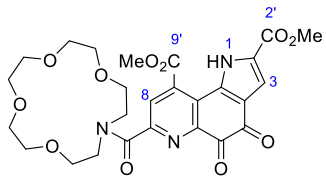

$PQQ_{15\text{-}5}$

Only small effects on the chemical shifts of PQQ's aromatic protons were observed when increasing the temperature from - 41 °C to 60 °C, indicating that no new species have been formed. However, the proton resonances of the aza-crown moiety showed a clear temperature induced change indicating the presence of dynamic intramolecular processes. When increasing the temperature from - 41 °C to 30 °C, the two triplets between 3.71 and 3.84 ppm (- 41 °C) gradually coalesced to a multiplet, which eventually exhibited a triplet multiplicity at temperatures higher than 40 °C. The proton resonance at 3.64 ppm (- 41 °C) gradually disappeared upon temperature increase. The singlet at 3.59 ppm (- 41 °C) progressively decreased with temperature increase from - 41 °C to 30 °C and a new resonance at 3.63 ppm appeared at 20 °C and gradually increased with higher temperatures. In addition, a broad signal appeared at 3.69 ppm at 60 °C. Furthermore, when increasing the temperature from - 41 °C to

60 °C, the multiplet around 3.55 ppm (- 41 °C) and the triplet at 3.46 ppm (- 41 °C) gradually merged to a broad peak with higher intensity. The results point to a flexible crown ether moiety exhibiting different possible conformations. In solution the molecule rapidly interchanges among the conformations, however the fluxionality could be reduced at low temperatures, which results in sharp hydrogen atom resonances.

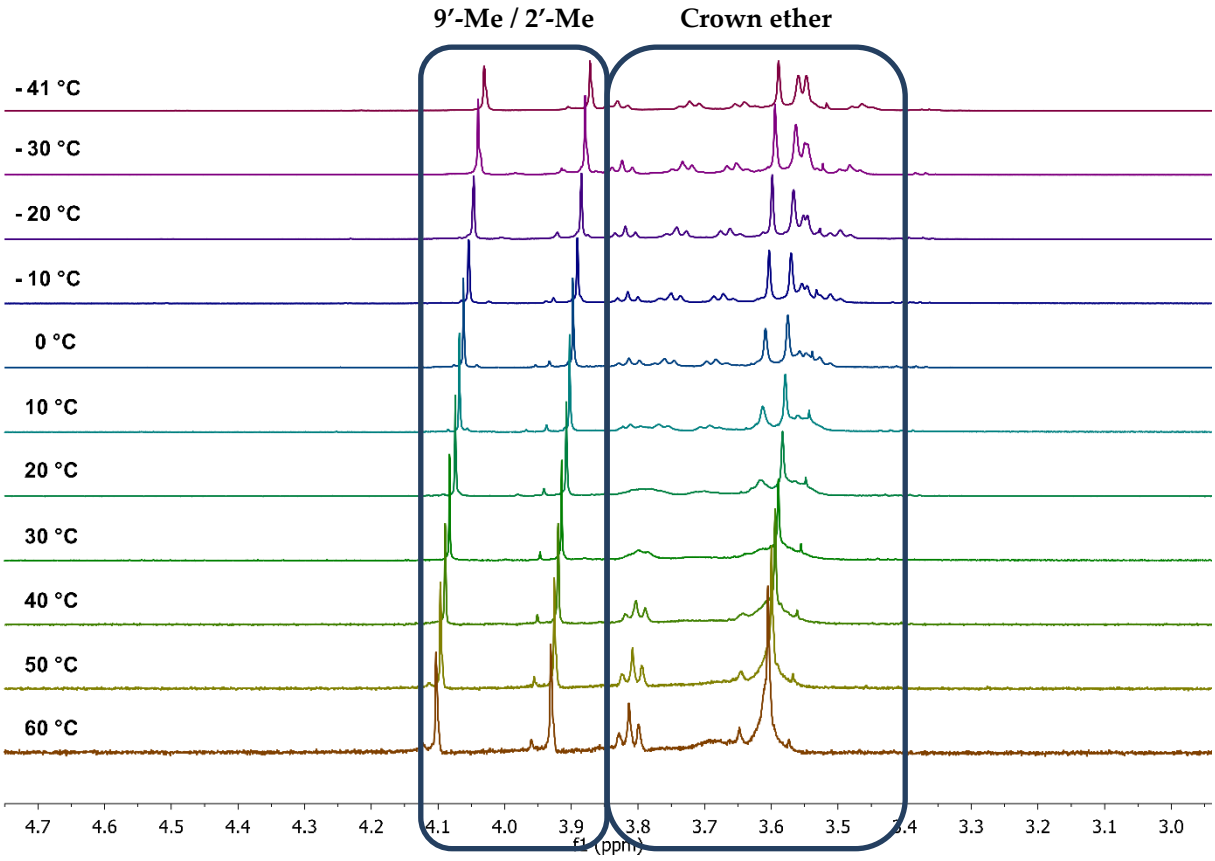

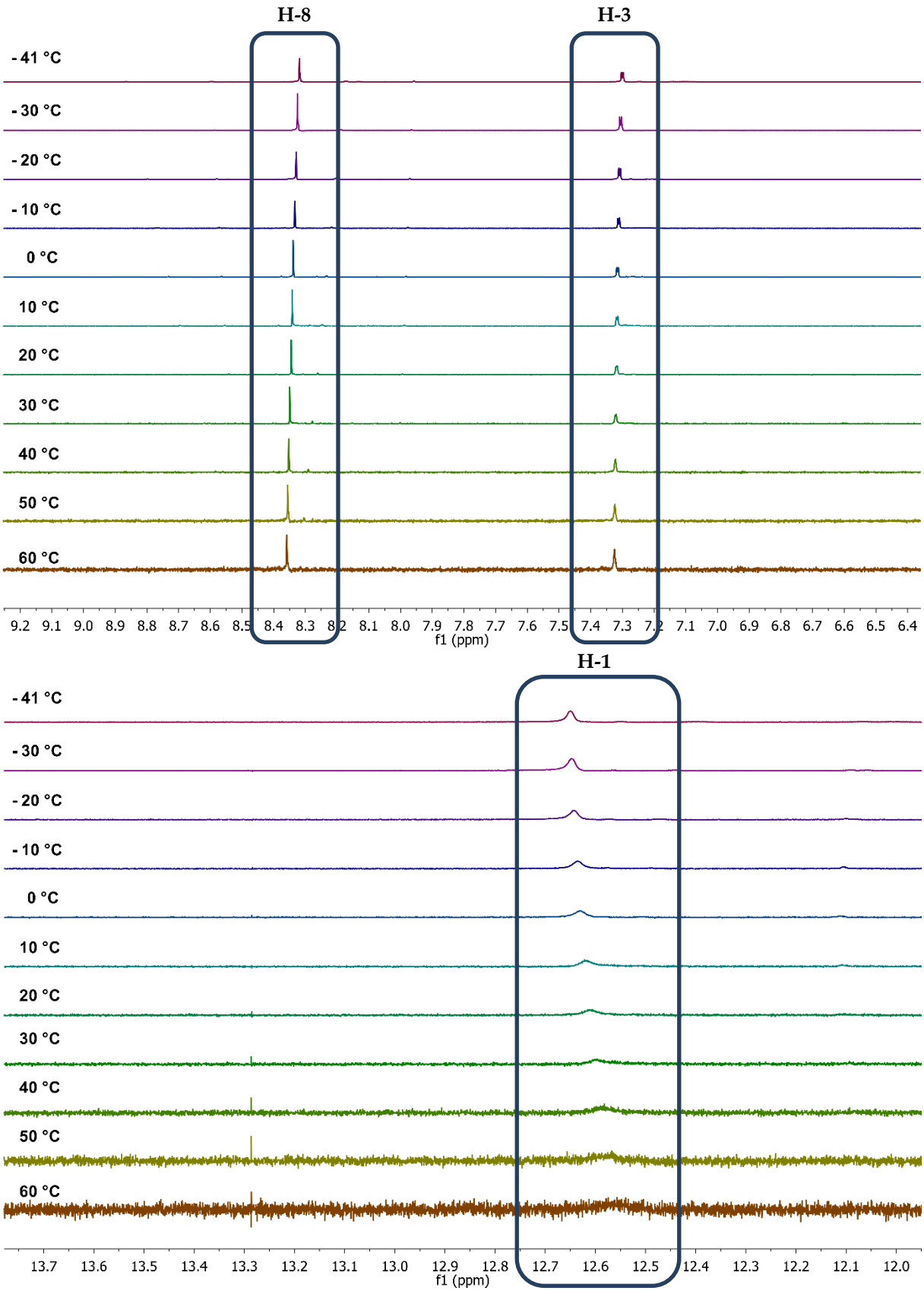

*Figure VI.33: Temperature-dependent ^{1}H NMR measurements of ligand **PQQ**$_{15\text{-}5}$. The resonance signal around 13.3 ppm has an integral of only 0.16 with reference to the integral of H-1.*

5.5. Shape measures calculations for the structures of $[PQQ_{15\text{-}5}+Ln+NO_3]^{2+}$

The CShM values S can theoretically range between 0 (perfect fit to the ideal reference geometry) and 100 (no geometric similarity). Smaller S indicates smaller average deviation from the reference geometry. Table VI.8 shows the CShM for the 7 reference geometries with the S smallest, absolute values. All other reference geometries consistently gave much higher values for S.

Table VI.8: Continuous shape measure (CShM)[265–267] values S for the inner-sphere coordination geometries of the complexes $[PQQ_{15\text{-}5}+Ln+NO_3]^{2+}$.

	S (relative to the Gd complex)	S (relative to the La complex)	$S_{CSAPR\text{-}9}$[a]	$S_{JCSAPR\text{-}9}$[b]	$S_{CCU\text{-}9}$[c]	$S_{JCCU\text{-}9}$[d]	$S_{TCTPR\text{-}9}$[e]	$S_{JTCTPR\text{-}9}$[f]	$S_{MFF\text{-}9}$[g]
La	0.153	≡ 0	4.791	5.232	5.182	6.332	5.123	6.951	4.484
Ce	0.050	n.d.	4.432	4.858	4.955	6.029	4.791	6.495	4.128
Pr	0.033	n.d.	4.424	4.853	4.826	5.898	4.820	6.524	4.115
Nd	0.022	n.d.	4.306	4.734	4.782	5.847	4.669	6.424	4.037
Pm	0.012	n.d.	4.247	4.679	4.878	5.925	4.640	6.368	3.958
Sm	0.011	n.d.	4.192	4.650	4.894	5.966	4.599	6.293	3.905
Eu	0.008	n.d.	4.141	4.612	4.860	5.958	4.518	6.305	3.907
Gd	≡ 0	n.d.	4.022	4.484	4.791	5.855	4.462	6.240	3.783
Tb	0.088	n.d.	3.260	3.801	5.143	6.222	3.737	5.626	3.111
Dy	0.102	n.d.	3.246	3.771	5.173	6.225	3.751	5.586	3.084
Ho	0.107	n.d.	3.135	3.672	5.120	6.175	3.585	5.408	3.005
Er	0.118	n.d.	3.114	3.632	5.132	6.158	3.581	5.377	2.991
Tm	0.111	n.d.	3.159	3.646	5.125	6.124	3.609	5.382	3.043
Yb	0.108	n.d.	3.168	3.652	5.159	6.157	3.617	5.391	3.056
Lu	0.220	0.656	2.808	3.408	5.326	6.405	3.344	5.150	2.684

[a] Capped square-antiprism (spherical); [b] Capped square-antiprism (Johnson solid J10); [c] Spherical-relaxed capped cube; [d] Capped cube (Johnson solid J8); [e] Spherical tricapped trigonal prism; [f] Tricapped trigonal prism (Johnson solid J51); [g] Irregular Muffin shape.

5.6. Inner-sphere bond lengths for the structures of $[PQQ_{15\text{-}5}+Ln+NO_3]^{2+}$

Figure VI.34 shows the labeling scheme for the binding donor atoms in the DFT-optimized structures of the complexes $[\mathbf{PQQ}_{15\text{-}5}+Ln+NO_3]^{2+}$ with the lanthanum species as a representative example. Table VI.9 contains the bond lengths Ln-X (X =O, N) in these compounds.

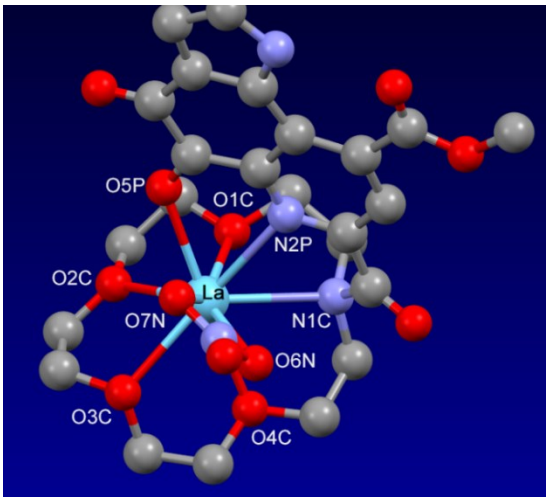

*Figure VI.34: Representative coordination geometry of the binding donor atoms around the lanthanum center in [**PQQ**$_{15\text{-}5}$+La+NO_3]$^{2+}$. The hydrogen atoms are omitted for clarity.*

*Table VI.9: Bond lengths (Å) for the different distances Ln-X (X =O, N) in the complexes [**PQQ**$_{15\text{-}5}$+La+NO_3]$^{2+}$. The labels for the donor atoms are given in Figure VI.34.*

	Ln-O1C	**Ln-O2C**	**Ln-O3C**	**Ln-O4C**	**Ln-N1C**	**Ln-N2P**	**Ln-O5P**	**Ln-O6N**	**Ln-O7N**
La	2.591	2.632	2.591	2.599	2.810	2.694	2.583		2.493
Ce	2.541	2.581	2.534	2.555	2.770	2.603	2.445	2.434	2.424
Pr	2.532	2.578	2.524	2.539	2.765	2.616	2.492	2.432	2.432
Nd	2.520	2.557	2.516	2.533	2.761	2.613	2.497	2.437	2.418
Pm	2.493	2.547	2.513	2.510	2.729	2.595	2.504	2.400	2.424
Sm	2.502	2.547	2.506	2.506	2.735	2.598	2.500	2.417	2.439
Eu	2.501	2.542	2.502	2.524	2.750	2.614	2.535	2.454	2.442
Gd	2.500	2.539	2.499	2.524	2.745	2.599	2.539	2.416	2.407
Tb	2.448	2.454	2.442	2.474	2.689	2.526	2.440	2.350	2.356
Dy	2.447	2.440	2.446	2.467	2.696	2.551	2.477	2.337	2.370
Ho	2.415	2.434	2.423	2.460	2.670	2.503	2.437	2.337	2.334
Er	2.407	2.429	2.417	2.456	2.671	2.495	2.433	2.325	2.327
Tm	2.407	2.432	2.415	2.461	2.690	2.502	2.447	2.331	2.339
Yb	2.409	2.438	2.417	2.466	2.697	2.510	2.460	2.336	2.352
Lu	2.374	2.394	2.390	2.430	2.613	2.448	2.400	2.291	2.308
1-(d_{Lu}/d_{La})	0.084	0.090	0.078	0.065	0.070	0.091	0.071	0.088	0.074

6. Alcohol Oxidation

6.1. Product Analysis with 2,4-DNPH

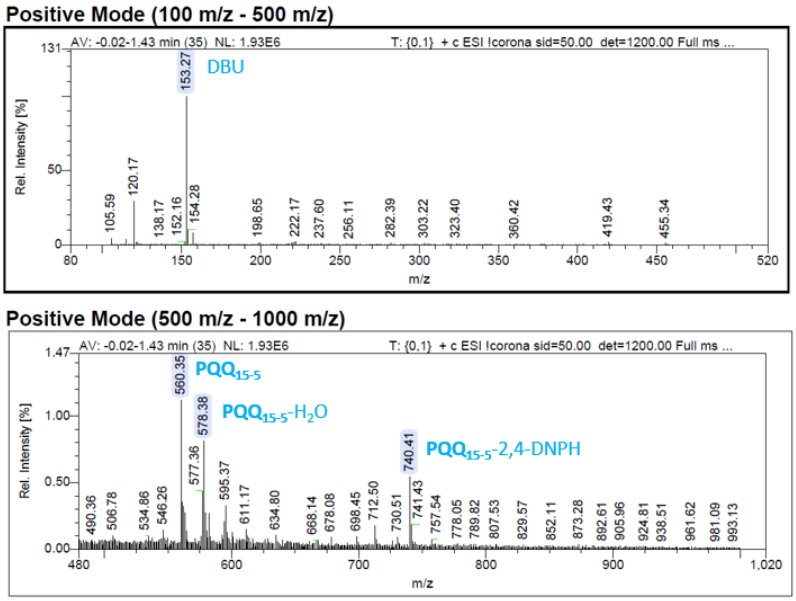

Figure VI.35: LC-MS analysis of an aliquot from the reaction mixture containing ***PQQ***$_{15\text{-}5}$*, Eu(OTf)*$_3$*, MeOH, DBU and 2,4-DNPH in acetonitrile. Calculated exact mass for of the* ***PQQ***$_{15\text{-}5}$*-2,4-dinitrophenylhydrazine adduct* ***30*** *[*$C_{32}H_{34}N_7O_{14}$*]*$^+$*: m/z = 740.2158.*

6.2. Method Development for Monitoring of Alcohol Oxidation

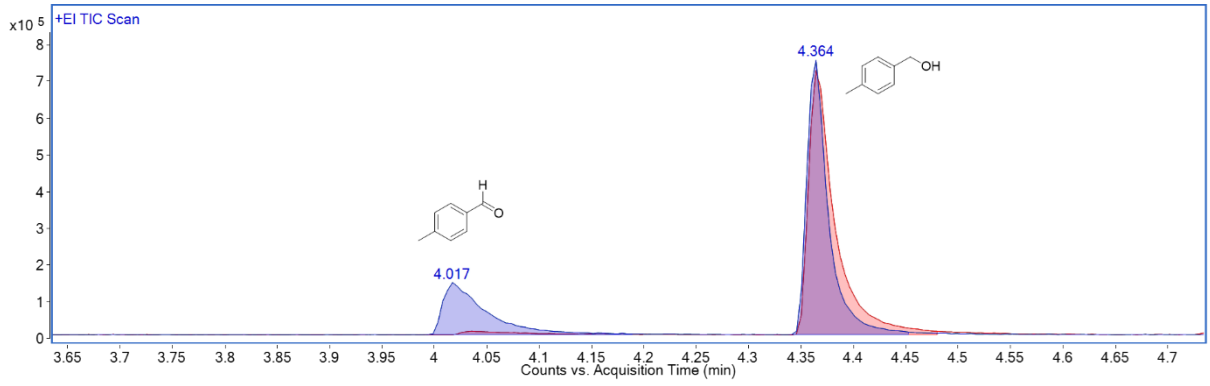

Figure VI.36: GC-MS traces of filtered (red) and unfiltered (blue) aliquots from a solution containing lanthanum(III) nitrate, 4-methybenzyl alcohol and DBU in acetonitrile.

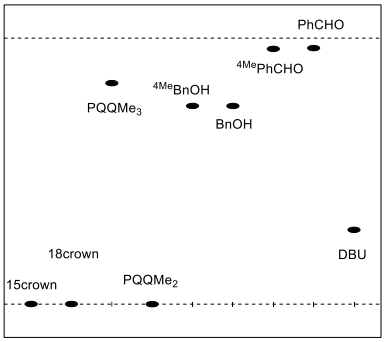

Figure VI.37: Graphic representation of TLC results (stationary phase: silica gel 60 F_{254} plates, mobile phase: acetonitrile).

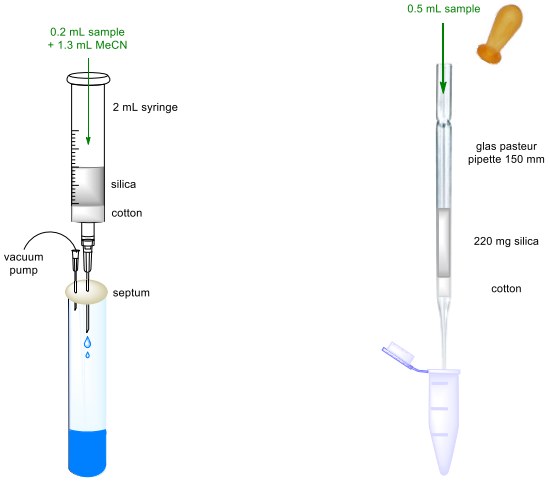

Figure VI.38: Graphic representation of aliquot work-up procedures. Images generated with the ChemDraw Professional 16.0.

7. List of Abbreviations

2D	two-dimensional
°C	degree Celsius
A	absorbance
A_0	initial absorbance
A_{max}	saturated absorbance
Å	angstrom
a.u.	arbitrary units
Bn	benzyl
BOP	benzotriazol-1-yloxytris-(dimethylamino)phosphonium hexafluorophosphate
c	concentration
calc.	calculated
CAN	ceric ammonium nitrate
CAPS	N-cyclohexyl-3-amino-propanesulfonic acid
CCS	collision cross section
CDI	1,1'-carbonyldiimidazole
CID	collision induced dissociation
cm	centimeter
CN	coordination number
conc.	Concentrated
COSY	two-dimensional correlation spectroscopy
CShM	continuous shape measure
CW	continuous-wave
Cy	cyclohexyl
cyt cL	cytochrome cL
d	day(s)
dB	decibel
DBU	1,8-diazabicyclo[5,4,0]undec-7-ene
DCM	methylene chloride
DFO(M)	deferoxamine (mesylate)
DFT	density functional theory
DIPE	diisopropyl ether
DMF	dimethylformamide
DMSO	dimethyl sulfoxide
DNPH	dinitrophenylhydrazine
EBT	Eriochrome Black T
EI	electron ionization
EDC	1-Ethyl-3-(3-dimethylamino-propyl)carbodiimide
EPR	electron paramagnetic resonance
eq.	equation
equiv.	equivalents
ESI	electrospray ionization
Et	ethyl
EtOAc	ethyl acetate
EtOH	ethanol
eV	electron volt
GC-MS	gas chromatography mass spectrometry

GDH	glucose dehydrogenase
GHz	gigahertz
FT	Fourier-transform
g	gram
h	hour(s)
HMBC	heterobinuclear multiple bond correlation
HMPT	hexamethylphosphoramide
HOBt	hydroxybenzotriazole
HPLC	high-performance liquid chromatography
HREE	heavy rare earth elements
HRMS	high resolution mass spectrometry
HSQC	heteronuclear single quantum coherence
Hz	hertz
i	iso
IMMS	ion mobility mass spectrometry
IMS	ion mobility measurements
IR	infrared
J	coupling constant
k	reaction rate constant
K	binding constant
K_{add}	equilibrium constant
kDa	kilodaltons
KIE	kinetic isotope effect
LanM	lanmodulin
LC-MS	liquid chromatography mass spectrometry
Ln	lanthanide
LREE	light rare earth elements
LTQ	linear trap quadrupole
M	molarity
mbar	millibar
MDH	methanol dehydrogenase
Me	methyl
MeOH	methanol
mg	milligram
MHz	mega hertz
min	minute(s)
mL	milliliter
mm	millimeter
mM	millimolar
mmol	millimole
mol%	mole percent
MRI	magnetic resonance imaging
mT	millitesla
MxaF	Ca^{2+}-dependent MDH enzyme
mxaF	gene encoding for MxaF
m/z	mass-to-charge ratio
μM	micromolar
μm	micrometer
μs	microsecond

NCE	normalized collision energy
NimH	nickel metal hydride
nm	nanometer
ns	nanosecond(s)
NMR	nuclear magnetic resonance
o	ortho
OTf	triflate
PDB	protein data bank
PedH	PQQ-dependent alcohol dehydrogenase
Ph	phenyl
pm	picometer
ppm	parts per million
PQQ	pyrroloquinoline quinone
PyBOP	benzotriazol-1-yloxytri-pyrrolidinophosphonium hexafluorophosphate
R	organic substituent
REE	rare earth element
R_f	retardation factor
r.t.	room temperature
s	second(s)
T	relaxation time
TBME	*tert*-butyl methyl ether
TEA	trimethylamine
TFA	trifluoroacetic acid
THF	tetrahydrofuran
TIMS	trapped ion mobility spectrometry
TLC	thin layer chromatography
TMS_2O	hexamethyldisiloxane
TOF-MS	time-of-flight mass spectrometry
t_R	retention time
TRF	time-resolved fluorescence
UV	ultraviolet
v	reaction rate
V	volt
v/v	volume percent
$\tilde{\nu}$	wavenumber
vis	visible
vs.	versus
wt.%	percentage by weight
X-ray	X-radiation
XoxF	Ln^{3+}-dependent MDH enzyme
xoxF	gene encoding for XoxF
δ	chemical shift (NMR)
ε	molar absorptivity
λ	wavelength
χ	mole fraction

8. List of Compounds

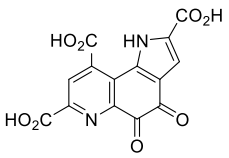

PQQ

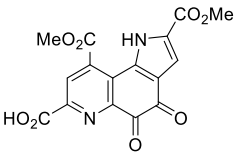

$PQQMe_2$

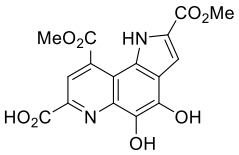

$PQQMe_2H_2$

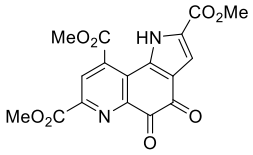

$PQQMe_3$

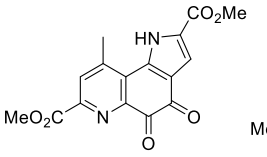

$P_{ME}QQ_{MEM}$

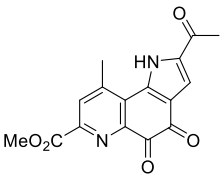

P_KQQ_{MEM}

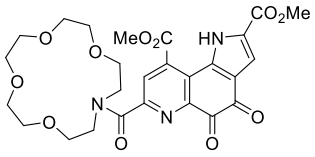

$PQQ_{15\text{-}5}$

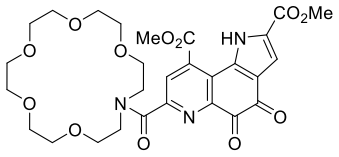

$PQQ_{18\text{-}6}$

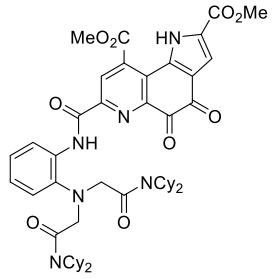

L_{PQQ}

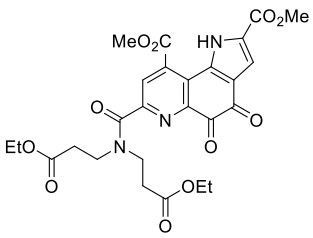

PQQ_{DEDP}

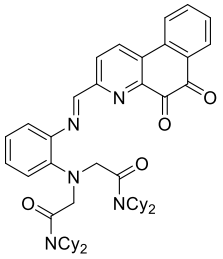

L_{QQ}

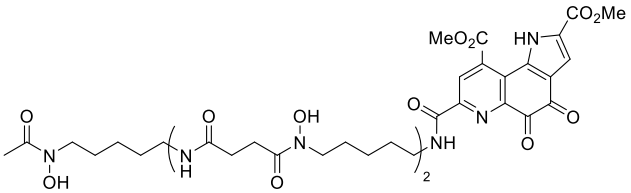

PQQ_{DFO}

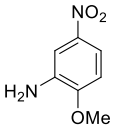

1

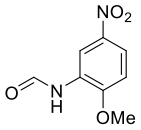

2

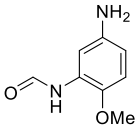

3

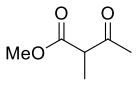

4

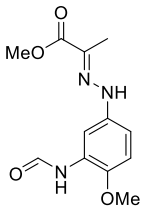

5

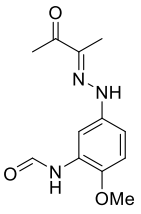

6

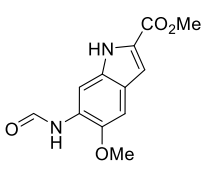

7

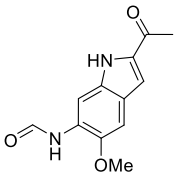

8

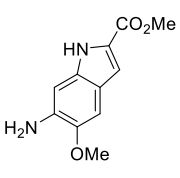

9

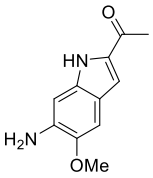

10

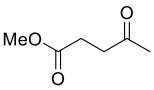

11

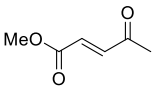

12

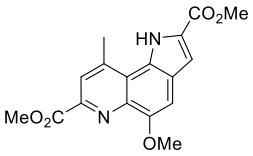

13

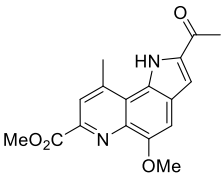

14

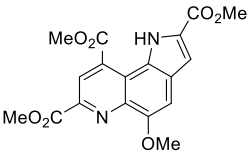

15

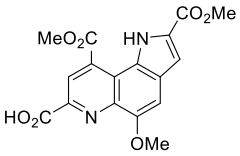

16

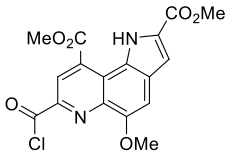

17

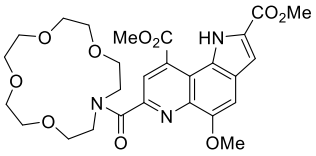

18

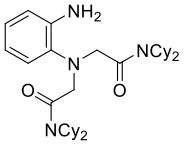

19

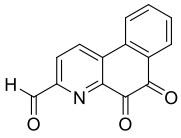

20

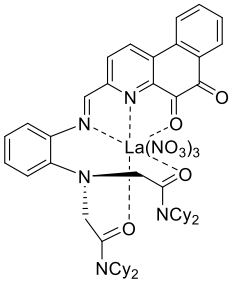

21

22

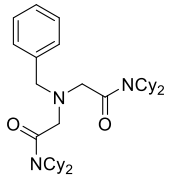

23

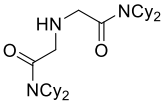

24

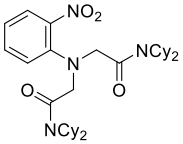

25

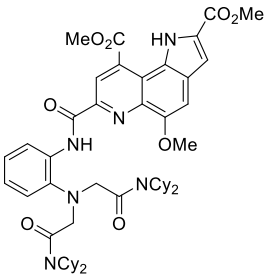

26

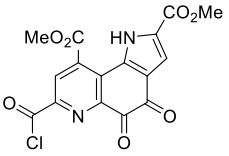

27

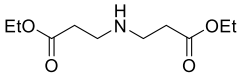

28

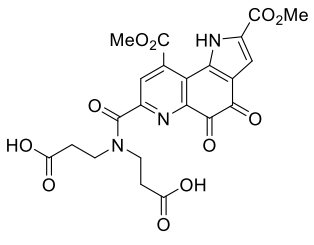

29

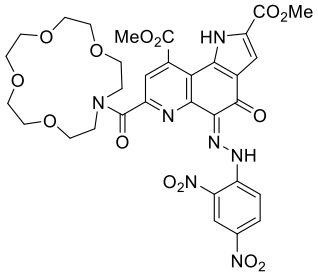

30

VII. REFERENCES

[1] E. J. Corey, A. Tramontano, *J. Am. Chem. Soc.* **1981**, *103*, 5599–5600.

[2] N. C. Martinez-Gomez, H. N. Vu, E. Skovran, *Inorg. Chem.* **2016**, *55*, 10083–10089.

[3] T. Nakagawa, R. Mitsui, A. Tani, K. Sasa, S. Tashiro, T. Iwama, T. Hayakawa, K. Kawai, *PLoS One* **2012**, *7*, e50480.

[4] S. Lim, S. J. Franklin, *Cell. Mol. Life Sci.* **2004**, *61*, 2184–2188.

[5] L. Chistoserdova, *World J. Microbiol. Biotechnol.* **2016**, *32*, 1–7.

[6] L. J. Daumann, *Angew. Chem. Int. Ed.* **2019**, *58*, 12795–12802.

[7] M. Peplow, *ACS Cent. Sci.* **2021**, *7*, 1776–1779.

[8] Y. Hibi, K. Asai, H. Arafuka, M. Hamajima, T. Iwama, K. Kawai, *J. Biosci. Bioeng.* **2011**, *111*, 547–549.

[9] N. A. Fitriyanto, M. Fushimi, M. Matsunaga, A. Pertiwiningrum, T. Iwama, K. Kawai, *J. Biosci. Bioeng.* **2011**, *111*, 613–617.

[10] A. Pol, T. R. M. Barends, A. Dietl, A. F. Khadem, J. Eygensteyn, M. S. M. Jetten, H. J. M. Op den Camp, *Environ. Microbiol.* **2014**, *16*, 255–264.

[11] A. M. Panichev, *Achiev. Life Sci.* **2015**, *9*, 95–103.

[12] T. Cheisson, E. J. Schelter, *Science* **2019**, *363*, 489–493.

[13] Z. M. Migaszewski, A. Gałuszka, *Crit. Rev. Env. Sci. Technol.* **2015**, *45*, 429–471.

[14] J. R. Rumble, *CRC Handbook of Chemistry and Physics*, CRC Press/Taylor & Francis, Boca Raton, **2019**.

[15] K. Hans Wedepohl, *Geochim. Cosmochim. Acta* **1995**, *59*, 1217–1232.

[16] D. I. Mendeleev, *Russ. J. Org. Chem.* **1869**, *3*, 25.

[17] D. I. Mendeleev, *Z. Chem.* **1869**, *12*, 405.

[18] D. A. Johnson, A. F. Williams, *Chimia* **2019**, *73*, 144–151.

[19] S. Cotton, *Lanthanide and Actinide Chemistry: Inorganic Chemistry.*, John Wiley & Sons, Ltd., Chichester, **2006**.

[20] R. D. Shannon, *Acta Crystallogr. Sect. A* **1976**, *32*, 751–767.

[21] C. H. Evans, *Biochemistry of the Lanthanides*, Springer US, New York, **1990**.

[22] J. A. Cotruvo, *ACS Cent. Sci.* **2019**, *5*, 1496–1506.

[23] E. R. Featherston, J. A. Cotruvo, *Biochim. Biophys. Acta, Mol. Cell. Res.* **2021**, *1868*, 118864.

[24] J. A. Mattocks, J. A. Cotruvo, *Chem. Soc. Rev.* **2020**, *49*, 8315–8334.

[25] M. Seitz, A. G. Oliver, K. N. Raymond, *J. Am. Chem. Soc.* **2007**, *129*, 11153–11160.

[26] J. A. Peters, K. Djanashvili, C. F. G. C. Geraldes, C. Platas-Iglesias, *Coord. Chem. Rev.* **2020**, *406*, 213146.

[27] R. E. Cramer, J. M. Rimsza, T. J. Boyle, *Inorg. Chem.* **2022**, *61*, 6120–6127.

[28] R. B. Jordan, *Inorg. Chem.* **2023**, *62*, 3715–3721.

[29] D. Lundberg, I. Persson, L. Eriksson, P. D'Angelo, S. De Panfilis, *Inorg. Chem.* **2010**, *49*, 4420–4432.

[30] S. A. Cotton, *C.R. Chim.* **2005**, *8*, 129–145.

[31] J.-C. G. Bünzli, in *Rare Earth Chemistry* (Eds.: R. Pöttgen, T. Jüstel, C.A. Strassert), De Gruyter, Berlin, **2020**,

pp. 185–200.

[32] P. Dangelo, A. Zitolo, V. Migliorati, G. Chillemi, M. Duvail, P. Vitorge, S. Abadie, R. Spezia, *Inorg. Chem.* **2011**, *50*, 4572–4579.

[33] R. F. Higgins, K. P. Ruoff, A. Kumar, E. J. Schelter, *Acc. Chem. Res.* **2022**, *55*, 2616–2627.

[34] L. J. Daumann, *ACS Cent. Sci.* **2021**, *7*, 1780–1782.

[35] H. G. Brittain, F. S. Richardson, R. B. Martin, *J. Am. Chem. Soc.* **1976**, *98*, 8255–8260.

[36] C. G. dos Remedios, *Cell Calcium* **1981**, *2*, 29–51.

[37] F. Xie, T. A. Zhang, D. Dreisinger, F. Doyle, *Miner. Eng.* **2014**, *56*, 10–28.

[38] J. A. Mattocks, J. J. Jung, C. Y. Lin, Z. Dong, N. H. Yennawar, E. R. Featherston, C. S. Kang-Yun, T. A. Hamilton, D. M. Park, A. K. Boal, J. A. Cotruvo, *Nature* **2023**, *618*, 87–93.

[39] K. Li, T. Liang, L. Wang, S. Tian, *Environ. Geochem. Health* **2018**, *40*, 2795–2805.

[40] Q. Liang, H. Yin, J. Li, L. Zhang, R. Hou, S. Wang, *Medicine* **2018**, *97*, e12717.

[41] B. Weaver, F. A. Kappelmann, A. C. Topp, *J. Am. Chem. Soc.* **1953**, *75*, 3943–3945.

[42] J. Roosen, K. Binnemans, *J. Mater. Chem. A* **2014**, *2*, 1530–1540.

[43] J. Florek, S. Giret, E. Juère, D. Larivière, F. Kleitz, *Dalton Trans.* **2016**, *45*, 14832–14854.

[44] H. Lumpe, A. Menke, C. Haisch, P. Mayer, A. Kabelitz, K. V. Yusenko, A. Guilherme Buzanich, T. Block, R. Pöttgen, F. Emmerling, L. J. Daumann, *Chem. Eur. J.* **2020**, *26*, 10133–10139.

[45] J. A. Bogart, B. E. Cole, M. A. Boreen, C. A. Lippincott, B. C. Manor, P. J. Carroll, E. J. Schelter, *PNAS* **2016**, *113*, 14887–14892.

[46] Z. Dong, J. A. Mattocks, G. J. P. Deblonde, D. Hu, Y. Jiao, J. A. Cotruvo, D. M. Park, *ACS Cent. Sci.* **2021**, *7*, 1798–1808.

[47] S. Demir, N. K. Brune, J. F. Van Humbeck, J. A. Mason, T. V. Plakhova, S. Wang, G. Tian, S. G. Minasian, T. Tyliszczak, T. Yaita, T. Kobayashi, S. N. Kalmykov, H. Shiwaku, D. K. Shuh, J. R. Long, *ACS Cent. Sci.* **2016**, *2*, 253–265.

[48] D. M. Park, D. W. Reed, M. C. Yung, A. Eslamimanesh, M. M. Lencka, A. Anderko, Y. Fujita, R. E. Riman, A. Navrotsky, Y. Jiao, *Environ. Sci. Technol.* **2016**, *50*, 2735–2742.

[49] Y. Ding, D. Harvey, N. H. L. Wang, *Green Chem.* **2020**, *22*, 3769–3783.

[50] J. A. Bogart, C. A. Lippincott, P. J. Carroll, E. J. Schelter, *Angew. Chem. Int. Ed.* **2015**, *54*, 8222–8225.

[51] B. E. Cole, I. B. Falcones, T. Cheisson, B. C. Manor, P. J. Carroll, E. J. Schelter, *Chem. Commun.* **2018**, *54*, 10276–10279.

[52] T. Cheisson, B. E. Cole, B. C. Manor, P. J. Carroll, E. J. Schelter, *ACS Sustainable Chem. Eng.* **2019**, *7*, 4993–5001.

[53] X. Z. Li, L. P. Zhou, L. L. Yan, Y. M. Dong, Z. L. Bai, X. Q. Sun, J. Diwu, S. Wang, J. C. Bünzli, Q. F. Sun, *Nat. Commun.* **2018**, *9*, 547.

[54] M. R. Healy, A. S. Ivanov, Y. Karslyan, V. S. Bryantsev, B. A. Moyer, S. Jansone-Popova, *Chem. Eur. J.* **2019**, *25*, 6326–6331.

[55] N. A. Thiele, D. J. Fiszbein, J. J. Woods, J. J. Wilson, *Inorg. Chem.* **2020**, *59*, 16522–16530.

[56] H. Fang, B. E. Cole, Y. Qiao, J. A. Bogart, T. Cheisson, B. C. Manor, P. J. Carroll, E. J. Schelter, *Angew. Chem. Int. Ed.* **2017**, *56*, 13450 –13454.

[57] G. J. P. Deblonde, J. A. Mattocks, D. M. Park, D. W. Reed, J. A. Cotruvo, Y. Jiao, *Inorg. Chem.* **2020**, *59*, 11855–11867.

[58] T. Lorenz, M. Bertau, R. Möckel, in *Rare Earth Chemistry* (Eds.: R. Pöttgen, T. Jüstel, C.A. Strassert), Walter De Gruyter GmbH, Berlin / Boston, **2020**, pp. 15–36.

[59] British Geological Survey, *Rare Earth Elements*, **2010**.

[60] V. Zepf, J. Simmons, A. Reller, M. Ashfield, C. Rennie, *Materials Critical to the Energy Industry. An Introduction*, BP P.L.C., London, **2014**.

[61] K. M. Goodenough, F. Wall, D. Merriman, *Nat. Resour. Res.* **2018**, *27*, 201–216.

[62] M. C. Heffern, L. M. Matosziuk, T. J. Meade, *Chem. Rev.* **2014**, *114*, 4496–4539.

[63] T. J. Clough, L. Jiang, K. L. Wong, N. J. Long, *Nat. Commun.* **2019**, *10*, 1420.

[64] D. M. J. Doble, M. Melchior, B. O'Sullivan, C. Siering, J. Xu, V. C. Pierre, K. N. Raymond, *Inorg. Chem.* **2003**, *42*, 4930–4937.

[65] P. Caravan, *Acc. Chem. Res.* **2009**, *42*, 851–862.

[66] C. J. Jocher, E. G. Moore, J. Xu, S. Avedano, M. Botta, S. Aime, K. N. Raymond, *Inorg. Chem.* **2007**, *46*, 9182–9191.

[67] A. C. Mendonça, A. F. Martins, A. Melchior, S. M. Marques, S. Chaves, S. Villette, S. Petoud, P. L. Zanonato, M. Tolazzi, C. S. Bonnet, É. Tóth, P. Di Bernardo, C. F. G. C. Geraldes, M. A. Santos, *Dalton Trans.* **2013**, *42*, 6046–6057.

[68] B. W. Stein, A. Morgenstern, E. R. Batista, E. R. Birnbaum, S. E. Bone, S. K. Cary, M. G. Ferrier, K. D. John, J. L. Pacheco, S. A. Kozimor, V. Mocko, B. L. Scott, P. Yang, *J. Am. Chem. Soc.* **2019**, *141*, 19404–19414.

[69] N. A. Thiele, J. J. Woods, J. J. Wilson, *Inorg. Chem.* **2019**, *58*, 10483–10500.

[70] Y. Qiao, E. J. Schelter, *Acc. Chem. Res.* **2018**, *51*, 2926–2936.

[71] T. C. Jenks, M. D. Bailey, J. L. Hovey, S. Fernando, G. Basnayake, M. E. Cross, W. Li, M. J. Allen, *Chem. Sci.* **2018**, *9*, 1273–1278.

[72] E. J. Coughlin, M. Zeller, S. C. Bart, *Angew. Chem. Int. Ed.* **2017**, *56*, 12142–12145.

[73] D. Schädle, R. Anwander, *Chem. Soc. Rev.* **2019**, *48*, 5752–5805.

[74] C. de Oliveira, S. J. Ramos, J. O. Siqueira, V. Faquin, E. M. de Castro, D. C. Amaral, V. H. Techio, L. C. Coelho, P. H. P. e Silva, E. Schnug, L. R. G. Guilherme, *Ecotoxicol. Environ. Saf.* **2015**, *122*, 136–144.

[75] N. A. Fitriyanto, M. Nakamura, S. Muto, K. Kato, T. Yabe, T. Iwama, K. Kawai, A. Pertiwiningrum, *J. Biosci. Bioeng.* **2011**, *111*, 146–152.

[76] X. Xu, W. Zhu, Z. Wang, G. J. Witkamp, *Sci. Total Environ.* **2002**, *293*, 97–105.

[77] G. S. Moeck, J. W. Coulton, *Mol. Microbiol.* **1998**, *28*, 675–681.

[78] M. Sandy, A. Butler, *Chem. Rev.* **2009**, *109*, 4580–4595.

[79] K. N. Raymond, E. A. Dertz, S. S. Kim, *PNAS* **2003**, *100*, 3584–3588.

[80] J.-C. G. Bünzli, *J. Coord. Chem.* **2014**, *67*, 3706–3733.

[81] F. H. Firsching, S. N. Brune, *J. Chem. Eng. Data* **1991**, *36*, 93–95.

[82] H. Lumpe, L. J. Daumann, *Nachr. Chem.* **2018**, *66*, 945–948.

[83] C. Anthony, L. J. Zatman, *Biochem. J.* **1964**, *92*, 609–614.

[84] C. Anthony, L. J. Zatman, *Biochem. J.* **1964**, *92*, 614–621.

[85] C. Anthony, *Arch. Biochem. Biophys.* **2004**, *428*, 2–9.

[86] J. Westerling, J. Frank, J. A. Duine, *Biochem. Biophys. Res. Commun.* **1979**, *87*, 719–724.

[87] C. Anthony, *Biochem. J.* **1996**, *320*, 697–711.

[88] D. R. Houck, J. L. Hanners, C. J. Unkefer, M. A. G. van Kleef, J. A. Duine, in *PQQ Quinoproteins*, Springer Netherlands, Dordrecht, **1989**, pp. 177–185.

[89] J. A. Duine, R. A. van der Meer, B. W. Groen, *Annu. Rev. Nutr.* **1990**, *10*, 297–318.

[90] C. Anthony, *Antioxid. Redox Signaling* **2001**, *3*, 804–813.

[91] R. Rucker, W. Chowanadisai, M. Nakano, *Altern. Med. Rev.* **2009**, *14*, 268–277.

[92] M. Akagawa, M. Nakano, K. Ikemoto, *Biosci. Biotechnol. Biochem.* **2016**, *80*, 13–22.

[93] J. P. Klinman, F. Bonnot, *Chem. Rev.* **2014**, *114*, 4343–4365.

[94] J. A. Duine, *J. Biosci. Bioeng.* **1999**, *88*, 231–236.

[95] P. D. Sarmiento-Pavía, M. E. Sosa-Torres, *J. Biol. Inorg. Chem.* **2021**, *26*, 177–203.

[96] J. G. Hauge, *J. Biol. Chem.* **1964**, *239*, 3630–3639.

[97] S. A. Salisbury, H. S. Forrest, W. B. T. Cruse, O. Kennard, *Nature* **1979**, *280*, 843–844.

[98] L. Chistoserdova, *Environ. Microbiol.* **2011**, *13*, 2603–2622.

[99] L. Chistoserdova, M. E. Lidstrom, *Microbiology* **1997**, *143*, 1729–1736.

[100] S. Schmidt, P. Christen, P. Kiefer, J. A. Vorholt, *Microbiology* **2010**, *156*, 2575–2586.

[101] E. Skovran, A. D. Palmer, A. M. Rountree, N. M. Good, M. E. Lidstrom, *J. Bacteriol.* **2011**, *193*, 6032–6038.

[102] N. Delmotte, C. Knief, S. Chaffron, G. Innerebner, B. Roschitzki, R. Schlapbach, C. Von Mering, J. A. Vorholt, *PNAS* **2009**, *106*, 16428–16433.

[103] A. Pol, K. Heijmans, H. R. Harhangi, D. Tedesco, M. S. M. Jetten, H. J. M. Op Den Camp, *Nature* **2007**, *450*, 874–878.

[104] S. Castaldi, D. Tedesco, *Chemosphere* **2005**, *58*, 131–139.

[105] Y. Wen Deng, S. Y. Ro, A. C. Rosenzweig, *J. Biol. Inorg. Chem.* **2018**, *23*, 1037–1047.

[106] B. Jahn, A. Pol, H. Lumpe, T. R. M. Barends, A. Dietl, C. Hogendoorn, H. J. M. Op den Camp, L. J. Daumann, *ChemBioChem* **2018**, *19*, 1147–1153.

[107] R. A. Schmitz, N. Picone, H. Singer, A. Dietl, K. A. Seifert, A. Pol, M. S. M. Jetten, T. R. M. Barends, L. J. Daumann, H. J. M. Op den Camp, *mBio* **2021**, *12*, e01708-21.

[108] J. T. Keltjens, A. Pol, J. Reimann, H. J. M. Op den Camp, *Appl. Microbiol. Biotechnol.* **2014**, *98*, 6163–6183.

[109] M. Ghosh, C. Anthony, K. Harlos, M. G. Goodwin, C. Blake, *Structure* **1995**, *3*, 177–187.

[110] E. F. Pettersen, T. D. Goddard, C. C. Huang, G. S. Couch, D. M. Greenblatt, E. C. Meng, T. E. Ferrin, *J. Comput. Chem.* **2004**, *25*, 1605–1612.

[111] C. Anthony, M. Ghosh, C. C. F. Blake, *Biochem. J.* **1994**, *304*, 665–674.

[112] N. M. Good, M. Fellner, K. Demirer, J. Hu, R. P. Hausinger, N. C. Martinez-Gomez, *J. Biol. Chem.* **2020**, *295*, 8272–8284.

[113] J. A. Bogart, A. J. Lewis, E. J. Schelter, *Chem. Eur. J.* **2015**, *21*, 1743 – 1748.

[114] L. Chistoserdova, M. G. Kalyuzhnaya, *Trends Microbiol.* **2018**, *26*, 703–714.

[115] H. N. Vu, G. A. Subuyuj, S. Vijayakumar, N. M. Good, N. C. Martinez-Gomez, E. Skovran, *J. Bacteriol.* **2016**, *198*, 1250–1259.

[116] F. Chu, D. A. C. Beck, M. E. Lidstrom, *PeerJ* **2016**, *4*, e2435.

[117] S. Masuda, Y. Suzuki, Y. Fujitani, R. Mitsui, T. Nakagawa, M. Shintani, A. Tani, *mSphere* **2018**, *3*, e00462-17.

[118] H. Lumpe, A. Pol, H. J. M. Op den Camp, L. J. Daumann, *Dalton Trans.* **2018**, *47*, 10463–10472.

[119] J. Huang, Z. Yu, J. Groom, J. F. Cheng, A. Tarver, Y. Yoshikuni, L. Chistoserdova, *ISME J.* **2019**, *13*, 2005–2017.

[120] N. Picone, H. J. Op den Camp, *Curr. Opin. Chem. Biol.* **2019**, *49*, 39–44.

[121] N. C. Martinez-Gomez, E. Skovran, *Science* **2015**, *348*, 862–863.

[122] A. M. Ochsner, L. Hemmerle, T. Vonderach, R. Nüssli, M. Bortfeld-Miller, B. Hattendorf, J. A. Vorholt, *Mol. Microbiol.* **2019**, *111*, 1152–1166.

[123] J. D. Semrau, A. A. DiSpirito, W. Gu, S. Yoon, *Appl. Environ. Microbiol.* **2018**, *84*, e02289-17.

[124] M. Taubert, C. Grob, A. M. Howat, O. J. Burns, J. L. Dixon, Y. Chen, J. C. Murrell, *Environ. Microbiol.* **2015**, *17*, 3937–3948.

[125] N. M. Good, H. N. Vu, C. J. Suriano, G. A. Subuyuj, E. Skovran, N. C. Martinez-Gomez, *J. Bacteriol.* **2016**, *198*, 3109–3118.

[126] M. Wehrmann, P. Billard, A. Martin-Meriadec, A. Zegeye, J. Klebensberger, *mBio* **2017**, *8*, e00570-17.

[127] N. M. Good, H. D. Lee, E. R. Hawker, M. Z. Su, A. A. Gilad, N. C. Martinez-Gomez, *Front. Microbiol.* **2022**, *13*, 820327.

[128] J. A. Cotruvo, E. R. Featherston, J. A. Mattocks, J. V. Ho, T. N. Laremore, *J. Am. Chem. Soc.* **2018**, *140*, 15056−15061.

[129] G. E. Kenney, A. C. Rosenzweig, *Annu. Rev. Biochem.* **2018**, *87*, 645–676.

[130] Z. Guo, O. Smutok, W. A. Johnston, C. E. Ayva, P. Walden, B. McWhinney, J. P. J. Ungerer, A. Melman, E. Katz, K. Alexandrov, *Angew. Chem. Int. Ed.* **2022**, *61*, e202109005.

[131] H. Lee, Y. J. Hong, S. Baik, T. Hyeon, D. H. Kim, *Adv. Healthcare Mater.* **2018**, *7*, 1–14.

[132] K. Satheeshkumar, P. S. Kumar, C. Nandhini, R. Shanmugapriya, K. N. Vennila, K. P. Elango, *Inorg. Chem. Commun.* **2022**, *139*, 109299.

[133] K. Takeda, R. Kusuoka, M. Inukai, K. Igarashi, H. Ohno, N. Nakamura, *Biosens. Bioelectron.* **2021**, 112831.

[134] V. A. Vetsova, K. R. Fisher, H. Lumpe, A. Schäfer, E. K. Schneider, P. Weis, L. J. Daumann, *Chem. Eur. J.* **2021**, *27*, 10087–10098.

[135] A. Schäfer, V. A. Vetsova, E. K. Schneider, M. Kappes, M. Seitz, L. J. Daumann, P. Weis, *J. Am. Soc. Mass Spectrom.* **2022**, *33*, 722–730.

[136] H. Lumpe, L. J. Daumann, *Inorg. Chem.* **2019**, *58*, 8432–8441.

[137] J. L. Nevarez, A. Turmo, J. Hu, R. P. Hausinger, *ChemCatChem* **2020**, *12*, 4242–4254.

[138] H. Lumpe, P. Mayer, L. J. Daumann, *Acta Crystallogr. Sect. C* **2020**, *76*, 1051–1056.

[139] K. Ikemoto, Y. Sakamoto, R. Tanaka, K. Ogata, N. Matsushita, S. Nakamura, *Cryst. Growth Des.* **2017**, *17*, 4118–4123.

[140] T. Ishida, M. Doi, K. Tomita, H. Hayashi, M. Inoue, T. Urakami, *J. Am. Chem. Soc.* **1989**, *111*, 6822–6828.

[141] Z. Zhang, L. M. V. Tillekeratne, R. A. Hudson, *Synthesis* **1996**, 377–382.

[142] S. Itoh, M. Ogino, Y. Fukui, H. Murao, M. Komatsu, Y. Ohshiro, T. Inoue, Y. Kai, N. Kasai, *J. Am. Chem. Soc.* **1993**, *115*, 9960–9967.

[143] S. Itoh, H. Kawakami, S. Fukuzumi, *J. Am. Chem. Soc.* **1997**, *119*, 439–440.

[144] S. Itoh, H. Kawakami, S. Fukuzumi, *Biochemistry* **1998**, *37*, 6562–6571.

[145] G. Büchi, J. H. Botkin, G. C. M. Lee, K. Yakushijin, *J. Am. Chem. Soc.* **1985**, *107*, 5555–5556.

[146] A. R. MacKenzie, C. J. Moody, C. W. Rees, *Tetrahedron* **1986**, *42*, 3259–3268.

[147] J. A. Gainor, S. M. Weinreb, *J. Org. Chem.* **1982**, *47*, 2833–2837.

[148] C. M. Glinkerman, D. L. Boger, *J. Am. Chem. Soc.* **2016**, *138*, 12408–12413.

[149] J. B. Hendrickson, J. G. de Vries, *J. Org. Chem.* **1985**, *50*, 1688–1695.

[150] J. A. Lewis, J. C. DiNardo, *Skin Treatments Containing Pyrroloquinoline Quinone (PQQ) Esters and Methods of Preparation and Use Thereof*, **2014**, US 2014/0178316 A1.

[151] J. V. Kempf, D. Gopal, W. Stalzer, *Synthesis of Pyrroloquinoline Quinone (PQQ)*, **2007**, US 2007/0072894 A1.

[152] M. Ameyama, M. Hayashi, K. Matsushita, E. Shinagawa, O. Adachi, *Agric. Biol. Chem.* **1984**, *48*, 561–565.

[153] A. H. Trotta, *Org. Lett.* **2015**, *17*, 3358–3361.

[154] E. Fischer, F. Jourdan, *Ber. Dtsch. Chem. Ges.* **1883**, *16*, 2241–2245.

[155] O. Doebner, W. von Miller, *Ber. Dtsch. Chem. Ges.* **1883**, *16*, 2464–2472.

[156] K. D. Karlin, *Science* **1993**, *261*, 701–708.

[157] R. Breslow, *Acc. Chem. Res.* **1995**, *28*, 146–153.

[158] G. Parkin, *Chem. Rev.* **2004**, *104*, 699–767.

[159] L. J. Daumann, G. Schenk, D. L. Ollis, L. R. Gahan, *Dalton Trans.* **2014**, *43*, 910–928.

[160] S. Groysman, R. H. Holm, *Biochemistry* **2009**, *48*, 2310–2320.

[161] J. A. Ibers, R. H. Holm, *Science* **1980**, *209*, 223–235.

[162] L. Götzke, G. Schaper, J. März, P. Kaden, N. Huittinen, T. Stumpf, K. K. K. Kammerlander, E. Brunner, P. Hahn, A. Mehnert, B. Kersting, T. Henle, L. F. Lindoy, G. Zanoni, J. J. Weigand, *Coord. Chem. Rev.* **2019**, *386*, 267–309.

[163] S. Itoh, H. Kawakami, S. Fukuzumi, *J. Mol. Catal. B: Enzym.* **2000**, *8*, 85–94.

[164] S. Itoh, X. Huang, H. Kawakami, M. Komatsu, Y. Ohshiro, S. Fukuzumi, *J. Chem. Soc., Chem. Commun.* **1995**, 2077–2078.

[165] S. Itoh, M. Mure, A. Suzuki, H. Murao, Y. Ohshiro, *J. Chem. Soc., Perkin Trans. 2* **1992**, *3*, 1245–1251.

[166] A. McSkimming, T. Cheisson, P. J. Carroll, E. J. Schelter, *J. Am. Chem. Soc.* **2018**, *140*, 1223–1226.

[167] H. Lumpe, Lanthanide Dependent Methanol Dehydrogenases: A Theoretical and Biomimetic Investigation, LMU München, **2019**.

[168] J. A. Duine, J. Frank Jzn, P. E. J. Verwiel, *Eur. J. Biochem.* **1980**, *108*, 187–192.

[169] S. Itoh, J. Kato, T. Inoue, Y. Kitamura, M. Komatsu, Y. Ohshiro, *Synthesis* **1987**, 1067–1071.

[170] V. A. Vetsova, *Synthesis of PQQ Precursors and MDH-Biomimetics*, **2018**.

[171] C. Schmuck, U. Machon, *Chem. Eur. J.* **2005**, *11*, 1109–1118.

[172] J. Coste, D. Le-Nguyen, B. Castro, *Tetrahedron Lett.* **1990**, *31*, 205–208.

[173] C. A. G. N. Montalbetti, V. Falque, *Tetrahedron* **2005**, *61*, 10827–10852.

[174] R. Paul, G. W. Anderson, *J. Am. Chem. Soc.* **1960**, *82*, 4596–4600.

[175] S. Roy, A. Mukherjee, B. Paul, O. Rahaman, S. Roy, G. Maithri, B. Ramya, S. Pal, D. Ganguly, A. Talukdar, *Eur. J. Med. Chem.* **2017**, *134*, 334–347.

[176] R. Shukla, A. Saeed, J. Simpson, D. Chopra, *CrystEngComm* **2017**, *19*, 5473–5491.

[177] B. Zhang, Z. Dou, Z. Xiong, N. Wang, S. He, X. Yan, H. Jin, *Bioorg. Med. Chem. Lett.* **2019**, *29*, 126714.

[178] J. C. Sheehan, P. A. Cruickshank, G. L. Boshart, *J. Org. Chem.* **1961**, *26*, 2525–2528.

[179] G. C. Windridge, E. C. Jorgensen, *J. Am. Chem. Soc.* **1971**, *17*, 6318–6319.

[180] R. H. Dekker, J. A. Duine, J. Frank, P. E. J. Verwiel, J. Westerling, *Eur. J. Biochem.* **1982**, *125*, 69–73.

[181] C. J. Unkefer, D. R. Houck, B. M. Britt, T. R. Sosnick, J. L. Hanners, *Methods Enzymol.* **1995**, *258*, 227–235.

[182] D. X. Hu, P. Grice, S. V. Ley, *J. Org. Chem.* **2012**, *77*, 5198–5202.

[183] M. J. Hudson, L. M. Harwood, D. M. Laventine, F. W. Lewis, *Inorg. Chem.* **2013**, *52*, 3414–3428.

[184] N. Kaltsoyannis, *Inorg. Chem.* **2013**, *52*, 3407–3413.

[185] L. J. Daumann, P. Werther, M. J. Ziegler, K. N. Raymond, *J. Inorg. Biochem.* **2016**, *162*, 263–273.

[186] L. J. Daumann, D. S. Tatum, B. E. R. Snyder, C. Ni, G. L. Law, E. I. Solomon, K. N. Raymond, *J. Am. Chem. Soc.* **2015**, *137*, 2816–2819.

[187] R. J. Abergel, A. D'Aléo, C. N. P. Leung, D. K. Shun, K. N. Raymond, *Inorg. Chem.* **2009**, *48*, 10868–10870.

[188] D. H. Zhu, M. J. Kappel, K. N. Raymond, *Inorg. Chim. Acta* **1988**, *147*, 115–121.

[189] L. C. Uhlir, P. W. Durbin, N. Jeung, K. N. Raymond, *J. Med. Chem.* **1993**, *36*, 504–509.

[190] S. M. Kraemer, J. Xu, K. N. Raymond, G. Sposito, *Environ. Sci. Technol.* **2002**, *36*, 1287–1291.

[191] R. C. Hider, X. Kong, *Nat. Prod. Rep.* **2010**, *27*, 637–657.

[192] G. Tircsó, Z. Garda, F. K. Kálmán, Z. Baranyai, I. Pócsi, G. Balla, I. Tóth, *J. Inorg. Biochem.* **2013**, *127*, 53–61.

[193] M. Bau, N. Tepe, D. Mohwinkel, *Earth Planet. Sci. Lett.* **2013**, *364*, 30–36.

[194] E. A. Christenson, J. Schijf, *Geochim. Cosmochim. Acta* **2011**, *75*, 7047–7062.

[195] Q. Laurent, L. K. Batchelor, P. J. Dyson, *Organometallics* **2018**, *37*, 915–923.

[196] F. Chu, M. E. Lidstrom, *J. Bacteriol.* **2016**, *198*, 1317–1325.

[197] Y. Zheng, J. Huang, F. Zhao, L. Chistoserdova, *mBio* **2018**, *9*, e02430-17.

[198] J. Huang, Z. Yu, L. Chistoserdova, *Front. Microbiol.* **2018**, *9*, 1366.

[199] A. M. Shiller, E. W. Chan, D. J. Joung, M. C. Redmond, J. D. Kessler, *Sci. Rep.* **2017**, *7*, 1–9.

[200] S. Tsushima, *Phys. Chem. Chem. Phys.* **2019**, *21*, 21979–21983.

[201] N. Nakamura, T. Kohzuma, H. Kuma, S. Suzuki, *Inorg. Chem.* **1994**, *33*, 1594–1599.

[202] S. White, G. Boyd, F. S. Mathews, Z. xiang Xia, W. wen Dai, Y. fan Zhang, V. L. Davidson, *Biochemistry* **1993**, *32*, 12955–12958.

[203] S. Suzuki, T. Sakurai, S. Itoh, Y. Ohshiro, *Inorg. Chem.* **1988**, *27*, 591–592.

[204] L. Tommasi, L. Shechter-Barloy, D. Varech, J.-P. P. Battioni, B. Donnadieu, M. Verelst, A. Bousseksou, D. Mansuy, J.-P. P. Tuchagues, *Inorg. Chem.* **1995**, *34*, 1514–1523.

[205] J. B. Noar, E. J. Rodriguez, T. C. Bruice, *J. Am. Chem. Soc.* **1985**, *107*, 7198–7199.

[206] M. Wanner, T. Sixt, K.-W. Klinkhammer, W. Kaim, *Inorg. Chem.* **1999**, *38*, 2753–2755.

[207] H. Mitome, T. Ishizuka, Y. Shiota, K. Yoshizawa, T. Kojima, *Inorg. Chem.* **2013**, *52*, 2274–2276.

[208] H. Mitome, T. Ishizuka, Y. Shiota, K. Yoshizawa, T. Kojima, *Dalton Trans.* **2015**, *44*, 3151–3158.

[209] B. Schwederski, V. Kasack, W. Kaim, E. Roth, J. Jordanov, *Angew. Chem. Int. Ed.* **1990**, *29*, 78–79.

[210] P. Di Bernardo, A. Melchior, M. Tolazzi, P. L. Zanonato, *Coord. Chem. Rev.* **2012**, *256*, 328–351.

[211] H. A. Benesi, J. H. Hildebrand, *J. Am. Chem. Soc.* **1949**, *71*, 2703–2707.

[212] T. A. Khan, M. Sheoran, V. Nikhil Raj M., S. Jain, D. Gupta, S. G. Naik, *Spectrochim. Acta, Part A* **2018**, *189*, 176–182.

[213] S. R. Patil, J. P. Nandre, D. Jadhav, S. Bothra, S. K. Sahoo, M. Devi, C. P. Pradeep, P. P. Mahulikar, U. D. Patil, *Dalton Trans.* **2014**, *43*, 13299–13306.

[214] S. A. Mizyed, M. Ashram, R. Saymeh, D. Marji, *Z. Naturforsch. B* **2005**, *60*, 1133–1137.

[215] K. Srinivasan, T. Stalin, K. Sivakumar, *Spectrochim. Acta, Part A* **2012**, *94*, 89–100.

[216] F. Yan, M. Wang, D. Cao, N. Yang, B. Ma, L. Chen, *J. Spectro.* **2013**, *2013*, 1–7.

[217] H. Tomiyasu, J. L. Zhao, X. L. Ni, X. Zeng, M. R. J. Elsegood, B. Jones, C. Redshaw, S. J. Teat, T. Yamato, *RSC Adv.* **2015**, *5*, 14747–14755.

[218] B. Chowdhury, S. Khatua, R. Dutta, S. Chakraborty, P. Ghosh, *Inorg. Chem.* **2014**, *53*, 8061–8070.

[219] B. Dolai, S. Nayim, M. Hossain, P. Pahari, A. Kumar Atta, *Sens. Actuators B* **2019**, *279*, 476–482.

[220] R. Waranyoupalin, S. Wongnawa, M. Wongnawa, C. Pakawatchai, P. Panichayupakaranant, P. Sherdshoopongse, *Cent. Eur. J. Chem.* **2009**, *7*, 388–394.

[221] L. Tang, F. Li, M. Liu, R. Nandhakumar, *Spectrochim. Acta, Part A* **2011**, *78*, 1168–1172.

[222] P. Thordarson, *Chem. Soc. Rev.* **2011**, *40*, 1305–1323.

[223] J. S. Renny, L. L. Tomasevich, E. H. Tallmadge, D. B. Collum, *Angew. Chem. Int. Ed.* **2013**, *52*, 11998–12013.

[224] P. Job, *Ann. Chim.* **1928**, *9*, 113 – 203.

[225] J. H. Yoe, A. L. Jones, *Ind. Eng. Chem. Anal. Ed.* **1944**, *16*, 111–115.

[226] R. M. Izatt, J. D. Lamb, J. J. Christensen, B. L. Haymore, *J. Am. Chem. Soc.* **1977**, *99*, 8344–8346.

[227] A. Roca-Sabio, M. Mato-Iglesias, D. Esteban-Gómez, É. Toth, A. De Bias, C. Platas-Iglesias, T. Rodríguez-Blas, *J. Am. Chem. Soc.* **2009**, *131*, 3331–3341.

[228] C. A. Chang, M. E. Rowland, *Inorg. Chem.* **1983**, 3866–3869.

[229] A. Hu, S. N. MacMillan, J. J. Wilson, *J. Am. Chem. Soc.* **2020**, *142*, 13500–13506.

[230] G. W. Gokel, D. M. Goli, C. Minganti, L. Echegoyen, *J. Am. Chem. Soc.* **1983**, *105*, 6786–6788.

[231] Y. Liu, B. H. Han, Y. T. Chen, *Coord. Chem. Rev.* **2000**, *200–202*, 53–73.

[232] R. Janßen, V. A. Vetsova, D. Putz, P. Mayer, L. J. Daumann, *Synthesis* **2023**, *55*, 1000–1006.

[233] C. P. Nash, *J. Phys. Chem.* **1960**, *64*, 950–953.

[234] H. Tsukube, S. Shinoda, *Chem. Rev.* **2002**, *102*, 2389–2403.

[235] Z. Liu, W. He, Z. Guo, *Chem. Soc. Rev.* **2013**, *42*, 1568–1600.

[236] G. Otting, *J. Biomol. NMR* **2008**, *42*, 1–9.

[237] F. Piccinelli, M. Leonzio, M. Bettinelli, M. Monari, C. Grazioli, A. Melchior, M. Tolazzi, *Dalton Trans.* **2016**, *45*, 3310–3318.

[238] I. Hemmilä, V. Laitala, *J. Fluoresc.* **2005**, *15*, 529–542.

[239] J.-C. G. Bünzli, C. Piguet, *Chem. Soc. Rev.* **2005**, *34*, 1048–1077.

[240] K. M. Orcutt, W. Scott Jones, A. McDonald, D. Schrock, K. J. Wallace, *Sensors* **2010**, *10*, 1326–1337.

[241] W. Zagorec-Marks, L. G. Dodson, P. Weis, E. K. Schneider, M. M. Kappes, J. M. Weber, *J. Am. Chem. Soc.* **2021**, *143*, 17778–17785.

[242] J. R. N. Haler, V. Lemaur, J. Far, C. Kune, P. Gerbaux, J. Cornil, E. De Pauw, *J. Am. Soc. Mass Spectrom.* **2020**, *31*, 633–641.

[243] J. F. Greisch, P. Weis, K. Brendle, M. M. Kappes, J. R. N. Haler, J. Far, E. De Pauw, C. Albers, S. Bay, T. Wurm, M. Rudolph, J. Schulmeister, A. S. K. Hashmi, *Organometallics* **2018**, *37*, 1493–1500.

[244] K. Michelmann, J. A. Silveira, M. E. Ridgeway, M. A. Park, *J. Am. Soc. Mass Spectrom.* **2015**, *26*, 14–24.

[245] S. M. Stow, T. J. Causon, X. Zheng, R. T. Kurulugama, T. Mairinger, J. C. May, E. E. Rennie, E. S. Baker, R. D. Smith, J. A. McLean, S. Hann, J. C. Fjeldsted, *Anal. Chem.* **2017**, *89*, 9048–9055.

[246] H. E. Revercomb, E. A. Mason, *Anal. Chem.* **1975**, *47*, 970–983.

[247] F. Furche, R. Ahlrichs, C. Hättig, W. Klopper, M. Sierka, F. T. Weigend, *WIREs Comput. Mol. Sci.* **2014**, *4*, 91–100.

[248] *Turbomole V7.5.1*, Development Of University Of Karlsruhe And Forschungszentrum Karlsruhe Gmbh, Turbomole Gmbh, **2021**.

[249] P. A. M. Dirac, *Proc. R. Soc. A* **1928**, *117*, 610–624.

[250] J. P. Perdew, Y. Wang, *Phys. Rev. B* **1992**, *45*, 13244–13249.

[251] J. P. Perdew, Y. Wang, *Phys. Rev. B* **2018**, *98*, 079904.

[252] J. C. Slater, *Phys. Rev.* **1951**, *81*, 385–390.

[253] J. Tao, J. P. Perdew, V. N. Staroverov, G. E. Scuseria, *Phys. Rev. Lett.* **2003**, *91*, 146401.

[254] K. Eichkorn, O. Treutler, H. Öhm, M. Häser, R. Ahlrichs, *Chem. Phys. Lett.* **1995**, *240*, 283–290.

[255] A. Schäfer, H. Horn, R. Ahlrichs, *J. Chem. Phys.* **1992**, *97*, 2571–2577.

[256] F. Weigend, *Phys. Chem. Chem. Phys.* **2006**, *8*, 1057–1065.

[257] F. Weigend, R. Ahlrichs, *Phys. Chem. Chem. Phys.* **2005**, *7*, 3297–3305.

[258] F. Weigend, M. Häser, H. Patzelt, R. Ahlrichs, *Chem. Phys. Lett.* **1998**, *294*, 143–152.

[259] M. D. Hanwell, D. E. Curtis, D. C. Lonie, T. Vandermeersch, E. Zurek, G. R. Hutchison, *J. Cheminf.* **2012**, *4*, 17.

[260] C. Larriba, C. J. Hogan Jr, *J. Comput. Phys.* **2013**, *251*, 344–363.

[261] C. Larriba, C. J. Hogan Jr, *J. Phys. Chem. A* **2013**, *117*, 3887–3901.

[262] T. Wu, J. Derrick, M. Nahin, X. Chen, C. Larriba-Andaluz, *J. Chem. Phys.* **2018**, *148*, 074102.

[263] S. Warnke, J. Seo, J. Boschmans, F. Sobott, J. H. Scrivens, C. Bleiholder, M. T. Bowers, S. Gewinner, W. Schöllkopf, K. Pagel, G. Von Helden, *J. Am. Chem. Soc.* **2015**, *137*, 4236–4242.

[264] Y. J. Zheng, T. C. Bruice, *PNAS* **1997**, *94*, 11881–11886.

[265] M. Pinsky, D. Avnir, *Inorg. Chem.* **1998**, *37*, 5575–5582.

[266] S. Alvarez, P. Alemany, D. Casanova, J. Cirera, M. Llunell, D. Avnir, *Coord. Chem. Rev.* **2005**, *249*, 1693–1708.

[267] S. Alvarez, D. Avnir, M. Llunell, M. Pinsky, *New J. Chem.* **2002**, *26*, 996–1009.

[268] M. Llunell, D. Casanova, J. Cirera, P. Alemany, S. Alvarez, *Shape 2.1*, Universitat De Barcelona, Barcelona, Spain, **2013**.

[269] A. Ruiz-Martínez, D. Casanova, S. Alvarez, *Chem. Eur. J.* **2008**, *14*, 1291–1303.

[270] A. Ruiz-Martínez, D. Casanova, S. Alvarez, *Dalton Trans.* **2008**, 2583–2591.

[271] E. A. Quadrelli, *Inorg. Chem.* **2002**, *41*, 167–169.

[272] D. Brynn Hibbert, P. Thordarson, *Chem. Commun.* **2016**, *52*, 12792–12805.

[273] M. Prejanò, T. Marino, N. Russo, *Chem. Eur. J.* **2017**, *23*, 8652–8657.

[274] M. Leopoldini, N. Russo, M. Toscano, *Chem. Eur. J.* **2007**, *13*, 2109–2117.

[275] X. Zhang, S. Y. Reddy, T. C. Bruice, *PNAS* **2007**, *104*, 745–749.

[276] S. Y. Reddy, T. C. Bruice, *J. Am. Chem. Soc.* **2003**, *125*, 8141–8150.

[277] Y. J. Zheng, Z. X. Xia, Z. W. Chen, F. S. Mathews, T. C. Bruice, *PNAS* **2001**, *98*, 432–434.

[278] J. M. Cox, D. J. Day, C. Anthony, *Biochim. Biophys. Acta* **1992**, *1119*, 97–106.

[279] R. Zhang, R. Zhang, R. Jian, L. Zhang, M. T. Zhang, Y. Xia, S. Luo, *Nat. Commun.* **2022**, *13*, 1–10.

[280] W. L. Dorfner, P. J. Carroll, E. J. Schelter, *Org. Lett.* **2015**, *17*, 1850–1853.

[281] C. F. H. Allen, *J. Am. Chem. Soc.* **1930**, *52*, 2955–2959.

[282] O. L. Brady, *J. Chem. Soc.* **1931**, 756–759.

[283] H. van Koningsveld, J. C. Jansen, J. A. Jongejan, J. J. Frank, J. A. Duine, *Acta Crystallogr. Sect. C* **1985**, *41*, 89–92.

[284] M. Prejanò, N. Russo, T. Marino, *Chem. Eur. J.* **2020**, *26*, 11334–11339.

[285] I. Kaljurand, A. Kütt, L. Sooväli, T. Rodima, V. Mäemets, I. Leito, I. A. Koppel, *J. Org. Chem.* **2005**, *70*, 1019–1028.

[286] S. Itoh, H. Kawakami, S. Fukuzumi, *J. Am. Chem. Soc.* **1998**, *120*, 7271–7277.

[287] S. Gómez-Manzo, A. A. González-Valdez, J. Oria-Hernández, H. Reyes-Vivas, R. Arreguín-Espinosa, P. M. H. Kroneck, M. E. Sosa-Torres, J. E. Escamilla, *FEMS Microbiol. Lett.* **2012**, *328*, 106–113.

[288] C. W. M. Kay, B. Mennenga, H. Görisch, R. Bittl, *FEBS Lett.* **2004**, *564*, 69–72.

[289] H. Metz, G. Völkel, W. Windsch, *Phys. Status Solidi A* **1990**, *122*, K73–K76.

[290] Bruker BioSpin EPR, *EMXnano, Application User Manual*, Rheinstetten, **2016**.

[291] T. Sarna, J. S. Hyde, H. M. Swartz, *Science* **1976**, *192*, 1132–1134.

[292] S. W. Meinhardt, T. Ohnishi, *Biochim. Biophys. Acta* **1992**, *1100*, 67–74.

[293] W. E. Antholine, J. S. Hyde, H. M. Swartz, *J. Magn. Reson.* **1978**, *29*, 517–522.

[294] K. Karandashev, Z.-H. Xu, M. Meuwly, J. Vaníček, J. O. Richardson, *Struct. Dyn.* **2017**, *4*, 061501.

[295] H. Gu, S. Zhang, *Molecules* **2013**, *18*, 9278–9292.

[296] D. Roston, Z. Islam, A. Kohen, *Molecules* **2013**, *18*, 5543–5567.

[297] E. M. Simmons, J. F. Hartwig, *Angew. Chem. Int. Ed.* **2012**, *51*, 3066–3072.

[298] K. Francis, G. Gadda, in *Methods Enzymol.*, Elsevier Inc., **2019**, pp. 115–143.

[299] M. Gómez-Gallego, M. A. Sierra, *Chem. Rev.* **2011**, *111*, 4857–4963.

[300] Z. Mao, C. T. Campbell, *ACS Catal.* **2020**, *10*, 4181–4192.

[301] A. L. Knasin, E. J. Schelter, in *Methods Enzymol.*, Elsevier Science, **2021**, pp. 19–55.

[302] M. G. Goodwin, C. Anthony, *Biochem. J.* **1996**, *318*, 673–679.

[303] S. I. Chan, P. Chuankhayan, P. K. Reddy Nareddy, I.-K. Tsai, Y.-F. Tsai, K. H.-C. Chen, S. S.-F. Yu, C.-J. Chen, *J. Am. Chem. Soc.* **2021**, *143*, 3359–3372.

[304] S. Stoll, A. Schweiger, *J. Magn. Reson.* **2006**, *178*, 42–55.

[305] *Bruker (2015). SAINT. Bruker AXS Inc., Madison, Wisconsin, USA.*, **2015**.

[306] *Bruker (2001). SADABS. Bruker AXS Inc., Madison, Wisconsin, USA.*, **2001**.

[307] G. M. Sheldrick, *Acta Crystallogr. Sect. A* **2015**, *A71*, 3–8.

[308] L. J. Farrugia, *J. Appl. Crystallogr.* **2012**, *45*, 849–854.

[309] T. Urakami, A. Tanaka, K. Yamaguchi, T. Tsuji, E. Niki, *BioFactors* **1995**, *5*, 139–146.

[310] M. Travnicek, J. Pospisil, M. Potacek, *Collect. Czech. Chem. Commun.* **1999**, *64*, 1993–2006.

[311] G. Tóth, B. Balázs, G. Horváth, D. Magiera, H. Duddeck, I. Bitter, *J. Inclusion Phenom. Macrocyclic Chem.* **2002**, *43*, 145–148.

[312] M. Niemeyer, *Z. Anorg. Chem.* **2006**, *632*, 1449–1456.

[313] A. Krasovskiy, F. Kopp, P. Knochel, *Angew. Chem. Int. Ed.* **2006**, *45*, 497–500.

[314] H. Diehl, F. Lindstrom, *Anal. Chem.* **1959**, *31*, 414–418.

[315] R. T. Gettar, E. A. Gautier, R. E. Servant, D. A. Batistoni, *J. Chromatogr. A* **1999**, *855*, 111–119.

[316] M. D. Yilmaz, H. A. Oktem, *Anal. Chem.* **2018**, *90*, 4221–4225.